Electrochemical carbon dioxide capture *via* mineralisation or reduction

Mark Robert Dowsett

Doctor of Philosophy

University of York

Chemistry

September 2020

Thesis Abstract

Since the start of the industrial revolution, global temperatures have risen by approximately 1 °C. The human population is now starting to notice the effects of this change. Polar ice caps are melting at an ever faster rate,[1] flooding[2] is becoming more commonplace and wildfires are repeatedly raging across more parts of the globe.[3] The temperature rise has been correlated with increases in atmospheric carbon dioxide (CO_2) levels. Researchers are attempting to find routes to capture CO_2 for permanent storage or to upgrade it for use as valuable chemical feedstocks. Electrochemical CO_2 capture methods are attractive owing to their ability to harness renewable energy sources such as solar energy. In Chapter 2, a technology for achieving carbon capture and mineralisation using aqueous electrochemistry is described. The conversion of waste metal sources into metal carbonates is explored. The CO_2 capture is enhanced by a supercapacitive swing adsorption effect that concentrates carbon dioxide in solution.

As an alternative application, CO_2 can be electrochemically reduced with electrons and protons to form valuable feedstock molecules such as carbon monoxide or fuel-type molecules such as ethane. To perform this electrochemistry on an industrial scale, the cathode catalyst must be highly efficient and selective. A novel type of electrocatalyst is synthesised in Chapter 3 using protected diazonium salts to modify a copper electrode, and the resultant materials are tested for their performance in the reduction of CO_2 in Chapter 4. Finally, in Chapter 5 a novel strategy for the development of a sub-monolayer modification on an electrocatalyst is explored, this may be another useful tool for designing a new type of organically modified cathodes for electrocatalysis.

Contents

List of Tables

List of Figures

Acknowledgements

My first and biggest thanks go to my supervisors Dr Alison Parkin and Prof. Mike North for their excellent support for 4 years. I would like to thank Alison in particular for the intelligent and hilarious supervisor meetings that often descended into madness. You have brought me on as a scientist and a person. To Mike, thank you for the knowledgeable guidance and a great trip to Whitby. I would also like to thank Dr Richard Douthwaite for the very helpful meetings and the use of his equipment.

To the excellent folks in the workshops that have helped to design and build most of the materials that made this PhD possible, thank you. In particular to Tim Ayres for personal support and the finest soldering I can image. To Abby Mortimer also for the exciting chats and ridiculously complex glasswork. Finally to Mark and Stuart for their sheer craftsmanship and willingness to help. In a similar fashion I would like to thank Dr David Pugh for a great many things including telling me that a particular synthesis was “not going to be easy”.

Nicholas Yates I feel deserves his own paragraph. For the biggest personality you could imagine, I will (and do) certainly miss having you around asking inappropriate questions. I’ve loved working alongside you and you have been an excellent scientist to chat things through with. You will go far and I look forward to watching that happen.

All the folks in the Parkin, Fascione and Willems group have been an absolute joy to work with and I will never forget the memories we had. Harriet Chidwick you have been the most excitable and hilarious neighbour, I will miss our early morning swims and the “work” chats. Emily Flack and Robin Brabham have made my whole PhD the enjoyable experience it has been – I don’t know what to say apart from “dream team”. To Julia Walton, you deserve a medal for the effort you put in to go above and beyond. Tessa, Darshita and Richard thank you for the wonderful chats, especially about weddings and Richard’s fantastic mentoring skills. Thank you to everyone else who passed through lower B-block for making my time enjoyable including Lewis, Jenny, Tasha, Tom, Katie and Sol. To Katie Lamb who helped me at the start of my PhD, thank you for all your hard work and answering endless questions! To the students that I worked with along the way, Cassie, Adam and John – you helped to make this possible and I wish you the best wherever you go. I spent a good deal of time with several members of the Douthwaite group and loved every second, so thank you to Mina, Joy and Will. Finally, thank you to Will Drysdale and his moral support.

Thank you to my mum, dad and sister for their unerring support, distractions and hilarity. You have been there through this all and I couldn't ask for more. My final thanks must go to my wife Eleanor, whom I married toward the end of my PhD. You have been with me through all of the ups and downs; I doubt I would still be standing without your support.

To all those who have been there past and present, thank you for a wonderful part of my life.

Author’s declaration

I declare that this thesis is a presentation of original work and I am the sole author. This work has not previously been presented for an award at this, or any other, University. All sources are acknowledged as references. Some results were generated in collaboration with other students or have been analysed in light of findings provided by co-workers. The specific details and credit are provided in summary at the start of each Results Chapter, as well as being detailed in the relevant parts of the main text.

Chapter 1. Thesis Introduction

This thesis describes the development of new methodologies for electrochemical carbon dioxide mineralisation (Chapter 2) and carbon dioxide electroreduction (Chapters 3-5). Global warming and the role that CO_2 emissions have played in causing a global temperature increase are discussed before the common methods of mitigating carbon emissions through carbon capture and storage (CCS) are explored. Research into upgrading CO_2 into a useful by-product has been conducted by a broad scientific community and developments in one of the most environmentally friendly methods, carbon dioxide electroreduction (CO2ER), are explored.

1.1 The CO_2 problem and global warming

Anthropogenic sources have released 1340 Gt of CO_2 since the start of the industrial revolution, which is believed to have caused a global average temperature increase of 1 °C.[4] Global attention is being focussed on the climate change this is causing and the loss of habitat and resources that accompany it. A vast amount of research is being undertaken to mitigate further CO_2 emissions and stop further dramatic increases in global temperature.[5] There are a growing number of models that predict the temperature change for the 21st century. One such model, known as Representative Concentration Pathways (RCPs), correlates different CO_2 emission scenarios with the possible temperature profiles (Figure 1).[6] Recent estimates state that to avoid a 2 °C global temperature increase, no more than an additional 1100 Gt of CO_2 may be released before the end of 2050.[7] If this CO_2 level is exceeded the corresponding temperature increase is predicted to have a significant impact on the planet's ecosystem and negative consequences for the human race.

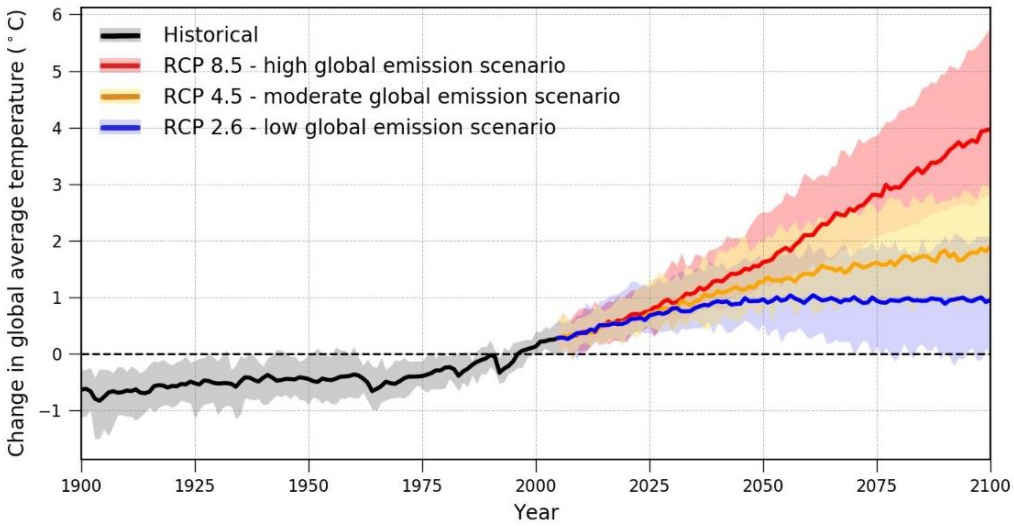

Figure 1. RCP temperature models relative to the 1986-2005 reference period. Reproduced from reference 6.

It is worth noting that CO_2 emissions are not the only contributor to global warming. Other gases such as methane and chlorofluorocarbons (CFCs) have significant impacts on the global temperature. This is often known as global radiative forcing, wherein any given gaseous emission contributes toward the global temperature increase. The relative impacts of each gas are calculated from the global emission of that gas and its potential for temperature increase, known as global warming potential. By 2018, CO_2 accounted for approximately 65% of the global radiative forcing effect, whilst methane accounted for approximately 15%.[8]

1.1.1 Major sources of CO_2

It is not surprising that the largest planetary emission source of CO_2 is the direct combustion of fossil fuels,[9] a process which is typically used to generate electricity or power transportation. A summary of the largest CO_2 emission sources in the USA (2017) is given in Figure 2. Calcination of limestone for cement production (Reaction 1), iron and steel production and the chemical industries were amongst some of the largest polluters in terms of CO_2 emissions.[10, 11]

$$CaCO_3 \xrightarrow{\Delta} CaO + CO_2 \qquad \text{(Reaction 1)}$$

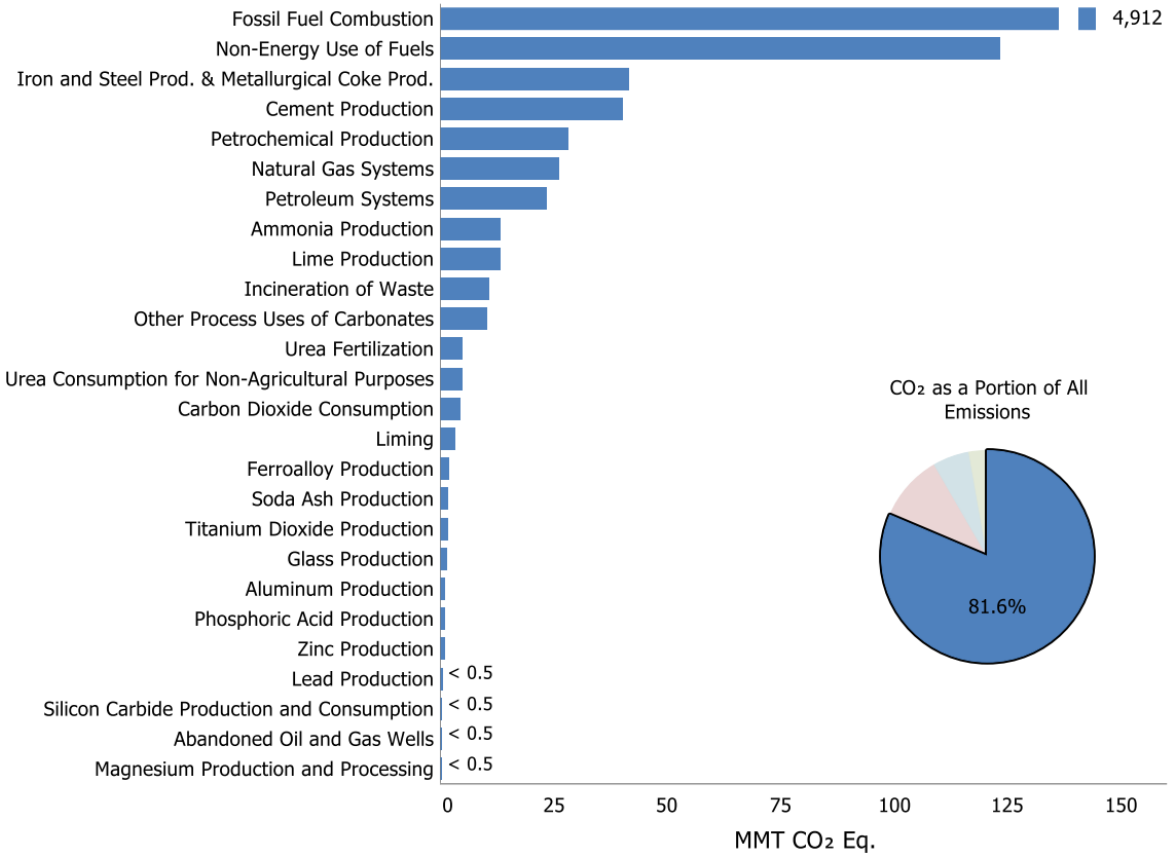

Figure 2. United States CO_2 emission sources in 2017. Reproduced from reference 11.

1.1.2 Removing CO_2: CCS or CCU

To counteract ever rising CO_2 levels, humanity must either reduce source emissions or prevent the CO_2 that is produced from being released into the atmosphere. Reducing source emissions addresses the problem directly and may be achieved by utilising other primary energy sources such as solar, wind or tidal energies. However, making this switch requires significant amounts of time. Given the urgency of this global crisis (see Figure 1), scientists have investigated both CCS and carbon capture and utilisation (CCU) technologies to mitigate carbon emissions in the interim period. Mitigating carbon emissions by CCS technology means attempting to either lock CO_2 into an inert bulk material that can be stored, or involves sequestering a purified CO_2 gas stream underground at high pressures.[12] On the other hand, CCU refers to the conversion of CO_2 into high value products, which can make such a process more economically viable.

Large point emission sources of CO_2 such as coal-fired gas stations, cement production or chemical industry plants have a variety of compositions of output gas which can provide a challenge for researchers given that some CCS/CCU technologies only work at specific concentrations, or can be

poisoned by other effluent materials.[13, 14] For example the flue gas exit stream from coal-fired gas power stations typically contains only 7-14% CO_2, where often N_2 and O_2 are the majority component, whilst Ar and SO_x can be key contaminants.[15]

Capturing CO_2 always comes with an energy penalty that must be considered in the process lifecycle.[16] The input of energy required to drive the process or to synthesise required materials must be weighed against the carbon captured by the material and compared to the carbon emitted to drive the carbon capture process. This idea is illustrated in Figure 3 which highlights the impact a CO_2 absorption bed may have on a power plant where total CO_2 production is higher due to the energy penalty in running the technology, but the CO_2 emitted is significantly lower than without the technology. Coal-fired gas stations typically emit 3.6 GJ per tonne of CO_2 which can be converted to 158 kJ mol_{CO2}^{-1}.[17] This is the benchmark that any CO_2 capture technologies typically need to fall below to become a net absorber of CO_2 (CCS application) and must be accounted for in value added applications (CCU).

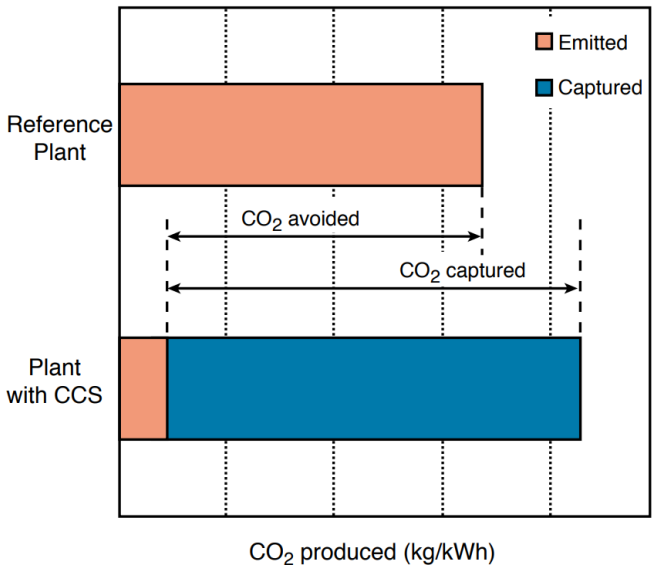

Figure 3. Example CO_2 emissions from power plants with and without a carbon capture technology. Reproduced from reference 18.

For CCS technologies to be viable, they must be cheap to run and versatile enough to attach to existing infrastructure.[16] This is often achieved by using cheap or waste products as CO_2 sorbents or synthetic reversible binding agents. Electrochemistry can be used to increase the efficiency of CCS technologies and provide new sources of CO_2 sorbent.[19] These ideas are explored in the following sections for their viability relative to energy requirements, scalability and/or profitability.

CCU technologies are not required to be as cheap as those for CCS, provided the product is of high enough value.[20] CCU is often achieved with expensive catalysts due to the difficulty in converting CO_2 to anything except a carbonate. Researchers have performed high temperature reactions such as methanation, reverse water-gas shift or the Fischer-Tropsch synthesis over catalysts typically containing precious metals to generate high value products from CO_2.[21-23] Low-temperature chemical catalysis is also possible to molecules such as cyclic carbonates.[24] Electrochemistry can be used in CCU applications as it removes the need for expensive and low Turnover Frequency (TOF) molecular catalysts. One of the most intense areas of research in this field is CO2ER which is the attempt to turn CO_2 selectively into one of its reduction products. CO2ER catalysis has been extensively explored since 1988 following pioneering work by Hori *et al.*[25] This has included a huge range of electrocatalytic conditions and catalytic cathode surfaces which will be discussed herein relative to product distributions. A variety of electrode modifications are also discussed for the impact they may have in creating a new generation of CO2ER electrocatalytic surface.

1.2 CO_2 capture and storage techniques

Current CCS technologies typically fall into one of three categories: post-combustion, pre-combustion and oxyfuel combustion.[18] Post-combustion involves binding CO_2 from a gas stream before releasing it again when required. This method can lead to a concentrated CO_2 gas stream and has previously been performed using materials containing oxygenate or amine species. Pre-combustion involves coal gasification, converting the fossil fuel to syngas (CO and H_2) mixtures followed by the water gas shift reaction (Reaction 2). H_2 can be separated from this syngas mixture to leave a pure CO_2 feed with H_2 as a valuable by product. Oxyfuel combustion involves burning fossil fuels in a pure oxygen atmosphere which produces a pure CO_2 and water gas feed, from which water can be easily condensed out.

$$CO + H_2O \longrightarrow CO_2 + H_2 \quad \text{(Reaction 2)}$$

Unfortunately, pre-combustion and oxyfuel technologies cannot easily be integrated into existing infrastructure and need dedicated facilities.[26] Post-combustion methods are the most versatile of the techniques as they can usually be appended to structures such as coal fired gas stations. Some post-combustion methods of carbon capture that rely on either oxygenate- or amine-based materials are described herein. It has also been shown that electrochemistry can be applied to

oxygenate and amine species CCS methods to further increase CO_2 capture rates and capacities and an electrochemical method for amine CO_2 capture is also detailed. Electrochemical capture of CO_2 using oxygenate species *via* metal recycling has also been performed, which is discussed alongside the research in Chapter 2.

1.2.1 CO_2 capture with solid materials

Post-combustion methods for CCS applications must be scalable to be able to mitigate the annual global CO_2 emissions (51.8 billion tonnes in 2019).[27] To mitigate emissions on this scale, a bulk material that is either naturally occurring or an industrial waste product must be used. Alternatively, a material that can reversibly bind CO_2 can be reused, wherein CO_2 is temporarily stored before it is released to regenerate the storage material as well as a concentrated CO_2 gas feed that can be sequestered.

1.2.1.1 Bulk solid materials for irreversible CO_2 capture

The use of naturally occurring or industrial waste solid materials can be an excellent method to permanently bind CO_2 in a solid form that can be easily handled and removed for burial. Often these solid materials contain alkaline oxides such as MgO and CaO because these react with CO_2 to produce solid carbonates. For example, waste cement primarily contains CaO and it can therefore be wetted and placed under high pressures of CO_2 to form a $CaCO_3$ precipitate.[28] This process could be achieved with an energy consumption of 0.42 MWh t_{CO2}^{-1} (66.5 kJ mol_{CO2}^{-1}). Large amounts of waste cement can be obtained from building demolition, however there are significant challenges that may increase cost and energy consumption such as extraction and transport. As an alternative, some studies have produced relatively pure CaO for CO_2 binding by calcinating limestone. Whilst this may be efficient for removing CO_2 at point sources, the process ultimately becomes a circular process of releasing and binding CO_2 that does not yield net absorption.[10]

Bulk materials such as fly ash and red mud also contain significant amounts of alkaline oxides and have been tested for CO_2 capture.[29, 30] Fly ash is a waste product produced when burning coal and is generally a fine powder, making it ideal as a high surface area and low-cost capture bed for CO_2. Chinese fly ash accounts for >50% of global production (580 million tonnes of Chinese fly ash) and typically contains just under 15% of activate alkaline oxides. Given that some studies have found that 0.102 kg of CO_2 can be capture per kg of fly ash, approximately 59 million tonnes of CO_2 could

easily be captured anually.[31] This method is an attractive CO_2 capture method as fly ash is generated at the coal fired gas stations and so does not require transport. Unfortunately, the amount of fly ash produced in China could only capture 0.16% of global CO_2 emissions.

Another source of alkaline metals for CO_2 capture can be found in hard water. High concentrations of 0.82 g L^{-1} and 2.58 g L^{-1} for Ca^{2+} and Mg^{2+} ions respectively can be found in waste water from desalination plants.[32, 33] Researchers have used these relatively high concentrations with a membrane separated electrochemical water splitting system to capture CO_2.[34] A cathode reduces water to hydrogen gas and hydroxide ions, the former is transported to the anode while the latter go on to bind calcium and magnesium cations and CO_2, forming carbonate materials. This process, balanced by the oxidation of hydrogen produced at the cathode, was proposed to be profitable due to the commercial value of the metal carbonates. Pure $CaCO_3$ and $MgCO_3$ could be sequentially produced by adjusting the pH at which electrolysis was performed (Figure 4) and taking advantage of precipitation of compounds at variable pH. The process could capture 4.65 tons of CO_2 within 1000 m^3 of seawater with an energy penalty of 5.68 MWh, meaning that this process would be difficult to scale and may only be performed for financial purposes.[34]

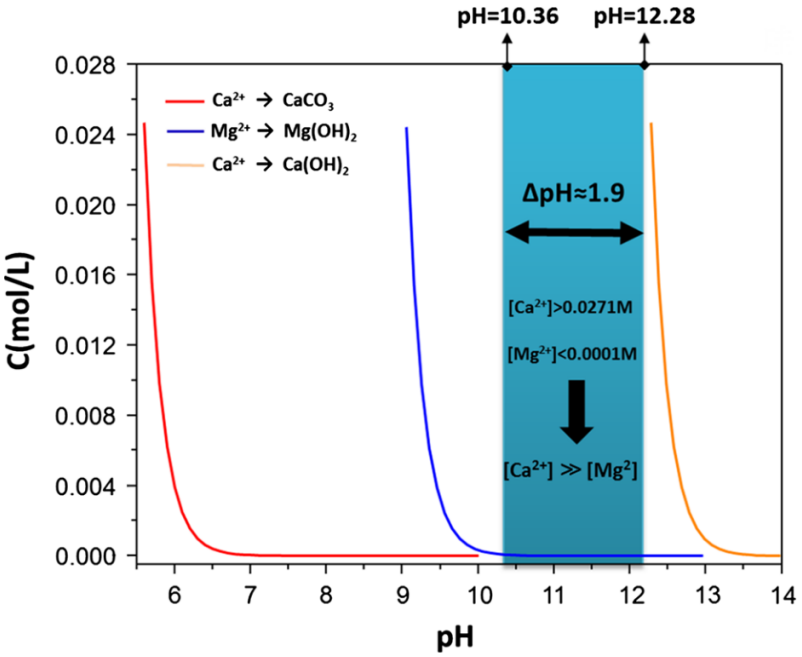

Figure 4. Concentration profiles of Ca^{2+} and Mg^{2+} with changing pH for hard water membrane electrolysis for CO_2 capture. Reprinted by permission from Copyright Clearance Center: Springer Nature, Environmental Earth Sciences, Reference 34, Copyright 2015.

1.2.1.2 Synthetic materials for reversible CO_2 capture and purification

As an alternative to the single-use materials detailed in the previous section, where low cost is an important driver, materials have also been sought that can temporarily store CO_2 and release it when required for either purification or sequestration purposes. Given that materials such as these are capable of reversible CO_2 binding, a higher cost can be tolerated, and researchers have aimed to synthesise materials with maximised binding capacity.

Taking inspiration from naturally occurring minerals, oxygenate and amine functionalities have been used to introduce a Lewis basic binding site to stabilise CO_2 as a carbonate or carbamate. Zeolites, porous and high surface area aluminosilicates, have been used for their product retention and storage capabilities.[35, 36] They can be used to readily bind CO_2 owing to Lewis basic oxide sites and are capable of releasing CO_2 upon heat treatment (a significant number of zeolites are thermally stable up to 800 °C).[37] Metal-Organic Frameworks (MOFs) have also been explored for similar reasons, often presenting both oxide and other organic moieties for CO_2 binding. Amine functionalities can be present in MOF linkers and have been shown to increase CO_2 binding.[38-40] These amine functionalities have also been introduced into zeolite materials for the same reason.[37] Some materials for reversible CCS applications such as zeolites and MOFs can be produced from green materials such as rice husks or red mud.[37, 41]

1.2.2 Post-combustion CCS through amine scrubbing

The previous sections described some materials that can be used to irreversibly bind CO_2 for permanent storage. Alternatively, CO_2 can be reversibly removed from a gas stream through a technique called amine scrubbing, a technique that has been in use for 90 years.[42] During the first step of the process, an aqueous solution of monoethanolamine (MEA) is sprayed over the flue gas to promote CO_2 diffusion into the droplets where a carbamate salt is formed (Reaction 3). The carbamate salt can be decomposed later at temperatures between 100-120 °C to create a pure CO_2 gas stream for compression and storage.[42, 43] The pure CO_2 gas can be compressed to 100-150 bar for geological sequestration. This process requires approximately 0.37 MWh t_{CO2}^{-1} (58.6 kJ mol_{CO2}^{-1}) which is significantly lower than the energy output of coal fired gas stations (158 kJ mol_{CO2}^{-1}).[17, 42] Given that the majority of MEA can be regenerated and that this technique has a relatively low energy of CO_2 capture, this process is likely to become one of the major options for mitigating large point sources of CO_2.[44] Unfortunately MEA is prone to oxidative and thermal degradation by

contaminants in the effluent stream or temperatures much above 100 °C which has led to researchers trialling alternative amine sources such as piperazine.[43]

$$2\ RNH_2 + CO_2 \rightleftharpoons [RNH_3^+][RNHCOO^-] \quad \text{(Reaction 3)}$$

1.2.3 Electrochemically mediated amine regeneration

Electrochemically mediated amine regeneration (EMAR), where electrochemistry is used to replace heat treatment of amines in amine scrubbing, is an example of ongoing research directly targeted at improving the recyclability of a carbon capture technology *via* the use of electrochemistry.[19, 45] Ethylene diamine is used in the electrolyte to form carbamate salts with CO_2. When CO_2 is desired to be released for purification purposes, Cu^{2+} is electrochemically produced from a Cu anode at low voltages which decomposes the carbamates (Scheme 1). This becomes an electrocatalytic process due to the counter process being the reductive decomposition of the copper-amine complex. A theoretical calculation for a whole EMAR process including capture of CO_2 from a flue gas source as well as subsequent compression of pure CO_2 gas to 150 bar yielded energy penalty of 37-52 kJ mol_{CO2}^{-1}.[46, 47] Given that this process is electrochemically driven, driving this process with solar energy would reduce the energy penalty further. This technique has the potential to develop on existing amine scrubbing technology, however the energy penalties observed do not account for the complete process for sequestration of CO_2.

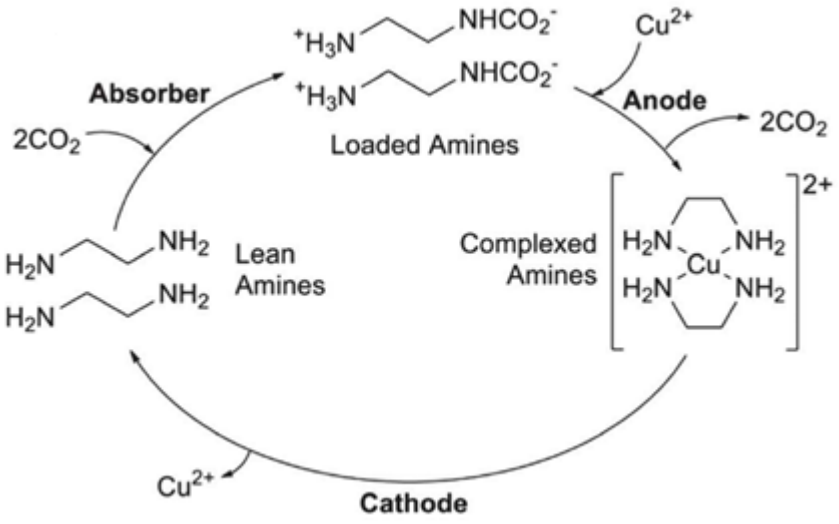

Scheme 1. Electrochemically mediated amine regeneration (EMAR) process showing the role of a copper anode. Reproduced with permission from reference 19. Copyright 2014, Royal Society of Chemistry.

Most CCS technologies rely on capture of CO_2 using Lewis basic sites such as oxides or amines. CCS processes that are most scalable rely on abundant waste resources or on regenerative systems. Chapter 2 demonstrates a technique for using waste metals for CCS using electrochemistry. These will be viewed in the context of global CO_2 emissions and the energies required for CO_2 capture. The importance of the interactions amine functional groups can have with CO_2 is revisited in Chapter 4 as part of our rational design of a CO_2 electro-reduction catalyst.

1.3 CO_2 electrochemical reduction

CO2ER was first performed in the 19th century, though it wasn't until the 1980s that the field received significant interest due to oil embargos in the 1970s.[48] By combining CO_2 with protons and electrons to produce useful hydrocarbon products, researchers target the production of fuel-type molecules or the building blocks used to create them, such as syngas (mixtures of CO and H_2). It is hoped the electrochemical reduction reactions can be powered by renewable and sustainable primary energy sources such as solar and wind technologies so that hydrocarbons can move from a CO_2-emitting primary energy source to a carbon-neutral secondary energy storage source. With 1146 papers published in 2018, some progress has been made toward fuel-type molecules, however many papers selectively generate single products that are valuable in their own right but are not fuel-type molecules. To activate the multitudes of reactions available, CO2ER electrocatalysts have been designed that are either solid state cathodes, small molecule catalysts, or more recently a mixture of the two.[49] This thesis provides a novel synthesis of a new type of CO2ER catalyst in Chapter 3 that is an organically modified solid state copper cathode. This new family of cathodes are then used for CO2ER catalysis in Chapter 4. Finally, Chapter 5 explores a novel electrode modification strategy designed to create new types of organically modified metal surfaces for CO2ER which remain untested.

1.3.1 Product distributions and competing reactions

A wide range of products can be synthesised from CO_2 reduction because of the range of accessible electroreduction pathways, as shown in Table 1. As well as simple one carbon (C_1) CO2ER products such as carbon monoxide, C-C bond coupling enables the formation of higher order products, where a six carbon (C_6) molecule is the longest chain produced.[50] The most common reaction products are low hydrocarbon species in the range $C_{1\text{-}2}$ such as carbon monoxide, methane, ethane, ethene and

related oxygenated species such as formic acid, as highlighted in Table 1.[51] When performing CO2ER, the different reduction reactions compete and the precise product cannot be controlled simply by setting the electrode potential according to the thermodynamic reduction potential values. This is because the overpotentials required for the reaction vary depending upon both electrode composition and morphology. Other conditions such as the electrolyte, temperatures and cell design can influence product selectivity and turnover frequencies. Some of these routine influences are discussed in the following sections. Some of the most desired products in CO2ER are CO, formic acid, ethene and higher order hydrocarbons (C_{3+}). At the frontier of product selectivity, C_1 products can be produced at >90%,[52, 53] C_2 products at >70%[54] and C_{3+} at >10%,[55] however high selectivities are often achieved at low current densities to supress competing reactions which can render some electrocatalysts unsuitable for use in chemical industry.

Table 1. Standard reduction potentials of CO_2 to low hydrocarbons in aqueous solutions at 1 atm and 25 °C, calculated according to the Nernst equation. Adapted from references 51 and 56.

Half-electrochemical reactions	**Standard electrode reduction potentials (V *vs*. SHE)**
$CO_{2\,(g)} + 4H^+ + 4e^- \rightleftharpoons C_{(s)} + 2H_2O_{(l)}$	0.210
$CO_{2\,(g)} + 2H_2O + 4e^- \rightleftharpoons C_{(s)} + 4OH^-_{(l)}$	-0.627
$CO_{2\,(g)} + 2H^+ + 2e^- \rightleftharpoons HCOOH_{(l)}$	-0.250
$CO_{2\,(g)} + 2H_2O + 2e^- \rightleftharpoons HCOO^-_{(aq)} + OH^-_{(aq)}$	-1.078
$CO_{2\,(g)} + 2H^+ + 2e^- \rightleftharpoons CO_{(g)} + H_2O_{(l)}$	-0.106
$CO_{2\,(g)} + 2H_2O + 2e^- \rightleftharpoons CO_{(g)} + 2OH^-_{(aq)}$	-0.934
$CO_{2\,(g)} + 4H^+ + 4e^- \rightleftharpoons CH_2O_{(l)} + H_2O_{(l)}$	-0.070
$CO_{2\,(g)} + 3H_2O + 4e^- \rightleftharpoons CH_2O_{(l)} + 4OH^-_{(aq)}$	-0.898
$CO_{2\,(g)} + 6H^+ + 6e^- \rightleftharpoons CH_3OH_{(l)} + H_2O_{(l)}$	0.016
$CO_{2\,(g)} + 5H_2O + 6e^- \rightleftharpoons CH_3OH_{(l)} + 6OH^-_{(aq)}$	-0.812
$CO_{2\,(g)} + 8H^+ + 8e^- \rightleftharpoons CH_{4\,(g)} + 2H_2O_{(l)}$	0.169
$CO_{2\,(g)} + 6H_2O + 8e^- \rightleftharpoons CH_{4\,(g)} + 8OH^-_{(aq)}$	-0.659
$2CO_{2\,(g)} + 2H^+ + 2e^- \rightleftharpoons H_2C_2O_{4\,(aq)}$	-0.500
$2CO_{2\,(g)} + 2e^- \rightleftharpoons C_2O_4^{2-}{}_{(aq)}$	-0.590
$2CO_{2\,(g)} + 12H^+ + 12e^- \rightleftharpoons CH_2CH_{2\,(g)} + 4H_2O_{(l)}$	0.064
$2CO_{2\,(g)} + 8H_2O + 12e^- \rightleftharpoons CH_2CH_{2\,(g)} + 12OH^-_{(aq)}$	-0.764
$2CO_{2\,(g)} + 12H^+ + 12e^- \rightleftharpoons CH_3CH_2OH_{(l)} + 3H_2O_{(l)}$	0.084
$2CO_{2\,(g)} + 9H_2O + 12e^- \rightleftharpoons CH_3CH_2OH_{(l)} + 12OH^-_{(aq)}$	-0.744

Proton sources are required to upgrade CO_2 to hydrogenated products *via* protonation of both oxygen and carbon atoms. Thus, CO2ER is routinely performed in aqueous electrolytes or with organic electrolytes containing protons. The use of proton sources often introduces the competing hydrogen evolution reaction (HER).[51] In general, suppression of HER is related to a decreased binding affinity of hydrogen atoms to the catalyst surface.[57] The following sections aim to paint a picture of the wide variety of variables which influence CO2ER product selectivity, while mechanistic models which explain these observations are outlined at the start of Chapter 4.

1.3.2 Conditions

Many reaction conditions are known to influence CO2ER product selectivity such as temperature, pH and electrolyte composition, pressure, mass transport and applied voltage.[25, 58] Voltage is the most routinely investigated parameter when testing a new catalytic surface due to the different overpotentials required to produce certain products at a range of current densities, as detailed in Section 1.3.2.4. Most researchers test their CO2ER electrocatalysts at room temperature (20 or 25 °C) and pressure in a 0.1 M or 0.5 M $KHCO_3$ aqueous electrolyte, although other aqueous salts have been used.[59, 60] Whilst organic solvents have been investigated for their role in CO2ER, aqueous systems are the most common as water provides a readily available proton source.[61, 62]

1.3.2.1 Electrolyte effects: solvent, salt and pH

Electrolytes are typically chosen for either CO_2 absorption capacity or pH buffering capacity. Aqueous solvent systems have become the benchmark for CO2ER due to the provision of a readily available proton source that is tolerant of many different salts. Figure 5 demonstrates the changing CO_2 concentration across a pH range in aqueous carbonate systems, one of the most common CO2ER electrolytes. In aqueous systems, the solubility of CO_2 in water is relatively low at 35 mmol dm^{-3}. Other organic solvents and ionic liquids have also been investigated and can exhibit significantly higher concentrations of dissolved CO_2, which has led to the reduced competition between CO2ER and HER in organic solvents.[61, 62]

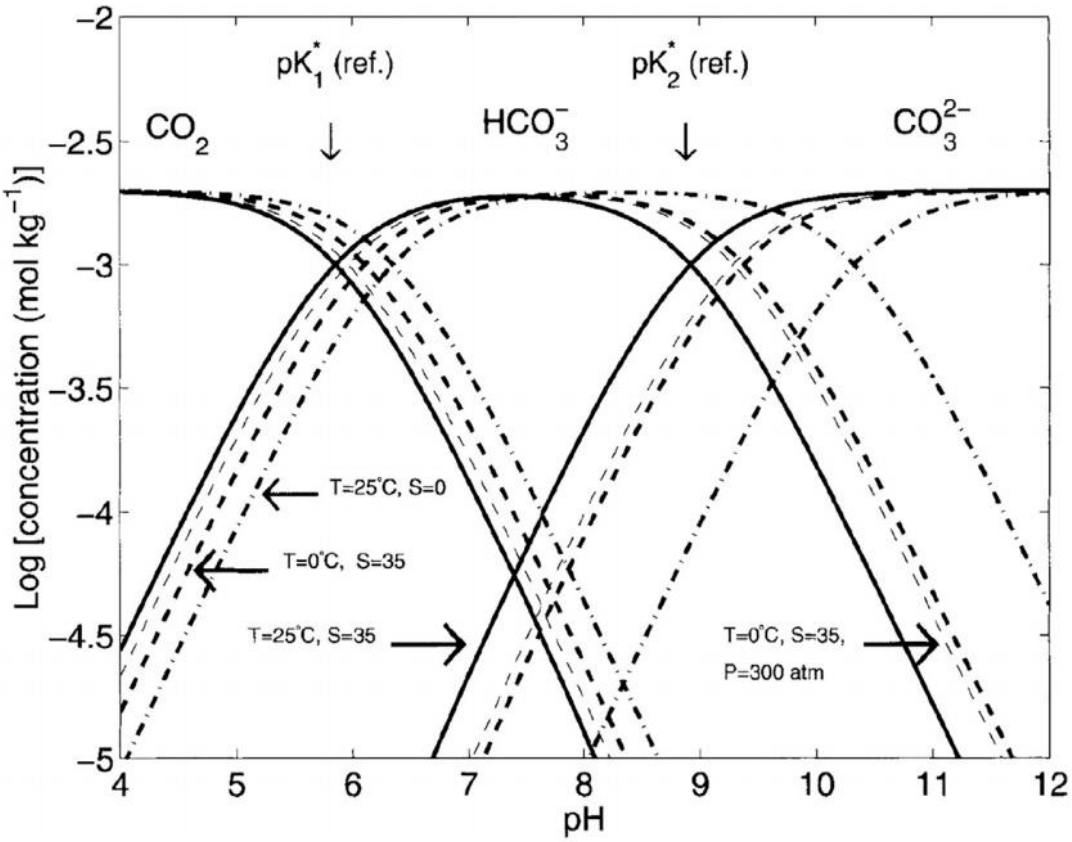

Figure 5. CO_2 solubility as a function of pH at different temperatures, salinities and pressures. Salt salinity: 35 g kg^{-1}. Reproduced from reference 63.

Most aqueous protic salts including carbonates, hydroxides, phosphates and sulfates have been investigated for their influence of CO2ER products and achieved current densities, whilst aprotic alkali halide and BF_4 salts have also been tested.[64, 65] These salts are recruited either for their local pH buffering capacity or for stabilisation of reaction intermediates at the electrode surface. There have been numerous studies on the solubility of CO_2 with common CO2ER electrolytes at different concentrations (Figure 6a).[66] These have a notable impact upon CO2ER selectivity (Figure 6b), however the response is not immediately predictable between different electrocatalysts and salts. Common methods of increasing the amount of dissolved CO_2 include bubbling through the solution and using gas diffusion electrodes.

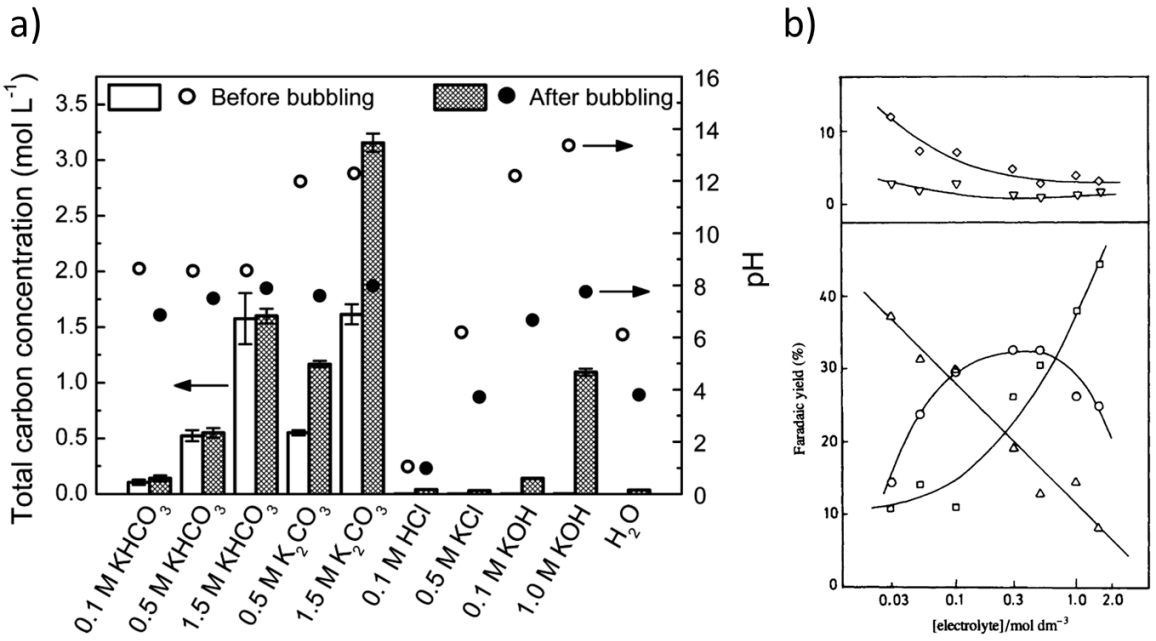

Figure 6. a) Total carbon concentration before and after bubbling CO_2 (100 mL min^{-1}) to saturation through various electrolytes. b) The effect of $KHCO_3$ electrolyte concentration on CO2ER products; Δ, C_2H_4; ○, CH_4; □, H_2; ◊, EtOH; ∇, Pr^nOH. Figure (a) reprinted (adapted) with permission from reference 66, Copyright (2015) American Chemical Society. Figure (b) reproduced from reference 67, Copyright 2014, Royal Society of Chemistry.

Several studies have correlated the increase in size of alkali metal cations with an increase in higher order hydrocarbon selectivity such as ethene and ethanol.[68] These trends only occur with some electrode materials and so it is hard to accurately predict trends.[69] Equally there is no obvious trend for higher order hydrocarbon selectivity using different anionic halides, however researchers have reported an increase in selectivity for methane when using an iodide salt.[70] The interplay between ion selectivity and product distribution in CO2ER is thought by some researchers to relate to the hydration sphere and possible buffering effect of the water molecules as well as the surface structures these agglomerates form.[71] In principle, this indicates a range of electrode-electrolyte interfaces are possible that could be understood using different electric double layer models. Unfortunately, there is no universal model that applies to most electrode surfaces.

Ionic liquids have been used to increase CO_2 solubility but have been found to affect CO2ER selectivity significantly. Ionic liquids can be used to stabilise the intermediate of CO_2 adsorption by interaction of a positive charge with the $[CO_2]^{\cdot-}$ initial reduction intermediate. This has previously been achieved using the $[Bmim][CF_3SO_3]$ in propylene carbonate solution.[72] Some cases have identified a >90% FE to CO.[73] The same mechanism has also been identified using pyridinium salts which display high selectivity toward methanol.[74] Ionic liquids help achieve high CO2ER selectivities by suppression of HER owing to the exclusion of water. Unfortunately, ionic liquids are hygroscopic

which can be difficult to avoid during operation of industrial processes. Studies have shown that increased water content promotes HER over CO2ER.[73]

1.3.2.2 Temperature & Pressure

In early work by Hori *et al.*, product distribution of CO2ER was found to be highly dependent on temperature.[75] Using a copper foil cathode in 0.5 M $KHCO_3$, the faradaic efficiency for methane production during galvanostatic electroreduction of CO_2 (5 mA cm^{-2}) could be decreased from 65% to almost 0% by increasing the temperature from 0 °C to 40 °C, whilst ethene selectivity rose from 4% to 20%. This study was supported by a later study by Kaneco *et al.* wherein copper cathodes again promoted methane formation in a 0.5 M $KHCO_3$ electrolyte cooled to 0 °C, but also produced formic acid.[76] Both studies highlighted a decrease in HER efficiency with decreasing temperatures owing to promotion of CO2ER. It was hypothesised that CO2ER was promoted at lower temperatures due to the preference for increased proton-coupled electron transfer, however this was not fully investigated.

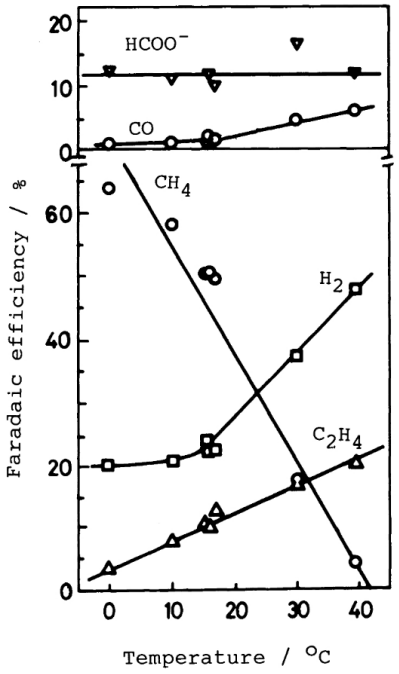

Figure 7. Product distribution variations with temperature in copper CO2ER in 0.5 M $KHCO_3$ at a current density of 5 mA cm^{-2}. Reproduced from reference 75.

A systematic study of variable pressure (1-60 atm CO_2) CO2ER was performed by Hara *et al*.[77] Under galvanostatic control, a copper electrode in aqueous 0.1 M $KHCO_3$ electrolyte showed peak faradaic efficiency toward higher order hydrocarbons, particularly methane and ethene, at pressures of 40-50 atm. Unfortunately, at higher pressures (>40 atm), this study could not account for increasing

amounts of current (FE < 85%), thus it remains unclear if even higher pressures would produce C_{3+} products.

For industrial applications, extreme temperatures and pressures have also been applied in CO2ER inside a solid oxide electrolysis cell (SOEC). These systems often feature a nickel supported on a metal oxide support. One example of a SOEC, a Ni/12.2% $Cr_2O_{3-\delta}$ electrocatalyst, operated at 800 °C and a 1.6 V potential difference which produced an extremely high current density of 2.07 A cm^{-2}. This produced a faradaic efficiency of over 90% toward CO.[78] Whilst practically this produces a valuable chemical feedstock, the system requires high thermal energy input to produce a low-order hydrocarbon that can otherwise be produced at room temperature at a slower rate.[79]

1.3.2.3 Mass transport

Mass transport is generally regarded as one of the most important aspects of CO2ER, though is one of the most difficult to control. Use of pH, electrolyte concentration, temperature, pressure and novel cell and electrode design (for example Gas Diffusion Electrodes) are some ways of boosting concentrations of CO_2 and proton sources at the electrode surface. For targeting specific products, it appears there is a balance to be struck between the two reagents; complete saturation of the electrode with CO_2 appears to yield CO and ethene type products, whilst low amounts of CO_2 and high H^+ concentration yields competing HER or low order hydrocarbons such as formic acid. Therefore, it is of interest to probe mass transport effects, though this area is often unstudied. This can be achieved using a rotating disk electrode (RDE) to induce convection throughout the cell and observe the impact on diffusion. Cyclic voltammetry was used by Ooka *et al.* to show that the absorption of CO_2 at a polycrystalline copper surface could inhibit HER. Figure 8 indicates example CVs at different rotation rates for aqueous CO2ER.[80] The study highlighted that there were two different routes in aqueous HER; 1) reduction of protons from the phosphate salt (designated HER-1) and 2) reduction of water molecules (designated HER-2). It found that HER-1 did not interfere with CO2ER at all, but that HER-2 competes with CO2ER. HER-2 was observed to inhibit CO2ER less at higher rotation rates.

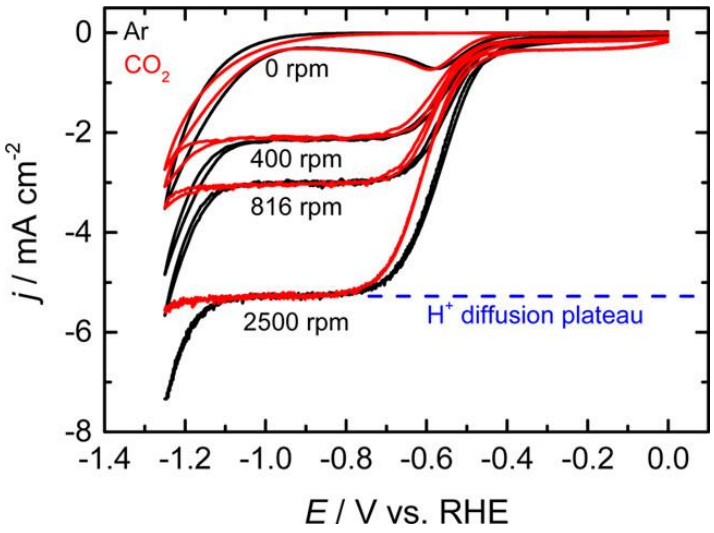

Figure 8. CVs of a polycrystalline copper RDE in 10 mM phosphate + 0.1 M $NaClO_4$ (pH 2.5) at various rotation rates saturated with Ar (Black) or CO_2 (red). Reprinted in part with permission from reference 80. Copyright 2017, ACS.

Whilst studies using RDEs for CO2ER are uncommon, some researchers have used RRDEs to quantitatively analyse the amount of product formed during cyclic voltammetry. An anodic platinum counter electrode ring surrounds a cathodic copper disk electrode. During voltammetry, the platinum ring electrode oxidises any products released by the CO2ER cathode, such as the reoxidation of $HCOO^-$ to CO_2. Detection was achieved by sweeping the disk electrode (0 - -1.2 V vs RHE) whilst the ring electrode was held at a single positive potential (trialled between +0.7 - +1.1 V vs RHE). Unfortunately, this technique converts reduction products at the Pt counter electrode and means that products cannot be observed with other quantitative techniques.[81]

1.3.2.4 Voltages

Most electrocatalytic surfaces are studied across a range of operating voltages to probe different overpotentials and influence reaction kinetics. A three-electrode configuration is routinely employed to perform either chronoamperometry (CA, constant potential) or chronopotentiometry (constant current). CA is often performed to evaluate the performance of a catalyst at a range of voltages typically between -0.4 and -2.0 V *vs* RHE, with studies venturing as low as -5.0 V *vs* Ag/AgCl in a cold LiOH/methanol electrolyte.[82] Figure 9 shows an example study of a family of related copper electrocatalysts across a voltage range achieving similar current densities and different overpotentials, where the electrochemically-active surface area was determined by impedance spectroscopy *via* electric double layer capacitance (see section 1.3.5.4). This study showed that the surface roughness could influence the voltage at which there were appreciable CO2ER current densities and high Faradaic efficiencies. In general terms, a smoother surface was more selective

for higher order hydrocarbons however other factors such as surface oxide content also played a role.

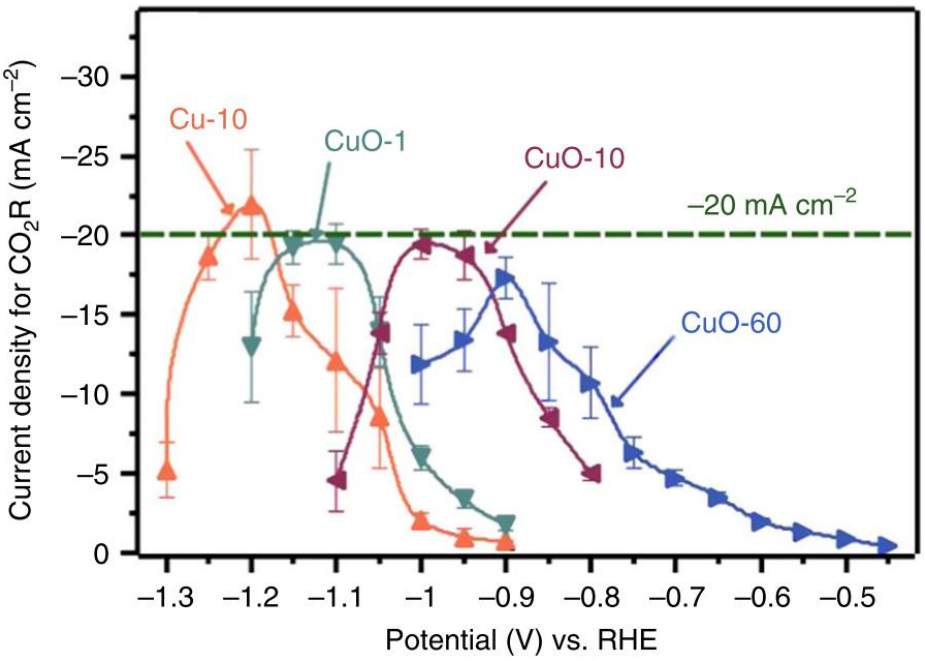

Figure 9. Current densities toward CO2ER products over a voltage range for four copper electrocatalysts in 0.1 M $KHCO_3$ (bulk pH 6.8). Experiments performed over 60 minutes. Reproduced from reference 83.

1.3.3 Single metal heterogeneous CO2ER catalysts

Due to the requirement for facile, reversible redox state changes, the transition metals have been extensively explored for their potential to electro-catalyse CO_2 reduction. For such technology to be sustainable and scalable, precious metal electrodes cannot be used. Group 6 (molybdenum, chromium and tungsten) were found to be inefficient catalysts for CO_2 electroreduction.[84] In general group 8-10 metals (iron, cobalt and nickel) have good selectivity toward H_2, CO and low-order hydrocarbons.[51, 85-87] Single metal CO2ER electrocatalysts are initially chosen for their specificity for either low order hydrocarbons (C_1 products only) such as gold, silver and zinc. Opposingly, copper is typically used to target higher order hydrocarbons. These observations can be correlated with the binding strength of a key intermediate in the CO2ER mechanism, M-CO. This idea is explored further in Chapter 4.[88]

In the 1980s, as CO2ER increasingly became of interest in the research community, Hori *et al.* demonstrated that single metal cathodes produce vastly different CO2ER products under different conditions, as detailed above.[25, 75, 89] The products formed with the highest Faradaic efficiency were

formic acid, carbon monoxide, methane or hydrogen when in aqueous $KHCO_3$ solution (Table 2), wherein copper was the most efficient metal for producing methane.[89] The following sub sections explore selectivities that common single-metal electrocatalysts can exhibit. Each metal below has been studied with a wide range of surface morphologies and some of those are discussed where authors have hypothesised how surface morphologies can influence product selectivities.

Table 2. Cathode materials for CO2ER and their products. Reproduced from reference 89.

Electrode	Electrode potential (V vs. SHE)	Faradaic efficiency/ %, Lower limit/upper limit				
		$HCOO^-$	CO	CH_4	H_2	Total
Cd[a]	-1.66 ± 0.02	65.3/ 67.2	6.2/ 11.1	0.2	14.9/ 22.2	93/ 100
Sn[a]	-1.40 ± 0.04	65.5/ 79.5	2.4/ 4.1	0.1/ 0.2	13.4/ 40.8	94/ 110
Pb[a]	-1.62 ± 0.03	72.5/ 88.8	0.3/ 0.6	0.1/ 0.2	3.8/ 30.9	94/ 100
In[a]	-1.51 ± 0.05	92.7/ 97.6	0.9/ 2.2	0.0	1.6/ 4.5	93/ 102
Zn[a]	-1.56 ± 0.08	17.6/ 85.0	3.3/ 63.3	0.0	2.2/ 17.6	90/ 98
Cu[b]	-1.39 ± 0.02	15.4/ 16.5	1.5/ 3.1	37.1/ 40.0	32.8/ 33.0	87/ 92
Ag[b]	-1.45 ± 0.02	1.6/ 4.6	61.4/ 89.9	0.0	10.4/ 35.3	99/ 106
Au[b]	-1.14 ± 0.01	0.4/ 1.0	81.2/ 93.0	0.0	6.7/ 23.2	100/ 105
Ni[b]	-1.39	0.3	0.0	1.2	96.3	98
Fe[b]	-1.42	2.1	1.4	0.0	97.5	101

a) Current density: 5.5 mA cm^{-2}. b) Current density: 5.0 mA cm^{-2}. Concentration of $KHCO_3$: 1.0 mol dm^{-3} for Cu electrode and 0.5 mol dm^{-3} for other electrodes.

1.3.3.1 Copper

Copper electrodes can be produced with a significant number of morphologies and oxidation states, with several reviews on nanostructured copper electrocatalysts.[90, 91] Initially copper foil was used to give a cheap and readily available catalyst with high surface area, however recent trends in copper electrocatalysis have used nanostructures to target a variety of reaction conditions. Some of these nanostructures include nanoparticles,[92, 93] nanowires,[94] nanocubes,[95, 96] nanofoams,[97] nanoneedles,[98] nanosheets[99] and nanoprisms.[100] The role of single crystal faces of copper have been extensively studied, however is not discussed here.[101, 102]

Copper nanowires (Figure 10) have been grown on a Cu surface by immersion of a copper foil into a $Cu(OH)_2$ solution with $(NH_3)_2S_2O_8$ and NaOH.[103, 104] These functionalities gave rise to an increase in hydrocarbon product chain length. This was interpreted in terms of an increased local pH at the

electrode surface and an enhancement of the CO coupling mechanism. Longer nanowires gave rise to higher order hydrocarbon specificity as well as HER suppression.

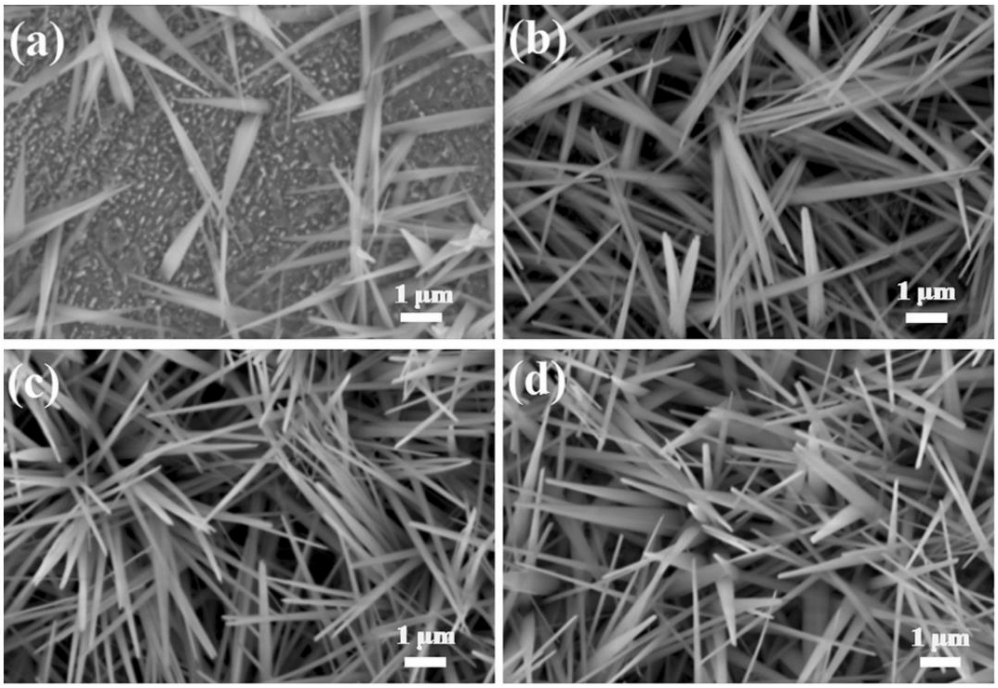

Figure 10. Scanning Electron Microscopy (SEM) images (a-d) of $Cu(OH)_2$ nanowires with a synthesis time of 1, 3, 5 and 8 minutes respectively. Figure reproduced with permission from reference 103. Copyright Wiley, 2016.

Copper nanofoams can be synthesised by electrodeposition of copper at very high current densities (>0.5 A cm^{-2}).[105] The evolution of hydrogen gas at the cathode generates bubbles around which a thin layer of $CuSO_4$ electrolyte gathers and reaches the cathode. The $CuSO_4$ is then electrodeposited onto the electrode which retains the bubble structure and generates a nanofoam. These copper nanofoams produced a 3-fold increase in geometric current density (at very high electrolyte concentrations only) and at a 10-fold increase in faradaic efficiency for hydrocarbon products relative to a polished copper sheet.[97] The increase in efficiency was attributed to surface roughness, hierarchical porosity and hence confinement of reactive species.

Nanocubes of copper were synthesised and loaded onto both a copper foil support and a carbon support. The addition of nanocubes increased the selectivity toward ethene significantly between -0.90 and -1.1 V *vs* RHE from 20-50% FE. A range of nanocube sizes were synthesised and used for CO2ER, the largest of which at 580 nm gave the highest overall selectivity to CO2ER over HER. It was noted that the cubes became damaged over time which led to a small decrease in CO2ER selectivity, though overall CO2ER selectivity remained constant after 150 min at -1.05 V *vs* RHE. The study was able to relate an increased ratio of Cu^{1+}/Cu^0 present in the cube structures that correlated to increased selectivity for C_2-C_3 products.

The role of copper oxides is highly disputed in CO2ER literature.[106] Several early papers assign the production of hydrocarbons such as methanol with high faradaic efficiencies to the presence of oxides for CO_2 binding or Cu^{1+} or Cu^{2+} sites for increased Cu-CO binding strength.[107, 108] Other studies have claimed that copper oxide electrodes inhibit protonation and so support production of ethene and similar species.[109] Should oxides remain on the surface of electrocatalysts during CO2ER, they have been shown to chemisorb CO_2.[110] Whilst is it unlikely that any surface oxides remain at most potentials commonly used in CO2ER,[111] bulk oxides may be retained during electrolysis and influence the surface electronics.[108, 112, 113] There have been a significant number of studies that attempt to relate catalyst structure and stability to products *via* specific mechanisms.[114-116] Comparison of electrocatalyst materials and mechanistic routes is often difficult owing to the range of testing conditions as highlighted in the previous sections.

1.3.3.2 Gold and silver

Gold and silver electrodes have also been produced to feature similar nanoscale features as copper.[117, 118] Both gold and silver metals are known to have a weak binding affinity for CO intermediates and so often are used for exclusive CO production.[79] Gold nanowires have been shown to produce CO with increased reduction kinetics.[119] One avenue of research in gold and silver CO2ER is attempting to increase the number of high-index or edge sites as these have been shown to have higher activity toward CO production.[120, 121] An example of an extremely multi-faceted and high-index gold CO2ER catalyst was a concave rhombic dodecahedral nanocatalyst (Figure 11) which exhibited FE > 90% toward CO at -0.6 V vs RHE in 0.5 M $KHCO_3$ relative to amorphous gold at FE < 10%.[122] The catalyst was still observed to be stable after 8 hours performing CO2ER.

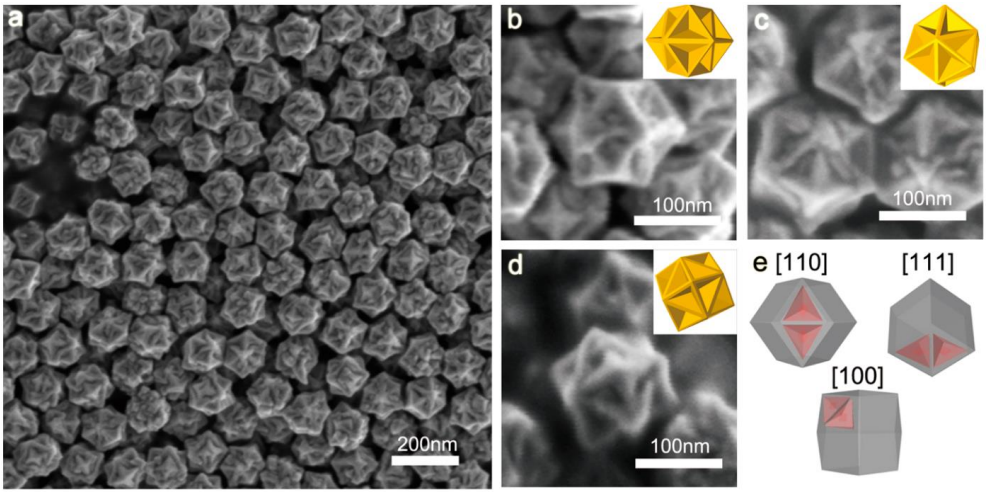

Figure 11. A gold concave rhombic dodecahedral nanocatalyst for CO2ER produced by adding 4-aminothiophenol during growth from gold seeds. Reprinted with permission from reference 122. Copyright (2015) American Chemical Society.

1.3.3.3 Other metals

Zinc electrocatalysts are generally able to produce only C_1 species in CO2ER, where formate is the most common product. Zhang *et al.* used zinc foil covered in zinc nanoparticles for CO_2 reduction in aqueous solutions.[123] Zn powder shows high formate selectivity (78%) for 10 minutes before rapidly declining, indicating a large amount of catalyst deactivation.[124] Zinc electrodes have also be modified with nanoplates and dendrites (Figure 12) for enhance CO selectivity. [125, 126]

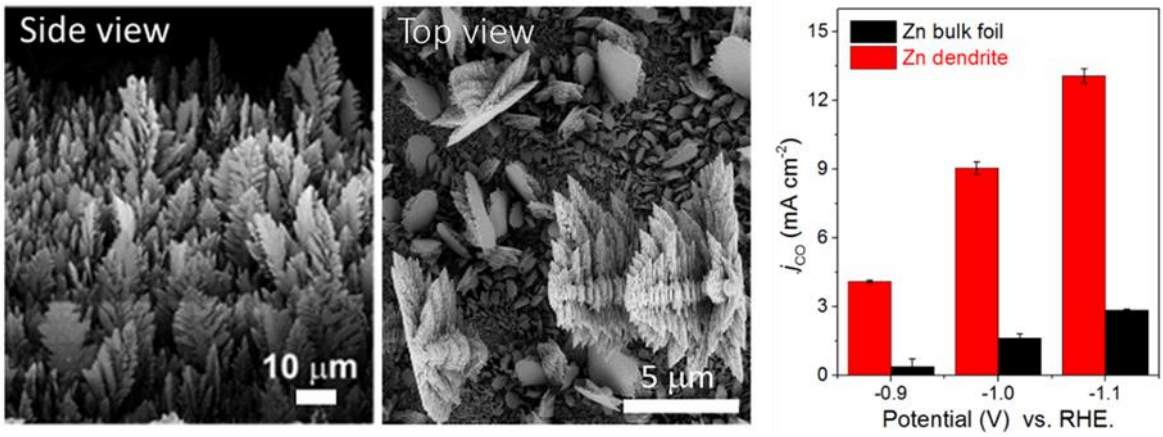

Figure 12. Zinc nanodendrites (left, middle) and the partial current density toward CO in CO2ER versus bulk zinc foil (right). Adapted with permission from reference 126. Copyright (2015) American Chemical Society.

Tin based electrocatalysts have also been used to exclusively transform CO_2 into CO or formate with very high efficiencies (>90%).[127] These electrocatalysts are not well understood though have been used by many researchers for increasing selectivity to formate and CO.[128] Tin dioxide has also been used as a core shell support for a copper coating which again significantly boosts CO or formate (voltage dependant) partial current densities relative to analogous catalysts that did not contain tin.[129]

1.3.4 Complex CO2ER catalysts

Following on from single metal studies of CO2ER, other types of cathodic electrocatalysts have been synthesised for use in this reaction. Electrocatalysts utilising different materials such as mixed metal systems, metals stabilised on carbon supports and multi-element molecular catalyst systems have all been tested. Novel electrocatalysts have been synthesised to target a specific reduced-CO_2 product or product chain length, increase turnover rates or improve energy efficiency. Some of these complex CO2ER electrocatalytic surfaces are discussed in this section to illustrate the vast

array of materials which have been synthesised and tested in the search for optimised CO2ER catalysts.

1.3.4.1 Mixed metal catalysts

Following CO2ER studies of the catalytic performance of almost all of the readily available transition metals in their pure form, the common technique of creating mixed metal catalytic surfaces has become a key area of CO2ER research.[130] This area of research targets changing the electronics of the catalyst to hit a "sweet spot" of the CO binding energy to target one specific product.[131] Figure 13 illustrates some of the key alloys that have been studied for CO2ER and how their CO binding energy correlates with major product selectivities. Mixed metal materials can be produced as either homogeneously mixed metals, layered thin films or as core-shell nanoparticles/nano-assemblies. Compared to pure copper, copper and gold bimetallic nanoparticles were found to promote CO production in favour of higher order hydrocarbons due to decreased binding strength of COOH and CO intermediates relative to bulk metal.[132] A copper foil impregnated with gold nanoparticles with an Au:Cu exposed surface ratio of 3:1 increased the C_{2+}/C_1 product ratio significantly relative to a pure Cu electrode at voltages more positive than -1.0 V *vs* RHE.[133]

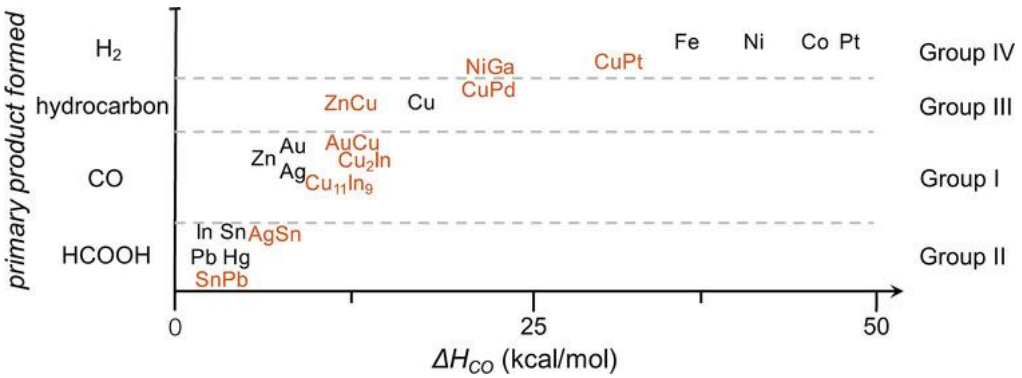

Figure 13. Major observed products for various electrocatalytic alloys correlated with CO2ER intermediate M-CO binding energy. Reproduced with permission from reference 131. Copyright Wiley, 2018.

1.3.4.2 Metal and carbon catalysts

Utilising conductive carbon sources as the solid support for an electrocatalyst is attractive due to the low cost, abundance and ease of use. Whilst most common forms of conductive carbon are very poor at CO2ER, requiring very high overpotentials for very low current densities, it makes a significantly cheaper and often high surface area support for modification with metal nano-assemblies.[134] One example modified high surface area carbon paper with copper nanocubes

and compared the CO2ER performance with copper foil modified with the same copper nanocubes and a pure copper foil sheet.[95] The modified carbon electrodes exhibited some activity toward CO2ER primarily attributable to the copper nanocubes, indicating that unmodified carbon supports do not typically perform CO2ER catalysis.

Carbon supports are known to have the ability to interact with CO_2, especially when they have been doped with nitrogen.[135] A metal-free N-doped graphene oxide was prepared by activation of graphene oxide with $SOCl_2$ and subsequent reaction with pyridoxine. This catalyst displayed moderate FE toward ethanol (36%) and acetone (8%) at -0.4 V *vs* RHE. Unfortunately, this selectivity was not retained at more negative potentials. One of the best N-doped carbon metal-free electrocatalysts for CO2ER was able to produce 93.5% FE toward methane with a current density six times higher than a pure copper electrode, however this selectivity was observed using an ionic liquid electrolyte and is not directly comparable with electrocatalysts studied in aqueous solutions.[136] Researchers have also combined metal nano-assemblies with N-doped carbon and other notable carbon structure such as MOFs.[137] Copper oxide nanoparticles were embedded onto an N-doped carbon which appeared to double the ethene faradaic efficiency relative to pure copper oxide nanoparticles and copper oxide nanoparticles embedded on an undoped carbon support.[138]

1.3.4.3 Molecular electrocatalysts

Molecular electrocatalysts can be used as homogenous catalysts for CO2ER in an alternative approach to using conventional solid cathodes to catalyse the reaction. Most molecular electrocatalysts feature a chelated metal which is primarily limited to iron[139, 140] and cobalt,[141] however newer electrocatalysts are emerging with copper,[142] manganese[143] and platinum group metals such as ruthenium.[144] Generally, electron transfer occurs from an inert solid electrode to the molecular catalyst dissolved in solution and then it is this small metal-centred molecule which acts as the active site centre that reduces CO_2.[145] This approach can allow fast CO2ER TOFs and high faradaic efficiencies toward a single product owing to the well-defined CO_2 binding site. Whilst almost all complexes target CO or formate as products, one recent example produced methanol using a cobalt phthalocyanine complex immobilised on carbon nanotubes.[146] The majority of molecular CO2ER electrocatalysts generate C_1-products due to the catalysts' common inability to hold multiple CO intermediates in the close proximity required for C-C coupling.[147] However, a dinuclear copper complex was produced by Bouwman *et al.* that could simultaneously bind two CO_2 units and produce oxalate ions, a useful feedstock for chemical synthesis.[148]

The ligands used in molecular CO2ER complexes often impose a square planar or octahedral geometry upon the central metal ion. Square planar complexes are open to axial binding of CO_2 molecules and can be synthesised easily using porphyrin or phthalocyanine derivatives or bidentate ligands. Aside from the core ligand structures, amines have become a popular additions to these complexes as they have been known to provide good proton delivery in the HER field as [NiFe]-hydrogenase mimics, where the structure in Figure 14 can exhibit a fast TOF of 350 s^{-1} for hydrogen production.[149-151] The success of this complex was attributed to the attraction of protons to the complex by the amine functional groups and also the stabilisation of HER intermediates. The effect of amine modification is discussed further in Chapter 4.

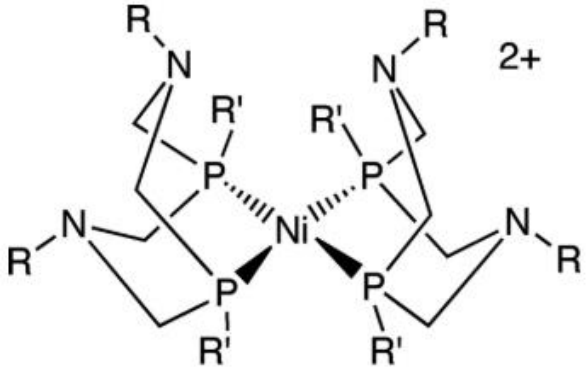

Figure 14. A nickel phosphine catalyst with pendant amine groups used for HER. Reproduced from reference 151. Copyright (2007) National Academy of Sciences.

1.3.4.4 Electrode immobilised molecular catalysts

Relative to heterogeneous electrocatalysis, homogeneous molecular catalysis offers greater selectivity towards one specific CO2ER product.[150, 152] However, industrial scale-up of molecular catalyst based CO2ER technology can be difficult due the cost associated with synthesising homogeneous catalysts and the difficulty in separating the CO2ER products and the catalyst.[153] Coupled systems have therefore been generated where molecular CO2ER electrocatalysts are covalently linked to non-catalytic conducting surfaces; this approach yields functionalised electrodes which combine an efficient method for electron delivery with the ease of product-catalyst separation that arises from heterogeneous catalysis and the enhanced product selectivity of molecular catalysis. Often such surface-bound CO2ER molecular catalysts have a metallocycle structure, for example a cobalt porphyrin complex attached to Boron-Doped Diamond (BDD) reduced CO_2 to CO (Figure 15) by cyclic voltammetry, where only gaseous CO was found as a product using FTIR spectroscopy.[154] Unfortunately no current densities for CO turnover were

determined. Such molecular-tethering modifications have not achieved high efficiency production of $C_{\geq 2}$ products.[155]

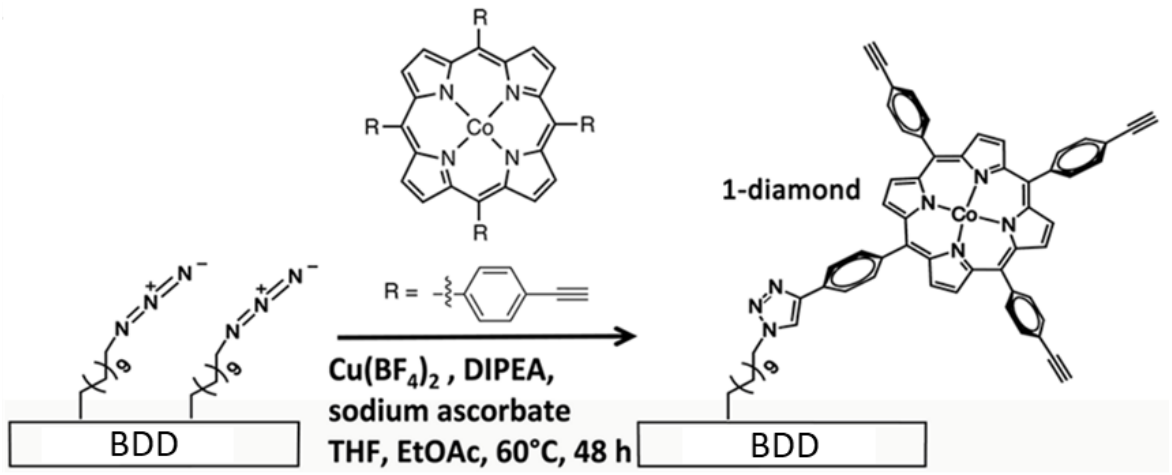

Figure 15. Electrochemical functionalisation of a BDD electrode with a cobalt porphyrin catalyst. Reprinted with permission from reference 154. Copyright (2012) American Chemical Society.

1.3.4.5 Polymers and deposited films

Polymers and thin-film modifications can be applied to CO2ER electrocatalytic surfaces to modify the reaction environment in terms of both CO_2 binding and proton delivery. These scaffolds often also modify the conductance and capacitance properties of the electrode.[156, 157] Amine functionalities have been incorporated within these polymer networks and deposited films to because of their role in enhancing proton mobility, which has been ascribed to increasing hydrogenation rates in CO2ER.[158, 159] Polyaniline (PANi), a nitrogen-containing polymer, is known to exhibit charge storage by the incorporation of protons at nitrogen sites, a phenomenon known as pseudo-capacitance.[160, 161] PANi can be produced by oxidative electropolymerisation of aniline onto most electrode surfaces. One such example is highlighted below where aniline was polymerised onto a graphene oxide surface (Figure 16).[162]

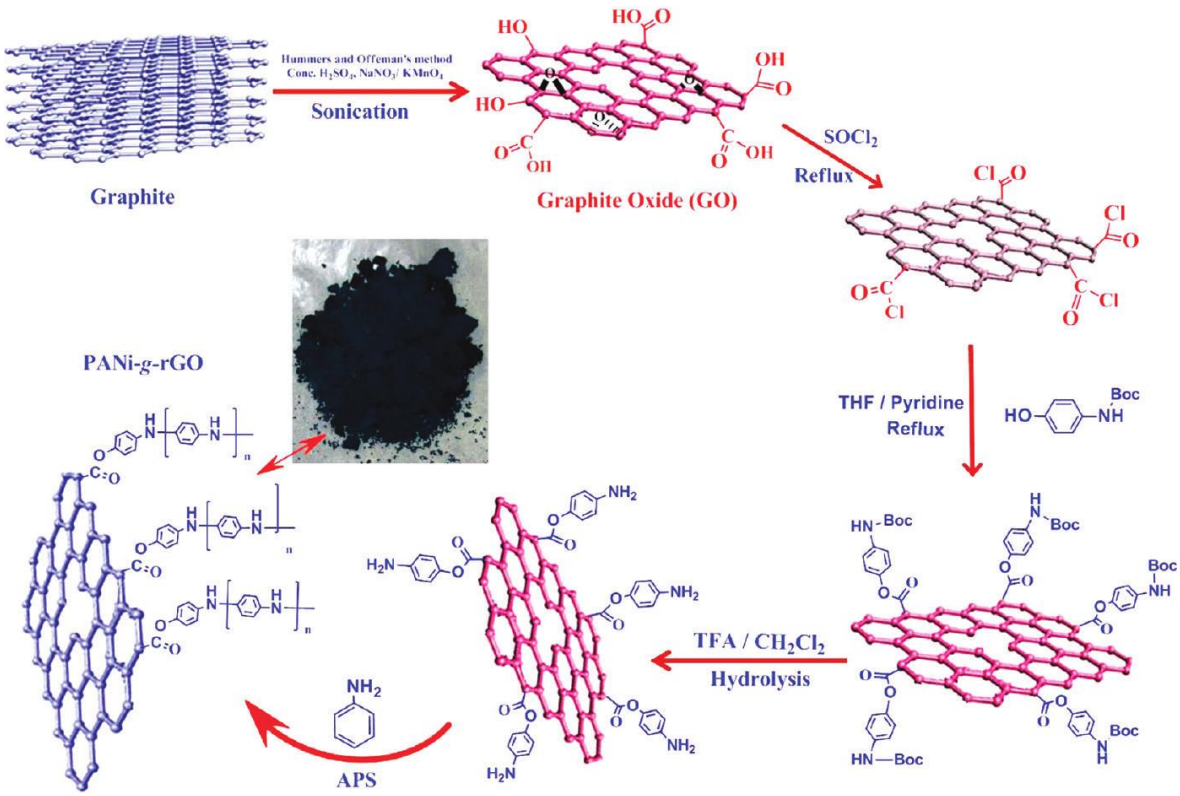

Figure 16. Kumar's method for graphene oxide functionalisation with PANi *via* carboxylate groups for esterification and subsequent polymerisation. Reprinted with permission from reference 162. Copyright (2012) American Chemical Society.

The combination of PANi and metal surfaces or nanoparticles has been shown to increase CO2ER selectivity.[163] Grace *et al*. showed a PANi electrode embedded with Cu_2O nanoparticles that could produce high Faradaic efficiencies toward acetic acid (63%) and formic acid (30%).[164] The group proposed that a synergistic effect of the basic Cu_2O sites and the ability of PANi NH functional group to hydrogen bond to CO_2 yielded that high CO2ER selectivity. Later studies have confirmed the production of C_1 and C_2 acid and alcohol species on PANi electrodes modified with metal nanoparticles, where PANi-only electrodes exhibited very poor CO2ER turnover.[163] PANi support structures have also been found to both physisorb and chemisorb CO_2 molecules by CO_2-temperature programmed desorption, supporting the hypothesis by Grace *et al.* that PANi can create a unique binding environment by interacting with CO_2.[163]

Many other polymeric structures have been tested for CO2ER selectivity, such as porous polymer networks.[165] One illustration was the incorporation of existing molecular catalyst technologies with heterogeneous surfaces. Cai *et al.* electropolymerized amine terminated metal-free porphyrin structures to generate a porous structure on a gold electrode (Figure 17).[166] This showed >90% FE to CO at -0.7 *vs* RHE, where the film thickness could significantly influence the TOF towards CO. The

authors concluded that the electropolymerized porphyrin layers both concentrated and activated CO_2 molecules close to the electroactive metal surface.

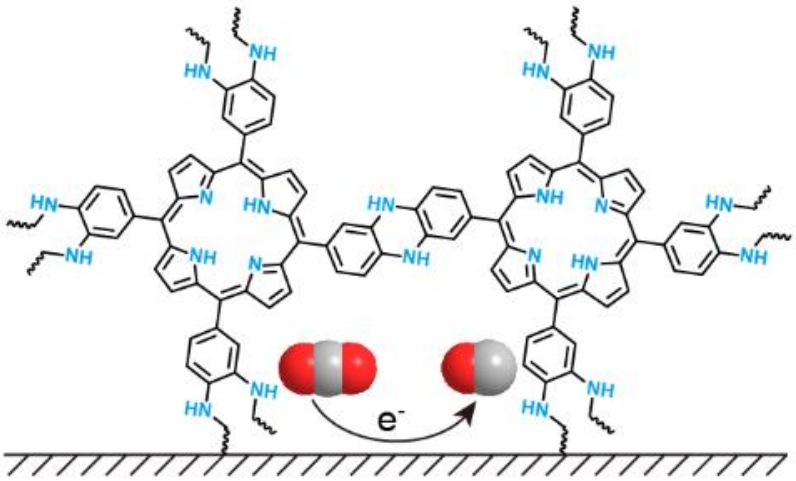

Figure 17. Porphyrin surface macrostructures for CO2ER. Reprinted with permission from reference 166. Copyright (2018) American Chemical Society.

In a similar vein, small molecule pyridinium additives have also been electropolymerized onto copper electrodes by Peters *et al*.[167] A range of N-substituted pyridinium additives were deposited on polycrystalline copper and the resultant surfaces exhibited a wide range of selectivities for CO2ER, from >90% faradaic efficiency for H_2 to 70-80% FE for C_2 and C_3 products. An additive of N-tolyl pyridinium chloride on polycrystalline copper exhibited the highest $C_{\geq 2}$ selectivity at 75%, however no specific mechanism was proposed to differentiate between the selectivities caused by the different modifiers. Generally, H_2 production was increased by all N-substituted pyridinium additives except when pyridinium was substituted at the N position with a benzyl derivative which gave rise to HER suppression in favour of C_{2+} product formation.

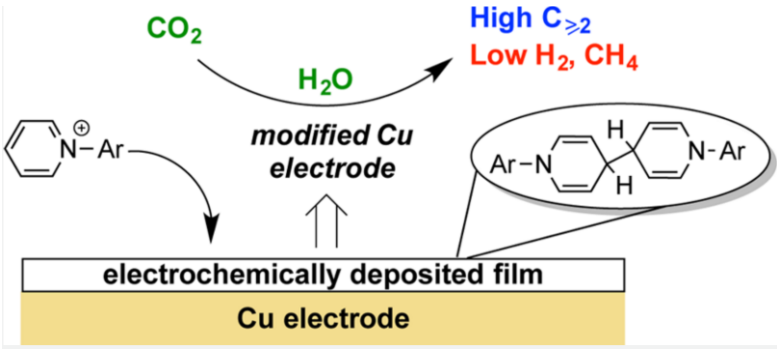

Figure 18. Electrochemically deposited N-substituted pyridinium additives. Reproduced with permission from reference 167. Copyright American Chemical Society, 2017.

1.3.5 Organic modifications of heterogeneous electrocatalysts

To date, most surface modifications/functionalisations of solid state CO2ER catalysts have been restricted to either covalently attached macrostructures or non-covalently attached polymeric or molecular films, as described in the previous section.[163, 165, 167] Conversely, electrode modifications using small molecules have been widely studied for applications such as electrochemical sensing.[168, 169] One of the Aims of this PhD (Chapters 3-5) was to explore the feasibility of covalently modifying the surface properties of copper with small molecules (i.e. altering functionalisation, hydrophobicity and local pH) and to determine the resultant impact this change in surface chemistry had on CO2ER.[170, 171] The following subsections therefore outline some of the common methods for generating a monolayer of well-defined small molecule surface structures on an electrode. Diazonium salt grafting, SAM formation and aryl iodide grafting are detailed alongside a description of a common method for electrochemical characterisation of modified surfaces known as electrochemical impedance spectroscopy (EIS).[166, 172]

1.3.5.1 Diazonium salts

Diazonium salts, molecules containing the R-N≡N$^+$ moiety, have been known since the mid-1800s, with the Sandmeyer reaction (1884) becoming one of the first applications of diazonium chemistry in synthetic functional group interconversion.[173, 174] However, the first use of diazonium molecules for electrode surface functionalisation was not until 1992, when Saveant *et al*. described how a glassy carbon electrode could be modified by 4-nitrophenyldiazonium tetrafluoroborate (NPDT) to add a nitrobenzene functionality to the surface (Figure 19).[175]

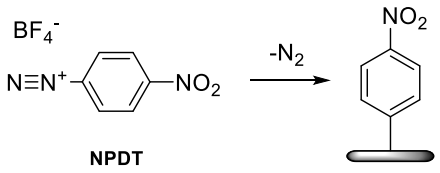

Figure 19. Modification of a glass carbon electrode with 4-nitrophenyldiazonium tetrafluoroborate (NPDT).[175]

Since then, electrode modifications using diazonium salts have been most extensively performed on carbon, platinum, gold and silicon substrates,[176-179] as detailed in an extensive review by Bélanger and Pinson.[180] This diazonium electro-grafting process can be performed in a range of solvents such as ionic liquids, water or acetonitrile.[181, 182] A wide range of diazonium salts can be made accessible by the use of an aniline precursor that can be converted to a diazonium salt *in-situ*

in the presence of sodium nitrite and acid, where the solution can be used as an electrolyte for the electrode modification step (Figure 20).[183]

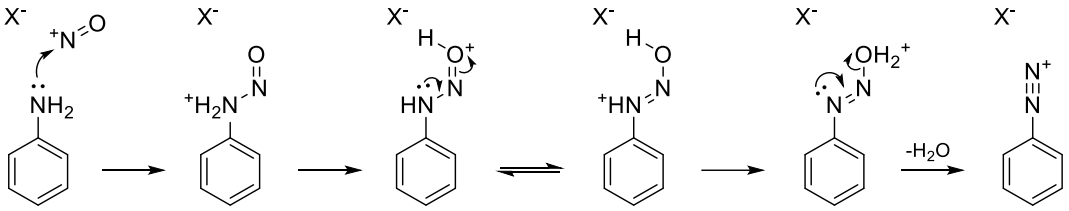

Figure 20. *In-situ* diazotisation of aniline by the nitrosonium cation (NO^+) produced by sodium nitrite and acid.

The modification of electrodes with diazonium salts can be either electrochemically driven or can occur spontaneously. In most diazonium literature, electrode modifications are driven electrochemically by performing cyclic voltammetry (CV, Figure 21) in which a reductive sweep drives a one electron reductive activation of the diazonium salt, whereby the gain of an electron and the loss of N_2 produces a benzyl radical intermediate which will form a covalent bond directly to the electrode surface. This process is usually fast and often this one electron activation is only seen in the initial scan. Some metal electrodes such as copper can also be spontaneously modified, however this relies on the thermodynamically favourable oxidation of M^0 to M^{1+} and accompanying reduction of the diazonium centre to a carbon radical species.[183-188]

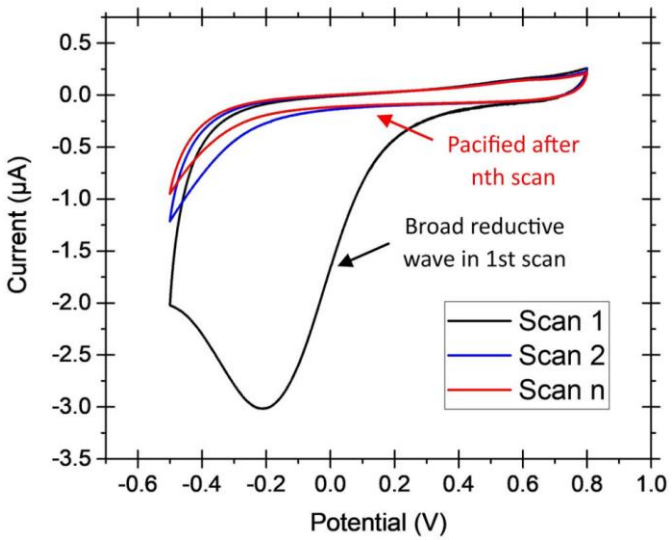

Figure 21. Characteristic electro-grafting of a diazonium salt onto a glassy carbon electrode. Reproduced from reference 189.

One major problem with the use of diazonium salts for electrode modification is that multilayers are readily formed due the reactive nature of the radicals.[190] Several strategies have been employed to limit multilayer formation for specific applications, such as using radical scavengers like DPPH to

reduce the concentration of aryl radicals or protection-deprotection strategies involving chemical protecting groups that can be cleaved (discussed further in Chapter 3).[191-193]

1.3.5.2 Self-assembling monolayers (SAMs)

An alternative method for creating a well-defined structure on a metal electrode surface is by the formation of a SAM. SAM formation occurs by spontaneous formation of a metal-thiol bond. Typically, thiol surface modifications have been mostly studied on gold electrodes by binding alkanethiol molecules through formation of an Au-S bond. This type of modification has also been shown to exist on copper and other metal electrodes, where the majority of metal surfaces form a densely packed layer of alkanethiol.[194, 195] This chemistry is harnessed to form self-assembled monolayers (SAMs) without the need for electrochemical grafting.[196] These layers form readily due to the van der Waals interactions and hydrophobic forces between typically long alkyl backbones. SAMs on gold electrodes are typically formed by immersing the electrode into a 1 mM solution of a thiol terminated molecule for 24 hours, where the assembly time carries a strong correlation with the density of the monolayer formed.[197] The density of SAM packing can be qualitatively assessed by cyclic voltammetry (charge transfer to solution redox species). Routine quantitative determination of surface coverage is done by either EIS (see section 1.3.5.4) or attaching a redox active head group to the SAM such as a ferrocencyl group.[198, 199] Thiol monolayers can be electrochemically cleaved as the metal-sulfur bond can be reduced.[200, 201] This phenomenon will be discussed further in Chapter 3.

SAM surface density can be purposefully decreased in order to target applications such as enhanced protein adsorption.[202] Whilst it is possible to use low self-assembly times, Juan and Carmichael were able to generate a decreased surface density using an asymmetric dialkyldithiophosphinic acid in an anhydrous toluene solution (Figure 22).[203] Other groups have used mixed thiol solutions to generate multi-component SAMs as well as SAMs terminated in reactive head groups such as azides.[204]

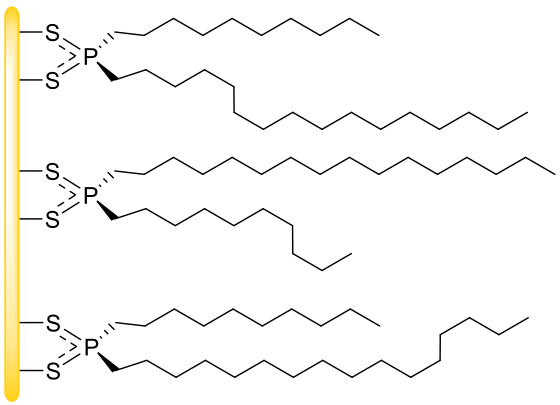

Figure 22. Loosely packed self-assembled monolayers of dialkyldithiophosphinic acid on a gold electrode.[203]

1.3.5.3 Aryl iodides

Benzyl iodine moieties have been used for reductively graft aryl units to electrodes surfaces in a similar fashion to diazonium salt electro-grafting. This has taken place using both diaryliodonium salts and more recently, simple aryl iodides (Figure 23). Diaryliodonium salts exhibit relatively mild reduction potentials of *ca* -0.8 V *vs* SCE and so can be applied with most electrodes and solvent systems.[205] The use of aryl iodides carries a significant amount of scope due to their regular use and ease of production in organic chemistry, however the systems with which they can be used may be limited due to the harsh reduction potential of -2.2 V *vs* SCE.[206]

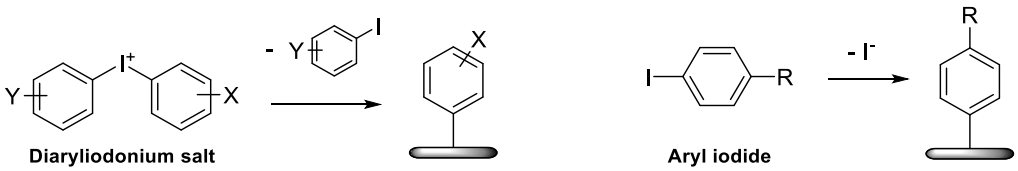

Figure 23. Electrode modifications with iodine containing precursors.

1.3.5.4 Electrochemical Impedance Spectroscopy

The formation of the organic surface modifications described in this section can be studied by a variety of electrochemical methods. EIS is a powerful electrochemical technique that can be used to study surface chemistry with respect to charge storage and resistive components.[207] This can reveal the impact that surface modifications such as those above can have on material surface properties.[208] This technique will be used to quantify surface properties of electrodes before and after modification with organic moieties in Chapter 3 as well as for estimation of double layer capacitance in Chapter 1Chapter 4.

The EIS technique generates data that can be modelled against an equivalent electrical circuit containing capacitors, resistors and related circuit elements.[209] When the components of the model accurately fit the data, this enables the quantitative characterisation of an electrochemical system in terms of resistance and capacitance which can be used to derive information about the surface of electrodes such as morphology, surface composition and the surrounding electric double layer. This technique has been used previously to study topics such as metal corrosion, material coatings, energy storage and surface modifications.[210-212]

The technique is performed by applying an AC voltage to a working electrode and analysing the phase shift and change in magnitude of the resulting AC current relative to the voltage input.[212] The amplitude of the AC voltage is usually between 1-20 mV to assume a pseudo-linear current-voltage response as most real electrochemical systems do not give a linear current-voltage response. The phase shift is measured over a range of frequencies which yields information about the impedance of the system.[213] A Nyquist plot separates the imaginary and real resistive components of the systems impedance across a frequency range. Figure 24 shows an example of a Nyquist plot for a simple single time constant circuit. A capacitor module (C) and a resistor module (R) are placed in parallel. If this was observed for electrochemical data, the capacitor may indicate the capacitance of the electric double layer and the resistor may indicate a charge transfer resistance.

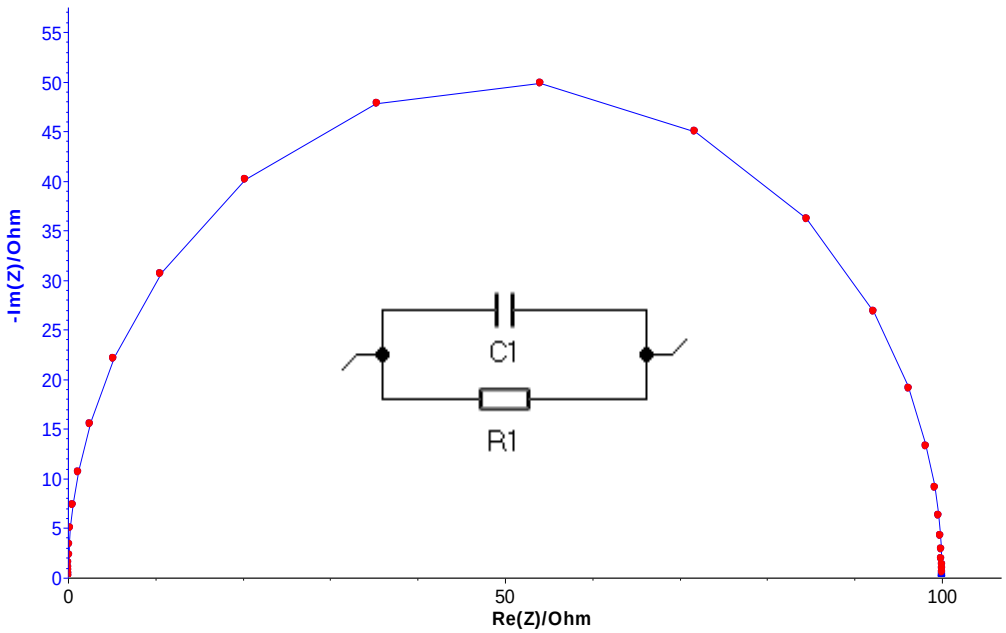

Figure 24. An example Nyquist plot for a single time constant circuit (inset).

Real systems contain more complex elements, particularly if a redox process is available.[212, 214] One of the most common equivalent circuits used to describe an electrochemical cell is the Randles

circuit (Figure 25). R_s models specifically the solution resistance and R_{CT} models the charge transfer resistance. Separating the two values can develop understanding about surface passivation, for example if a metal surface gains an inhibiting oxide layer, the R_{CT} will likely increase. C_{DL} demonstrates the electric double layer formation and is appropriate for uniform electrode surfaces. Z_w indicates Warburg impedance which indicates that a diffusion element is present surrounding charge transfer.[215] This is explained by the fact that at varying frequencies of voltage oscillation, the rate of diffusion of reactants will differ. At higher frequencies, this is not seen to be present as the movement of reactants becomes averaged out and is not limited by diffusion. A typical Warburg impedance is seen on a Nyquist plot as a 45° line.

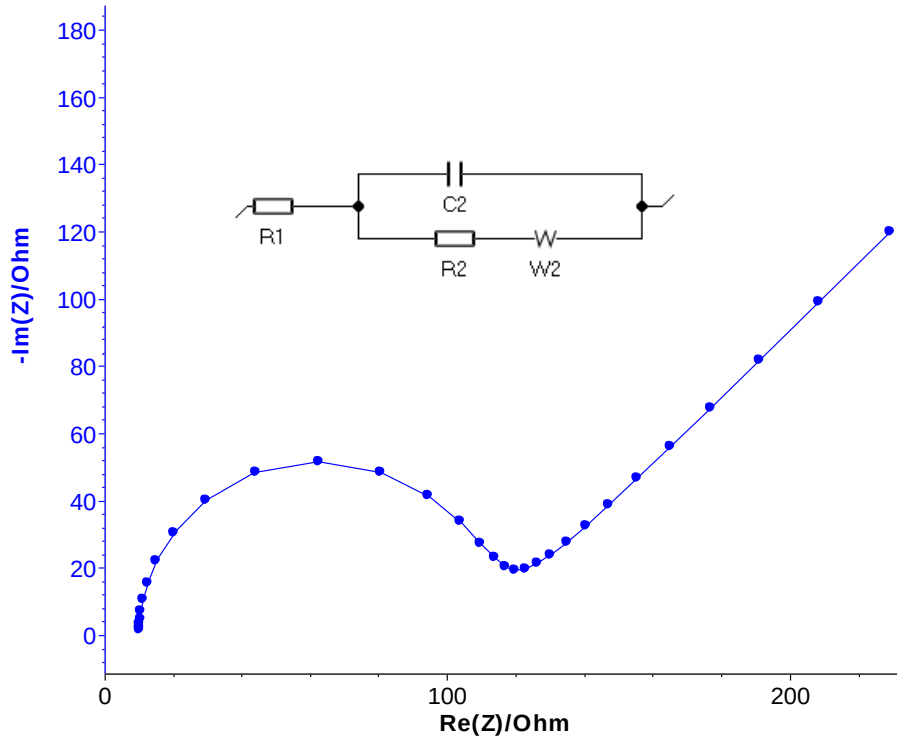

Figure 25. An example Nyquist plot for Randles circuit (inset). R1 = R_s; C2 = C_{DL}; R2 = R_{CT}; W2 = Z_w

1.4 Thesis aims

This introduction has highlighted the need for the development of carbon removal technologies. New techniques for carbon capture and storage are needed that require low power inputs and could capture and store large quantities of CO_2 using readily-available waste products or catalytic materials. This thesis will explore the development of a novel electrochemical CCS technique that mineralises CO_2 in a solid form by combining dissolved CO_2 with sacrificial electro-oxidised aluminium or iron metal.

An alternative to storing captured CO_2 is to perform carbon capture and utilisation. The most researched field for CCU technologies is CO2ER catalysis which has been described in this introduction in terms of the how electrocatalysis can be performed and some of the cathode materials that have been used. To create a new family of electrocatalysts for CO2ER, this thesis explores the modification of copper electrodes *via* diazonium electrochemistry. These modified copper surfaces are subsequently tested for their efficacy in CO2ER, where methods for cell operation and product analysis are developed. Whilst waiting for analytical equipment to become available for CO2ER product analysis, the experiments described in the final chapter were conducted to demonstrate the feasibility of a novel strategy for constructing a sub-monolayer of diazonium functionalisation on an electrode, this is a general methodology which could ultimately be used to create new types of electrocatalysts, including CO2ER electrodes.

Chapter 2. Electrochemical CO_2 Mineralisation

Chapter Declaration

The data reported in this chapter was gathered as part of a wider collaborative project, and in the following sections I explicitly highlight my contributions. The original Al|C dual anode and Pt cathode CO_2 mineralisation electrochemical cell was designed by Dr Katie J. Lamb and her 2017 PhD thesis reports her work in varying the electrolyte concentration, using seawater as the electrolyte and powering the device *via* solar panels. This initial work by Dr Lamb also included setting up methods for analysing the carbon content in both the solid and liquid products by thermogravimetric analysis coupled to an infrared gas analyser (TGA-IR) and titration analysis, respectively, and setting up the methods for the Powder X-Ray Diffraction (pXRD). I joined the project as Dr Lamb was writing up her thesis. I have used her electrochemical cell and analysis methods in this work. This work was published in a joint first author ChemSusChem paper in 2018.[216] I then developed a new "adjustable" electrochemical cell. Under my direct day-to-day guidance and using my experimental design plans a final year Chemistry Undergraduate student, Cassandra Lewis (MChem 2018), ran many of the experiments using the adjustable cell design; I assisted in all the data analysis. This work was published in 2018 with me as the sole first author.[217]

2.1 Abstract

This chapter explores a new CCS technique for the electrochemical mineralisation of CO_2 using waste metal sources as a sacrificial anode. A novel dual-component anode design combines the sacrificial oxidation of iron and aluminium substrates with a graphite substrate for supercapacitive concentration of solution CO_2. Electrochemical methods are usually advantageous because processes often require low energy inputs, meaning the technology could be powered directly by renewable electricity (for example solar energy) without further energy inputs, e.g. heat treatment. The role of each anodic component is investigated to determine a mechanism of operation using two different electrochemical cell designs. The results are discussed relative to energy cost and the maximum amount of carbon that could be stored. Some of limitations of the overall CCS technique are discussed with regard to materials, electrical parameters and efficiency of carbon capture.

2.2 Introduction

The urgent requirement for carbon capture and storage (CCS) and several possible methods for achieving this were described in the Thesis Introduction. Post-combustion methods of CCS can be appended to power plants which gives a requirement on the energy efficiency of the CCS technology. Coal-fired power stations typically produce 3.6 GJ per tonne of CO_2 emitted (GJ t_{CO2}^{-1}), any post-combustion CCS method used must require less than 158 kJ mol_{CO2}^{-1}.[17] Greener power stations that emit less carbon dioxide can utilise less efficient CCS technologies, for example natural gas combustion plants produce energy at a carbon-release cost of 428 kJ mol_{CO2}^{-1} and may utilise more energy intensive CCS technologies.[218] As described in the Thesis Introduction, amine scrubbing or electrochemically mediated amine regeneration CCS techniques both require approximately 50 kJ mol_{CO2}^{-1} for operation. This satisfies the energy requirements for capture, however these technologies are largely used for CO_2 purification and do not consider downstream sequestration. Studies involving direct mineralisation of CO_2 using readily available Lewis basic materials have not offered a full life-cycle energy cost. Therefore, a technology using readily available materials for direct mineralisation has not been found and studied for scalability.

The work herein describes the merging of two different CCS processes in a novel dual-material anode electrochemical cell design. The theoretical concept described by G. H. Rau[219] for the use of a sacrificial metal anode in carbon capture is combined with the idea of carbon-mediated capacitive carbon trapping demonstrated by Landskron *et al*.[220, 221] The system is probed for its efficacy in CCS applications by product analysis, energetics analysis and by exploring new materials to expand the system's scope. This work has already been published as in references 216 and 217.

2.2.1 Electrochemical metal recycling for CO_2 mineralisation

Sacrificial electrochemical metal oxidation has been coupled to CO_2 capture technologies in "metal-CO_2 batteries". Highly reactive metals (M^0) such as Li,[222-224] Na,[225, 226] and Mg[226] have been sacrificially oxidised to drive oxygen reduction. The resultant oxide or superoxide ions in the electrolyte bind CO_2 as carbonate ions that combine with the oxidised metal to form metal carbonates such as Li_2CO_3. This method can generate a high potential difference between the oxidised and reduced metal state which may make this useful for battery technologies. Unfortunately, owing to the limited availability and/or expensive nature of these reduced metals,

the technology is unsuitable for large scale CO_2 capture and mineralisation. A related family of cells was therefore developed by Al Sadat and Archer to incorporate aluminium as the oxidizable metal anode for operation at room temperature. The Al-CO_2 electrochemical cell functions by production of a superoxide from dissolved O_2 at the stainless steel cathode that catalyses conversion of dissolved CO_2 into $C_2O_4^{2-}$ that binds to oxidised Al^{3+} species as aluminium oxalate $Al_2(C_2O_4)_3$, a solid that can be stored or used to release the C_2-product. The cell also exhibited simultaneous power output, however the use of an ionic liquid electrolyte and a high-CO_2 content gas mixture (80% CO_2, 20% O_2) may make this a difficult process to use at an industrial scale.[227]

In 2004, a simple carbon capture cell was theorised by G. H. Rau that utilised sacrificial iron as an oxidizable metal.[219] Oxidation of iron metal was hypothesised to drive hydrogen gas production whilst under a CO_2 gas stream. As a simultaneous chemical process, the CO_2 gas would diffuse into the electrolyte as carbonate ions and bind to the oxidised metal species as highlighted below.[228] In theory this process should be spontaneous owing to the standard potentials (E^0) required for hydrogen production (0.0 V vs SHE) and iron oxidation (-0.44 V vs SHE).[229] In reality, however, this is unlikely due to the well-known effect of passivation which involves the coating of reactive metal surfaces in metal oxides which can increase the required overpotential for further corrosion.[230] The technology hypothesised by Rau had not been explored experimentally until this work began.

Anodic iron oxidation and CO_2 capture:

$$Fe^0_{(s)} + CO_2 + H_2O \longrightarrow Fe^{II}CO_{3\,(s)} + 2H^+_{(aq)} + 2e^-$$

In theory, aluminium may also be used for this process due to the ready formation of aluminium carbonates. The lower standard electrode potential of aluminium (E^0 = -1.66 V vs SHE)[229] relative to iron may decrease the energy input by lowering the required overpotential. Both aluminium and iron are investigated for the CCS efficiency in this chapter. To further the efficacy of this technique for CCS, a technique to increase the concentration of CO_2 in the electrolyte is employed as described in the next section.

2.2.2 Increasing CO_2 concentration in an aqueous electrolyte

In 2014 the Landskron group (Lehigh University, USA) first reported the development of a supercapacitive swing adsorption (SSA) electrochemical cell for the purification of CO_2 from a mixed gas feedstock of CO_2 and N_2.[220, 221] By applying a potential difference of 1 V across two carbon electrodes in a 1 M aqueous NaCl solution under a 15% CO_2 / 85% N_2 static gas atmosphere they were able to selectively move CO_2 into solution, with a decrease in the CO_2 gas level of approximately 6% (Figure 26a). It was assumed that this technology works because the application of the voltage leads to the capacitive charging of the anode electrode with anions, including HCO_3^-. A diagram of a possible cathodic electric double layer is highlighted in Figure 26b for reference.[207, 231, 232] The charging of the anode with HCO_3^- ions disturbs the gas-solution phase equilibrium, causing further gaseous CO_2 to dissolve as H_2CO_3. The gas separation achieved by applying a potential difference of 1 V was shown to be sustainable and reversible across a series of charge-discharge cycles.

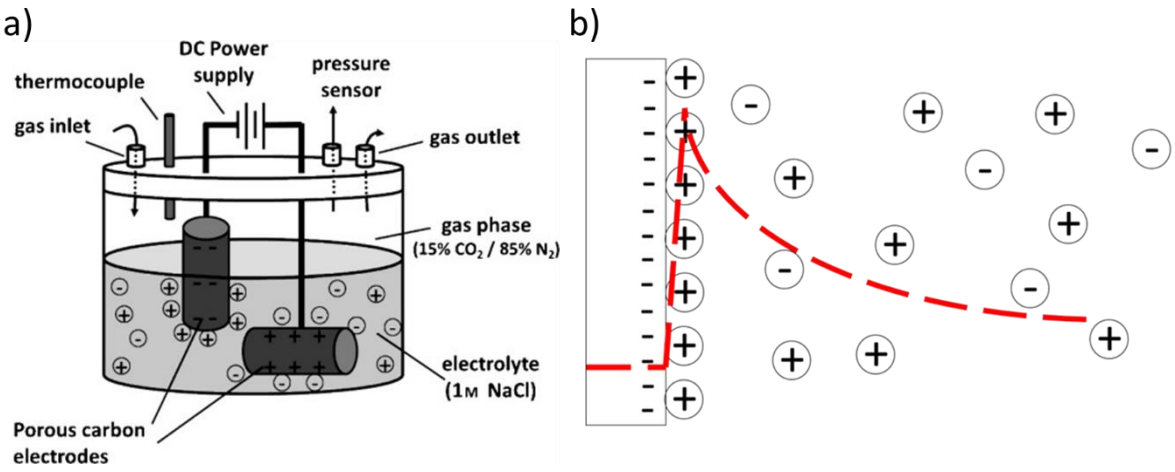

Figure 26. a) Experimental set-up for SSA experiments featuring different exposed surface area electrodes. b) Formation of an electric double layer at a cathode surface where + and – indicate charges with an overlaid potential difference curve at given distances from the electrode surface (red). (a) reproduced with permission from reference 220. Copyright Wiley, 2014.

In more recent work in 2017, the Landskron group used the SSA effect in a single electrochemical cell module that concentrated a 15% CO_2 gas stream into a 46% CO_2 gas stream by utilising a charge-discharge cycle.[221] Their coin-type electrochemical cell has an energy consumption of 57 kJ mol_{CO2}^{-1} (1.28 GJ per ton CO_2), an ideal low-energy cost for a CCS applications, although this value does not account for further sequestration energy costs.

2.2.3 Previous work on electrochemical CO_2 mineralisation

Before I started working on this project, Dr Katie Lamb had created an electrochemical cell to combine the theoretical electrochemical carbon capture device illustrated by G. Rau with the novel supercapacitive carbon capture technique discovered by the Landskron group.[219, 220] The electrochemical cell used by Dr Lamb is the same "standard cell" described in the next section. The "standard cell" was found to be an effective carbon capture device that mineralised carbon dioxide into an oxidised aluminium structure when aluminium metal was used as a sacrificial component. Some initial work was performed to ascertain the carbon capture efficiency of the separate aluminium and graphitic anode components. Cathodic processes were also probed by Dr Lamb, where close to 100% Faradaic efficiencies to hydrogen gas was found when using the platinum cathode (analysis by GC). Dr Lamb also probed the operating conditions of the cell by varying the electrolyte concentration, using seawater as the electrolyte and powering the device *via* solar panels. These results and the results recorded in this chapter use the methods of analysis outlined by Dr Lamb for determining carbon content in the liquid (titration analysis) and solid (TGA-IR) products as well as structural analysis of the solid product by powder XRD.

2.3 Results and Discussion

Two gas-tight electrochemical cells were made for this work, both of which are shown in Figure 27. The "standard cell" produced by Dr Lamb was used for sections 2.3.1 to 2.3.5, whilst the "adjustable cell" that I designed was used in section 2.3.6. Further images of the cells and their configurations are shown in Appendix 1 (page 60). Both cells could utilise a dual material anode set-up; the standard cell had the aluminium and graphite electrodes touching whilst the sheet electrodes used in the adjustable cell could be separated *via* different anode slots. For all CCS experiments in both cells, unless otherwise specified, the cell and stirred electrolyte (1 M NaCl) was equilibrated under a flow of 5% CO_2 / 95% N_2 gas for 7 hours at the open circuit potential (OCP) before a 10 mA current step for 24 hours (or 18 h for some "adjustable cell" experiments) and a further OCP step for at least 3 hours. Carbon capture analysis was performed by titration for solution-based carbonate species and TGA-IR for solid analysis. Further experimental and analysis procedures are detailed in section 7.1.

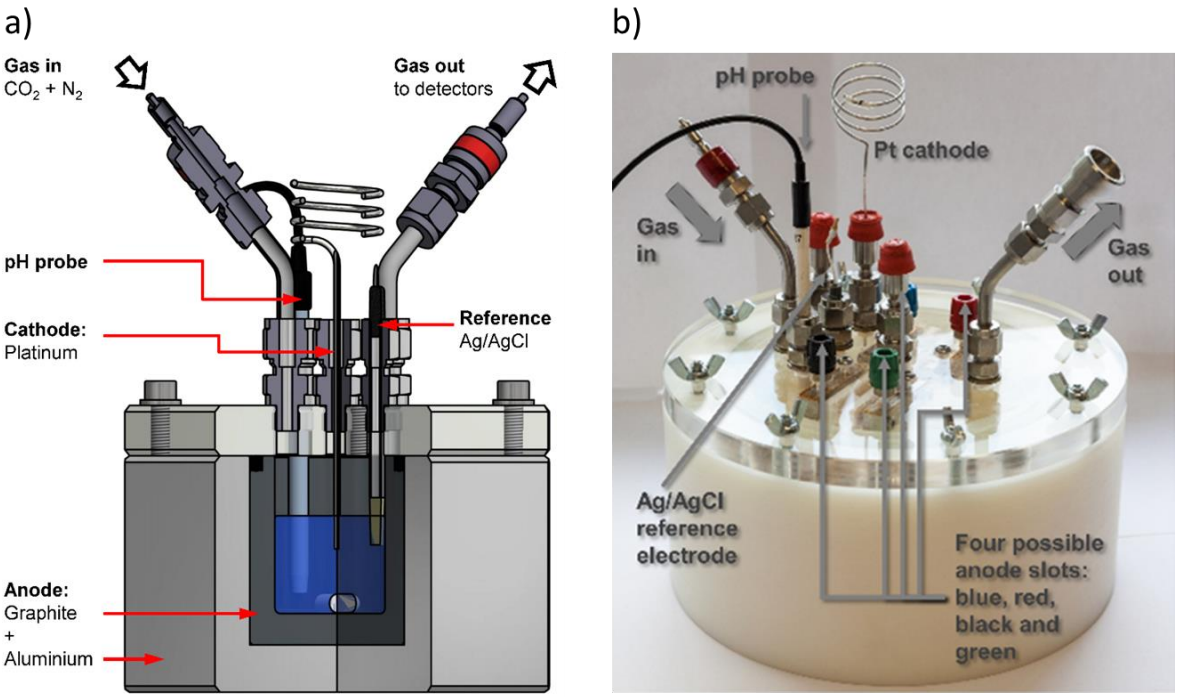

Figure 27. Electrochemical cells used for carbon capture and mineralisation. The "standard cell" (a) had a removable graphite insert and had a typical operating volume of 60 mL. The "adjustable cell" (b) could clamp up to four sheet anode components *via* connectors at the blue, red, black and green slots. The adjustable cell had a typical operating volume of 600 mL, though an insert could lower the volume to 250 mL.

Herein, CCS experiments using the dual-material anode are repeated according to Dr Lamb's methodology and analysed for the energetics of carbon capture. The aluminium and graphite anode components are studied independently for their role in carbon capture and storage. A mechanism

is proposed for the formation of mineralised carbonates following electrochemical studies by cyclic voltammetry and EIS. The standard cell is also probed for its use with different materials and energy input. This work was published in a joint first author ChemSusChem paper in 2018.[216] Finally, the scope of the CCS technique is explored using the adjustable cell by changing surface area ratios and the currents employed. Work using the adjustable cell has been published as a follow up paper in Dalton Transactions.[217]

2.3.1 A dual-material anode for enhanced CO_2 capture *via* supercapacitive swing adsorption

The standard cell was tested for the total carbon captured and the associated energy of capture using the standard CCS method as in section 7.1. Chronopotentiometry was recorded alongside *in-situ* instrument recordings of the solution pH and the concentration of CO_2 in the effluent gas (Figure 28). During chronopotentiometry, the cathode voltage drops to approximately -1.3 V vs Ag/AgCl which indicates the platinum cathode is performing proton reduction to hydrogen gas ($2H^+ + 2e^- \rightarrow H_2$, E^0 = -0.21 V vs Ag/AgCl at pH 0). Concurrently the voltage of the dual-material anode operates at approximately -0.55 V vs Ag/AgCl for 7 hours before the oxidation processes require more positive overpotentials. This may be due to diffusion limitations within the electrochemical cell, primarily caused by the graphite liner physically blocking some access routes to the aluminium block. The CO_2 concentration in the effluent gas shows a rapid response to the 10 mA current step that is sustained throughout the experiment, indicating continual absorption of CO_2 by the CCS technology. Whilst the CO_2 gas sensor appears to give quantitative measurements, the sensor was not properly calibrated and was shown to be unreliable by Dr Lamb. The pH during electrolysis using the $Al_{block}|C|Pt$ cell rapidly stabilised at pH 9.0 within 3 hours. This indicates that a buffering system is set up throughout electrolysis which is most likely due to the presence of aqueous HCO_3^- species.

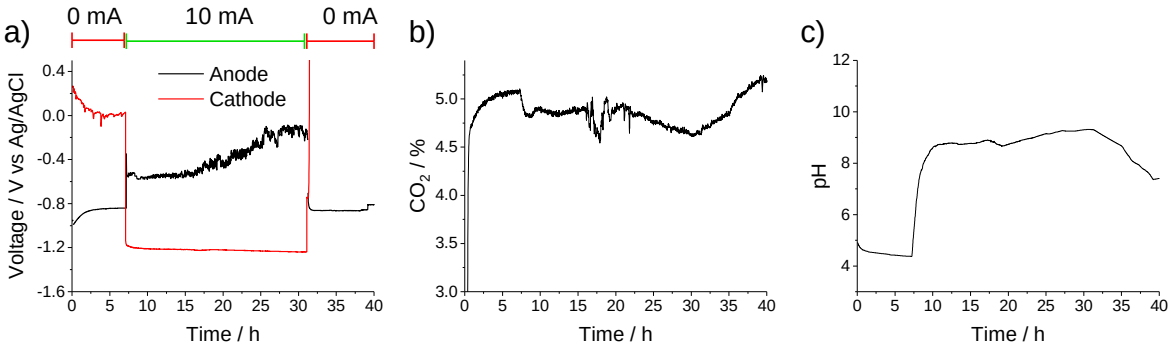

Figure 28. Experimental traces for electrochemical CCS using a $Al_{block}|C|Pt$ cell featuring a) voltage traces, b) effluent CO_2 concentration and c) pH-time traces. Electrolysis performed in 1 M NaCl (60 mL) for 24 h at room temperature.

As the experiment proceeded a grey precipitate was observed to form in the electrolyte solution of the electrochemical cell. This solid was filtered and dried *in vacuo* after the experiment. The carbon content in both the solid and filtered electrolyte were analysed using TGA-IR and Vogel's titration method, respectively (see sections 7.1.3 and 7.1.4).[233] The carbon content of the filtered aluminium-based solid and the electrolyte were shown to have captured 0.84 mmol (solid) and 2.08 mmol (solution) of CO_2. The total energy in joules consumed over the 10 mA portion of the experiment can be calculated using Equation 1 and the average potential difference in volts, V, applied current in Amps, I, and time in sec, t. The energy input throughout this CCS experiment was 719 J and therefore the experiment yielded an overall carbon capture efficiency of 247 kJ mol_{CO2}^{-1}. This energy of capture makes this technology viable for use with natural gas power plants but not with coal-fired power plants.[218] These results are in agreement with those obtained by Dr Lamb.

$$W = V \times I \times t$$

Equation 1. W: work / J; V: potential difference / V; I: current / A; t: time / s

As a point of comparison, this experiment was repeated without the use of a current step, with OCP measured for 38 hours (data not shown), which yielded no solid precipitate and 1.29 mmol of CO_2 captured in the electrolyte. This indicates that the SSA effect observed by Landskron *et al.* is occurring in this electrochemical cell as the solution-phase carbon is significantly higher when a voltage has been applied. This effect will be explored further in section 2.3.3.

2.3.2 Control electrochemical CCS using an aluminium-only anode

A control CCS experiment was performed using an aluminium-only anode component in an $Al_{block}|Pt$ configuration. The effect of removing the graphite component from the CCS technology is observed in the instrument traces in Figure 29. Whilst the cathode voltage and CO_2 effluent trace appear similar, the anode voltage is significantly more negative (-0.72 V vs Ag/AgCl) and closer to the OCP at which no current flows (-0.77 V vs Ag/AgCl). The smaller overpotential required is likely caused by easy solution access to a much larger aluminium surface area and the low standard electrode potential for aluminium oxidation ($Al \rightarrow Al^{3+} + 3e^-$, E^0 = -1.87 V vs Ag/AgCl). The pH measurements in this experiment failed, however separate recordings by Dr Lamb indicated that pH rose linearly from approximately pH 5.3 to pH 9.0 across the 24-hour current step (Figure 29c).

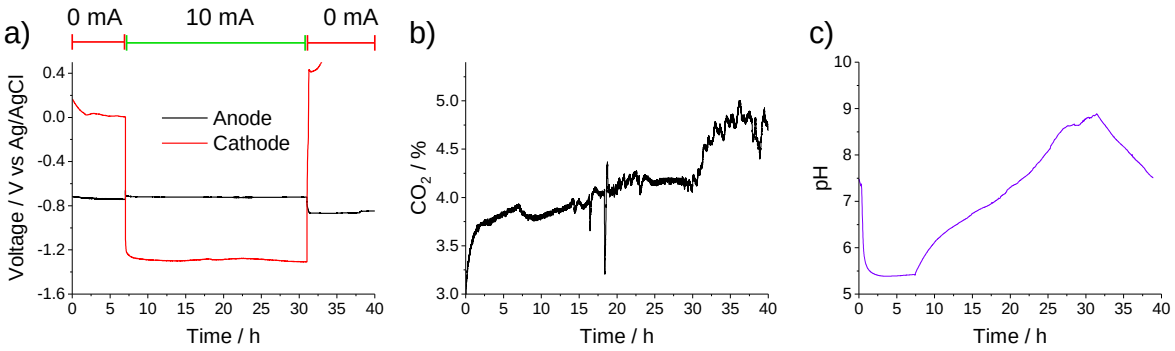

Figure 29. Experimental traces for electrochemical CCS using a Al_{block}|Pt cell featuring a) voltage traces, b) effluent CO_2 concentration and c) a pH trace obtained by Dr Lamb in an independent experiment with the same method. Electrolysis performed in 1 M NaCl (60 mL) for 24 h at room temperature.

The energy input throughout this CCS experiment was 490 J whilst the CO_2 captured as carbonates in solution was 0.76 mmol and the solid captured 0.32 mmol. Therefore, the combined system had a total CCS energy efficiency of 452 kJ mol_{CO2}^{-1}. The slower increase in electrolyte pH throughout this experiment relative to the standard dual-material cell indicates that the HCO_3^- buffering system is achieved faster when the graphite anode component is included. It is therefore surmised that the graphite increases the rate at which CO_2 is drawn into the solution and the rate at which the $CO_2 \rightleftharpoons H_2CO_3 \rightleftharpoons H^+ + HCO_3^-$ equilibrium is established. This correlates with the increase in energy cost of carbon capture from 247 to 452 kJ mol_{CO2}^{-1} upon exclusion of the graphite liner.

2.3.3 Studying the graphite for supercapacitive swing adsorption

Following the aluminium-only anode control experiments, a graphite-only anode experiment was carried out. This required the design of a new cell holder as detailed in Appendix 1 (page 60), Figure 37c. Electrolysis was again performed using a 24-hour, 10 mA current step as shown in Figure 30. Relative to the aluminium-only experiment shown above, the graphitic anode reached a far more positive potential during the 10 mA current step at approximately +1.23 V vs Ag/AgCl. This is consistent with the anodic catalysis of water oxidation countering the proton reduction occurring at the platinum cathode. This increased potential difference between the two electrodes equates to an energy of 2244 J. The carbon capture occurred primarily at the start of the experiment before a steady state with very low CO_2 uptake was observed for the remainder of the electrolysis. The pH profile also rapidly achieves a steady state which is likely caused by the balance of proton reduction and water oxidation at the cathode and anode electrodes, respectively.

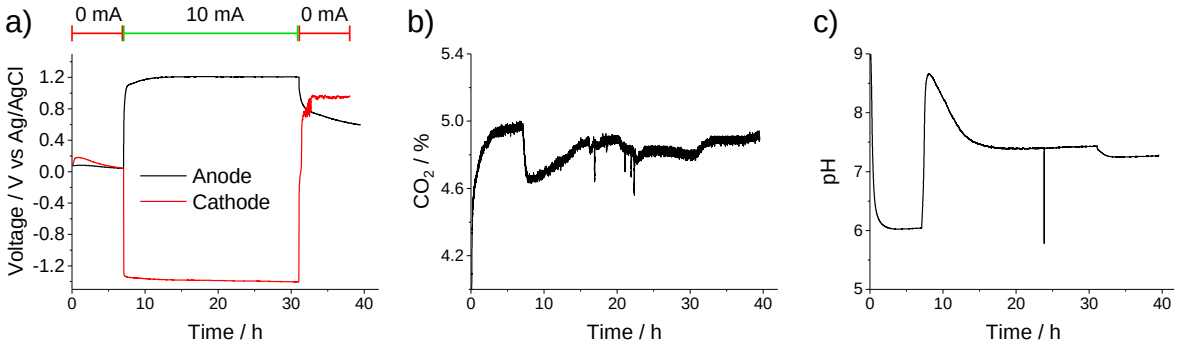

Figure 30. Experimental traces for electrochemical CCS using a C|Pt cell featuring a) voltage traces, b) effluent CO_2 concentration and c) pH-time traces. Electrolysis performed in 1 M NaCl (60 mL) for 24 h at room temperature.

Owing to the absence of aluminium species and the primary reactions being water-splitting half reactions, no solid precipitate was formed. The electrolyte however did capture 1.89 mmol of CO_2 in the electrolyte at an energy capture efficiency of 1187 kJ mol_{CO2}^{-1}. The CO_2 captured is significantly higher than even the total CO_2 capture in the Al_{block}|Pt experiment which strongly suggests the properties of the graphitic liner induces the SSA effect. The quantity of CO_2 captured in the solution is very similar to that found in the Al_{block}|C|Pt standard cell, indicating that there is rapid equilibration to a higher carbon concentration in solution in the presence of a graphite electrode relative to an aluminium electrode.

The electrochemical role of the graphitic liner was investigated further by both cyclic voltammetry and electrochemical impedance spectroscopy. The C|Pt cell was placed under a static 5% CO_2 / 95% N_2 atmosphere for cyclic voltammetry experiments. Cyclic voltammetry (Figure 31a) indicated that there were no redox peaks caused by the graphite electrode at the typical operating voltages during a standard electrolysis experiment. The capacitive and resistive elements observed in the voltammetry experiments were investigated further by EIS.

By placing the C|Pt cell under a static N_2 atmosphere, the interaction of the graphitic liner with the surrounding electrolyte could be studied. EIS was performed across a voltage range (-0.8 - 0.0 V vs Ag/AgCl) to follow the range of possible behaviours throughout a standard electrolysis experiment (Figure 31b). The raw data (not shown) was modelled against an equivalent circuit containing a Gerischer element and a parallel capacitor-resistor circuit (Figure 31b insert). The capacitance was extracted using this model across the voltage range, where the capacitance peaked at voltages closer to -0.35 V vs Ag/AgCl. At the typical operating voltage (approx. -0.55 V vs Ag/AgCl) of the dual-material anode during CCS electrolysis, the capacitance exhibited was 2.4 µF cm^{-2} (using a geometric surface area of 157.8 cm^2) which is consistent with a standard electric double layer.[234] Therefore, it is most likely that the SSA effect observed by Landskron *et al.* occurs within the dual-

material anode cell where the redox inactive graphite liner exhibits an increased capacitance that "concentrates" more CO_2 into solution by attracting HCO_3^- ions into the electric double layer and disturbing the bulk $CO_2 \rightleftharpoons H_2CO_3 \rightleftharpoons H^+ + HCO_3^-$ equilibrium.

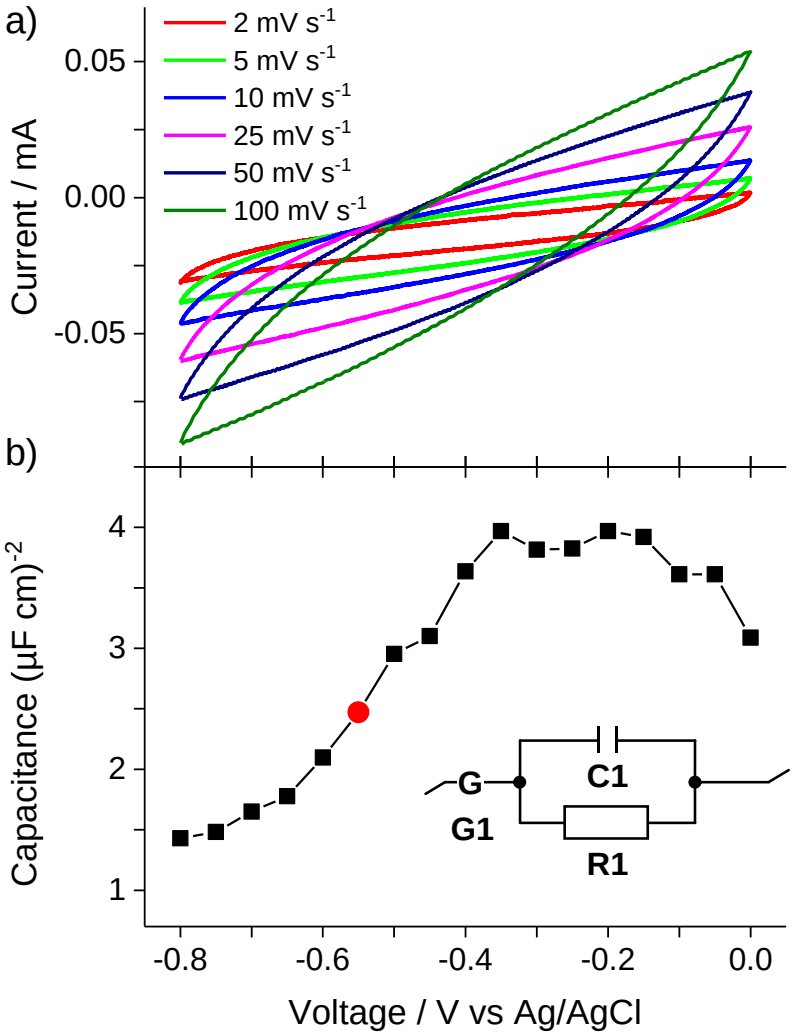

Figure 31. Electrocapacitive properties for a $Al_{block}|C|Pt$ cell across a voltage range exhibited by (a) cyclic voltammetry at different scan rates and (b) EIS modelled against an equivalent circuit (b, insert) to extract capacitance where G1: Gerischer, C1: capacitor, R1: resistor. The red circle data point (b) indicates the typical operating voltage of the graphite-aluminium dual anode during a standard electrochemical CCS experiment.

2.3.4 Product composition and mechanism analysis

To verify the mechanism for CO_2 mineralisation, the precipitate from the $Al_{block}|C|Pt$ dual-material anode cell was analysed to understand the nature of the carbon species, the crystallinity within the solid and the elemental ratio. ATR-IR of the solid powder revealed that a variety of carbonate species are present, as indicated by the broad peaks observed in the 1750-1350 cm^{-1} region (Figure 32a).[235] When conducting TGA-IR analysis to determine the solid's carbon content, the carbon mass

was lost from the solid primarily between 100-300 °C, indicating that the CO_2 was mineralised within the solid structure (Figure 32b). pXRD indicated that only small amounts of NaCl crystals were present within the solid, with no aluminium-based crystalline phases (Figure 32c). These data indicate that the solid is without long-range order and is likely completely amorphous. Further experiments performed by Dr Lamb further showed no long-range order by SEM imaging or by solid state Nuclear Magnetic Resonance (NMR). Complete pXRD and ATR-IR data is shown in Appendix 2 for different anode materials herein mentioned.

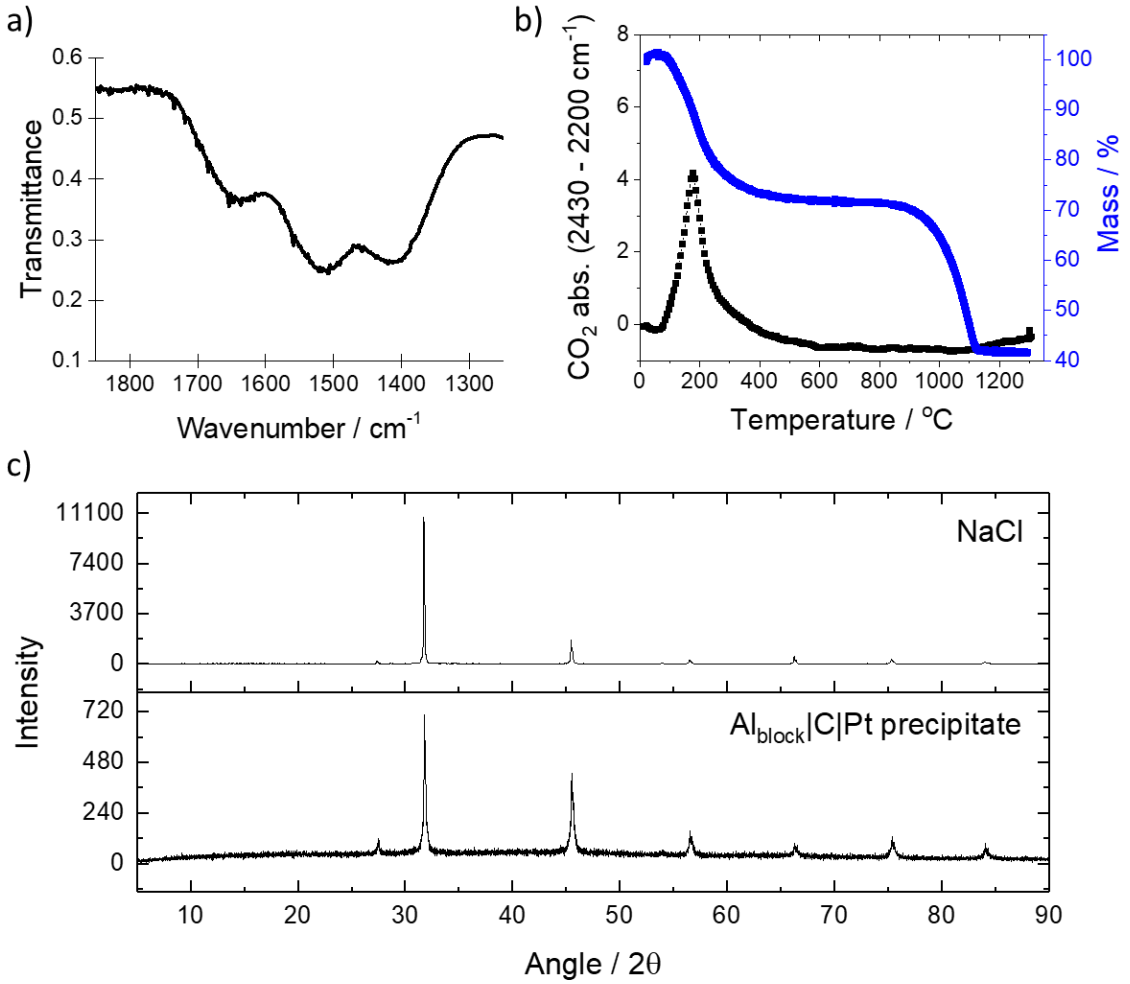

Figure 32. physical characterisation of the solid precipitate formed during a standard $Al_{block}|C|Pt$ experiment. Analysis by (a) ATR-IR focussing on the carbonyl region, (b) TGA-IR showing mass lost with temperature (blue) and IR radiation absorption by the effluent gas stream (black) and (c) pXRD indicating no long range order in the precipitate (bottom) except through NaCl crystals (top).

Given that no specific carbonate structures and compounds were identified, reactions A and B (below) were hypothesised as two competing reactions within aluminium based carbon capture devices. The primary reduction process in the cell is hydrogen production at the platinum cathode which accounts for the increase in pH throughout electrolysis by production of OH^- ions. This is countered by aluminium oxidation at the anode which passes 864 C of charge throughout a 24 h,

10 mA electrolysis experiment. Therefore, 2.98 mmol of Al^{3+} can be produced as $Al(OH)_3$. Alternatively, if H_2CO_3 is present in the electrolyte then cathode processes can reduce carbonate protons and mineralise carbonate species to form $Al(HCO_3)(CO_3)$. The total carbon mineralised during using a dual aluminium-graphite anode electrolysis experiment was 0.84 mmol, which indicated the ratio of reactions A:B is approximately 6:1. The aluminium-only anode cell mineralised 0.32 mmol of carbon and yielded a significantly decreased A:B reaction ratio of approximately 18:1. These calculations assume that no side reactions occur and that exactly 2.98 mmol of Al^{3+} is produced.

$$2Al + 6H_2O \rightarrow 3H_2 + 2Al(OH)_3 \qquad (A)$$

$$2Al + 4H_2CO_3 \rightarrow 3H_2 + 2Al(HCO_3)(CO_3) \qquad (B)$$

Inductively coupled plasma mass spectrometry (ICP-MS) analysis of the dual-material anode precipitate revealed the solid contained 11.57%$_{wt}$ Na and 17.43%$_{wt}$ Al. Therefore 3.00 mmol and 3.85 mmol of sodium and aluminium were captured, respectively, which is roughly in agreement with theoretical aluminium production by assuming 100% FE for oxidation of $Al \rightarrow Al^{3+} + 3e^-$. This may be an overestimate of the true value for aluminium owing to sample inhomogeneity or sample dryness, however it is unlikely that there was a significant amount of side reaction. As the cell operates under typically basic conditions, $Al(HCO_3)(CO_3)$ may react with solution based NaOH to form $NaAl(CO_3)(OH)_2$, a mineral known as dawsonite.[236] Production of dawsonite may be modest owing to the moderate basic pH (9-11) and thus no crystalline structures were observed (Figure 32c). The possibility of dawsonite production and separate NaCl species account for the relatively high sodium content in the solid.

The 3-fold increase in reaction selectivity toward reaction B over reaction A upon introduction of the graphite anode is being caused by the introduction of a supercapacitive swing adsorption effect.[220] The increased capacitance from the electric double layer (described in the previous section) attracts carbonate ions from the bulk electrolyte and perturbs the bulk equilibrium, which allows more CO_2 to dissolve as H_2CO_3. Therefore, the graphitic anode acts as a "reagent concentrator" for CO_2 in a localised environment close to the aluminium oxidation processes. This idea and the reactions highlighted above are summarised below in Figure 33.

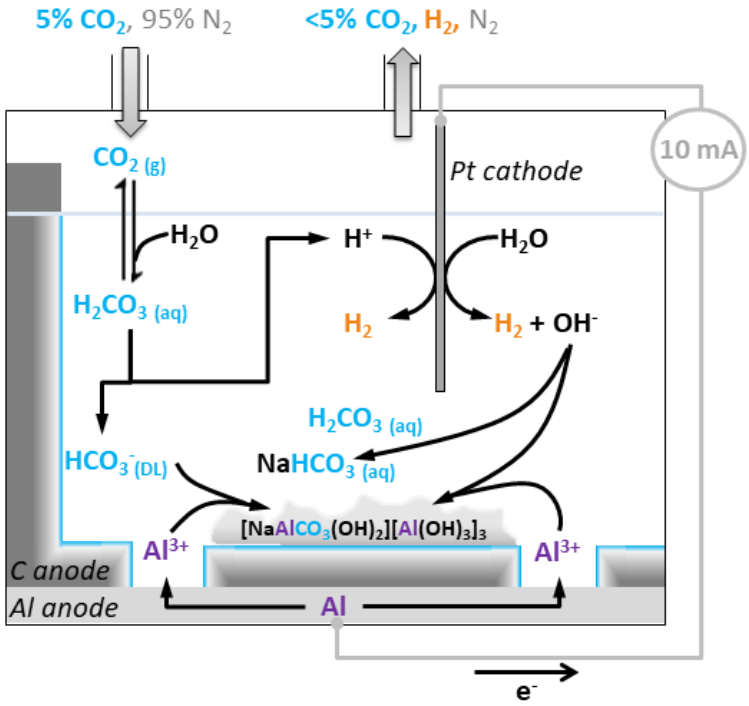

Figure 33. Proposed dual mechanisms for carbon dioxide capture and mineralisation. Mechanism B is highlighted in blue/purple.

2.3.5 Exploring the versatility of electrochemical CCS

This section explores the scope of this novel CCS technology with respect to improving the scalability of the process by exploring different anode materials, electrolytes and power sources. The cathode material is also modified away from platinum group metals to reduce the cost of the process. The process is analysed with respect to how this technology could be used with real world resources with a scalability analysis. Instrument traces for this section are shown in Appendix 3.

2.3.5.1 Different anode materials

For this method of CCS to be performed on a global scale, the ideal approach would be to use non-recyclable metals. To mimic "waste" aluminium products, simple aluminium foil was used to replace the aluminium block. By surrounding the graphitic block in fresh aluminium foil (Appendix 1 (page 60), Figure 37f) for each new experiment, any effects of previous metal corrosion were eliminated. Quantities of carbon capture and the associated energies for all anode components are shown below in Table 3. Waste aluminium performs with a similar efficiency for carbon capture to a solid aluminium block. A slight decrease in CO_2 capture energy penalty is observed, likely owing to inhibited oxidation of the aluminium block through repeated corrosion during electrolysis.

Table 3. Carbon captured within the standard electrochemical cell for experiments performed with variable anode components and a Pt cathode. Experiments performed for 24 h in a 60 mL electrolyte. Solution CO_2 errors all ± 0.1 mmol by analysis repetition. Solid analysis error obtained relative to previous data by Katie Lamb.

Anode	CO_2 (solution) / mmol	CO_2 (solid) / mmol	Total CO_2 / mmol	Energy Used / J	kJ mol_{CO2}^{-1}
Al_{block}|C	2.08	0.84 ± 0.2	2.91	719	247
Al_{block}	0.76	0.32 ± 0.1	1.08	490	452
C	1.89	-	1.89	2244	1187
Al_{waste}|C	1.93	0.78 ± 0.2	2.71	618	228
Fe_{disk}|C	4.19	0.32 ± 0.3*	4.51	1097	243

*Relative to experiment repetition

To expand the scope of this CCS technique, a mild steel disk (98 $\%_{wt}$ Fe) was used as the sacrificial metal component of the dual-anode set-up. The Fe_{disk}|C|Pt cell performed electrolysis for a standard 24 h, 10 mA experiment and yielded a similar energy of capture at 243 kJ mol_{CO2}^{-1} to that of the aluminium equivalent. During operation, the average anode voltage was at -0.23 V vs Ag/AgCl which was significantly more positive than most aluminium experiments at approximately -0.5 V vs Ag/AgCl. This likely stems from the more positive standard electrode potential for iron oxidation ($Fe \rightarrow Fe^{2+} + 2e^-$, -0.645 V vs Ag/AgCl) than aluminium oxidation ($Al \rightarrow Al^{3+} + 3e^-$, -1.865 V vs Ag/AgCl). Therefore, the iron-based cell incurred a higher energy penalty to achieve the required overpotential.

The amount of carbon captured within the iron solid was 0.32 mmol, significantly lower than the standard aluminium dual-material anode, however significantly more carbon was captured in the electrolyte for the iron-based experiment. These observations can be explained by considering the Pourbaix diagrams of aluminium and iron oxidation products (Figure 34). The primary aluminium species of $Al(OH)_3$ is a solid precipitate under typical experimental conditions (pH 6-10). For $Fe^{2+/3+}$ species in the presence of carbonate, the expected solid product is α-FeOOH which is insoluble in water at neutral pH.[237, 238] Insoluble iron carbonate species, known as carbonate containing green rust (GRc),[228] are not predicted to be present under typical experiment conditions (pH 7-9) which explains the high concentration of solution-based carbonate species and the low output of mineralised carbonate. Should the overpotential of the anode component be lowered toward the standard electrode potential for iron oxidation ($Fe \rightarrow Fe^{2+} + 2e^-$), the formation of iron carbonates could be more significant. This may be a future avenue for electrochemical research.

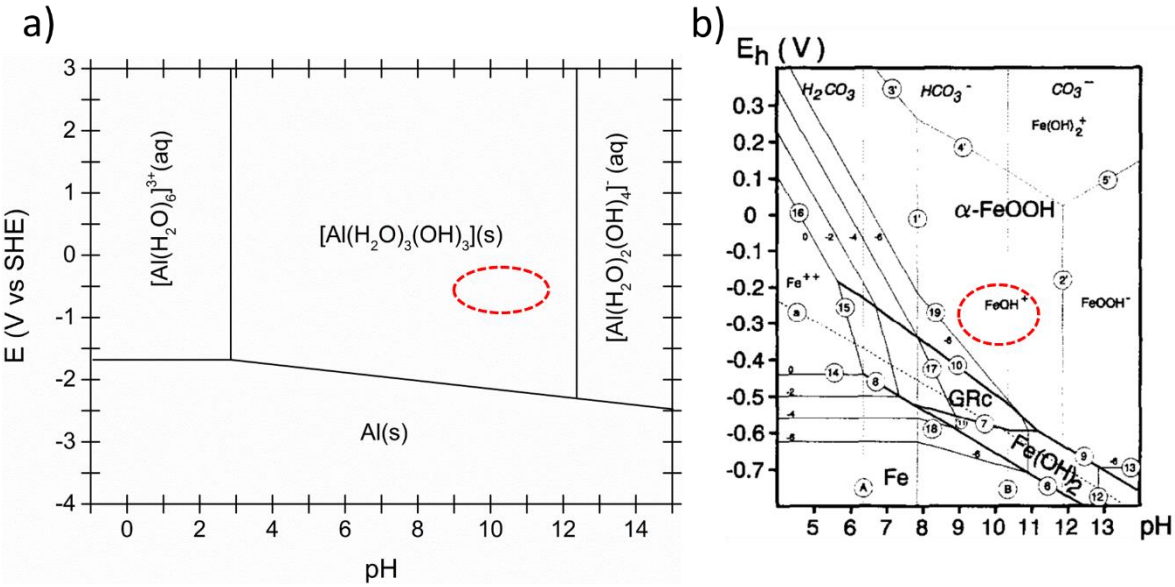

Figure 34. Pourbaix diagrams for (a) aluminium and (b) iron products at different pHs and voltages (V vs SHE). Iron Pourbaix diagram shown in the presence of carbonate ions in an aqueous solution, where GRc indicates Green Rust carbonate ($FeCO_3$). Red circles indicate typical operating conditions in this work. Figures (a) reproduced with permission from reference 239, Copyright 1995, N A C E International. Part (b) reprinted from reference 240, Copyright (1995), with permission from Elsevier.

2.3.5.2 Scalability analysis

ICP-MS analysis was performed on the resulting solids from both $Al_{block}|C|Pt$ and $Fe_{disk}|C|Pt$ experiments to determine the metal content relative to the total carbon captured. The analysis revealed that the aluminium system captured 2.91 mmol of carbon dioxide by utilising 3.85 mmol of aluminium. Should this be scaled up then 1.23 tonnes of carbon dioxide could be captured per tonne of aluminium. In the same vein, the iron system used 0.80 mmol of metal to capture 4.51 mmol of carbon dioxide, the equivalent of 4.44 tonnes of carbon dioxide could be captured per tonne of iron.

Given that the use of recyclable metals for CCS applications is not desirable owing to the possibility for re-use, non-recycled metals are ideal for this CCS application. The amount of aluminium that was not recycled in 2015 was 38 million tonnes and so approximately 47 million tonnes of CO_2 could be captured annually using this aluminium-based technology.[241] The same analysis for the iron-based cell using non-recycled steel (195 million tonnes in 2012) shows that approximately 866 million tonnes of CO_2 could be captured annually.[242] Global emissions caused by natural gas production (50 million tonnes per year, 2008) and oil refineries (850 million tonnes per year, 2008) could be mitigated by using this electrochemical CCS technique using sacrificial aluminium and iron/steel, respectively. It is important to note this is a preliminary analysis of the field and not a

full life cycle analysis where external factors such as transportation emissions may reduce the efficiency for carbon capture.

2.3.5.3 Cathode materials

The influence of the cathode on the overall cell energies was probed by exchanging a platinum (29700 \$ kg^{-1}) wire for cheaper and non-precious transition metals, iron (0.4 \$ kg^{-1}) and nickel (13.8 \$ kg^{-1}).[243, 244] All experimental traces are shown in Appendix 3. Pure iron and nickel wire electrodes with the same exposed geometric surface area as previous experiments were used as proton reducing cathodes. A nickel wire electrode with 11 times the geometric surface area ("Ni x11") as other cathodes was also used to understand any limiting overpotentials at the cathode. For all experiments recorded in Table 4, the anode voltages remained unaffected at -0.55 - -0.58 V vs Ag/AgCl and the amount of carbon captured did not change significantly. Similar cathodic voltages were obtained upon changing the metal, where platinum was the most efficient HER electrocatalyst with the lowest overpotential required. Whilst nickel appears to be the least thermodynamically favourable cathode, increasing the geometric surface area reduced the overpotential required to equal that of a smaller iron cathode.

Table 4. Carbon captured within the standard electrochemical cell for experiments performed with a variable cathode material and a Al_{waste}|C dual anode. Experiments performed for 24 h in a 60 mL electrolyte. Solution CO_2 errors all ± 0.1 mmol by analysis repetition.

Cathode	Cathode Voltage / V vs Ag/AgCl	CO_2 (solution) / mmol	CO_2 (solid) / mmol	Total CO_2 / mmol	Energy Used / J	kJ mol_{CO2}^{-1}
Pt	-1.26	1.93	0.78	2.71	618	228
Fe	-1.32	2.29	0.85	3.14	786	250
Ni	-1.44	2.12	0.73	2.85	812	285
Ni x11	-1.33	1.83	0.82	2.65	688	260

One of the key driving forces for HER kinetics is the thermodynamic stability of the M-H bond on the cathode surface. [245] These have been well studied and "volcano plots" map the correlation between bond strength and HER current density, where peak currents are observed at approximate bond strengths of 250 kJ mol^{-1} for single metal cathodes. The experimental observations for required cathode voltages roughly correlate with literature M-H bond strengths where Pt > Ni ≈ Fe (Pt: 251 kJ mol^{-1}, Ni: 197 kJ mol^{-1}, Fe: 188 kJ mol^{-1}).[245]

2.3.6 A new “adjustable” cell design

I designed a new “adjustable” cell design in order to further probe the scalability of electrochemical CCS mineralisation (Figure 27b).[217] The different slots available for anode components (Appendix 1 (page 60), Figure 38) allowed the electrodes to be physically separated unlike in the previous cell design. Furthermore, a range of anode surface areas could be probed by modifying the number of graphite and/or sacrificial metal electrodes.[217] Variations in electrode configurations are shown in Figure 38. The cell was used to mimic the standard $Al_{block}|C|Pt$ experiments of the previous sections, wherein a platinum cathode was used to counter anodic processes at a dual-material anode made from separate graphite and aluminium plates (Figure 35, purple). The plates were placed in the same electrode holder to mimic the “standard cell” arrangement. A larger volume 1 M NaCl electrolyte (600 mL) was used to understand the scalability implications. Whilst the change in the effluent CO_2 gas concentration was not recorded for these experiments, a new sensor array was designed so that the concentration of hydrogen gas produced at the cathode could be recorded, making use of the calibration curve shown in section 7.1.4. Comparable experiments were performed with the anode components separated (Figure 35, black) as well as without the graphitic component (Figure 35, light blue).

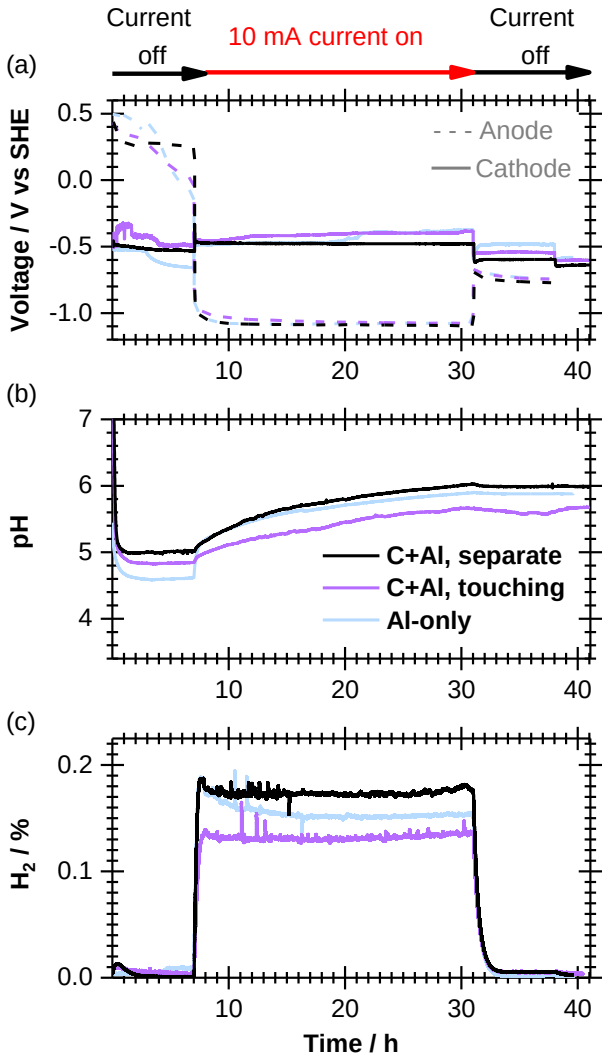

Figure 35. (a) Voltage, (b) pH and (c) %H_2 time traces from experiments where either an aluminium-only anode (blue), physically touching and electronically connected graphite and aluminium anode (purple), or physically separated but electronically connected graphite and aluminium anode components (black) were used. Experiments conducted under a continuous flow rate (50 mL min^{-1}) of 5% CO_2 / 95% N_2 gas. A platinum cathode was used in a 1 M NaCl (600 mL) electrolyte at room temperature.

Once the 10 mA current was applied, there was a concurrent increase pH and H_2 output of a similar magnitude for all cells. During electrolysis, the voltage of the anode components remained stable, with the C+Al (separate) set-up requiring the lowest overpotential throughout electrolysis. Whilst the power requirements and experimental traces are similar for the three anode variations, the carbon captured is shown to significantly increase upon introduction of a graphite electrode (Table 5). The carbon captured further increases by separating the two electrodes. It is most likely that this exposes a greater graphitic surface area that can exhibit an increased electric double layer for a SSA effect. Therefore this cell exhibits the same "reagent concentrator" effect as demonstrated in the previous cell and verifies the mode of action of the graphite, wherein the graphite can disturb the bulk equilibrium of dissolving CO_2 *via* concentration of HCO_3^- ions. Importantly, this effect is not required to occur immediately adjacent to the oxidizable aluminium anode. This is expected as

literature calculations of an electric double layer that show that beyond approximately 3 nm from an electrode surface, ion concentrations return to bulk values.[246] As electrodes are not required to be immediately adjacent to each other, it is likely that this CCS technique could easily be scaled-up.

Table 5. Carbon captured within the adjustable electrochemical cell. Experiments performed for 24 h at 10 mA for experiments in Figure 35. Solution CO_2 errors all ± 0.1 mmol by analysis repetition. Solid analysis error obtained by analysis repetition.

Anode	CO_2 (solution) / mmol	CO_2 (solid) / mmol	Total CO_2 / mmol	kJ mol_{CO2}^{-1}
Al-only anode	0.8	0.0 ± 0.1	0.8	690
C+Al anode, touching	1.4	0.4 ± 0.1	1.8	310
C+Al anode, separate	1.7	0.6 ± 0.2	2.3	230

2.3.6.1 Variable current and surface areas

The goal of any CCS technology is to achieve CCS on a large scale. In this instance, that involves oxidising large quantities of sacrificial aluminium as well as increasing the carbon to aluminium ratio in the captured solid. Carbon capture would ideally remove all CO_2 from a waste gas stream, however in the previous 10 mA, 24 hour runs that passed CO_2 gas at 50 mL min^{-1}, this was not the case. Previous experiments experienced a gas flow that passed approximately 150 mmol of CO_2 and captured approximately 2 mmol of CO_2, therefore only 1.4% of the CO_2 effluent was captured. To improve these carbon capture statistics, current ranges between 5 and 40 mA were used over an 18-hour period. Data shown in Appendix 3 (Figure 47), illustrates this electrolysis performed using a lower electrolyte volume of 250 mL. A range of graphite to aluminium ratios were also used to understand the maximum current densities possible before a dramatic increase in kinetic overpotential is required. The graphite to aluminium ratio was changed by increasing the number of graphite and/or aluminium plates used as anode components. Carbon captured throughout these experiments is detailed below (Table 6) alongside a theoretical calculation for the hydrogen generated at the cathode assuming a 100% Faradaic efficiency.

Table 6. Carbon captured within the adjustable electrochemical cell for experiments performed across a wide current range with variable anode components. Experiments performed for 18 h in a 250 mL electrolyte.

Anode	CO_2 (solution) / mmol	CO_2 (solid) / mmol	Total CO_2 / mmol	kJ mol_{CO2}^{-1}	Calculated Al^{3+} [a] / mmol	Ratio Al^{3+}:C_{solid}	Calculated H_2 [b] / mmol	Energy in – H_2 out [c] / kJ
5 mA, 1C+1Al	0.5	0.1	0.6	200	1.1	11:1	1.7	-0.4
10 mA, 1C+1Al	1.2	0.4	1.6	190	2.2	6:1	3.4	-0.7
10 mA, 2C+1Al	1.3	0.2	1.5	220	2.2	11:1	3.4	-0.6
10 mA, 3C+1Al	1.3	0.3	1.6	190	2.2	7:1	3.4	-0.7
10 mA, 2C+2Al	1.7	0.3	2.0	170	2.2	7:1	3.4	-0.6
20 mA, 1C+1Al	1.0	1.0	2.0	870	4.5	5:1	6.7	-0.2
20 mA, 2C+1Al	2.3	0.6	2.9	590[d]	4.5	8:1	6.7	-0.2
20 mA,	1.3	0.6	1.9	500	4.5	8:1	6.7	-1.0
20 mA, 1C+2Al	1.9	1.0	2.9	300	4.5	5:1	6.7	-1.1
20 mA, 2C+2Al	1.9	0.8	2.7	290	4.5	6:1	6.7	-1.1
40 mA, 1C+1Al	2.1	1.5	3.6	1330	9.0	6:1	13.4	0.9
40 mA, 2C+2Al	1.9	1.6	3.5	610	9.0	6:1	13.4	-1.7

[a] Assuming a 100% Faradaic efficiency for $Al \rightarrow Al^{3+} + 3e^-$. [b] Assuming a 100% Faradaic efficiency for $2H^+ + 2e^- \rightarrow H_2$. [c] Calculated using a value of −286 kJ mol^{-1} for the enthalpy of combustion for H_2.[247] [d] Calculated based on the integral of voltage-time data from 20 mA, 1C + 1Al.

The carbon captured in both the solid and the solution is represented graphically in Figure 36 for experiments with a 1:1 Al:C surface area. For both the 1C+1Al and 2C+2Al anode set-ups, the carbon captured in the solid rose linearly with the current passed. Interestingly, the carbon captured within the 250 mL solution appears to reach a maximum saturation point of approximately 1.8 mmol. This is achieved at a much lower current of 10 mA for the 2C+2Al system, rather than 40 mA for the 1C+1Al system. Therefore, increasing the current passed increases the ratio of carbon captured within the solid compared to the electrolyte. It is possible this is linked to the increased rate at which the solution is saturated with carbonate species due to the SSA effect, however more evidence is required to fully understand the relationship between the SSA capture of CO_2 with both current and overpotential effects.

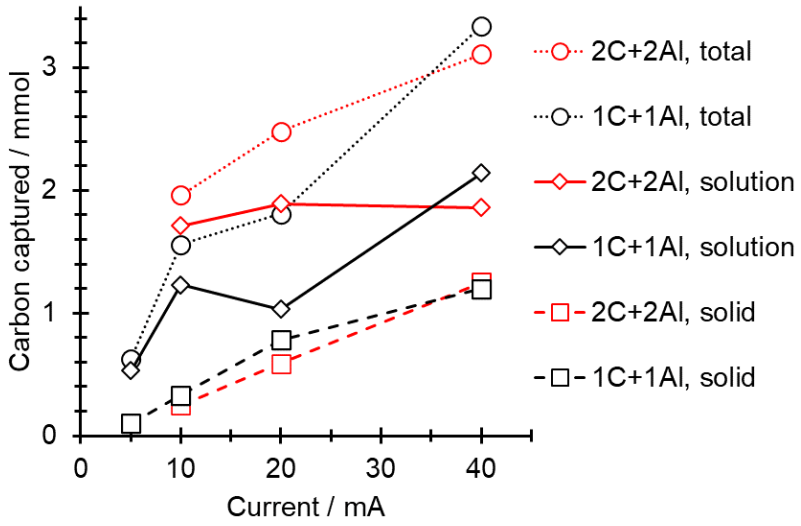

Figure 36. Carbon captured within the versatile electrochemical cell at different current ranges for 1C+1Al (black) and 2C+2Al (red) anode configurations.

The increasing energy cost associated with higher current experiments can be offset with the increase in hydrogen gas production at the cathode. Assuming a 100% Faradaic efficiency toward the HER at the cathode, the moles of hydrogen produced can be calculated. Should these undergo a combustion process (ΔH = -286 kJ mol^{-1}),[247] the process could release energy rather than require it. As there is no specific trend for electrode configurations and currents passed, this hypothetical data is not explored further.

The lowest energy of capture for any of the systems highlighted in Table 6 is the 2C+2Al (10 mA) system at approximately 170 kJ mol_{CO2}^{-1}. As a general rule, the higher surface area of aluminium at higher currents restricts the kinetic overpotential required for aluminium oxidation. This can be clearly seen using the increasing amount of aluminium in the 20 mA current experiments for 1C and 1, 1.5 and 2Al anode systems where the energy of capture decreases from 870 kJ mol_{CO2}^{-1} (1C+1Al) to 300 kJ mol_{CO2}^{-1} (1C+2Al). The intermediate 1C+1.5Al system provides the point at which an increased overpotential is required, as indicated by the anode voltage traces in Appendix 3, Figure 47 b, iii. Given that the overpotential is primarily limited by aluminium surface area, the 1C+1.5Al anode system has an approximate surface area of 31.4 cm^2 which gives a theoretical upper limit for current density of 0.6 mA cm^{-2}. Any industrial applications of this technology must increase the surface area of sacrificial aluminium relative to the current passed on this basis if targeting solid mineralisation.

Increasing the graphitic surface area for systems with the same aluminium content and current inputs does not appear to change the carbon captured at all (see 10 mA, (1-3)C+1Al). This holds true unless the aluminium surface area appears to be limiting as discussed previously. This indicates that the magnitude of the SSA effect can change with the anodic voltage, which is supported by EIS studies using the previous cell design (Figure 31).

For this CCS technique to be scaled, the aluminium surface area must not become limiting by exceeding a maximum anodic current density of 0.6 mA cm^{-2}. The SSA effect does not seem to depend specifically on graphitic surface area, but also upon the anodic voltage applied. Further EIS studies could be used to optimise this and a bipotentiostat could be used to independently control graphite and aluminium electrode voltages. As this technique currently yields an approximate energy cost of 200 kJ mol_{CO2}^{-1}, the technique would be a suitable CCS device for a natural gas combustion plant but unsuitable for a coal-fired gas station if powered by the respective energy source.[17, 218] Should the hydrogen gas produced in this cell be separated and used to power the process, this technology could be able to remove CO_2 from any localised emission sources.

2.4 Conclusions

A novel electrochemical CCS method has been explored that allows metals such as iron and aluminium to be used as sacrificial agents to mineralise carbon dioxide as carbonate ions within a solid. This sacrificial oxidation can be countered by cathodes able to perform proton reduction, where platinum, iron and nickel cathodes evolve hydrogen gas. The addition of a graphite electrode as a second anode component dramatically increases the carbon captured within the cell by acting as a "reagent concentrator". Redox inactive graphite electrodes can "concentrate" CO_2 by attracting carbonate ions into the electric double layer, wherein the bulk CO_2 dissolution equilibrium of $CO_2 \rightleftharpoons H_2CO_3 \rightleftharpoons H^+ + HCO_3^-$ is disturbed to promote fast equilibration to a higher solution concentration of carbonate ions. These processes were shown to rely on electrochemical capacitance by cyclic voltammetry and EIS measurements that indicated the capacitance exhibited was commensurate with a typical electric double layer. The mineralised solid produced exhibits no long-range order for either metal or carbon species and contains only amorphous carbonate ions. Combined with an elemental analysis of the solid, the mineralised product appears to most closely resemble the mineral Dawsonite ($NaAl(CO_3)(OH)_2$).[236]

Two electrochemical cells were used to support these findings where the initial "standard" $Al_{block}|C|Pt$ cell could operate with a 247 kJ mol_{CO2}^{-1} carbon capture efficiency. Under the same conditions with a larger electrolyte and small electrodes, the "adjustable" 1C|1Al|Pt (separate) cell could operate with a 230 kJ mol_{CO2}^{-1} carbon capture efficiency. In both cells, operating without the graphite electrode radically decreased the energy of carbon capture by a factor of approximately 2-3. The energy of carbon capture remained similar for aluminium foil used to mimic aluminium waste. Mild steel could also be used as the sacrificial metal which captured significantly more carbon than the aluminium-based cells, however this was done with a significantly higher energy penalty and led to a similar energy of capture. Unfortunately, most of the carbon was captured in the solution rather than as an isolable solid. It is possible that this solution CO_2 may be released in a "purification" application as performed by Landskron *et al*.[220, 221]

Experiments to probe the scale-up of this CCS process indicated that higher currents favoured the capture of carbon within the solid instead of the solution which is useful for scaling the process. It was found that a maximum anodic current density of 0.6 mA cm^{-2} could be applied before the voltage at the sacrificial metal dramatically increased along with the power used. All experiments herein indicate that this version of electrochemical CCS could be applied to the back of natural gas

power stations, however not to coal-fired power stations should the technology be powered by their respective energy sources.[17, 218] Alternatively, if this process could be powered by solar energy or by the hydrogen emitted from cathodic processes, then this technology would be viable for all CCS applications.

2.5 Appendix 1: Electrochemical cells

Standard cell

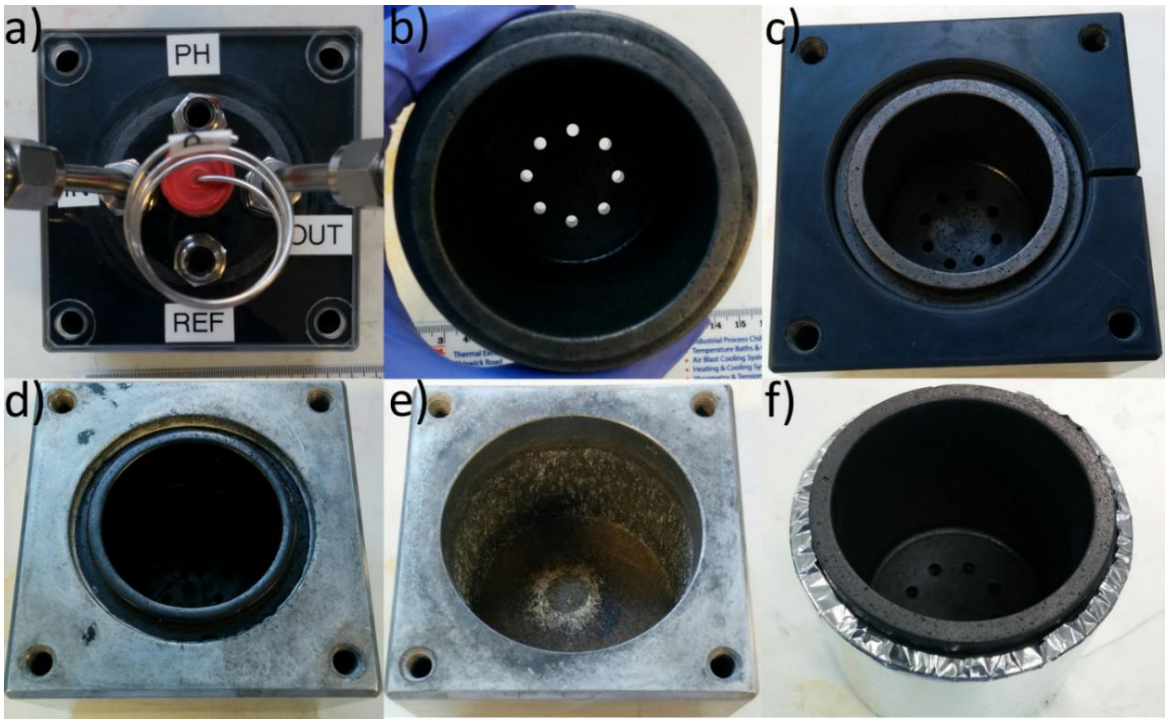

Figure 37. Electrochemical cells used for CO_2 capture featuring: a) the cell lid with ports for the cathode (center), a reference and pH probe and a gas inlet and outlet; b) a removable carbon cup with 8 x 3.2 mm holes drilled through the base, abbreviated simply as C; c) carbon cup in (b) held in an acrylic container; d) a carbon cup analogous to (b) irreversibly held inside a solid aluminium block, abbreviated as $C+Al_{block}$ when used as a dual anode standard cell; e) an aluminium block without a carbon liner, abbreviated as Al_{block}; f) a removable carbon cup, (b), wrapped in aluminium foil for use in the acrylic cell in (c), abbreviated as $C+Al_{waste}$.

Adjustable cell configurations

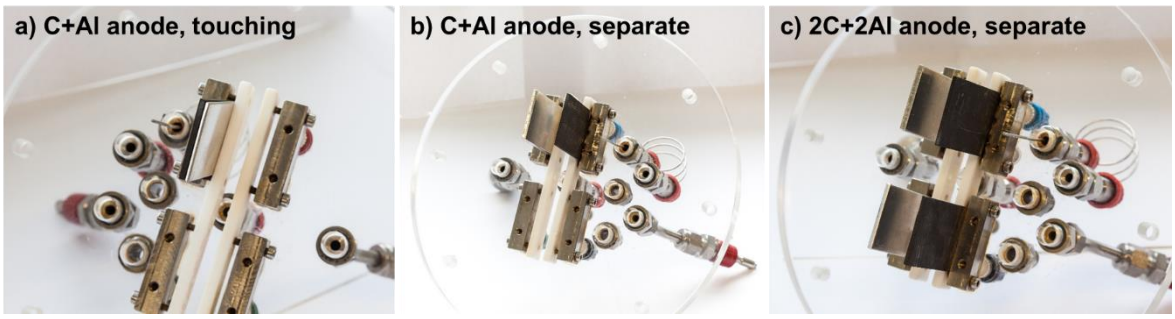

Figure 38. Anode electrode configurations using the adjustable cell. Full electrode plates were 50 x 30 x 2 mm.

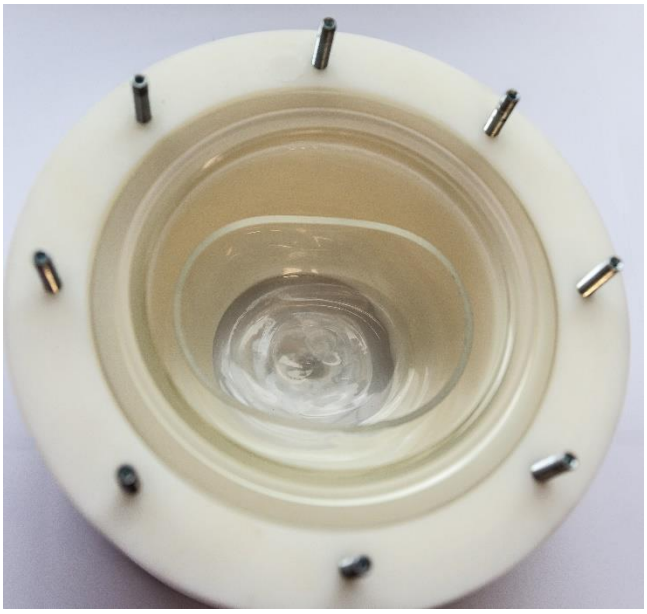

Figure 39. Photograph of the inner glass cell lining used to reduce the electrolyte solution volume from 600 mL to 250 mL.

2.6 Appendix 2: Powder XRD and ATR-IR data

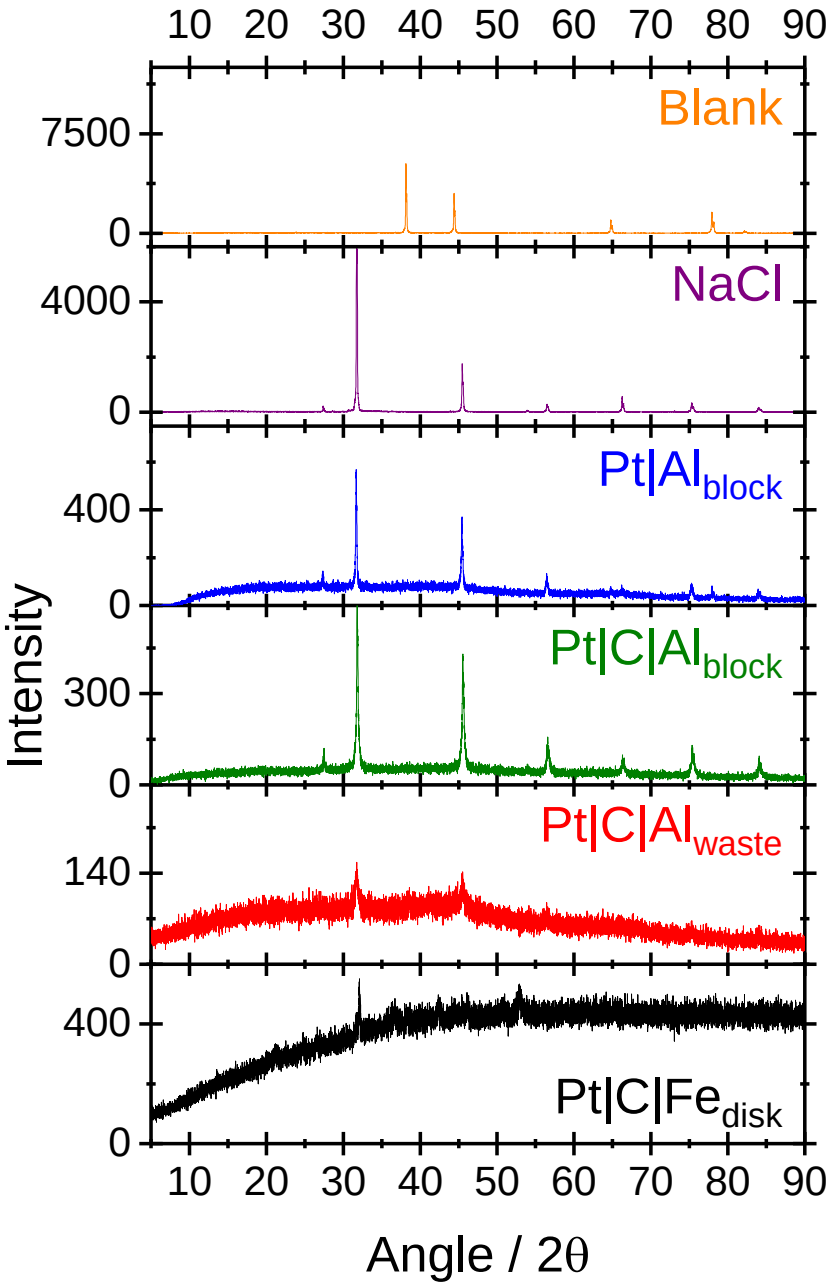

Figure 40. Powder XRD spectra of the resulting dried solids from CCS electrolysis experiments. Blank indicates any signals originating from the sample holder and NaCl is pure NaCl crystals.

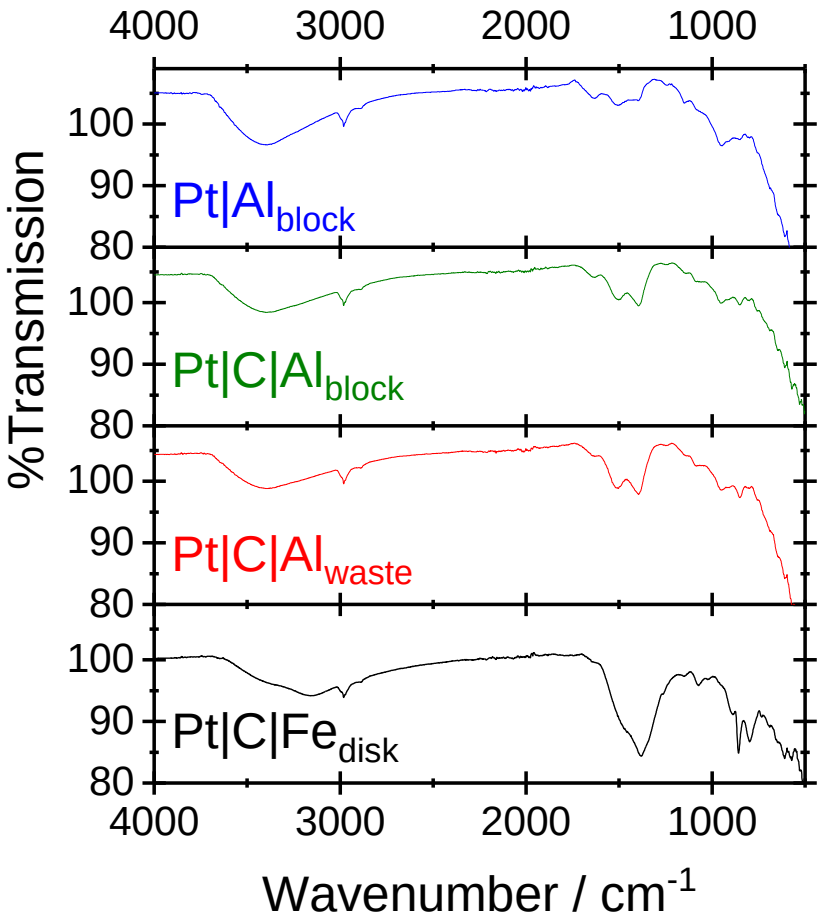

Figure 41. ATR-IR spectra of the resulting dried solids from CCS electrolysis experiments.

2.7 Appendix 3: Instrument traces for CCS electrolysis runs

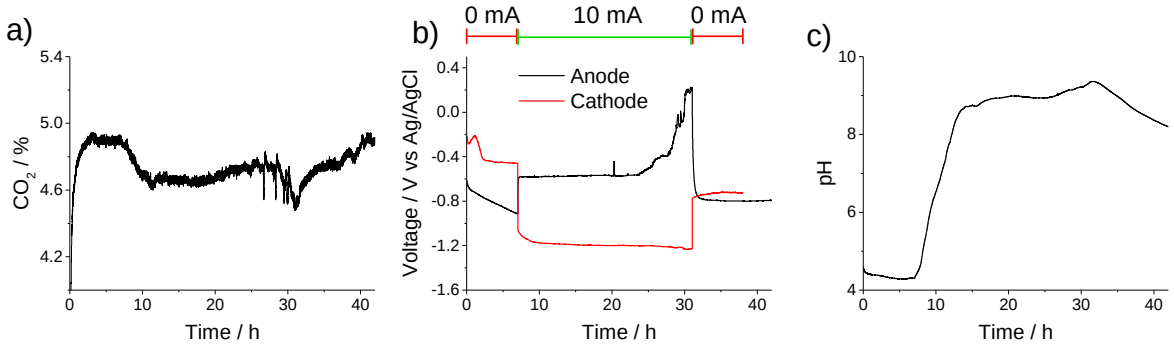

Figure 42. Experimental traces for electrochemical CCS using a $Al_{block}|C|Pt$ cell featuring a) effluent CO_2 concentration, b) voltage traces and c) pH-time traces. Electrolysis performed in 1 M NaCl (60 mL) for 24 h at room temperature.

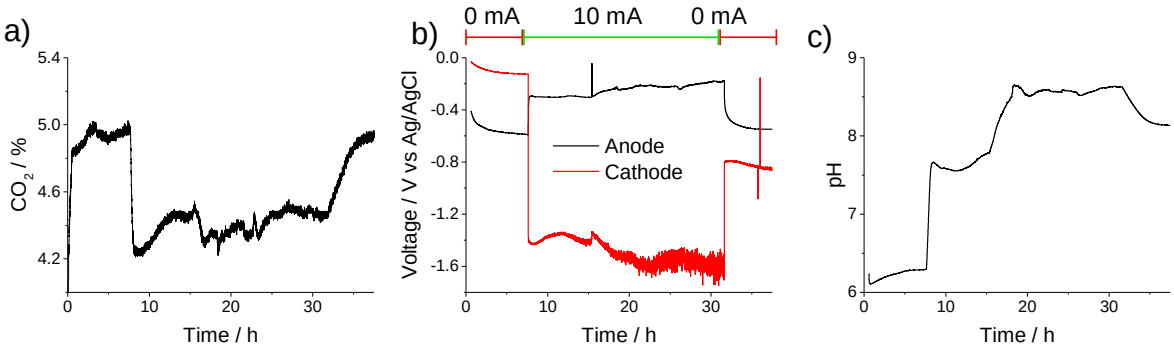

Figure 43. Experimental traces for electrochemical CCS using a $Fe_{disk}|C|Pt$ cell featuring a) effluent CO_2 concentration, b) voltage traces and c) pH-time traces. Electrolysis performed in 1 M NaCl (60 mL) for 24 h at room temperature.

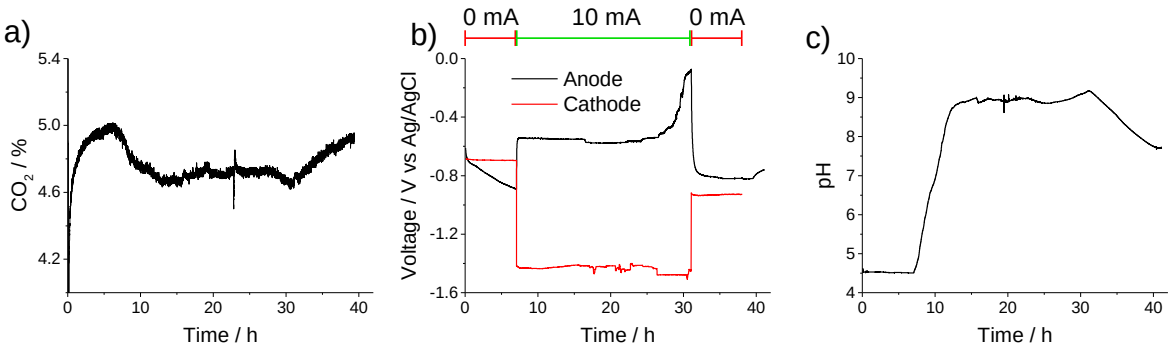

Figure 44. Experimental traces for electrochemical CCS using a $Al_{waste}|C|Fe$ cell featuring a) effluent CO_2 concentration, b) voltage traces and c) pH-time traces. Electrolysis performed in 1 M NaCl (60 mL) for 24 h at room temperature.

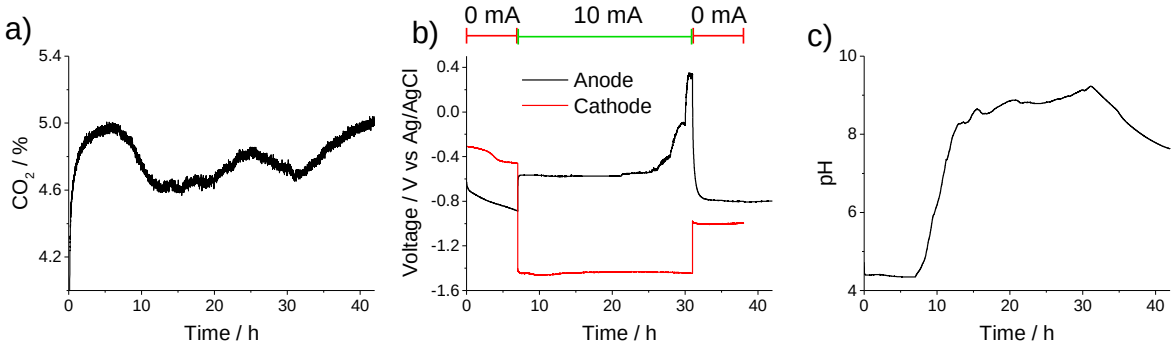

Figure 45. Experimental traces for electrochemical CCS using a $Al_{waste}|C|Ni$ cell featuring a) effluent CO_2 concentration, b) voltage traces and c) pH-time traces. Electrolysis performed in 1 M NaCl (60 mL) for 24 h at room temperature.

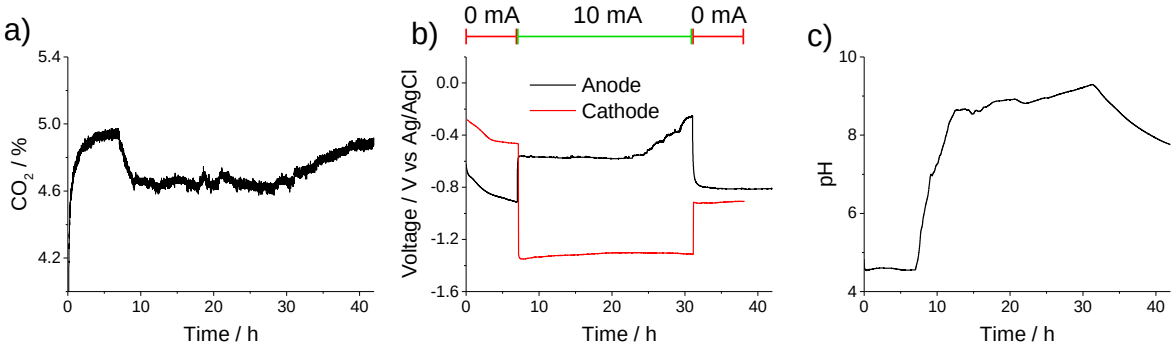

Figure 46. Experimental traces for electrochemical CCS using a $Al_{waste}|C|Ni(x11)$ cell featuring a) effluent CO_2 concentration, b) voltage traces and c) pH-time traces. Electrolysis performed in 1 M NaCl (60 mL) for 24 h at room temperature.

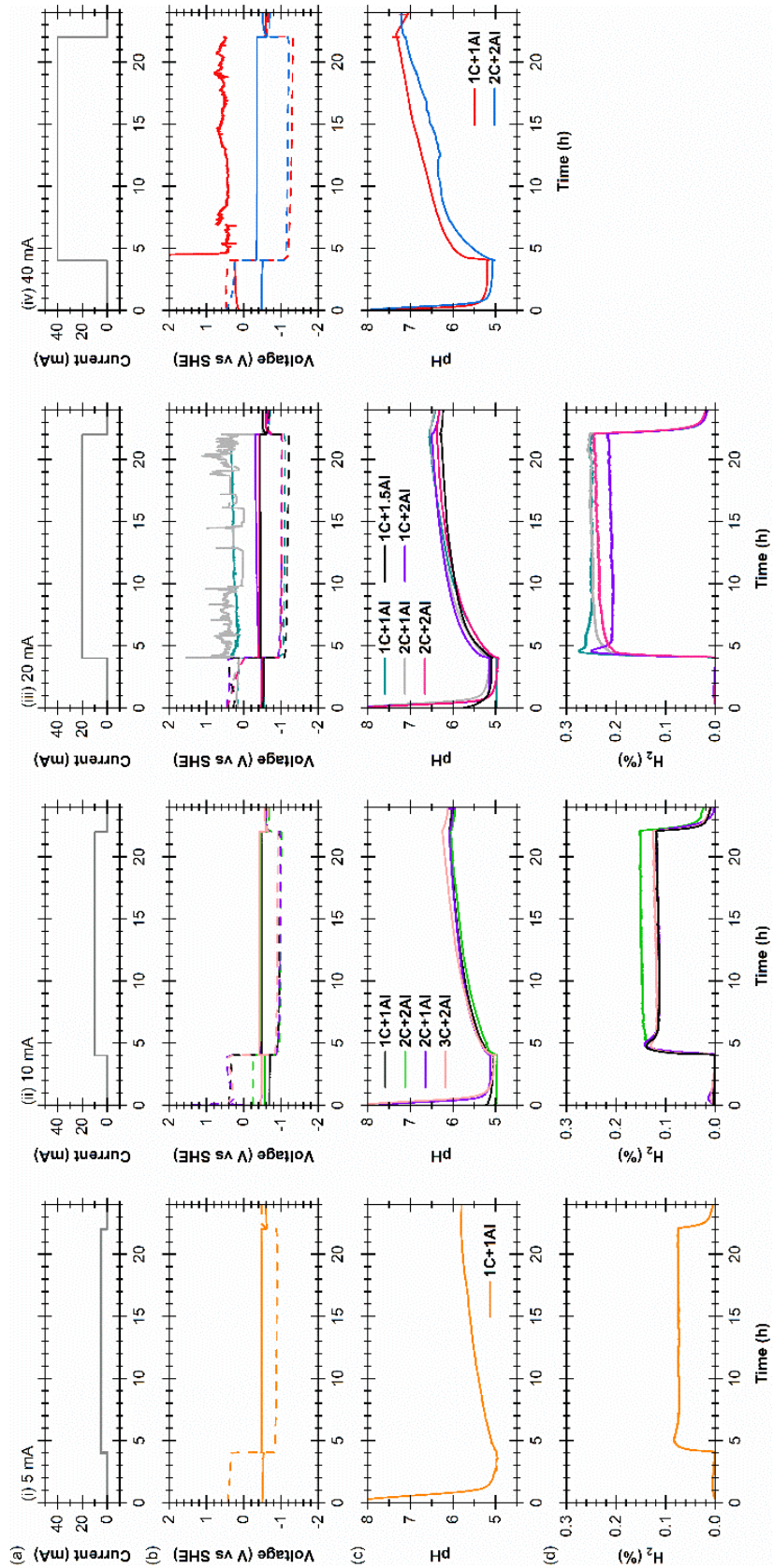

Figure 47. (a) Current input, (b) voltage, (c) pH and (d) $\%H_2$ time traces from experiments with variable dual-material anode configurations for electrochemical CCS within the "versatile" electrochemical cell. Experiments conducted under a continuous flow rate (50 mL min^{-1}) of 5% CO_2 / 95% N_2 gas. A platinum cathode was used in a 1 M NaCl (600 mL) electrolyte at room temperature.

Chapter 3. Modification of copper electrodes with amine terminated monolayers

Author Declaration

Molecule 5 was synthesised by Jack Dickenson-Fogg (MChem, 2018) under the supervision of Nick Yates. Adam Ward (MChem, 2019, supervised in day-to-day lab activities by me) assisted with recording cyclic voltammetry in section 3.3.4 for modification of amine functional groups with viologen moieties. Nick Yates performed all synthesis and method development work for oxylamine systems, except for the EIS and AFM measurements which I performed and have outlined. All other work presented in this chapter is my own.

3.1 Abstract

CO2ER catalysts have incorporated amine functionalities for more than 25 years. Generally, these functionalities have been incorporated into heterogeneous catalysts *via* the casting of films, often made of polymers or oligomers, onto the surface of the solid catalyst substrate.[248, 249] This chapter describes the design and implementation of a novel strategy for generating covalently-modified amine-functionalised copper electrodes using diazonium electro-grafting. Such surfaces are used for CO2ER in Chapter 4 of this thesis. In the results described here, a radical scavenger strategy and a protection-deprotection strategy are compared to determine the most reliable means of generating a monolayer of amine termini as opposed to a thick multilayer. It is concluded that a protection-deprotection strategy is more effective than a radical scavenger strategy based on the analysis of cyclic voltammograms of modified electrodes in ferricyanide solutions. The stepwise changes to a copper surface through the protection-deprotection strategy are then extensively explored using EIS, solution CV and redox tagging. Finally, these electrochemical surface characterisation methods are used to analyse near-monolayers generated from using a similar diazonium protection-deprotection strategy to derivatise glassy carbon electrodes with a monolayer of oxylamine derivatives that readily conjugate to aldehydes.

3.2 Introduction

Monolayer modifications on electrode surfaces have routinely been achieved with the use of diazonium salts on materials such as carbon, gold and silicon.[191, 250, 251] These modifications are largely driven by the need for electrochemical sensing applications, for example glucose bio-sensing.[252] Three main methods exist for producing a monolayer from a diazonium precursor: controlling the amount of radicals present *via* a radical scavenger,[191] steric blocking[253] or a protection-deprotection strategy.[193, 254] These strategies are discussed herein with the exception of steric blocking as the technique is difficult to perform. Studies by Menanteau *et al.* (radical scavenger)[191] and Hauqier *et al.* (protection-deprotection)[193] are herein discussed and repeated on a glassy carbon electrode to target the production of a monolayer. The most successful and widely applicable technique by Hauquier *et al.* is further expanded in a novel application onto a copper electrode. These diazonium modified copper electrodes will be used in Chapter 4 as a novel CO2ER catalyst, where further details on the choice of an amine headgroup will be provided in the introduction to that chapter.

As outlined in section 1.3.5.1, diazonium modification is a radical based mechanism. This can easily lead to formation of multilayers through the creation of further nitrobenzene radicals that can continue to bind and form a thick multilayer surface coating. Should the electro-grafted molecule contain an electroactive group for charge propagation, films up to 900 nm thick can be formed.[255] The mechanism in Figure 48 is commonly accepted as one of the main mechanisms of binding, however it is also possible for radical activation of the N≡N bond to lead to diazo linkages.[187]

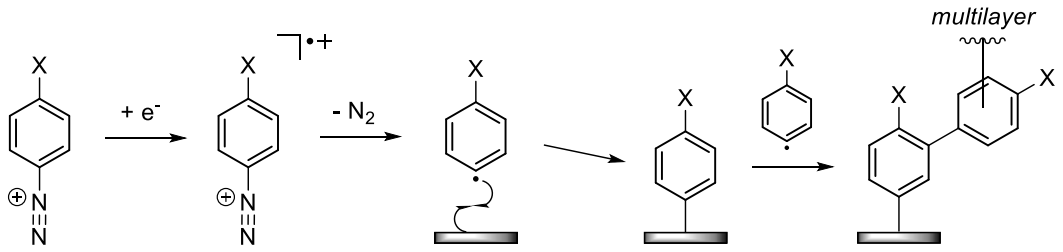

Figure 48. Reductive one electron grafting of a diazonium salt to an electrode surface. Adapted from reference 189.

Limiting the availability of the radical can reduce the propensity to form multilayers. Menanteau *et al.*[191, 192] introduced a radical scavenger, DPPH (Figure 49, right), to remove a large portion of the radicals generated near the electrode surface. Adding 2 mM DPPH into the electrolyte whilst performing electro-grafting ensured that the grafted film thickness dropped from 5.5 ± 0.5 nm (without DPPH) to 0.9 ± 0.5 nm, consistent with monolayer formation. Figure 49 shows the cyclic

voltammetry of the electrode grafting step in the presence of DPPH where the lack of a clear irreversible reduction peak (see introduction section 1.3.5.1) demonstrates that electrochemical grafting is inhibited. The observed peaks at $E_{1/2}$ 0.35 V are DPPH redox processes. The grafting procedure was performed with a range of DPPH concentrations (0 – 2 mM), where 2 mM DPPH was optimum for monolayer coverage.

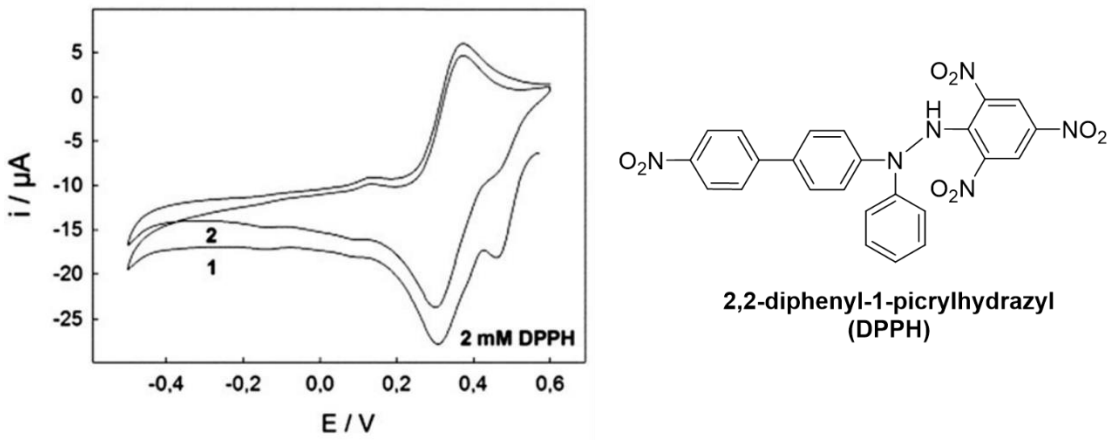

Figure 49. Electrochemical grafting by cyclic voltammetry (left) of NPDT in the presence of 2 mM DPPH (right). Grafting performed with a glassy carbon electrode at 50 mV s^{-1} relative to an $Ag/AgNO_3$ reference electrode. Adapted from reference 192 with permission from the PCCP Owner Societies.

Instead of inhibiting radical concentration, Hauquier *et al.* published a novel technique to generate a uniform monolayer of electrochemically grafted moieties from diazonium precursors *via* a protection-deprotection strategy (Figure 50).[193] Electrochemical grafting is performed using cyclic voltammetry, which produces a multilayer structure as previously discussed, however with a chemically protected amine functionality. As radical binding consequently occurred on top of the protecting group, chemical cleavage of the phthalimide group revealed a monolayer functionalisation. The redox communication of the electrode surface throughout the stages of modification was observed through the $[Fe(CN)_6]^{3-/4-}$ redox couple. Electrode passivation and reactivation were the multilayer was added and deprotected, respectively. Revealing amine functionalities in this way can also be achieved using other protecting groups such as Fmoc for monolayer modification.[256]

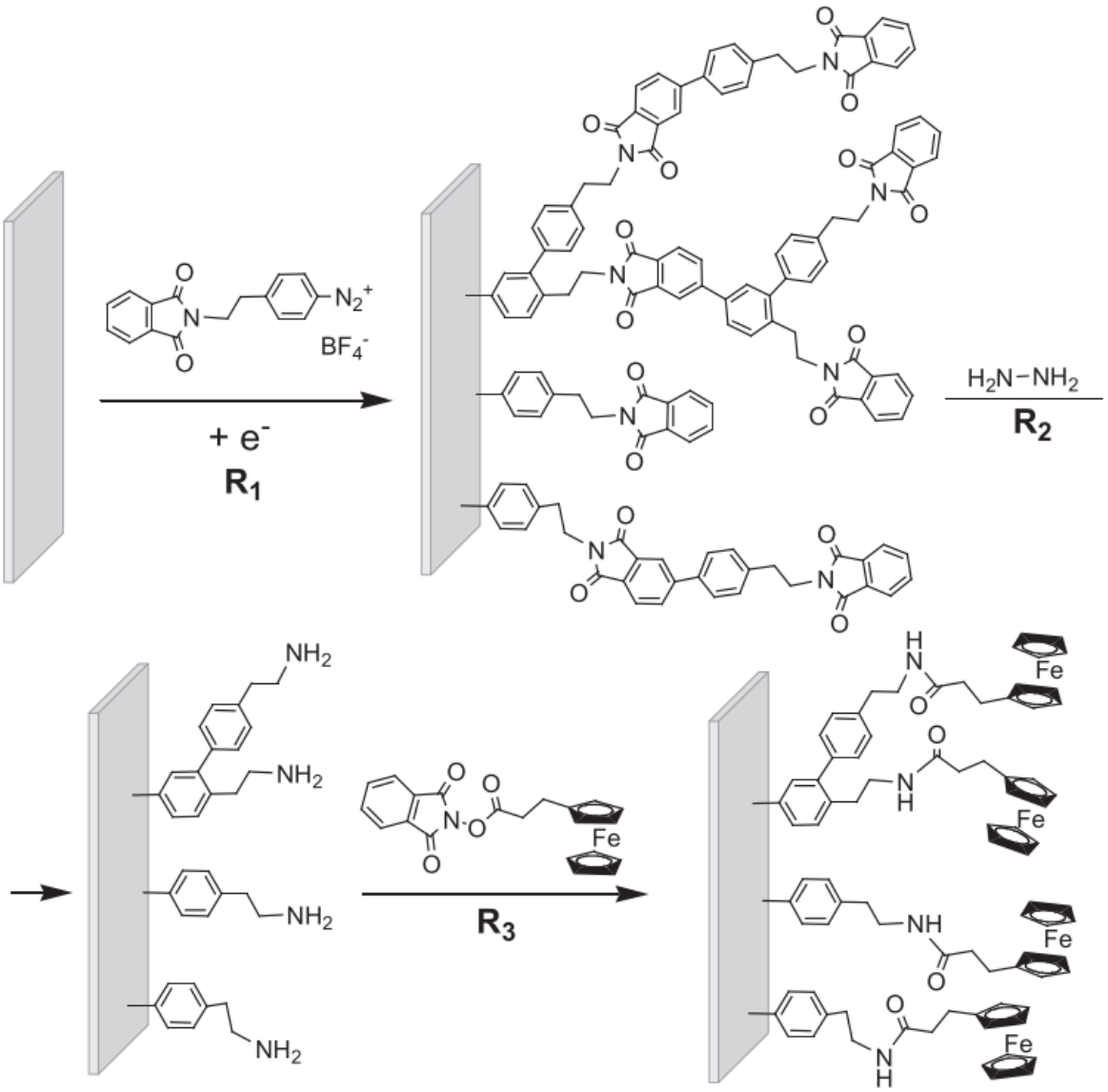

Figure 50. Installation of an amine terminated monolayer *via* a protection-deprotection strategy. Final step to install a ferrocene redox handle for detection by CV. Reprinted from reference 193, Copyright (2020), with permission from Elsevier.

The synthesis of monolayers has been well studied on some electrode materials such as carbon-based materials for applications such as biosensors.[252] Contrastingly, the functionalisation of other materials such as copper with monolayers have not been routinely reported. The first derivatisation of copper electrodes with diazonium salts was performed by Bernard *et al.* for corrosion inhibition.[257] They functionalised copper by electro-grafting NPDT to form a multilayer that was 5 ± 2 nm (6-7 aryl layers) thick. Others have modified copper in a similar way to increase corrosion inhibition, where only NPDT, polyphenylene, alkyl-diazonium and a few related para-substituted anilines have been electro-grafted to date.[186, 258-261] A unique and alternative application for the modification of copper has been to make copper superhydrophobic using para-alkyl-substituted aniline derivatives.[262]

No attempts have been made to form a monolayer functionalisation on copper using diazonium salts (this has only been achieved with SAMs)[194, 195, 263] or to use such functionalities and surface properties for catalysis. Therefore, this chapter aims to produce a copper electrode modified with a monolayer functionality *via* diazonium electrochemistry. This chapter reports initial experiments that reproduce the work by Menanteau *et al.*[191] and Hauqier *et al.*[193] on a glassy carbon electrode, as well as reporting the novel synthesis of new surface modifier molecules before the most successful and widely applicable monolayer modification strategy is applied to a copper electrode.

3.3 Results and Discussion

3.3.1 Molecules for amine modified surfaces

A variety of precursor molecules were sourced to probe two methods of creating an amine terminated monolayer: a radical scavenger method (using precursor molecules **1**, **2**) and a protection-deprotection strategy (using precursor molecules **3** – **6**). Molecules **1** and **2** were commercially available and used to mimic the work by Menanteau *et al*.[191, 192] Once electro-grafted, the nitro termini within these molecules can undergo electro-reduction to amine moieties for use in CO2ER applications. In order to extend the work of Hauqier *et al.*[193] on the protection-deprotection mechanism, molecules **3** – **6** were synthesised to represent a wider range of hydrophobicity and amine flexibility through alkyl chain motion (full synthesis in section 7.5.1) where all are novel procedures except for molecule **4**).[193] The structures of **1** – **6** are shown in Figure 51 alongside the target electrode surface state.

3, **4** and **5** were initially bought as benzyl alkyl amines (with or without a nitrated benzene), amine-protected using phthalic anhydride and then hydrogenated to produce the aniline from a nitrobenzene unit. A Grignard reagent was used to alkylate 4-bromoaniline to produce 4-(10-bromodecyl)aniline upon which phthalimide was reacted to produce molecule **6**. Molecules **2** – **6** contain aniline moieties that were converted *in-situ* into aryl diazonium moieties, according to section 7.2.2, whilst **1** was used as purchased. Some of these molecules are initially electro-grafted onto glassy carbon electrodes to permit comparison with literature work; later results then extend this study to copper electrode modification.

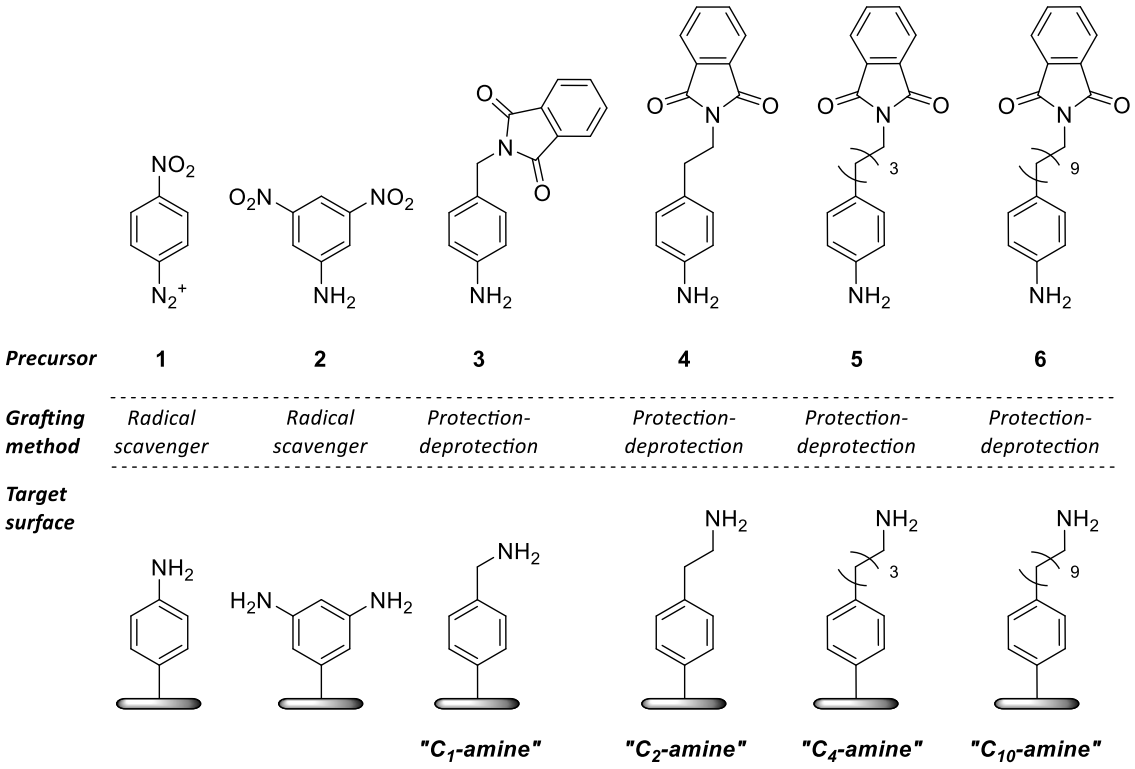

Figure 51. Target amine-modified electrode surfaces for potential use in CO2ER.

3.3.2 Radical scavenger and protection-deprotection grafting strategies on glassy carbon

All work in this section is performed on glassy carbon working electrodes to make it comparable to the literature procedures.[191, 193] The expected mechanisms are detailed in Figure 52 with details of the experimental conditions used throughout this chapter. The modification processes are qualitatively and semi-quantitatively analysed using solution-based ferricyanide cyclic voltammetry (to follow surface-solution conductivity) and electrochemical reduction of NO_2 groups (for surface coverage), respectively.

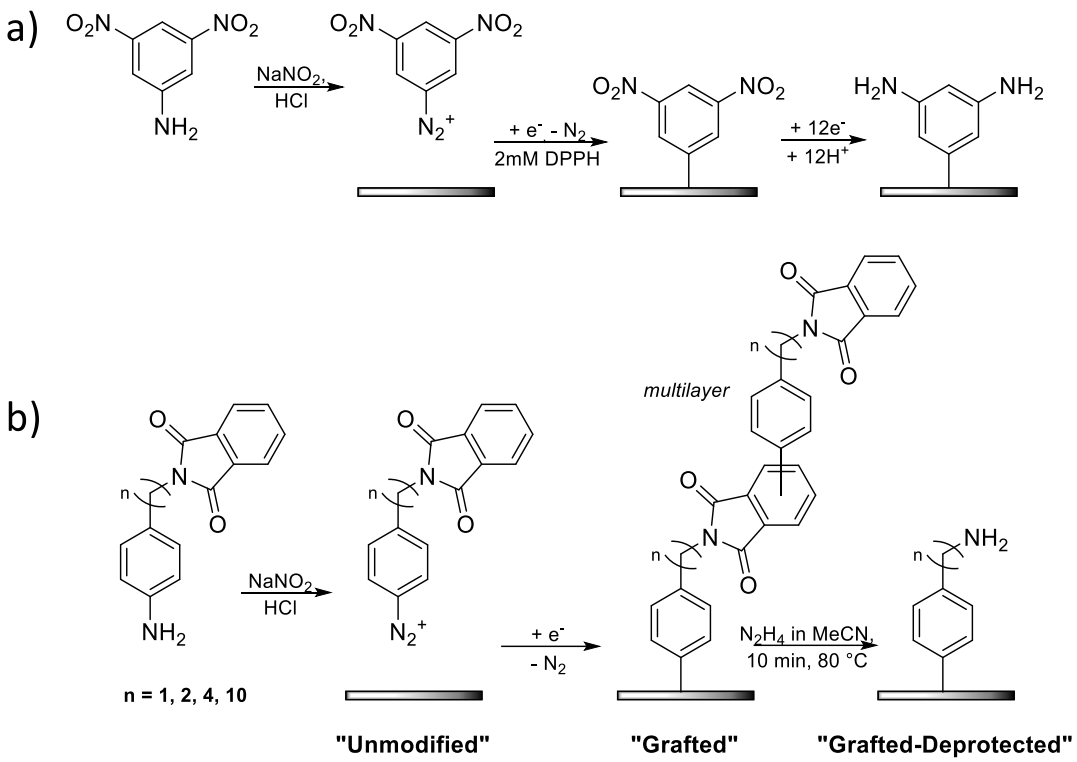

Figure 52. Expected electrode modification steps for monolayer amine functionalisation using a radical scavenger approach (a) or a protection-deprotection strategy (b).

3.3.2.1 Monolayer grafting on glassy carbon via radical scavenger grafting

Initial experiments were conducted using molecule **1** to mimic those by Menanteau *et al*.[191] As shown in Figure 53a, molecule **1** was electrochemically grafted onto a glassy carbon electrode *via* a reductive voltammetric sweep in the absence of DPPH (Figure 53a). The voltammetric trace is typical for the grafting of a diazonium salt, displaying a large reductive peak at 0.15 V vs Ag/AgCl which is attributed to the production of radicals that go on to covalently bind to the electrode surface. Atomic Force Microscopy (AFM) and X-Ray Photoelectron Spectroscopy (XPS) studies by Menanteau *et al.* have shown that this method typically produces a multilayer thickness of 5.5 ± 0.5 nm with approximately 6-7 layers of modification.[192] Following electrochemical grafting, the nitro groups on **1** were reduced using cyclic voltammetry (data not shown). Both an unmodified glassy carbon surface and the final amine-modified glassy carbon surface were tested qualitatively for their electron transfer to a solution of the redox active molecule potassium ferricyanide. The sharp oxidative (0.31 V) and reductive (0.19 V) peaks shown in Figure 53b illustrate fast electron transfer kinetics from an unmodified "blank" electrode surface to the ferricyanide molecule. Contrastingly, the modified electrode displayed significantly depressed peaks which demonstrate slower electrode kinetics, which indicates a thick semi-conductive layer has been formed.

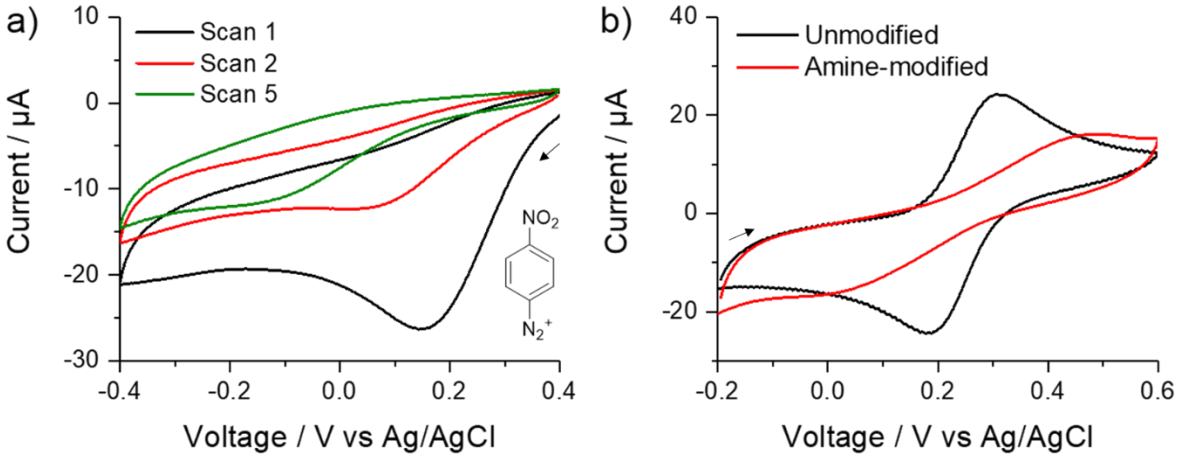

Figure 53. Electrochemical grafting (a) of **1** (inset) onto a glassy carbon electrode and the redox activity (b) of unmodified and amine functionalised surfaces with 1 mM $K_3Fe(CN)_6$. v: 500 mV s^{-1}. Black arrows indicate starting sweep direction.

Next, the modification of the carbon surfaces with **1** was repeated but in the presence of 2 mM DPPH in the grafting electrolyte, as described by Menanteau *et al*.[191] The results are shown in Figure 54a. The grafting CV simply shows a DPPH redox couple ($E_{1/2}$ = 0.27 V vs Ag/AgCl), whilst there is no obvious grafting peak at 0.15 V vs Ag/AgCl as was observed in the absence of DPPH. Therefore, it is likely that this step has reproduced the results of Menanteau *et al.*, indicating the final modified surface closely resembles a monolayer. The electrode conductivity toward potassium ferricyanide was also measured as previously in Figure 53b, where the redox communication of the nitro-terminated was also recorded. Figure 54b shows fast redox kinetics, in contrast to the electrode surface produced in the absence of DPPH whilst electro-grafting.

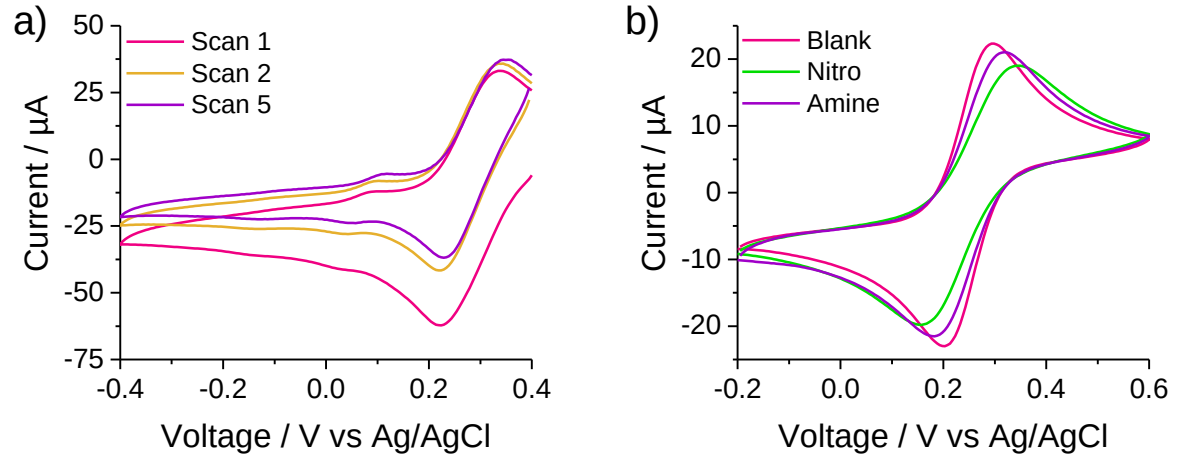

Figure 54. Electrochemical grafting of **1** (a) onto a glassy carbon electrode in the presence of 2 mM DPPH. Corresponding redox communication (b) of surface states to ferricyanide (1 mM in 0.1 M NaCl) throughout the grafting procedure. v: 500 mV s^{-1}.

To test the scope of this technique, the strategy was repeated with molecule **2**, a dinitro analogue of **1**, the grafting of which has not been previously reported in literature. **2** further requires the use of *in-situ* diazotisation *via* sodium nitrite and acid activation (mechanism in section 1.3.5.1), as illustrated in Figure 52a. The resulting grafting CVs and redox communication studies with ferricyanide are shown in Figure 55 for experiments performed with and without the presence of DPPH.

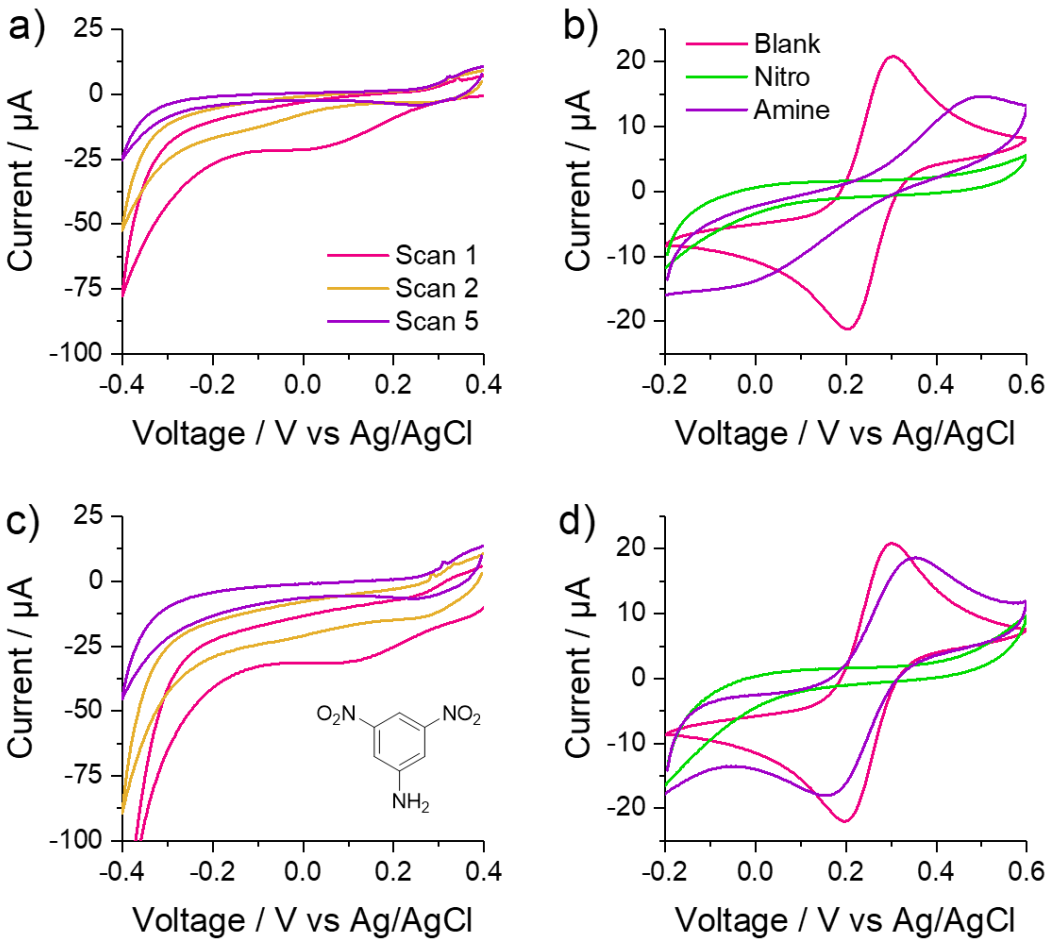

Figure 55. Electrochemical grafting of **2** (a, c) onto a glassy carbon electrode and (b, d) the electrochemical communication of surfaces throughout the modification procedure to 1 mM ferricyanide 0.1 M NaCl. Panels (a, b) correspond to modifications performed without a radical scavenger, while for experiments (c, d) 2 mM DPPH was present in the grafting step. v: 500 mV s^{-1}.

In the initial grafting of **2**, the cyclic voltammetry displays a significant diazonium reduction peak at 0.05 V vs Ag/AgCl in experiments conducted both with and without the addition of DPPH (Figure 55). Analysis of the ferricyanide CVs for the final amine modified surfaces shows that including DPPH in the grafting step does increase electrode-ferricyanide charge transfer kinetics. This indicates that presence of 2 mM DPPH does somewhat restrict the multilayer growth, however not completely.

For electrodes modified with the nitro-termini from **2**, the lack of any redox peaks in Figure 55b and d shows that electrode-ferricyanide charge transfer kinetics are completely inhibited upon electrode modification, regardless of the presence of DPPH. This is likely due to the electrostatic repulsion between negatively charged terminal oxygens within the nitro groups and the negatively charged $[Fe(CN)_6]^{3-}$ ion. Opposingly, these nitro termini likely attract positively charged diazonium salts during electrochemical grafting, which in turn increases the local concentration of radicals. This may explain why a higher concentration of DPPH appears to be required to inhibit multilayer formation by molecule **2** compared to molecule **1**.

Electrochemical reduction of the nitro termini produced immediately after grafting of molecules **1** and **2** yields a reduction peak at approximately -0.75 V vs Ag/AgCl (example in Figure 56). It was hoped that this would correspond to complete reduction from RNO_2 to RNH_2, however the presence of a reversible redox couple at $E_{1/2}$ = -0.24 V vs Ag/AgCl corresponds to hydroxylamine oxidation ($RNHOH \rightleftharpoons RNO + 2H^+ + 2e^-$).[191] Therefore, the reduction step of the nitro termini has occurred primarily to hydroxylamines *via* the reaction ($RNO_2 + 4H^+ + 4e^-$ -> RNHOH). Assuming this as the only pathway, the peak integrals were used to calculate the surface coverage by employing Equation 2.

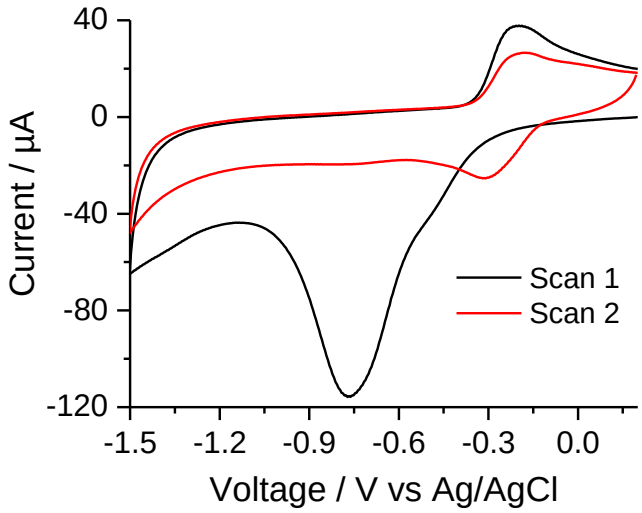

Figure 56. Reductive conversion of RNO_2 to RNHOH (-0.75 V) for glassy carbon functionalised with **2**. ν = 500 mV s^{-1}.

$$\Gamma = \frac{A}{\sigma \epsilon F \nu}$$

Equation 2. Conversion of peak area to surface coverage. Γ = surface coverage / mol cm^{-2}; A = peak area / A V; σ = electrode surface area / cm^2; ϵ = electrons per reactant molecule; ν = scan rate / V s^{-1}.

Surface coverage calculations were performed for the nitro conversion step of molecule **2** where electrochemical grafting had taken place both with and without the presence of 2 mM DPPH. The

inclusion of DPPH lowered the surface coverage slightly from 288 ± 12 pmol cm^{-2} (absence of DPPH) to 270 ± 3 pmol cm^{-2} (with DPPH). This agrees with the slower electrode kinetics when DPPH is not present during grafting, both of which support the notion that DPPH inhibits multilayer formation, though not drastically, for molecule **2** grafting. The surface coverage calculation was also applied to molecule **1** grafted with DPPH and yielded a surface coverage of 251 ± 14 pmol cm^{-2}. This drop in surface coverage is likely an effect of surface polarization effects as previously discussed. Menanteau *et al.* performed similar methodologies and found the grafting of molecule **1** yielded surface coverages of 240-540 pmol cm^{-2}. It was noted however that the film thickness did not always correlate with the number of electroactive groups and so this analytical method can only be regarded as semi-quantitative.

The ultimate aim was to find a method for modifying copper electrodes with a monolayer of amine functionalities for CO2ER. Whilst the presence of 2 mM DPPH can limit multilayer growth, the optimisation process of DPPH concentration to achieve a perfect monolayer coverage (as opposed to multilayer or sub-monolayer) does not make this a widely applicable technique for grafting a range of different amine containing substrates. Furthermore, it has been noted in literature that electrochemical reduction of nitro groups to amines can often be incomplete.[187] Therefore this method of achieving an amine terminated monolayer was not extended from glassy carbon to copper electrodes.

3.3.2.2 Monolayer grafting on glassy carbon via a protection-deprotection strategy

A different strategy for the production of an amine-decorated monolayer from diazonium precursors is through the use of protecting groups as illustrated by Hauquier *et al*.[264] Molecules **3** and **4** contain sterically protected amines, which are diazotised *in-situ* before electrochemical grafting to the glassy carbon electrode (Figure 57a). Following grafting, a hydrazine deprotection of the phthalimide group produces a monolayer *via* cleavage of the multilayer formed on the aromatic protecting group (see Figure 52). These surface modification steps are followed by ferricyanide CVs (Figure 57b). Multilayer grafting of diazonium salts **3** and **4** completely passivate the redox activity of the electrode toward ferricyanide as previously observed by Hauquier *et al*. However, after hydrazine deprotection, the redox activity of the ferricyanide at the amine monolayer is slightly enhanced relative to the “blank” unmodified glassy carbon electrode. This may be due to an

electrostatic attraction between the amine moieties (expected as RNH_3^+ at pH 7) and the ferricyanide anions.

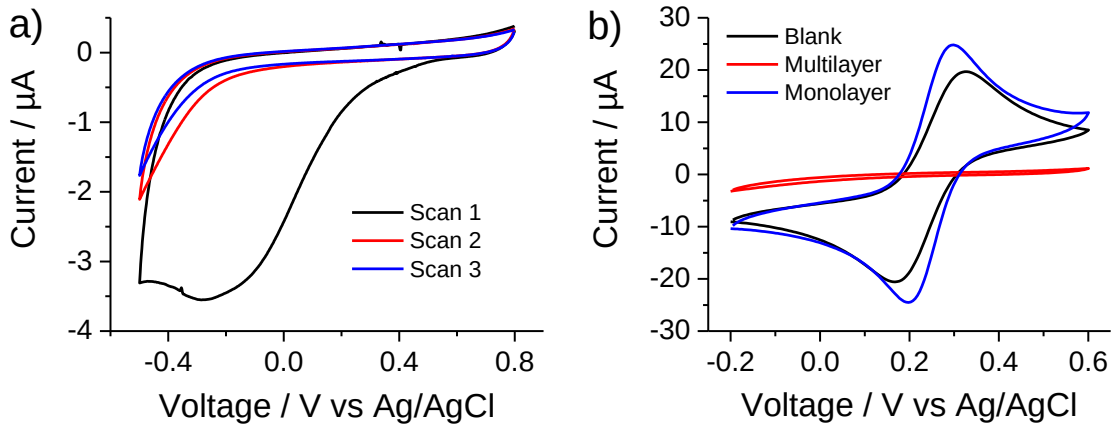

Figure 57. Grafting of molecule **4** (a) and CVs in 1 mM $K_3Fe(CN)_6$ / 1 M NaCl solution at various stages throughout a protection-deprotection strategy (b). v = 20 mV s^{-1} (a), 500 mV s^{-1} (b).

This method reliably showed fast redox kinetics for surfaces post-hydrazine treatment, which indicates that no thick films were formed on the electrode surface. The protection-deprotection strategy also has greater applicability as a wider range of functionalities could be introduced without the need for optimisation of experimental conditions specific to each electrode modifier. This work correlates with previous literature work on carbon electrodes and molecules **3** – **6** are studied for their modification of copper electrodes, the target surface for CO2ER applications.

3.3.3 Monolayer grafting on copper *via* a protection-deprotection strategy

The protection-deprotection strategy of the previous section was next used on a copper electrode inside a glovebox under a nitrogen atmosphere. After mechanical polishing, the copper electrodes were placed inside a nitrogen glovebox and CV performed to remove surface oxide species. Figure 58 shows reduction peaks at -0.6 and -1.5 V vs Ag/AgCl. This step was specifically included as in the Literature both Cu-C and Cu-O-C bonds have been observed by XPS for copper electrodes modified with diazonium salts.[265] Therefore this extra reduction step to strip oxides from the surface was necessary to ensure only Cu-C diazonium modifications were formed. This was chosen as Cu-O-C modifications could be reductively cleaved *via* Cu-O cleavage during CO2ER catalysis.

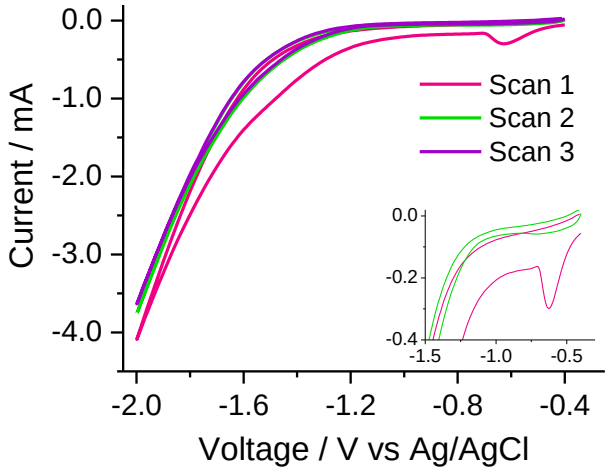

Figure 58. Oxide stripping of a copper electrode in 0.1 M NaCl under a N_2 atmosphere. v = 500 mV s^{-1}.

Following this, electrodes were grafted with molecules **3** – **6**, where reductive grafting appeared to take place at -0.7 V vs Ag/AgCl (Figure 59). Whilst spontaneous grafting of diazonium salts to on copper electrodes has been known to occur,[183, 185] this version of electrochemical grafting is designed to build up a thick, dense multilayer to ensure grafting on all copper surface planes. CV grafting was performed for a higher number of scans (30) than on glassy carbon (3) until electrochemical grafting was complete and no reduction peak was observed.

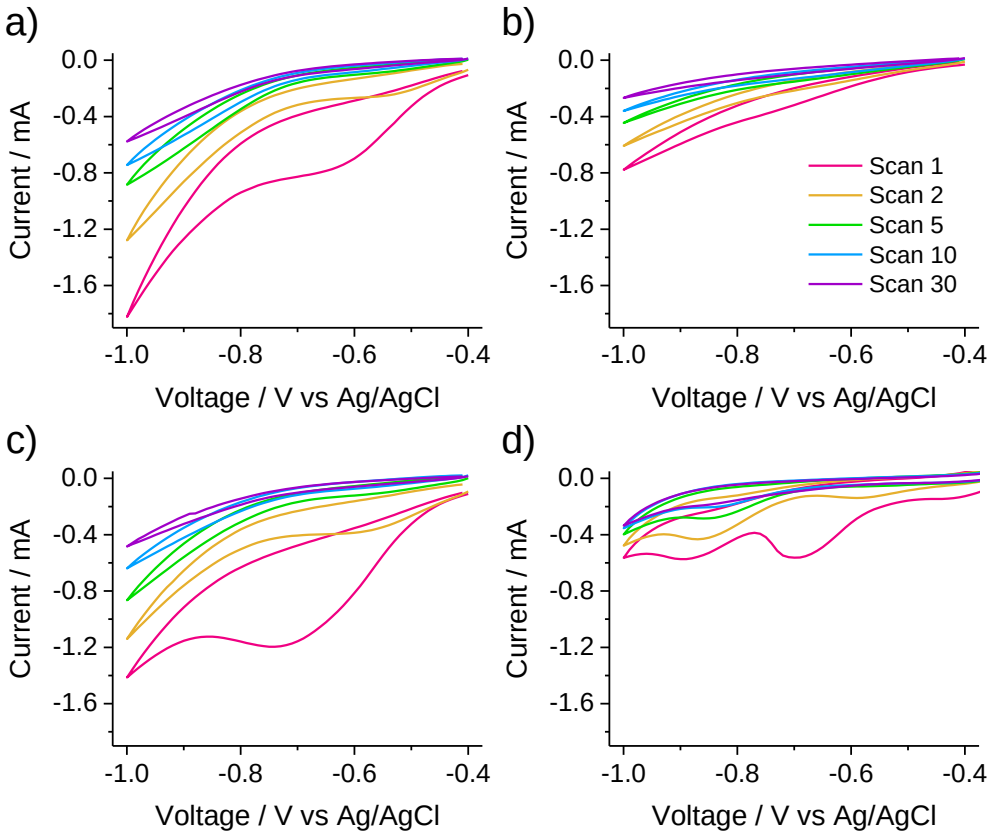

Figure 59. Electrochemical grafting of a) **3**, b) **4**, c) **5** and d) **6** onto a copper electrode under a N_2 atmosphere. v = 500 mV s^{-1}, 30 scans.

The progress of the modification procedure was qualitatively followed by using methyl viologen dichloride as a redox marker. This viologen was chosen as the redox marker as the first redox signal ($MV^{2+} + e^- \rightleftharpoons MV^+$) has an $E_{1/2}$ = -0.651 V vs Ag/AgCl[266] which occurs at significantly more negative potentials than copper oxidation which means there will be less chance of oxidative stripping of any surface modifications. All viologen species can undergo two separate reversible one electron reductions (Figure 60). The first reduction produces a radical intermediate that can undergo a further reduction to an uncharged molecule.

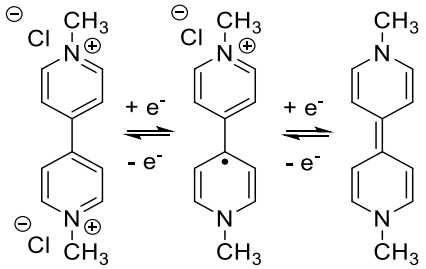

Figure 60. Methyl viologen redox processes.[267]

The first one-electron reduction process was used to follow copper electrode's charge transfer capabilities throughout the stages of modification. Figure 61a shows the redox ability of a copper electrode being modified with molecule **5**. All stages demonstrate fast redox kinetics apart from immediately after grafting as a "multilayer". The grafting stages of molecules **3** and **4** were also studied in the same way and the full data set is shown in Appendix 4 where the same trends are observed as in Figure 61. Molecule **6** however, known as C_{10}-amine, did not show the typical inhibited kinetics immediately following the grafting step. This indicates that a large non-conductive multilayer was not formed using this molecule. It is likely that the extra distance required for electron tunnelling to activate further solution-based diazonium salts was too great due to the significantly increased alkyl linker length in C_{10}-amine. This idea is explored more in section 3.3.5.1.

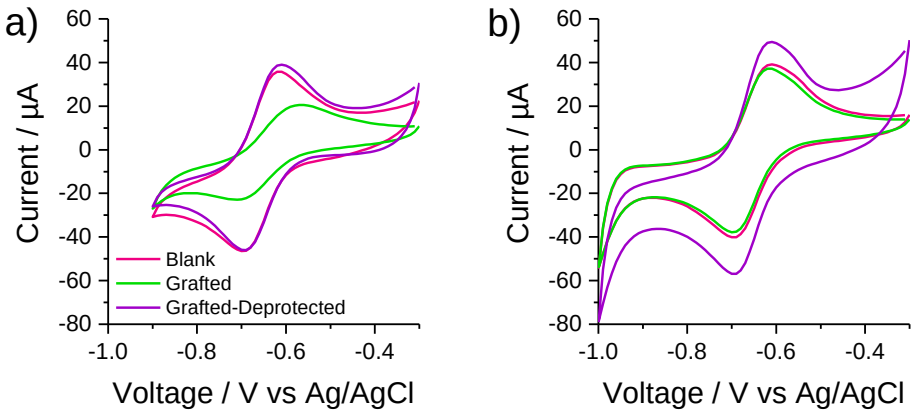

Figure 61. CVs throughout the grafting strategy of **5** (a) and **6** (b) in 1 mM methyl viologen dichloride with 0.1 M NaCl. v = 200 mV s^{-1}.

3.3.4 Viologen redox tagged amine-modified copper electrodes

To assess the surface coverage of amine-functionalities on the modified copper surfaces, NHS-activated methyl viologen (**7**) was synthesised from bipyridyl (full synthesis in section 7.5.2.1). This was a novel synthesis that used existing methods for functionalising bipyridyl. **7** was synthesised by two separate nucleophilic attacks of the nitrogen groups in bipyridyl with two different alkyl iodides and then subsequent activation of a terminal carboxylic acid to an NHS-ester. Asymmetric modification of the bipyridyl backbone was easily achieved due to precipitation of the single-modification product. This strategy was performed to permit amide bond formation between surface-bound amines and a redox probe (Figure 62), which has previously been achieved with other redox-tags such as ferrocene.[268]

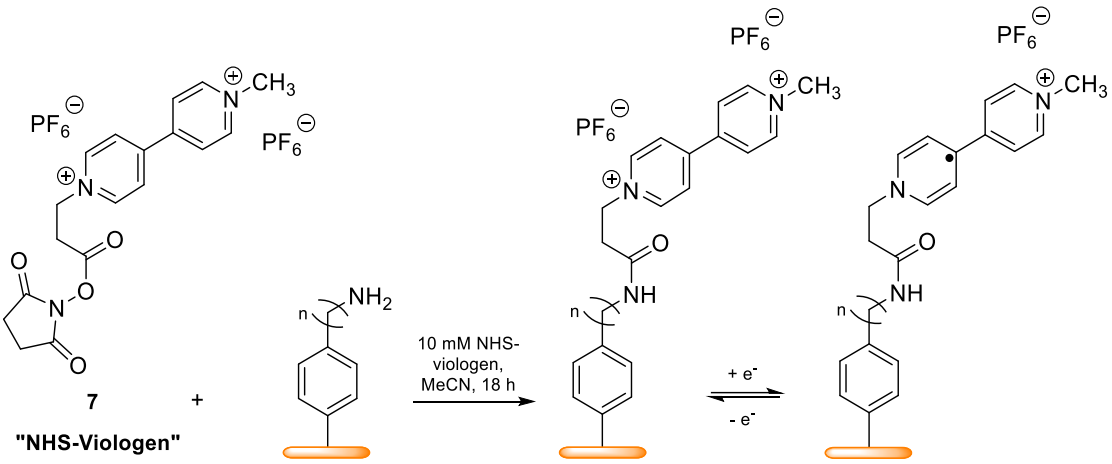

Figure 62. Chemical grafting of NHS-Viologen to an amine modified copper electrode.

An initial ligation was performed by incubating a copper electrode modified with C_1-amine (**3**) in a 10 mM solution of **7** for various time intervals to ensure modification went to completion (Figure 63). After sonication in water and acetonitrile, cyclic voltammetry was performed on the modified copper electrodes in a nitrogen-filled glove box. The modification appeared to be complete after 5 hours, however the electrode was left until 22 hours to ensure completion. The apparent decrease in redox peak areas are attributed to the degradation of the terminal viologen moieties.

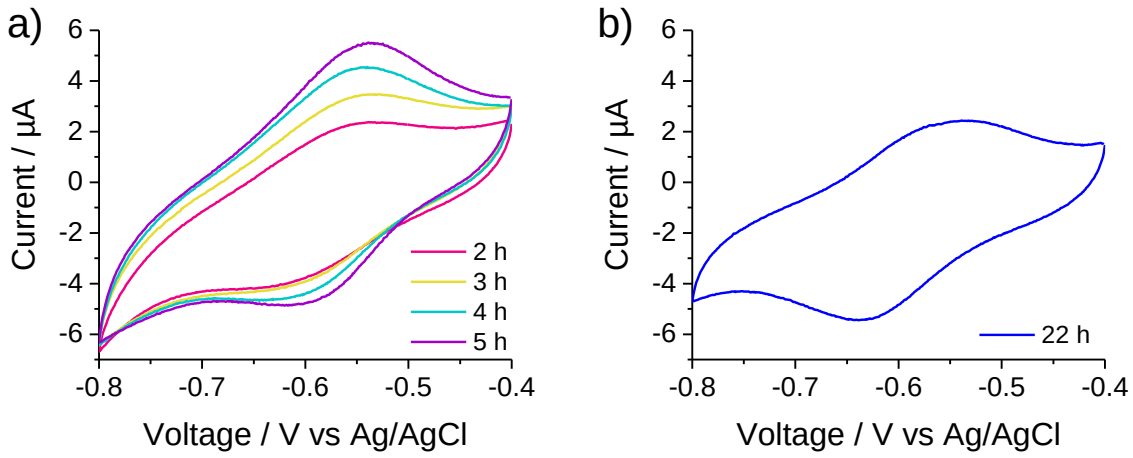

Figure 63. Electrochemical response of viologen units covalently attached to a copper-C_1-amine unit with grafting time. CV performed in 0.1 M NaCl, scan 3, v = 50 mV s^{-1}.

Following the modification in Figure 63, the same experiment was performed at scan rates from 50 – 500 mV s^{-1} (data not shown). Peak currents were extracted from all oxidative and reductive peaks relative to a non-linear baseline. This baseline was either third or fourth order polynomial and the analysis was performed using PSTrace software and an example peak current extraction for both an oxidative and reductive peak is shown below in Figure 64.

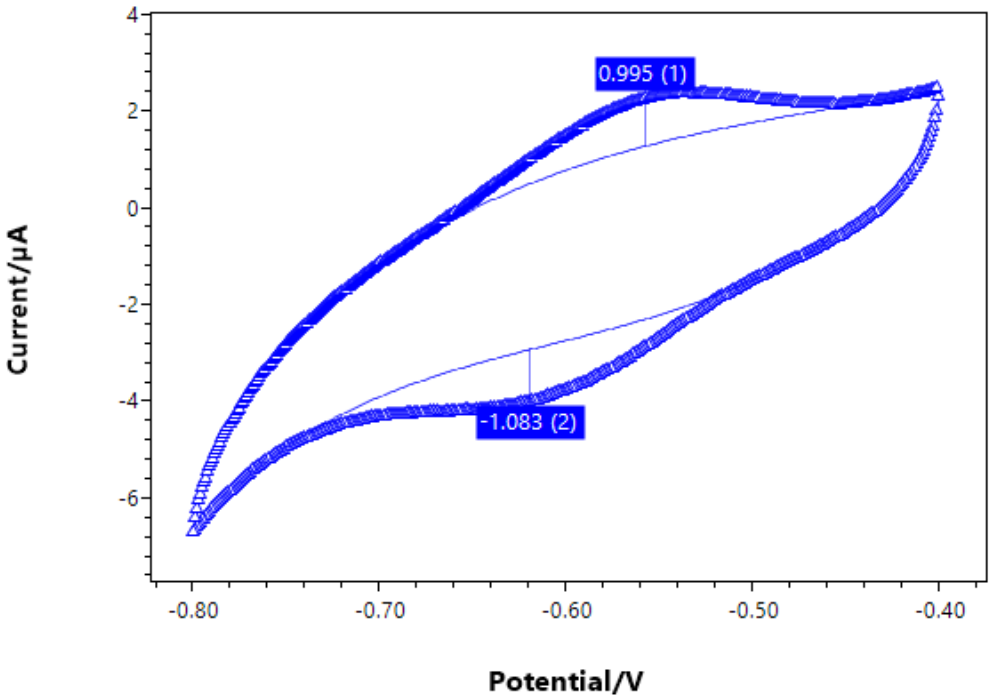

Figure 64. Example peak current extractions for a viologen-C_1-amine modified copper electrode using a third (reductive sweep) or fourth (oxidative sweep) polynomial baseline. Baseline shown as a thin blue line with raw data as blue triangles. CV conducted at 50 mV s^{-1}, scan 2 shown.

The extracted peak currents were correlated with scan rate and showed a linear relationship (Figure 65) which demonstrates that the viologen tags are surface confined according to an equation presented by Heering *et al.* (Equation 3) as opposed to the Randles-Sevcik equation for solution voltammetry (Equation 4). This is a strong indicator that covalent modification was successful and therefore that the protection-deprotection strategy produces a viable amine-terminated electrode surface. It is important to note that the peak-to-peak separation for the viologen signal is approximately 60 mV which would be expected for solution-based viologen species,[269] however this is not expected given the analysis below and by the fact that electrodes were rinsed, dried and analysed in fresh 0.1 M NaCl. The peak-to-peak separation likely exists for surface bound viologen due to resistances associated with electron tunnelling.

$$i_p = \frac{n^2F^2}{4RT}\nu A\Gamma$$

Equation 3. Linear relationship of peak current (i_p) to scan rate (ν) to describe surface confinement in film voltammetry.

$$i_p = 0.446FAC^0\left(\frac{nF\nu D_o}{RT}\right)^{\frac{1}{2}}$$

Equation 4. Randles-Sevcik equation with a peak current (i_p) to square-root scan rate (ν) relationship to describe a diffusion limited relationship in solution voltammetry.

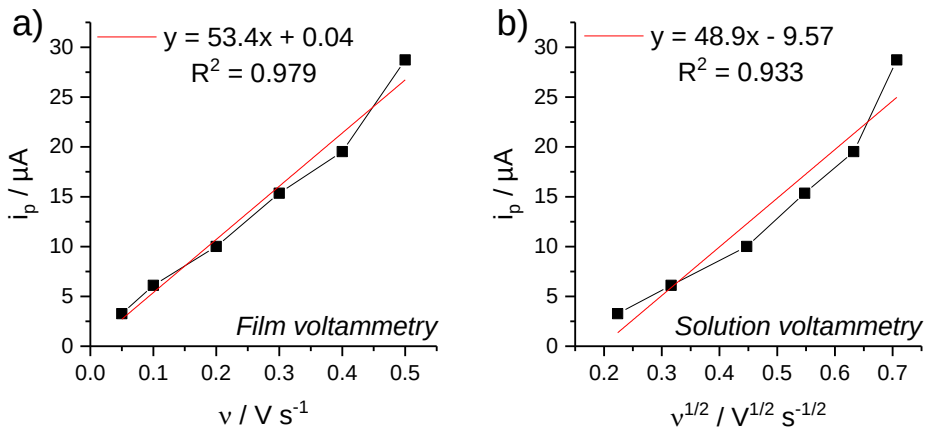

Figure 65. Peak current to scan rate relationships for C_1-amine modified copper coupled to a viologen redox tag.

The amine-to-viologen derivative ligation reaction was repeated with copper electrodes modified with molecules **3** – **6** (post-hydrazine deprotection) as well as an unmodified copper "Blank" surface in a 10 mM solution of **7** overnight (Figure 66).

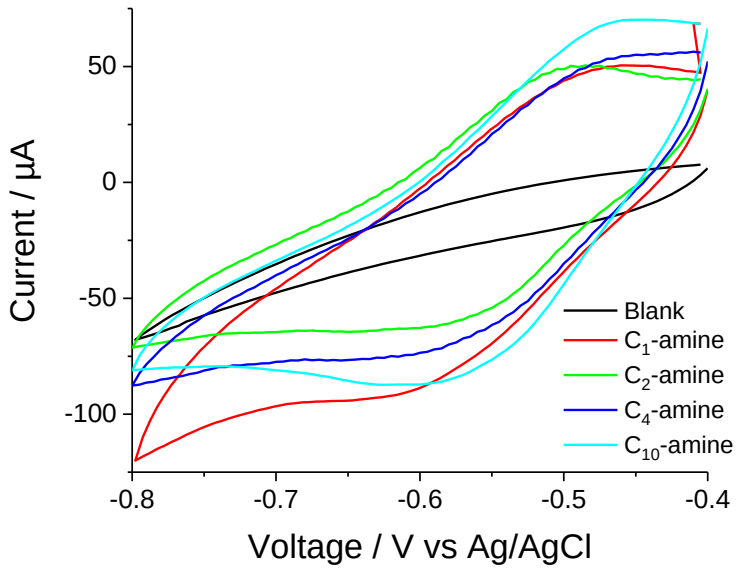

Figure 66. Cyclic voltammetry of a copper electrode modified with a monolayer of C_n-amine and exposed to NHS-Viologen for 18 hours. Recorded in 0.1 M NaCl, v = 100 mV s^{-1}, scan 3, rotation rate: 500 rpm.

Peak areas were extracted from data shown in Figure 66 and converted into surface coverages. As shown in Figure 67, this analysis reveals a typical viologen surface coverage of between 250-350 pmol cm^{-2}. Comparison with literature values for surface coverages of electroactive molecules on different electrode materials indicate that the viologen is forming a dense monolayer on the modified copper electrodes. Typically, "rougher" electrodes such as glassy carbon exhibit coverages of 100-250 pmol cm^{-2}, whilst very densely packed layers such as SAMs on gold can achieve coverages of 450 pmol cm^{-2}.[193, 270, 271]

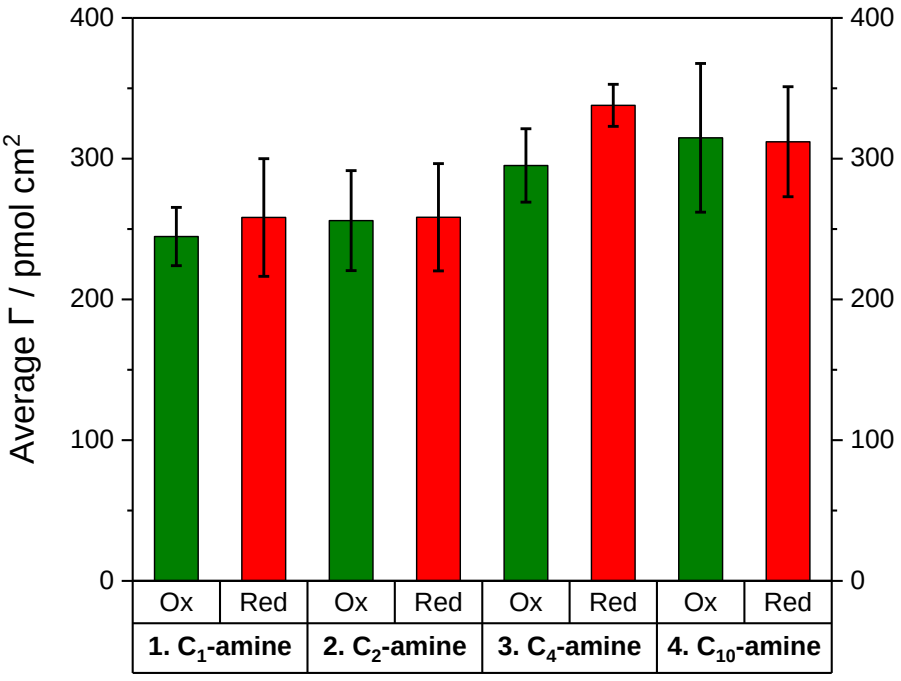

Figure 67. Surface coverages determined by non-linear baseline subtraction and integration of cyclic voltammetry redox peaks. Redox signals given from covalently attached viologen derivatives on a copper electrode.

3.3.5 Following the protection-deprotection strategy with C_4-amine modified copper electrodes and EIS

The previous section confirms that pendant amine groups are available on the copper electrode surface, however this does not determine the extent to which a monolayer has been formed. EIS was used to follow the modification steps of copper electrodes being modified with **3** – **6** using the protection-deprotection strategy (Appendix 5). Electrodes were submerged in a 1 mM methyl viologen dichloride in aqueous 0.1 M NaCl electrolyte for analysis to understand parameters surrounding charge transfer, electrode surface structure and reagent diffusion. EIS spectra for all surfaces and stages of modification are shown in triplicate in Appendix 5, whilst an example Nyquist plot is shown in Figure 68a for the three stages of modification using C_4-amine (**5**).

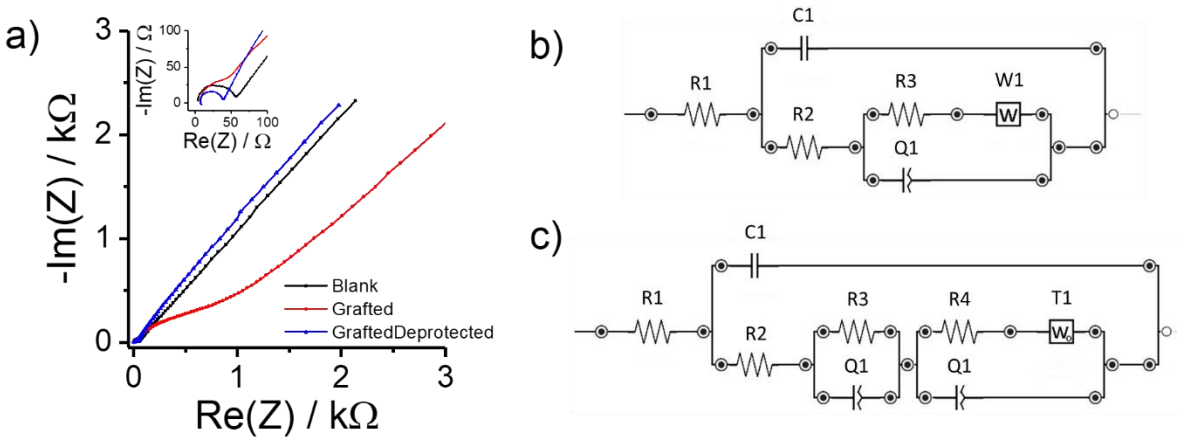

Figure 68. Nyquist plots at various stages of the protection-deprotection strategy of C_4-amine (a) and the equivalent circuits used to fit to the unmodified "Blank" and hydrazine-treated "GraftedDeprotected" (b) surface states and the post-graft (c) surface state. EIS recorded between f = 1 MHz – 0.1 Hz.

An unmodified "blank" copper electrode exhibits an equivalent circuit (Figure 68b) that is similar to the well-known Randles circuit which models simple charge transfer between a solution based redox species and an electrode surface surrounded by an electric double layer.[212] R1 models the solution resistance (R_{sol}) from the electrolyte, C1 the capacitance of the electric double layer (C_{DL}) and R2 the charge transfer resistance (R_{CT}) to the solution phase redox species. A Randles circuit has a regular Warburg element (W1) that accounts for semi-infinite linear diffusion, however this model contains an extra RC circuit combined with the Warburg element. R3, Q1 and W1 are assumed to be associated with the diffusion process of the viologen species to and from the electrode surface. The values of these elements are summarised for all stages in Table 7.

Table 7. Equivalent circuit element values through the protection-deprotection strategy of C_4-amine (**5**).

Equivalent circuit element	Blank	Multilayer	Monolayer
$\chi^2 \times 10^{-5}$	60	4.4	9.3
R_{sol} / Ω	7.67	6.68	6.95
C_{DL} / µF	0.046	0.077	0.090
R_{CT} / Ω	46.87	51.82	32.08
Q_M / µF*		1.130	
R_M / Ω		171.4	
Q_D / µF*	3.421	3.989	16.194
R_D / Ω	3.88	600.7	3.78
W1 / kσ	1.918	4.146	1.921

* Derived from CPE (see Appendix 5 for details of CPE)

After grafting of the electrode with C_4-amine (**5**) a third RC circuit appears (Figure 68c) with circuit elements R3 and Q1. R3 and Q1 represent increased impedance on the electrode surface and the potential charge stored within a non-uniform surface respectively. The emergence of this extra RC circuit and the extra impedance associated with it likely indicate the build-up of a thick multilayer that inhibits charge transfer. This correlates well with solution CV studies with viologen (see Figure 61a) where the "grafted" stage exhibited much slower redox kinetics than any other stage. Thus, R3 and Q1 are labelled as the multilayer resistance (R_M) and the multilayer charge storage (Q_M), respectively. It is interesting to note that the "Grafted" surface exhibits a high diffusional resistance, R_D, relative to other surface states which indicates solution-phase viologen molecules become hindered by or immobilised within the multilayer network.

Following hydrazine-deprotection, the RC circuit corresponding to the multilayer disappears. Combined with the knowledge that these electrodes are terminated with amine moieties (section3.3.4), this strongly suggests that an amine-terminated monolayer, very thin film or sub-monolayer has been formed on the copper electrode. Nyquist plots display similar values using identical equivalent circuit for the unmodified and "monolayer" functionalised surfaces which again correlates well with the fast redox kinetics displayed in solution-based viologen voltammetry (Figure 61a). Functionalisation with **5** as a monolayer doubles the amount of charge stored within the electric double layer whilst decreasing the R_{CT}. This is likely due to the charging of amine surfaces at neutral pH (RNH_3^+ expected). This change in behaviour at the local electrode surface is expected to have an impact on the product specificity when used as an electrocatalyst for CO2ER.

3.3.5.1 Comparison of various alkylamines on copper by EIS

The same equivalent circuits used in the previous section were applied to copper surfaces grafted with all synthesised alkyl amines, **3** –**6**. Nyquist plots from these models are shown in Figure 69, all of which show the same characteristic RC circuit for C_{DL} and R_{CT} with a clear diffusional Warburg-like 45° line. All surfaces exhibited the extra RC circuit attributable to a multilayer as described in the previous section with the exception of C_{10}-amine, **6**. Whilst C_{10}-amine did graft onto the electrode and was shown to be amine terminated in viologen film studies, the large alkyl chain inhibits the formation of a thick non-conductive multilayer on the electrode surface. This agrees well with the fast redox kinetics still exhibited at the "grafted" stage as in Figure 61b which marked C_{10}-amine as different to shorter alkyl amines.

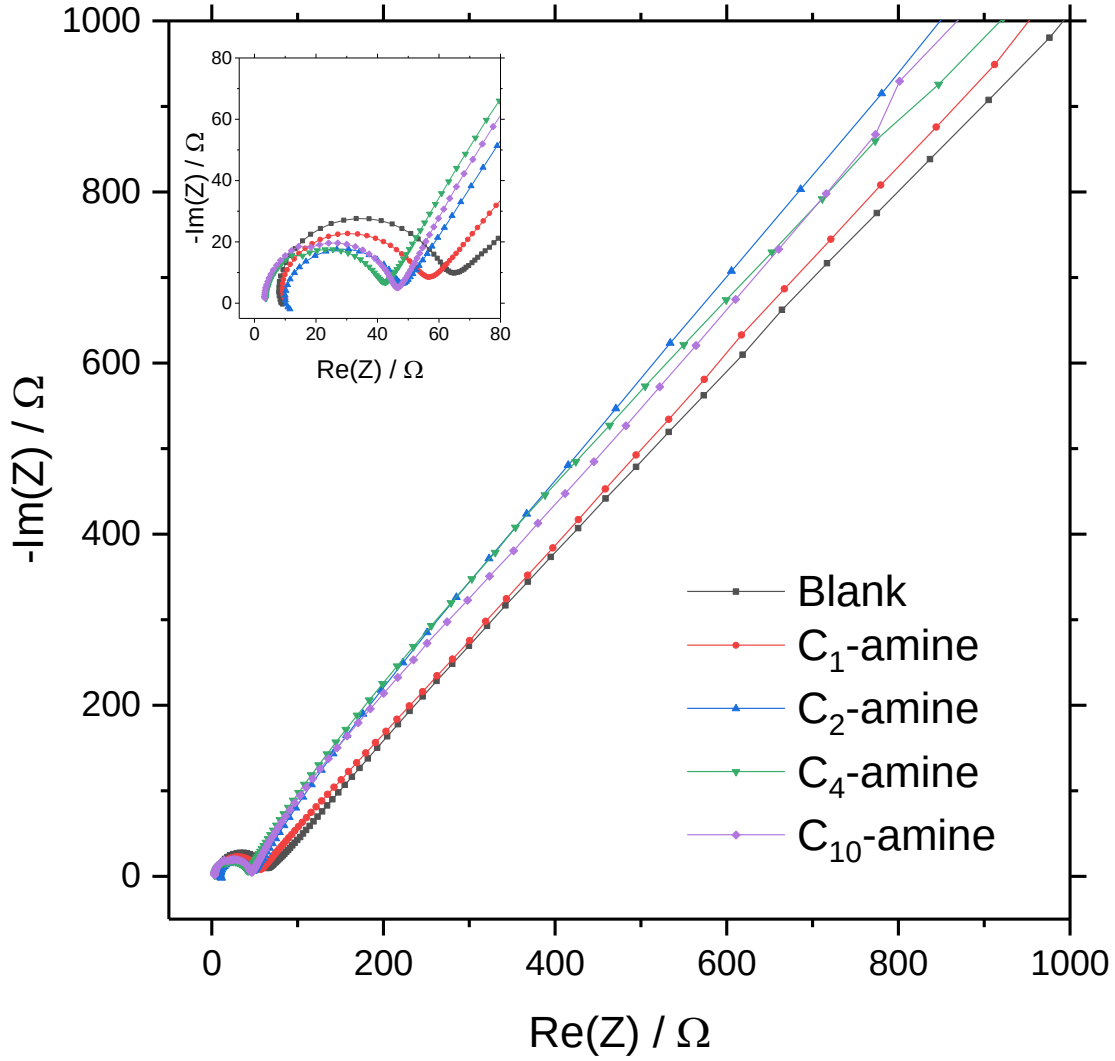

Figure 69. Nyquist plots of all surfaces post hydrazine deprotection on a copper electrode in 1 mM methyl viologen dichloride in aqueous 0.1 M NaCl. EIS recorded between f = 1 MHz – 0.1 Hz.

All electrode surfaces in Figure 69 were modelled against the equivalent circuit in Figure 68b. Values from the "Blank" unmodified copper surface was averaged over 12 experiments on this surface. Extracted values are details in Table 8 and key parameters are graphically represented in Figure 70. C_{DL} and R_{CT} exhibit no obvious trend upon modification, however this is likely due to both potentiostat limitations at high frequencies (equipment contour plots indicate 90-95% accuracy) as well as changes in surface structure between experiments due to mechanical polishing. At lower frequencies (accuracy >99%) diffusional parameters exhibit a clear trend. Upon functionalisation with short chain alkyl amines, both the diffusional resistance (R_D) and the diffusional capacitance (Q_D) decrease which indicates a faster rate of diffusion toward the electrode surface. This effect could lead to different electrocatalytic behaviours in CO2ER which may be influenced by reagent retention time at the electrode surface.

Table 8. Extracted equivalent circuit element parameters for (un)modified electrodes.

Surface	Blank**	C_1-Amine	C_2-Amine	C_4-Amine	C_{10}-Amine
$\chi^2 \times 10^{-5}$	90.5	22.5	216.7	19.8	20.0
R_{sol} / Ω	9.6	8.5	9.5	7.1	7.6
C_{DL} / µF	0.059	0.040	0.092	0.090	0.063
R_{CT} / Ω	54.2	52.2	35.4	32.6	46.2
Q_D / µF*	25.8	3.4	12.0	12.8	79.6
R_D / Ω	144.6	5.9	13.3	3.1	438.2
W1 / kσ	2.017	1.549	1.854	1.823	1.755

* Derived from CPE (see Appendix 5 for details of CPE)
** Averaged over 12 experiments

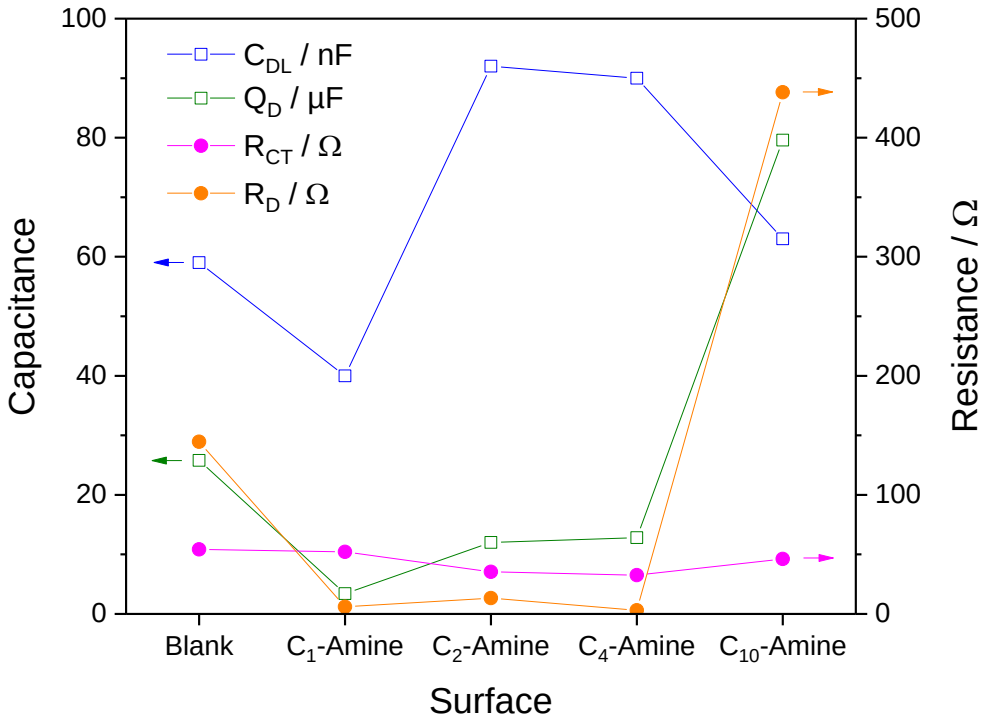

Figure 70. Key extracted equivalent circuit element parameters for unmodified and C_x-amine modified copper electrodes.

3.3.6 Oxylamine surfaces *via* a protection-deprotection strategy for aldehyde binding

The protection-deprotection strategy outlined in the previous sections is also applicable to related diazonium molecule derivatives that contain oxypthalimide groups, as shown in Figure 71. This section outlines the work I performed towards a paper by Yates *et al.* to demonstrate the applicability of the modification strategy with a wider substrate scope.[272] The content of this co-authored paper is described below as well as the researched I performed toward the paper.

Following electrode grafting with diazonium salts containing oxypthalimide groups, these surfaces can be deprotected to reveal an oxylamine terminus (Figure 71). Yates *et al.* demonstrated this technique by performing it on glassy carbon, BDD and gold electrodes.[272] The group further published that these oxylamine termini were capable of binding to aldehydes including some of those attached to biological substrates such as periodate-oxidized horseradish peroxidase enzyme. A control experiment was performed before introducing biological molecules, wherein propanal was used as the aldehyde that was bound to the oxylamine. Note that a triazene precursor was synthesised for ease of use given that it behaves as a "caged diazonium" that is activated by the presence of acid. The work that I performed toward this paper was performing and modelling EIS measurements similar to those outlined in section 3.3.5.1. I further performed the oxylamine modification on a gold coated Si(100) wafer and performed AFM analysis on it for depth profiling. These techniques allowed us to determine the electronic properties and structural characteristics of the electrode surfaces throughout the modification procedure. It provided further evidence that the aldehyde-oxime ligation reaction was functional and appropriate for further biomolecules.

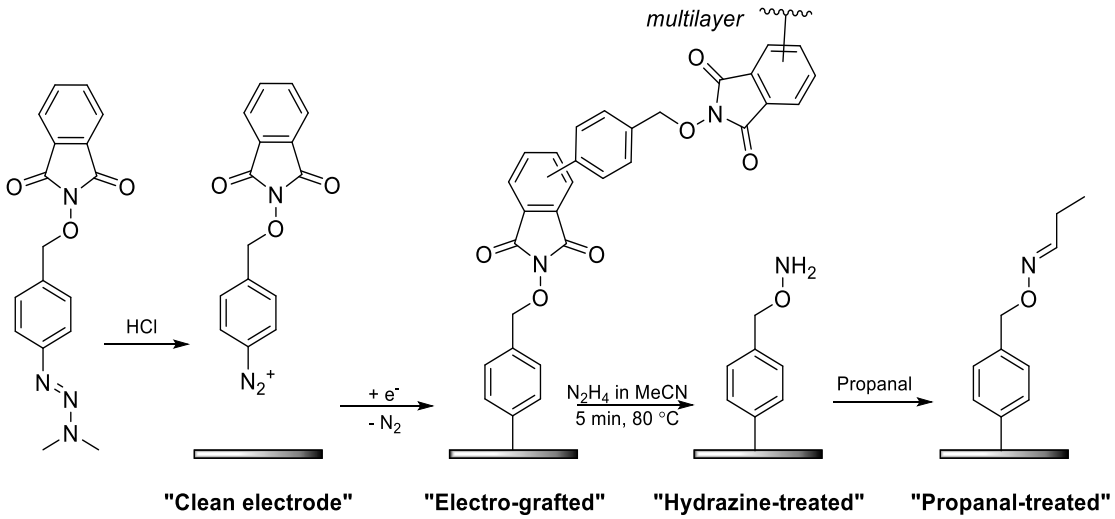

Figure 71. Protection-deprotection strategy for revealing an oxylamine surface. Adapted from reference 272.

3.3.6.1 EIS and solution voltammetry studies of oxylamine on glassy carbon

The functionalisation strategy exhibited the same changes in electronic properties as those modifications performed in previous sections using protected amine moieties. Electro-grafting of a thick multilayer deactivated any faradaic charge transfer to solution ferricyanide (Figure 73). Subsequent hydrazine deprotection restored the redox capabilities and later oxylamine "quenching" with propanal gave rise to slow redox kinetics. This was qualitatively observed by CV and quantitatively understood using EIS. Using a modified Randles circuit with a CPE instead of a pure capacitor (Figure 72), circuit element values were extracted for all surfaces.

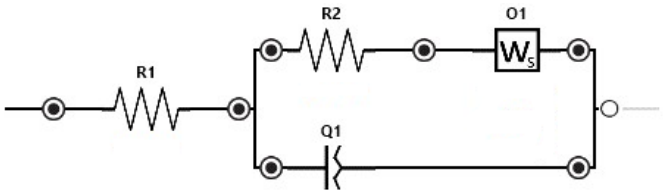

Figure 72. Equivalent circuit used to follow all stages of electrode modifications towards oxylamine termini.

The use of only a single RC circuit for this system even when initially electro-grafted indicates a dense coverage was observed. This fact is supported by the high R_{CT} which led to complete redox suppression for the electro-grafted surface state. Following hydrazine treatment, redox processes again possessed fast kinetics and a low R_{CT}, demonstrating the removal of a thick multilayer. Proof that terminal oxylamine could readily bind solution aldehydes was reflected by slower redox kinetics and a higher R_{CT} after the hydrazine treated electrode was submerged in propanal. This methodology later allowed binding of biomolecules to the electrode surface by way of fast aldehyde-oxylamine coupling.

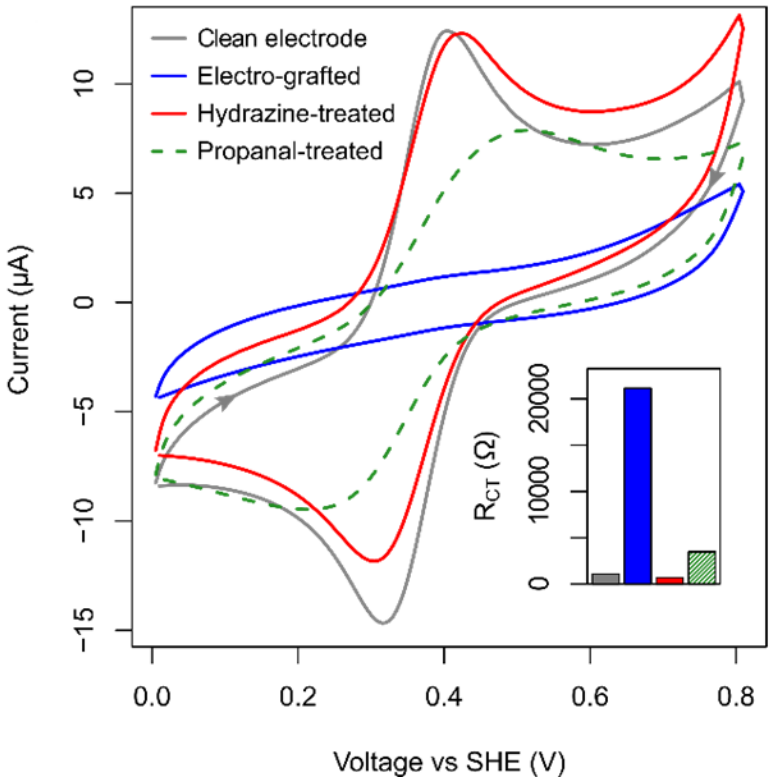

Figure 73. CV through the modification process in a 1 mM ferricyanide in aqueous 0.1 M NaCl at 500 mV s^{-1}. Inset: Extracted R_{CT} values from EIS measurements under the same conditions. Reprinted with permission from reference 272. Copyright (2020) American Chemical Society.

3.3.6.2 AFM studies of oxylamine on gold

Nick Yates performed a variety of analytical techniques to verify the near monolayer status of the oxylamine modification including XPS, Electrochemical Quartz-Crystal Microbalance (EQCM) and terminal redox tagging. To further this understanding, I performed AFM on these systems. An atomically flat gold substrate (Si(100) wafer coated) was analysed in an unmodified state and a propanal-treated state (Figure 74).

Surface roughness increased upon functionalisation to the propanal-treated surface state as observed in the roughness profiles (Figure 74iii). This indicates the largest height difference between the minimum and maximum observed heights was 5.7 ± 1.3 nm and 9.5 ± 0.4 nm for the unmodified and modified surfaces, respectively. A simple geometric calculation using Chem3D structures indicates the maximum length of 11.63 Å, therefore it is possible that the difference of approx. 3.8 nm observed between the two surface states correlates with some sites have up to 3 layers. This however only occurs at some locations and thus the best description, correlating with other analytical techniques, is of a near-monolayer coverage. This experiment alone does not conclusively prove that the depth profile has a minimum at the gold surface, which would require

scratching experiments, however the same methodology analysed by XPS supported the above conclusion by following element ratios. The surface structures, thicknesses and topology observed by Yates *et al.* is expected to be the same for the related alkylamines (section 3.3.1, **3** – **6**), for which electrochemical data agrees well with the oxylamine system.

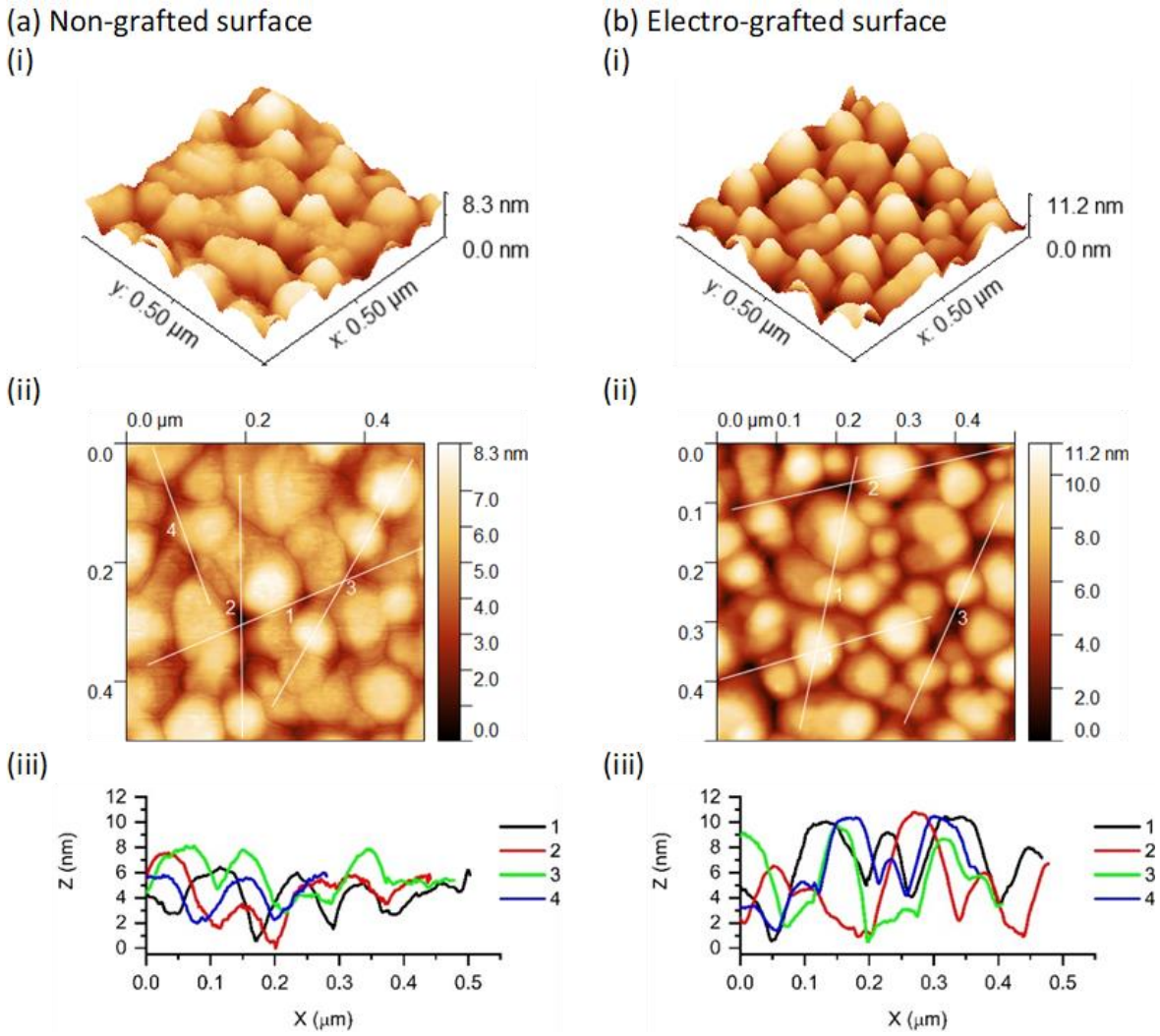

Figure 74. AFM analysis of a) an unmodified gold substrate and b) a grafted, hydrazine-treated and propanal-quenched electrode surface. (i) 0.5 x 0.5 µm² topographic pictures, (ii) AFM images, and (iii) roughness profiles corresponding to the lines drawn in the AFM images.

3.4 Conclusions

A robust protection-deprotection method for modifying electrode surfaces has been developed based on work by Hauquier *et al.* as performed on a glassy carbon surface.[193] Work outlined by Menanteau *et al.* was also reproduced, however the methodology requires optimisation for each new electrode modifier.[191, 192] The efficacy of the protection-deprotection method for a wider range of substrates led to the application of this strategy to a copper electrode surface, a surface that is rarely modified in literature except for corrosion inhibition applications.[260] This is the first modification procedure of it's kind for producing a monolayer coverage on copper.

Copper electrode modifications were studied using the electrochemical methods of solution voltammetry and EIS to show the surface conductivity properties throughout the protection-deprotection strategy. This highlighted extra resistance parameters due to multilayer formation and their subsequent removal upon deprotection. Amine termini were shown to be present through binding to a redox tag containing a viologen moiety. This method also showed applicability with closely related oxylamine systems that also yielded near-monolayer coverages, which was further supported by AFM measurements. The combination of this evidence demonstrates that amine terminated, near-monolayer functionalities could easily be installed on copper electrodes.

This work supplied a range of amine terminated near-monolayer modifications on copper surfaces that have previously been inaccessible. It is hoped that modifications such as these will allow a new range of surface functionalities and properties, such as hydrophobicity, to be accessed on electrocatalytic surfaces. These modifications will be applied for CO2ER catalysis in the next chapter.

3.5 Appendix 4: Cu functionalised with amine monolayers: solution studies of methyl viologen by cyclic voltammetry

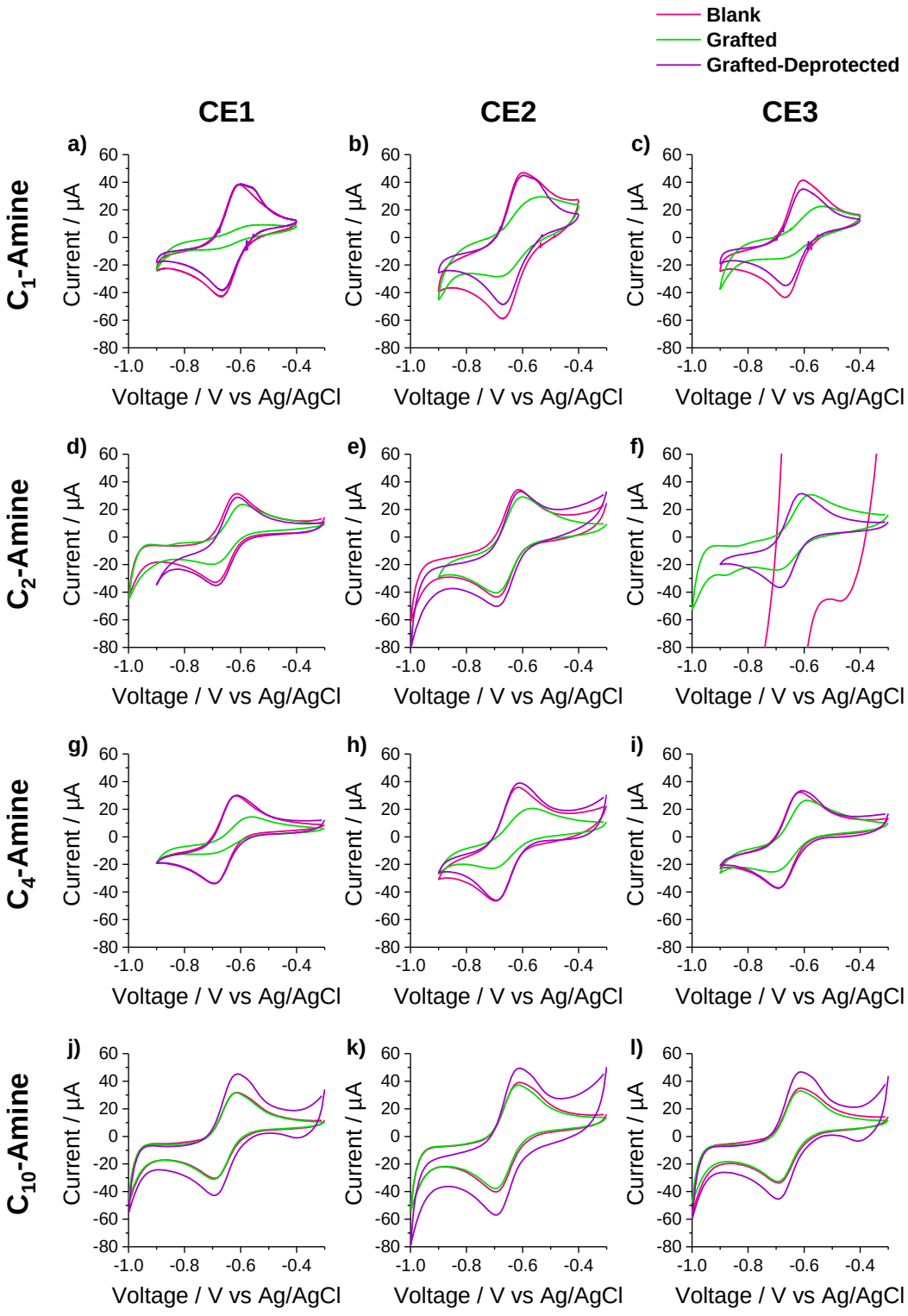

Figure 75. CV of 5 surfaces to be used in CO2ER. Recorded in 1 mM methyl viologen dichloride + 0.1 M $NaCl_{(aq)}$. Scanning started in reductive direction. v: 100 mV s^{-1}, scan 3 shown. (f, blank) recorded at v: 500 mV s^{-1}.

3.6 Appendix 5: Cu functionalised amine monolayers: solution studies of methyl viologen by EIS

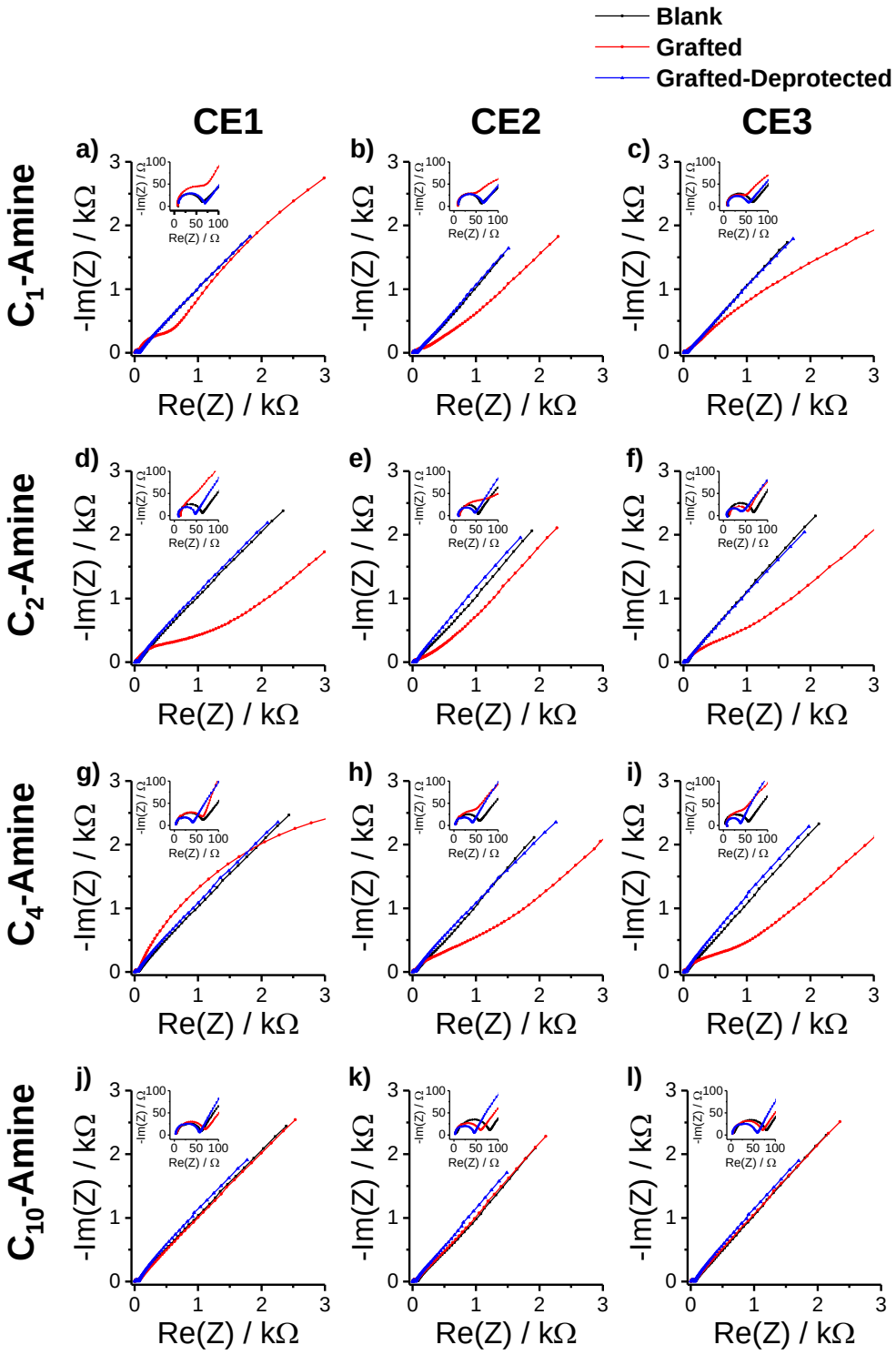

Figure 76. Nyquist plots (EIS) of 5 surfaces to be used in CO2ER. Recorded in 1 mM methyl viologen dichloride + 0.1 M $NaCl_{(aq)}$ at -0.63 V vs Ag/AgCl. t_{eq}: 30 s, E_a: 10 mV, *f*: 1 MHz – 0.1 Hz, 15 points per decade.

Table 9. Equivalent circuit element values for following a protection-deprotection strategy of amine modifications on copper electrodes.

Modifying molecule	Electrode	Surface State	χ^2	R_{sol} / Ω	C_{DL} / µF	R_{CT} / Ω	C_M / µT	ϕ_M	R_M / Ω	C_M / µF	Q_D / µT	ϕ_D	R_D / Ω	Q_D / µT	W1 / kσ
	CE1	Blank	1.00E-04	6.94	0.041	55.10					64.4	0.729	20.38	5.465	1.590
	CE1	Multilayer	2.00E-04	5.81	0.035	67.51	1416	0.882	407.8	1315.699	27.28	0.684	12770	16.760	2.472
	CE1	Monolayer	2.00E-04	8.66	0.04	58.24					58.71	0.771	8.372	6.110	1.581
	CE2	Blank	6.44E-05	7.85	0.13	52.14					418.4	0.553	480	114.303	3.123
C_1-Amine	CE2	Multilayer	2.00E-04	7.04	0.051	41.88	3.927	0.839	105	0.880	183.8	0.532	1023	42.255	2.185
	CE2	Monolayer	4.00E-04	9.08	0.035	53.44					117.1	0.652	4.379	2.054	1.479
	CE3	Blank	7.15E-05	7.28	0.049	55.58					70.83	0.756	23.43	8.974	1.442
	CE3	Multilayer	6.00E-04	6.24	0.04	42.42	3.77	0.970	51.44	2.894	86.42	0.554	6256	52.674	2.546
	CE3	Monolayer	7.55E-05	7.80	0.046	44.82					82.33	0.680	4.937	2.088	1.588
	CE1	Blank	9.20E-03	11.82	0.04	51.79					33.68	0.842	24.52	8.889	1.976
	CE1	Multilayer	7.35E-05	11.85	0.144	50.21	105	0.541	919.6	14.450	3.89	0.782	397.9	0.641	1.960
	CE1	Monolayer	6.20E-03	9.46	0.062	38.62					58.58	0.834	19.16	15.157	1.887
	CE2	Blank	2.00E-04	12.31	0.007	42.72					18.11	0.875	1.29	3.947	1.559
C_2-Amine	CE2	Multilayer	5.88E-05	7.64	0.165	32.10	407.7	0.388	333.5	17.518	104	0.600	83	4.376	1.987
	CE2	Monolayer	1.00E-04	11.07	0.1	35.91					123.6	0.763	9.267	15.083	1.799
	CE3	Blank	2.00E-04	12.22	0.052	55.77					59.47	0.822	4.03	9.780	1.911
	CE3	Multilayer	4.00E-04	19.42	0.016	33.94	99.77	0.602	726.4	17.597	5.945	0.905	135.8	2.815	2.012
	CE3	Monolayer	2.00E-04	7.91	0.115	31.73					89.76	0.715	11.6	5.811	1.875
	CE1	Blank	5.38E-05	8.06	0.075	55.98					30.82	0.816	9.927	4.970	2.058
	CE1	Multilayer	7.00E-04	9.00	0.069	58.60	19.46	0.797	5620	11.075	11.03	0.925	93.08	6.313	2.910
	CE1	Monolayer	1.00E-04	7.02	0.091	35.12					39.04	0.858	4.669	9.390	1.976
	CE2	Blank	3.60E-05	7.97	0.074	48.19					237.4	0.636	727.8	86.911	2.703
C_4-Amine	CE2	Multilayer	6.76E-05	6.72	0.071	55.03	6.742	0.796	225.1	1.278	23.2	0.729	839.1	5.365	3.696
	CE2	Monolayer	4.00E-04	7.18	0.088	30.73					52.84	0.874	0.99	12.757	1.573
	CE3	Blank	6.00E-04	7.67	0.046	46.87					47.89	0.765	3.88	3.421	1.918
	CE3	Multilayer	4.43E-05	6.68	0.077	51.82	5.219	0.821	171.4	1.130	20.84	0.726	600.7	3.989	4.146
	CE3	Monolayer	9.28E-05	6.95	0.09	32.08					72.84	0.845	3.781	16.194	1.921
	CE1	Blank	2.62E-05	10.27	0.066	50.81					22.08	0.883	3.164	6.214	1.976
	CE1	Multilayer	6.91E-05	9.16	0.071	59.54					20.64	0.844	5.391	3.837	2.084
	CE1	Monolayer	2.00E-04	7.44	0.059	49.98					74.73	0.861	4.495	20.544	1.635
	CE2	Blank	3.00E-04	11.51	0.064	69.29					10.05	0.976	0.079	7.115	1.568
C_{10}-Amine	CE2	Multilayer	5.00E-04	6.59	0.061	51.84					17.8	0.851	2.231	3.019	1.742
	CE2	Monolayer	2.00E-04	6.71	0.072	39.27					64.47	0.862	1.201	14.164	1.347
	CE3	Blank	1.20E-05	11.42	0.064	66.67					153.9	0.706	436.7	49.997	2.376
	CE3	Multilayer	4.90E-05	6.57	0.067	62.35					206.4	0.661	1155	98.935	3.318
	CE3	Monolayer	2.00E-04	8.71	0.057	49.44					301.2	0.705	1309	204.042	2.284

Chapter 4. Electrochemical CO_2 reduction at amine-modified copper electrodes

Author Declaration

The catalytic cyclic voltammograms in sections 4.3.1 and 4.5 (Appendix 6) were recorded by Adam Ward, a final year MChem student working under my day-to-day lab supervision. I performed all the analysis and data presentation. All other work presented in this chapter is my own.

4.1 Abstract

The previous chapter described the development of a diazonium-based protection-deprotection strategy for producing novel copper electrocatalysts covalently modified with amine-terminated organic monolayers. This chapter describes the use of this family of amine-terminated copper surfaces for CO2ER in aqueous solutions. A chronoamperometry method for CO2ER electrocatalysis is devised and complementary methods for liquid-phase and gas-phase product analysis using NMR and gas chromatography were established. Comparing the effect of the electrode modifier on the CO2ER product selectivity after chronoamperometry at -1.5 V vs Ag/AgCl suggests that hydrophobicity may be an important factor because modification with C_{10}-amine showed HER suppression and increased turnover rates to methane and formic acid relative to other modified surfaces. Chronoamperometry conducted over a wide voltage range for copper electrode coated with C_2-amine displayed increased current densities toward all products except methanol. These general rate enhancements can be attributed to improved proton mobility. Diazonium modifications are also shown to be semi-stable using the same viologen modification method outlined in Chapter 3. Finally, errors in the experimental procedure for CO2ER electrolysis are discussed and future work outlined.

4.2 Introduction

The Thesis Introduction provides an overview of the different approaches which researchers across the world have pursued in order to develop new CO2ER catalysts. It was shown that although amine functionalities have been incorporated into some CO2ER catalysts, such as within polymeric films on copper electrodes, the notion of diazonium electro-grafting amine functionalities onto copper for CO2ER has not been explored. While Chapter 3 shows how a diazonium method has been developed to achieve the electrode surface functionalisations shown in Figure 77, this chapter shows how these copper-amine surfaces function as CO2ER catalysts. To provide a contextual framework for the analysis of the results shown herein some generally accepted mechanisms for CO2ER are introduced and the potential role of amine groups and alkyl groups in directing CO2ER product selectivity is explored.

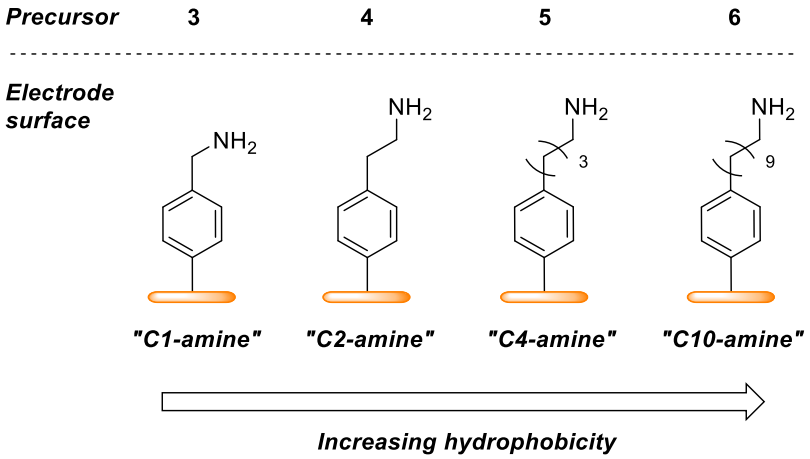

Figure 77. Surface modifiers for copper electrodes to be used in CO2ER catalysis.

4.2.1 Common CO2ER mechanisms

Figure 78 summarises the generally accepted set of reaction pathways thought to describe the origin of different products in heterogeneous CO2ER catalysis.[49, 116] When CO_2 interacts with a CO2ER cathode it can bind to either an oxide/hydroxide decorated metal or the metal surface in its zero oxidation state.[273] Thus, surfaces that routinely exhibit oxide/hydroxide species, such as tin and indium, are thought to bind CO_2 through the surface oxygen *via* a M-O-CO_2 structure. Molecules transitioning through this reaction intermediate are generally only able to produce C_1 species,

where formate is often the major product.[274] Alternatively, CO_2 can bind to a fully reduced M^0 site by forming an M-C bond which can give M-CO, M-CO_2^- or M-CO_2H as the first intermediate.[115] Addition of protons and electrons to these species can form all C_1 products, where higher order C_{2+} products are accessed *via* a C-C coupling step by insertion or addition of a *CO intermediate or neighbouring intermediate containing a direct M-C bond.[115, 273] To date, no bulk effect or mechanistic step has been unanimously agreed as a universal rate limiting factor for producing higher order hydrocarbons, with C-C coupling steps,[104] CO_2 activation steps,[275] solution CO_2 availability and proton availability having been discussed as possible rate limiting factors.[276-278]

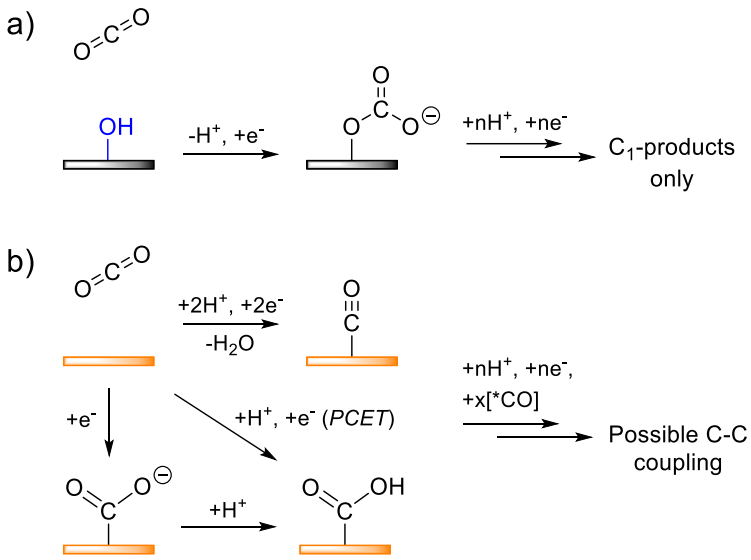

Figure 78. Possible CO2ER reaction pathways for CO_2 activation by addition of protons and/or electrons. a) formation of an M-O-C intermediate from a surface oxide/hydroxide to form C_1-only products. b) formation of M-C intermediates on a reduced M^0 surface; concerted addition of protons and electrons is known as proton coupled electron transfer (PCET).[115, 116, 273]

4.2.2 Rational design of electrocatalysts for CO2ER with organic modifications

The surface modifications highlighted in Figure 77 will be applied to a copper electrode surface in this chapter and the changes in CO2ER product selectivities rationalised relative to the mechanisms detailed in the previous section. The presence of amine groups is expected to both change the interaction of the surface with CO2ER intermediates and modify the pH at the electrode surface. The overall modification of the electrode surfaces with organic moieties may also change the

surface hydrophobicity. The following sections outlines how such changes to a copper surface have been found to impact CO2ER product selectivity in published studies.

4.2.2.1 Addition of amine functional groups for a secondary activation sphere

As mentioned in the introduction, inspired by HER molecular electrocatalysis design, synthetic chemists have constructed CO2ER homogenous catalysts containing amine functionalities (section 1.3.4.3). In CO2ER, the rationale is that the addition of amine handles adjacent to a metal centre can provide a secondary sphere activation, meaning that either protonated or deprotonated amine groups can interact with CO_2 or protons in the solution phase or bound to a metal centre.[279] If applied to a solid surface with multiple binding sites and intermediate species, this may allow stabilisation of some intermediates over others such as stabilisation of M-CO over M-O-CO_2. It is possible that amine functionalities may bind CO_2 directly as carbamates, as shown in the Introduction (Scheme 1), however it is unlikely that the kinetics of CO_2 binding to surface bound Lewis basic amines outstrip those of CO_2 reduction at a negatively charged cathode surface.

Chapovetsky *et al.* produced a cobalt aminopyridine macrocycle for CO2ER that contained secondary bridging amines, as shown in Figure 79.[152] The group also synthesised the same molecular catalysts with methylated and allylated tertiary amine bridging functionalities and saw that using the secondary amine yielded a turnover rate for CO production 300 times faster than the related tertiary amine catalysts. The group later published that there was a linear dependence on CO turnover number and the number of secondary amine groups available, as well as a Density Functional Theory (DFT) study that indicated secondary amine functionalities did not directly transfer protons.[280] Instead, NH functional groups were thought to hydrogen bond to proton donors in solution and provide an indirect route for protonation of bound carbon species. Neither the effect of primary amines nor the effect of amine distance from the metal electroactive centre has been explored by these Researchers.

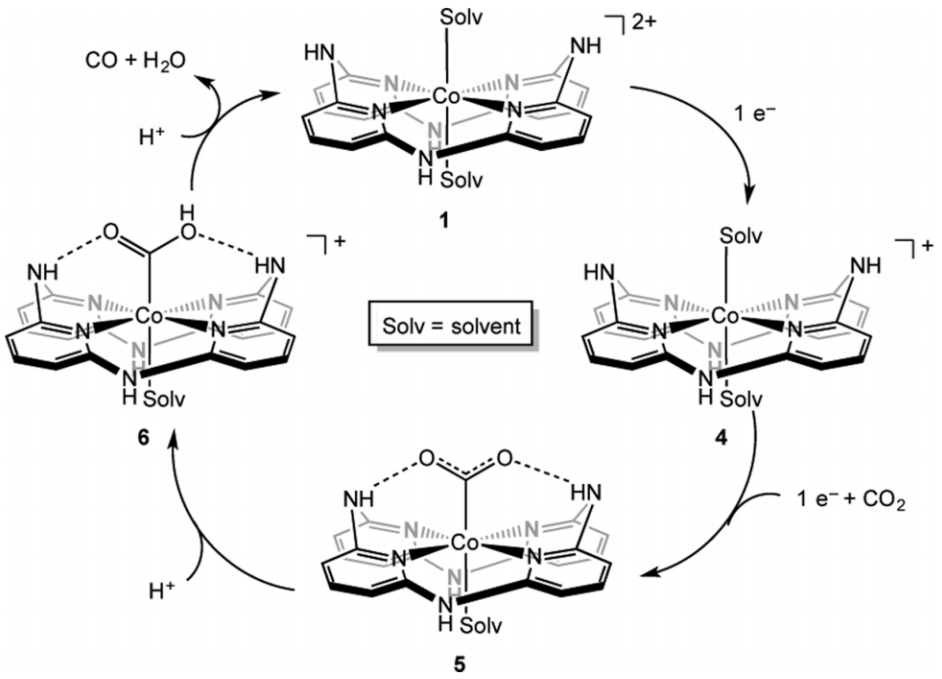

Figure 79. Secondary sphere activation of CO_2 bound to a cobalt aminopyridine macrocycle. Reprinted (adapted) with permission from reference 152. Copyright (2016) American Chemical Society.

Another cobalt complex synthesised by Roy *et al.* could produce formic acid with 90% FE in a DMF electrolyte.[281] The complex contained a diphosphine ligand with two pendant tertiary amine functional groups. The amine groups were attached to phenyl or benzyl functional groups to increase the basicity of the amine (with benzyl). Finally a related compound was synthesised without the amine functionality, [CpCo(dppp)I]I. It was found that the absence of the amine group decreased the catalytic current from 10 to 5 µA at -2.0 V vs $Fc^{+/0}$. The compound containing the most basic amine group showed the highest TOF for formic acid at >1000 s^{-1}. Mechanistic studies revealed that the amine group could scavenge protons from solution to form R_3NH^+ and allow a PCET to generate a hydride intermediate. The basic amine groups could also hydrogen bond to water molecules in the solvent which stabilised dissolved CO_2 molecules prior to hydride transfer (and production of formate).

Within molecular CO2ER electrocatalysts, amine functional groups have been well established as having an impact on product selectivities.[152, 281-283] It appears that the protonation state of amine groups can influence the hydrogen bonding network with either solution-phase CO_2 or CO_2 bound to the active metal centre. Amine groups may also present other indirect influences on product distributions by facilitating the production of hydride species which are key in producing some CO2ER products such as formate. This has led to the rational design of surface modifiers in Figure

77 with primary amine groups at different distances (via different alkyl linker lengths) from the electroactive copper surface.

In heterogenous CO2ER, confining amine functionalities to a cathode also appears to enhance electrocatalysis for similar reasons as molecular electrocatalysts. This chapter uses copper functionalised with a thin film of small molecules. Therefore, this study is most comparable to work by Xie *et al.* who compared the amino acid modification (by adsorption) of copper foil, annealed copper and copper pre-functionalised with copper nanowires.[284] All amino acid modified surfaces exhibited significantly increased CH_4 and C_2H_4 selectivity in CO2ER (Figure 80a, b). Success from amino acid modification was attributed to stabilisation of COOH and CHO intermediates by RNH_3^+ as indicated by a DFT study (Figure 80c). The most efficient system for higher order hydrocarbons, using glycine, was able to reach >20% FE to ethene whilst supressing HER.[284] This effect of intermediate stabilisation from a small molecule film is one of the possible effects that could be probed using amine functional groups at different distances from the surface (Figure 77).

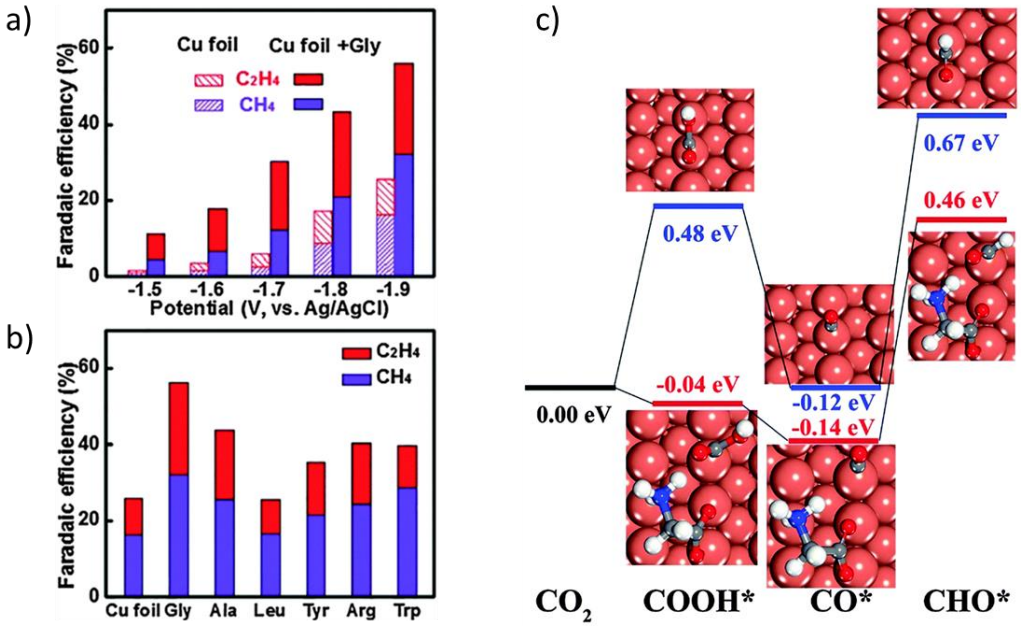

Figure 80. CO2ER on copper electrodes functionalised with a film of amino acids. Faradaic efficiencies toward CH_4 and C_2H_4 for a) unmodified and glycine-modified copper over a potential range and b) copper foil modified with a variety of amino acids at -1.9 V vs Ag/AgCl. DFT calculations (c) for CO2ER on a copper electrode with (blue) and without (red) zwitterionic glycine. Figures reproduced (adapted) with permission from reference 284. Copyright 2016, RSC Publishing.

4.2.2.2 The influence of pH on CO2ER product selectivity

In molecular HER catalysts, amines can be added to act as proton transfer reagents.[151] It is possible that rather than stabilising CO_2 binding, proton transfer may be the dominant effect of the modification studied here, which may increase the rate of CO2ER or of HER. The effect of bulk solution pH on CO2ER was discussed in the Introduction chapter, where it was highlighted that it can have a significant influence on the dissolved concentration of CO_2 and CO_2-derived carbonate species (section 1.3.2.1)[63] which can influence CO2ER reaction selectivity. Reactions at basic pH generally favour C-C coupling to give formation of C_{2+} products.[67, 274, 285]

During aqueous CO2ER a high local pH (pH >10)[286] is readily formed at the cathodic surface owing to the reduction of H_2O to H_2 and OH^- in the competing HER.[287] Thus, the generation of hydrocarbon products could be hampered by an insufficient supply of protons, which could be mitigated by high concentrations of protic buffers.[67] Amine based proton carriers such as protonated pyridine (pKa 5.2)[288] have been used as additives to an aqueous electrolyte for CO2ER catalysis (Figure 81).[288] A platinum electrode in the presence of 10 mM protonated pyridine in 0.5 M KCl (pH 5.3) was able to produce formic acid and methanol with faradaic efficiencies of up to 4.5% and 28% FE.[288] Given that unmodified platinum electrodes are generally only able to produce carbon monoxide or formic acid,[289] the formation of methanol was driven largely by the reduction of pyridinium ions to a radical that could bind solution-phase CO_2 and perform inner-sphere PCET. This idea of using amine functionalities as proton-mediators or direct sites for binding CO_2 may be present for the modified surfaces in Figure 77.

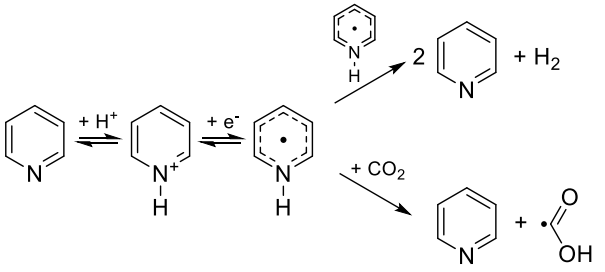

Figure 81. Pyridine ions proposed as proton carriers for both HER and CO2ER products. Adapted from reference 288.

4.2.2.3 Copper with carbon polymers for CO2ER cathode hydrophobicity

As well as containing amine functionalities, the electrode modifiers that have been synthesised also contain an alkyl chain (Figure 77), and grafting this onto the copper surface would be expected to increase the hydrophobicity of the electrode. In recent years, increasing the hydrophobicity of an CO2ER electrode surface has been shown to increase production of higher-order hydrocarbon species.[290] A copper dendrite electrocatalyst coated in 1-octadecanethiol was synthesised by Wakerley *et al.* (Figure 82). The hydrophobic surface trapped CO_2 gas bubbles on the surface of the electrode, whereas a non-coated "wettable" copper dendrite surface did not. This led to a dramatic change in the CO2ER product selectivities. Whilst the HER was significantly suppressed from 70 to 10% FE upon introduction of the hydrophobic coating, the selectivity toward carbon monoxide, methane, ethene, ethanoic acid and ethanol production was boosted and the selectivity toward formic acid and ethane lowered. The major CO2ER product using the hydrophobic surface was a 56% FE to ethene.[291] Increasing the surface hydrophobicity by modifications such as those containing longer alkyl chains in Figure 77 is expected to increase the availability of CO_2 and lower the water content at the surface.[54] This may increase the rate of formation of intermediates such as M-CO which may be combined to form C_{2+} products.

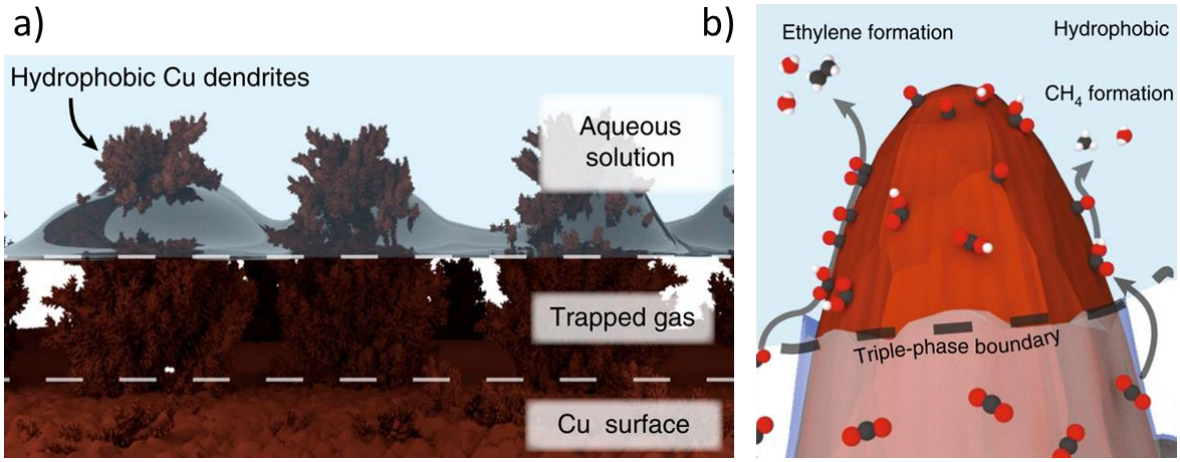

Figure 82. A copper dendrite electrocatalyst coated in 1-octadecanethiol submerged in aqueous solution (a) and a schematic of the active Cu-dendrite sites during CO2ER electrolysis that exhibit a triple-phase boundary (b). Reproduced with permission from Copyright Clearance Center: Springer Nature, Nature Materials, reference 291. Copyright (2019).

4.3 Results and Discussion

The electrocatalytic copper-alkylamine surfaces derived from diazonium electrochemistry in the previous chapter (Figure 77) are designed to change a range of local surface effects. The aim of this work was to determine if changes in the CO2ER products could be linked to the structure of the amine surface modifiers, with the different spacer lengths between the electrode surface to the amine functional group expected to impact on both any secondary sphere activation process and the surface hydrophobicity.

4.3.1 Probing catalytic activity by cyclic voltammetry under N_2 and CO_2

To investigate if the modification of a copper surface with the four different amine terminated molecules detailed in Figure 77 changes the electrocatalytic properties in CO2ER, catalytic voltammetry experiments were conducted. Three copper electrodes, CE1-3, were either modified with a C_x-amine, as detailed in the previous chapter, or used as an unmodified surface. CVs probing the reductive electrocatalytic activity of unmodified copper and copper modified with different amine monolayers were recorded in 0.5 M $KHCO_3$ under both a 100% N_2 atmosphere and a 100% CO_2 atmosphere at two rotation speeds; 500 and 3000 rpm (sample data in Figure 83, complete data in Appendix 6). The different gas atmospheres were selected to probe the different reduction currents under conditions of either pure H_2 evolution (the only electroreduction process expected under 100% N_2) or competing HER and CO2ER (both processes expected under a CO_2 atmosphere). Different rotation speeds were used to probe the impact of diffusion limitation on the catalytic electroreduction. Although all three electrodes (only CE2 data shown below) were manufactured in-house using the same design, CE2 and CE3 give similar results, whereas CE1 appears to have a smaller electrochemical surface area (ECSA). It is therefore easiest to analyse trends looking at data from CE2 and CE3. ECSA of these copper electrodes was not determined as copper oxidation and re-reduction could remove surface modifications and would not allow for comparison of unmodified copper to modified copper surfaces.

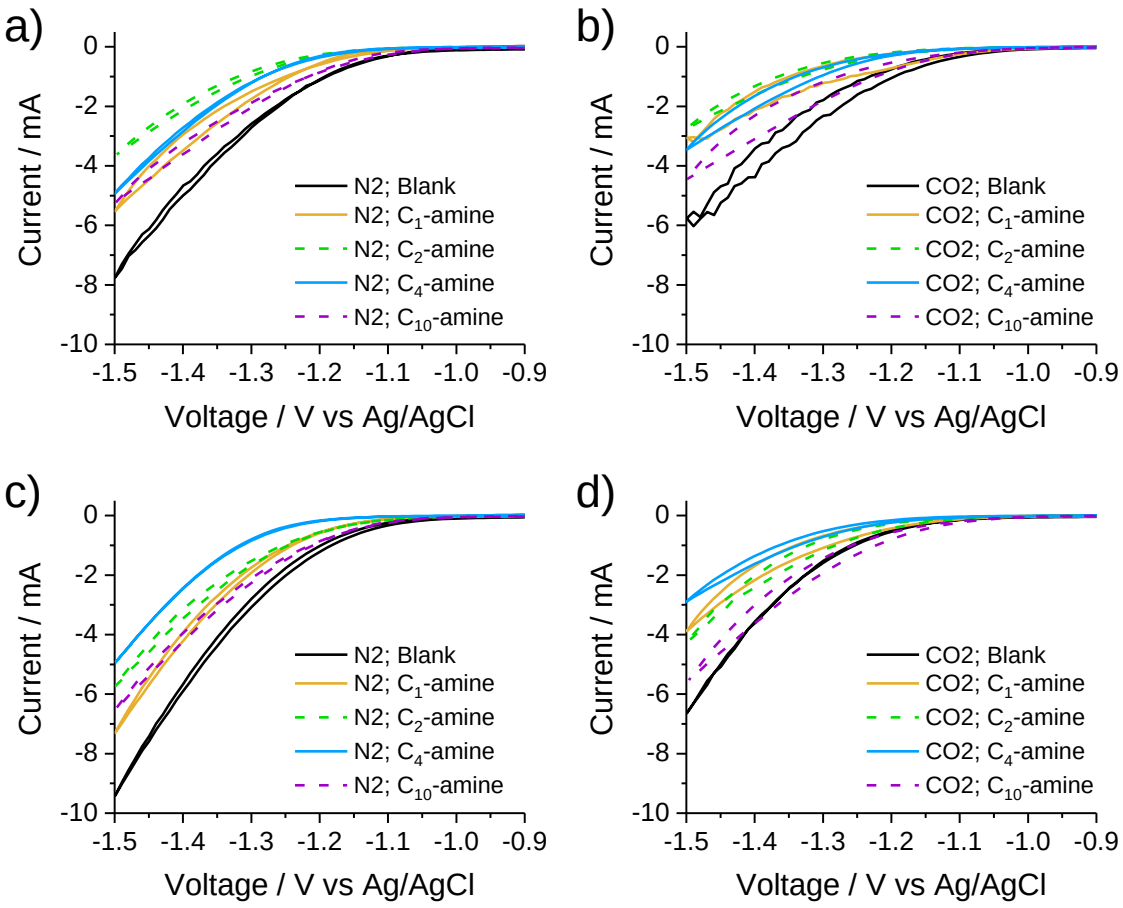

Figure 83. Catalytic CVs of amine-modified and unmodified copper electrode 2 (CE2) at (a, b) 500 rpm and (c, d) 3000 rpm under (a, c) N_2 and (b, d) CO_2 atmospheres.

In general, faster electrode rotation rates yielded a more pronounced difference in the catalytic current between N_2 and CO_2 atmospheres. This is because the current under N_2 increases as a function of rotation rate, while the current under CO_2 remains largely unaffected. This shows that in this experimental configuration the rate determining step in the HER involves diffusion of either proton reagents to the surface or hydrogen product away from the surface. The general decrease in electrode kinetics upon switching to a CO_2 atmosphere has been reported previously by Zheng *et al.* for PANi electrodes modified with metal nanoparticles.[163] This was suggested to be due to competitive binding of CO_2 over H^+ to electrocatalytic sites, where CO2ER exhibits slower reaction kinetics than HER. Interestingly, the C_{10}-amine surface does not follow this trend. Instead, even at high rotation rates very similar currents are observed under both CO_2 and N_2. Given that the number of electrocatalytic sites will have been decreased upon electrode modification and that other amine modifications yielded very similar surface coverages and thus similar decreases in ECSA, the ability of a C_{10}-amine modified surface to retain electroactivity must be attributable to a significant change in surface property.

The observed changing surface properties associated with C_{10}-amine may stem from increased hydrophobicity which may attract and retain CO2ER reaction intermediates (Figure 84a). Alternatively, a unique reaction environment closer to a molecular catalyst may have been created (Figure 84b and c), wherein the amine unit is folded over to create a secondary activation sphere with ligand-like interactions. It is likely that other C_x-amine modifiers may exhibit these effects to a greater or lesser extent. CO2ER catalysis was therefore performed on all amine modified copper surfaces to probe product specificity and mechanism of action. Electrocatalysis will be performed at 3000 rpm due to larger currents being passed which supports more accurate product analysis.

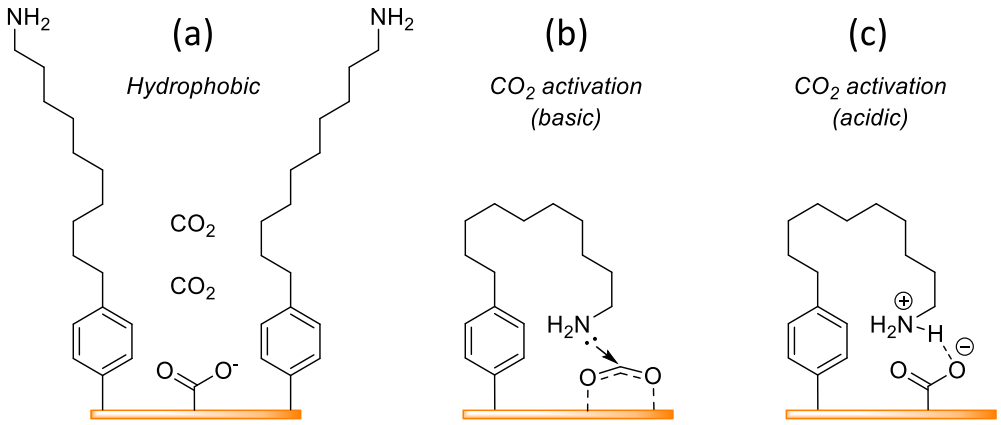

Figure 84. Possible CO2ER enhancement mechanisms for C_{10}-amine.

4.3.2 Methodology for CO2ER product analysis

Achieving accurate product analysis in research scale CO2ER experiments is recognised as being a challenge within the chemical community.[292] Research is often carried out at current densities around 5 mA cm^{-2} (unmodified copper foil) and with relatively small surface area electrodes.[89] When these experimental parameters are combined with short reaction times (30-180 min), products in analytical samples are often at micromolar concentrations and these solutions are often further diluted for analysis. Such low concentration solutions can therefore easily contain similar amounts of reaction products and accidental contaminants (such as plasticware leaching PEG compounds or detergent remnants on washed glassware), meaning rigorous control experiments are required and multiple repeats. Methods for liquid product analysis by water-supressed ^{1}H NMR and gas product analysis by *ex-situ* GC are outlined below. To enable efficient data analysis across the many experimental repeats and the five different electrode surfaces tested (four amine modifiers and an unmodified copper control) many of the possible liquid products that can be

synthesised during CO2ER are searched for using a semi-automated database system which is also described.

4.3.2.1 ^{1}H NMR liquid analysis

Liquid phase products were analysed from the electrolyte from working electrode compartment in a membrane divided H-cell (5 mL). All peaks present in the water-supressed ^{1}H NMR spectra were integrated relative to a DMSO reference peak (2.618 ppm, 6H). Peak shifts of common CO2ER liquid phase products were found using separate samples in 0.5 M $KHCO_3$ prepared in the same manner as experimental samples as in section 7.4.3 (Table 10).

Table 10. Experimentally determined water-supressed ^{1}H NMR shifts for standard solutions in 0.5 M $KHCO_3$.

Species	Shift 1 / ppm	Shift 2 / ppm	Shift 3 / ppm
Acetaldehyde	1.256	9.564	
Acetic Acid	1.807		
Acetone	2.119		
Ethanol	1.070	3.547	
Formic Acid	8.344		
Methanol	3.248		
Propan-1-ol	0.780	1.434	3.454
Propan-2-ol	1.060	3.907	
Propanal	0.936	2.452	9.585
Propanoic Acid	0.942	2.069	

These values were used with tolerances of 0.005 ppm (unless $\delta < 1.000$ ppm where tolerance = 0.003 ppm) to match to peaks in experimental data using a Microsoft Access database. Using the DMSO calibrant concentration and the current-time integral from chronoamperometry, moles of products, partial current densities and faradaic efficiencies could be calculated. The data analysis process is outlined in Appendix 7, where a sample NMR spectrum from a post-electrocatalysis electrolyte is also shown.

4.3.2.2 Gas analysis by ex-situ GC

Where resources are available, researchers often use *in-situ* gas analysis for real time monitoring of product ratios throughout catalysis. However, in my work instrument availability meant I was required to collect all product gases into a single leak-free gas bag for *ex-situ* analysis by GC. To verify this methodology, the GC was calibrated to simulate expected product concentrations post-

CO2ER catalysis. Furthermore, CO2ER reaction conditions and cell performance were optimised and tested with an unmodified gold electrode in a control experiment as this surface is expected to yield only gaseous products, primarily H_2 and CO in aqueous systems.[79, 293]

4.3.2.2.1 Gas Chromatography (GC) Calibration

GC calibration was performed as in section 7.4.2.1 for common CO2ER gaseous products; H_2, CO, CH_4, C_2H_4 and C_2H_6. Hydrogen gas was detected by a Thermal Conductivity Detector (TCD) and all other products by a Flame Ionisation Detector (FID). Peak integrals gave linear correlations with injection amounts (Figure 85, Table 11). It is noted that datapoints recorded for H_2 at lower than 1 nmol concentration did not fit the linear trend due to instrument sensitivity. The injection volume into the GC was 2.5 mL and so both x-axes in Figure 85 were multiplied up to the total gas bag volume of 1155 mL for determination of faradaic efficiency.

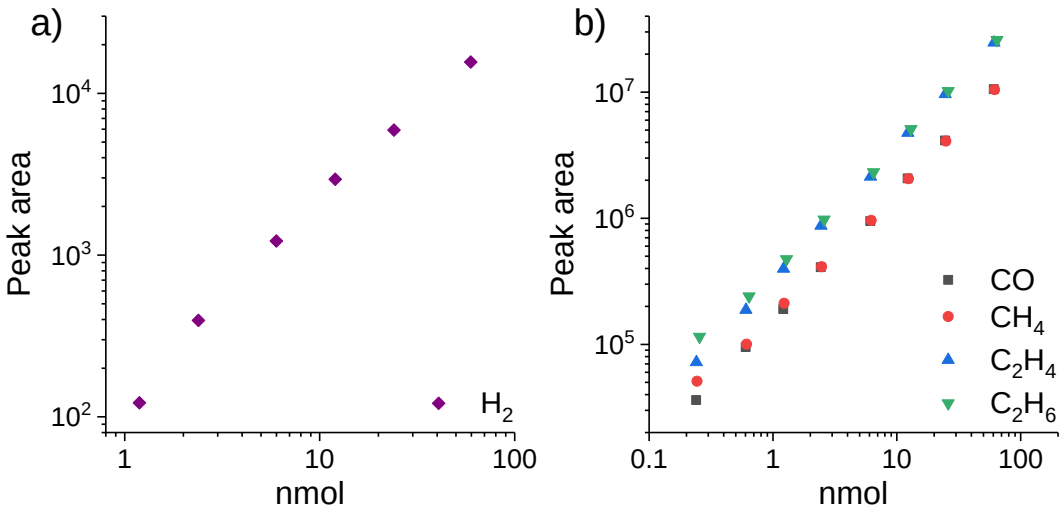

Figure 85. GC Calibration data for common CO2ER gas products. Products detected by TCD (a; H_2) or a methaniser-FID system (b; CO, CH_4, C_2H_4, C_2H_6).

Table 11. Retention times and linear regression parameters for GC calibration. All gases except H_2 were forced through the origin.

Gas	R_T / min	Gradient	Intercept	R^2
H_2	1.73	266.5	-293.8	0.9997
CO	4.00	1.733×10^5	0	0.9998
CH_4	7.90	1.690×10^5	0	0.9998
C_2H_4	17.4	4.030×10^5	0	0.9996
C_2H_6	18.7	4.006×10^5	0	0.9998

4.3.2.2.2 Methodology verification using a gold electrode control experiment

Both chronoamperometry (Run 1 and Run 2) and chronopotentiometry (Run 3) were performed on a gold control system for CO2ER (Figure 86a). Products were analysed only by GC (Figure 86b) to give final faradaic efficiencies (Figure 86c). Under the experimental conditions, H_2 was the primary product, with CO also being present as the major CO2ER product. Whilst small levels of methane were detected, no other gaseous products were observed.

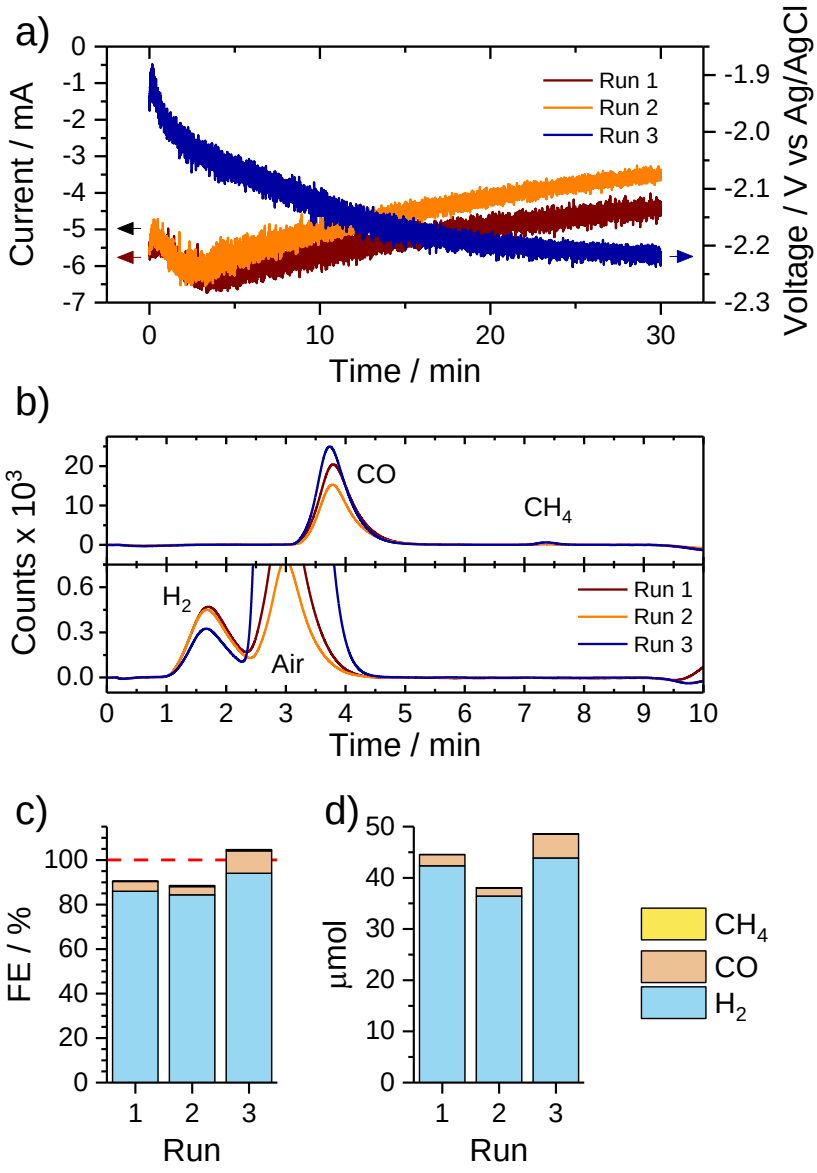

Figure 86. CO2ER catalysis by (a) CA (red and orange) at -2.0 V vs Ag/AgCl and CP (blue) at 5 mA cm^{-2} in 0.5 M $KHCO_3$ using an RDE at 3000 rpm. (b) Analysis of gas products by GC (c) and conversion to faradaic efficiency and (d) µmol of product.

To convert chronoamperometry traces to total charge passed for molar and faradaic efficiency calculations, the current was averaged over the time course of the experiment and multiplied by the duration of the experiment to obtain the integral and total charge passed ($Q = I \times t$). In a similar fashion, the charge passed during a chronopotentiometric experiment was calculated using the applied current over the timescale of the experiment. Following calculation of the moles of gas products relative to the calibration data in section 4.3.2.2.1, the moles of electrons required to synthesise each gas product was calculated (relative to data in Table 1). This data was related to the total charge passed (in moles by division of the Faraday constant) to yield the Faradaic efficiency for each gas product.

In Figure 86, both electrolysis techniques yielded faradaic efficiencies of close to 100%, with chronoamperometry displaying yields around 90% whereas chronopotentiometry showed 105%. Chronopotentiometry showed a higher ratio of $CO:H_2$, which is expected due to the higher overpotentials employed.[118] For fair comparison of modified copper catalyst surfaces at equivalent overpotentials, chronoamperometry will be employed using this method of gas analysis as well as water supressed ^1H NMR of liquid products.

4.3.3 CO2ER catalysis using amine modified copper electrodes

CO2ER catalysis was performed on all amine modified copper surfaces as studied in Chapter 3 (Figure 77). These surfaces were studied at -1.5 V vs Ag/AgCl for ready comparison to literature, whilst a C_2-amine modified copper electrocatalyst was compared to an unmodified copper electrocatalyst over a wider voltage window to further understand the impact amine modification may have on electrode surface properties.

4.3.3.1 Electrocatalysis at -1.5 V vs Ag/AgCl using a range of C_x-amine modified copper linker lengths

Chronoamperometry at -1.5 V vs Ag/AgCl was performed on four amine modified catalytic surfaces and compared to an unmodified surface. This was performed on three separate electrodes where all chronoamperometry traces are shown in Appendix 8 (Figure 98). Data from 30+ electrolysis runs with incomplete product analysis are not shown (e.g. during method development). Figure 87

shows the current-time reaction profiles of electrode CE2. Whilst it appears that the unmodified copper surface passes more current than all modified surfaces, this is not a reliable trend upon repetition with other electrodes as shown in Appendix 8 (Figure 98).

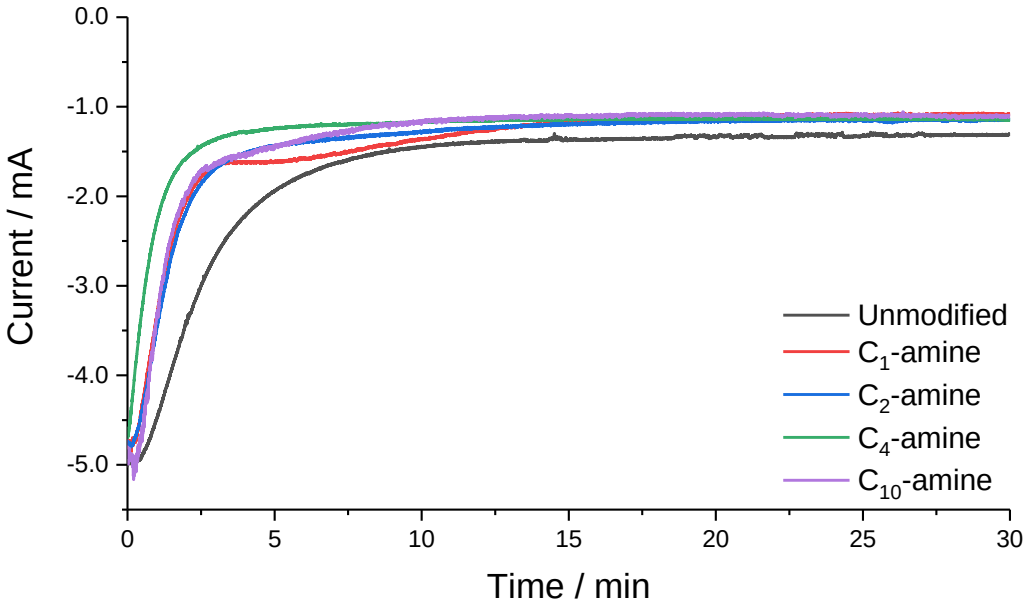

Figure 87. CA at -1.5 V vs Ag/AgCl at 3000 rpm in 0.5 M $KHCO_3$ for amine modified and unmodified copper electrocatalysts for CE2 only.

Following the product analysis method outlined in section 4.3.2 for both liquid and gas products, Faradaic efficiencies were derived for all catalytic surfaces and are shown in Appendix 9 (Figure 100). Under these catalytic conditions, HER significantly outcompeted CO2ER, with most catalytic runs exceeding FE_{H2} >90%. To easily identify changing CO2ER selectivities, partial current densities are shown in Figure 88. The proportion of the total current passed toward one product was calculated relative to the surface area using the moles of product, and thus electrons to create them, that had been calculated from NMR and GC product analysis. Whilst there are differences between electrodes (CE1-3) in terms of total current passed, averaged partial current densities may reveal a subtle trend. Specifically, from the average values copper modification with short-chain amine moieties (C_1, C_2, C_4) yields an increase in partial current density for H_2 (700-800 µA cm^{-2}), CO (20-50 µA cm^{-2}) and HCOOH (80-140 µA cm^{-2}). CH_3OH and CH_4 production did not give an obvious or reliable trend upon modification with short chain amine moieties. Contrastingly, C_{10}-amine modification is much closer to the unmodified copper values for H_2 and CO. C_{10}-amine modified catalysts generally produce more HCOOH, CH_3OH and CH_4 than shorter chain amine modifications at the expense of CO production. Very small amounts of C_{2+} products were produced on any electrode surface, with no obvious or reliable trends observed upon modification.

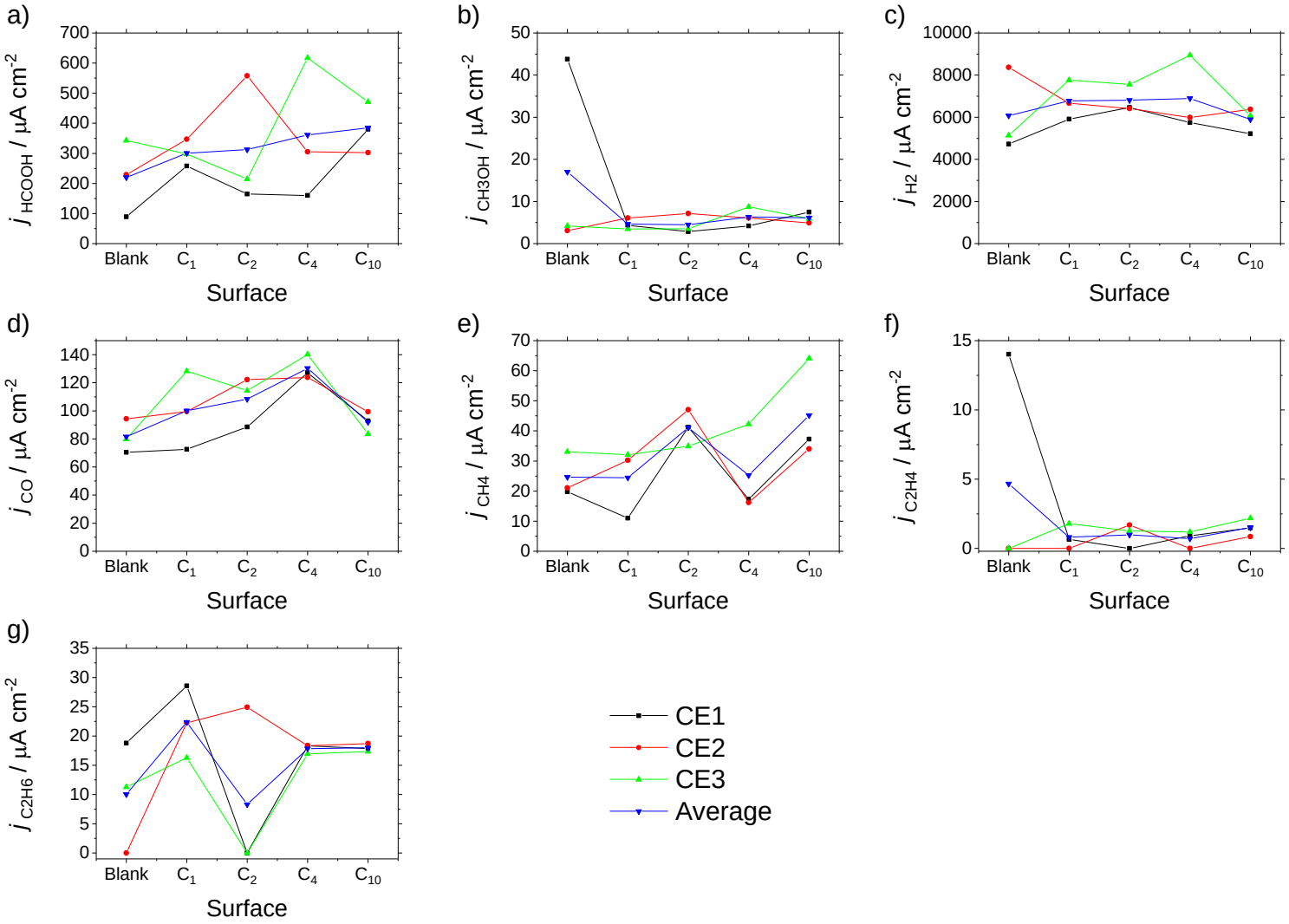

Figure 88. Partial current densities for unmodified "Blank" and C_X-amine modified copper electrodes for CO2ER catalysis at -1.5 V vs Ag/AgCl. Electrodes CE1-3 used for repeat experiments.

These observations indicate that short chain alkylamine modifications may increase electrocatalytic selectivity for $2e^-$ reductions (primarily HER over CO2ER) whilst long-chain alkylamine modifications such as C_{10}-amine suppress HER and favour formation of higher order hydrocarbons. The increase in production of H_2, CO and HCOOH is attributed to the amine functionality. The amine terminus in short-chain alkylamine modifications may be offering a ligand-like activation to CO2ER intermediate bound to the copper electrode surface, as previously discussed in molecular electrocatalysts.[152] It is possible this would favour formation of specific C_1 species owing to a well-defined reaction environment. A concurrent or alternative effect of the amine terminus is that the local pH has become more acidic where the amine group acts as a proton shuttle, as discussed in section 4.2.2.2.[288, 294] An increase in electric double layer concentration of protons has been observed to increase HER turnover with aryl-ammonium ions at copper cathodes.[294] These aryl-ammonium ions acted as a proton shuttle from the bulk solution into the electric double layer by use of the amine moieties. Increased proton availability would be expected to increase HER primarily, however general CO2ER rate enhancements would likely be observed as most mechanistic steps involve protonation of intermediates.

Relative to short chain modifications, functionalisation with C_{10}-amine led to increased selectivity for higher order hydrocarbons instead of favouring CO and H_2 production. This can be attributed to increased hydrophobicity, wherein both dissolved CO_2 and CO2ER intermediates were retained at the electrode surface for longer to allow for further reduction steps, as well as expulsion of water from near the electrode surface for a decreased HER. HER was observed to have dropped relative to an unmodified electrode by 200 $\mu A\ cm^{-2}$, which indicates that the hydrophobicity exhibited by the longer alkyl chain outweighs any HER enhancements caused by the amine functional group.

The idea of increased hydrophobicity correlates with the EIS experiments with solution phase methyl viologen in Chapter 3 (Figure 70). A drastic increase in diffusional resistance (R_D) and charge stored due to diffusion limitations (Q_D) was observed upon functionalisation of copper with C_{10}-amine. This indicated that methyl viologen, a relatively hydrophobic redox marker, was retained at the surface more than an unmodified copper surface. Interestingly, R_D and Q_D decrease significantly upon modification with short chain alkylamines which indicated more hydrophilicity than an unmodified surface.

It appears that the modification using an amine head-group influences the CO2ER selectivity relative to an unmodified copper surface, however this may be due to pH of the local environment being modified, or that the amine group is able to stabilise reaction intermediates. In a similar vein, the covalent modification with long alkyl chains using C_{10}-amine appears to increase the surface hydrophobicity. Both C_2-amine and C_{10}-amine are of interest to understand these effects in a stepwise fashion where Figure 89 summarises some of the possible interactions. C_2-amine is selected for initial comparison with an unmodified copper electrocatalyst for study across a wide voltage range, where the influence of ligand-like interactions and local pH will be probed.

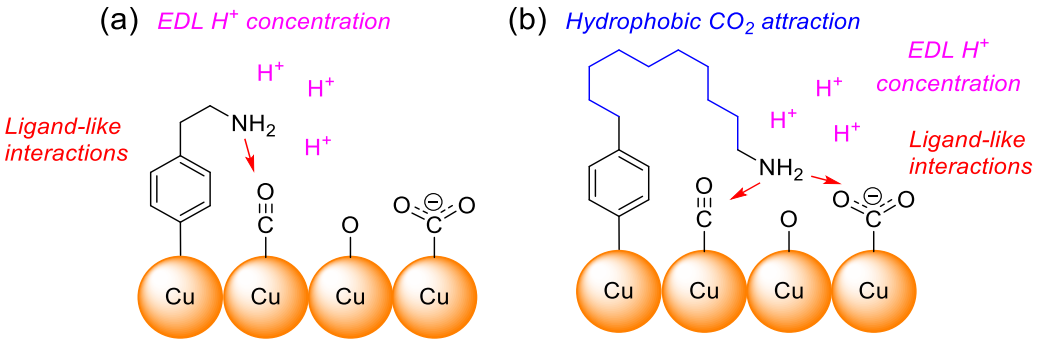

Figure 89. Possible effects of copper electrode modification on the local environment for a) C_2-amine and b) C_{10}-amine.

4.3.3.2 Electrocatalysis over a voltage range for unmodified and C_2-amine modified copper

To elucidate the effect of surface modification with short chain alkyl amines, a copper electrocatalyst modified with C_2-amine was compared to an unmodified copper electrocatalyst for CO2ER performance at voltages between -1.0 and -2.0 V vs Ag/AgCl. CA profiles recorded at 0.25 V intervals are shown in Appendix 8 and their corresponding Faradaic efficiencies shown in Appendix 9. The average Faradaic efficiencies are shown below in Figure 90 across three electrodes. HER is consistently the most competitive reaction except at -1.0 V vs Ag/AgCl where hydrogen levels were beyond the limit of detection due to the low currents passed at non-forcing overpotentials. At -1.0 V, CO2ER is selective toward methane production for both electrocatalysts, however modification with C_2-amine appears to increase the methane selectivity significantly.

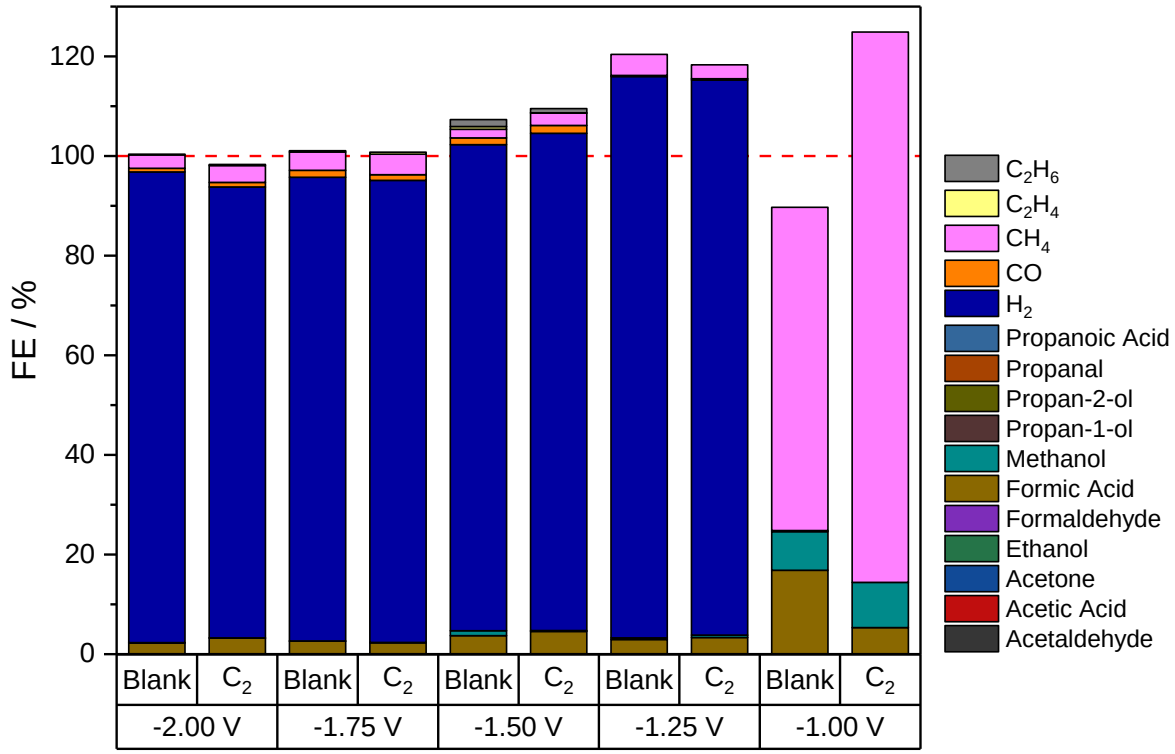

Figure 90. Average Faradaic efficiencies (CE1-3) for CO2ER catalysis at different voltages for an unmodified copper electrode ("Blank") and a C_2-amine modified copper electrode (C_2).

Partial current densities were again extracted from product distributions and are shown in Figure 91 (H_2 shown in full view in Appendix 9, Figure 102 and Figure 103). Both surfaces show formic acid to be the most selective CO2ER product, however again C_2-amine appears to have the highest turnover rate on average. Voltages of -2.0 V vs Ag/AgCl are expected to produce quantifiable quantities of C_{2+} products for unmodified copper,[67] however as none are observed here it is likely that that the experimental method is not optimised for CO2ER over HER. This is likely a repercussion of electrode rotation, where the mobility of protons is enhanced relative to dissolved CO_2 at higher rotation rates.

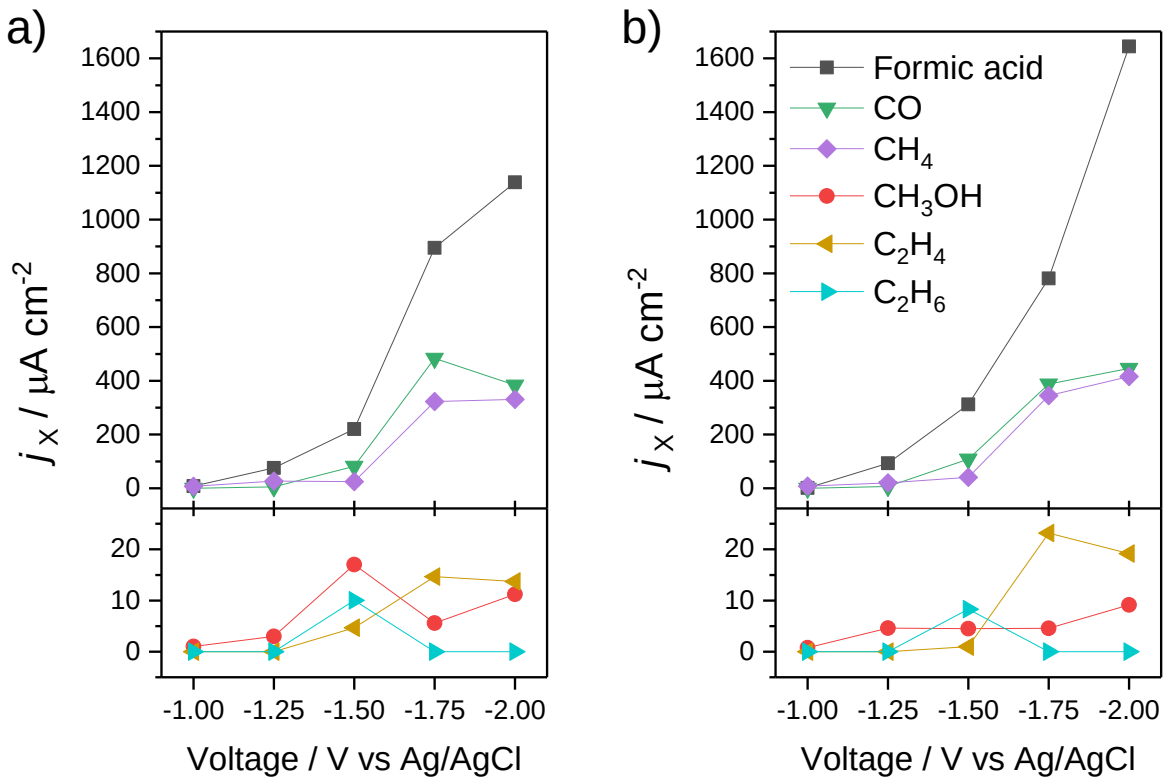

Figure 91. Partial current densities toward common CO2ER products at different voltages for a) an unmodified copper electrode and b) a copper electrode modified with C_2-amine.

To visualise the change of CO2ER partial current densities in a meaningful way, the percentage change in current density upon modification at different voltages is shown in Figure 92 for the low order hydrocarbons. Whilst there are some inconsistencies, some general conclusions can be drawn if -1.0 V vs Ag/AgCl is ignored where errors (discussed in the following section) may easily have distorted the results. Modification with C_2-amine generally increased the current densities toward formic acid, CO, CH_4 and C_2H_4 (at high overpotentials) whilst methanol was decreased. The supressed formation of methanol upon modification likely indicates that the catalytic pathway to methanol *via* the OCH_2 intermediate is inhibited.[295] This process relies upon initial binding Cu-C followed by protonation and a switch to Cu-O-C. This route is unique to formation of alcohol species and may be inhibited due to the decreased numbers of copper binding sites that are occupied by amine surface modifiers.

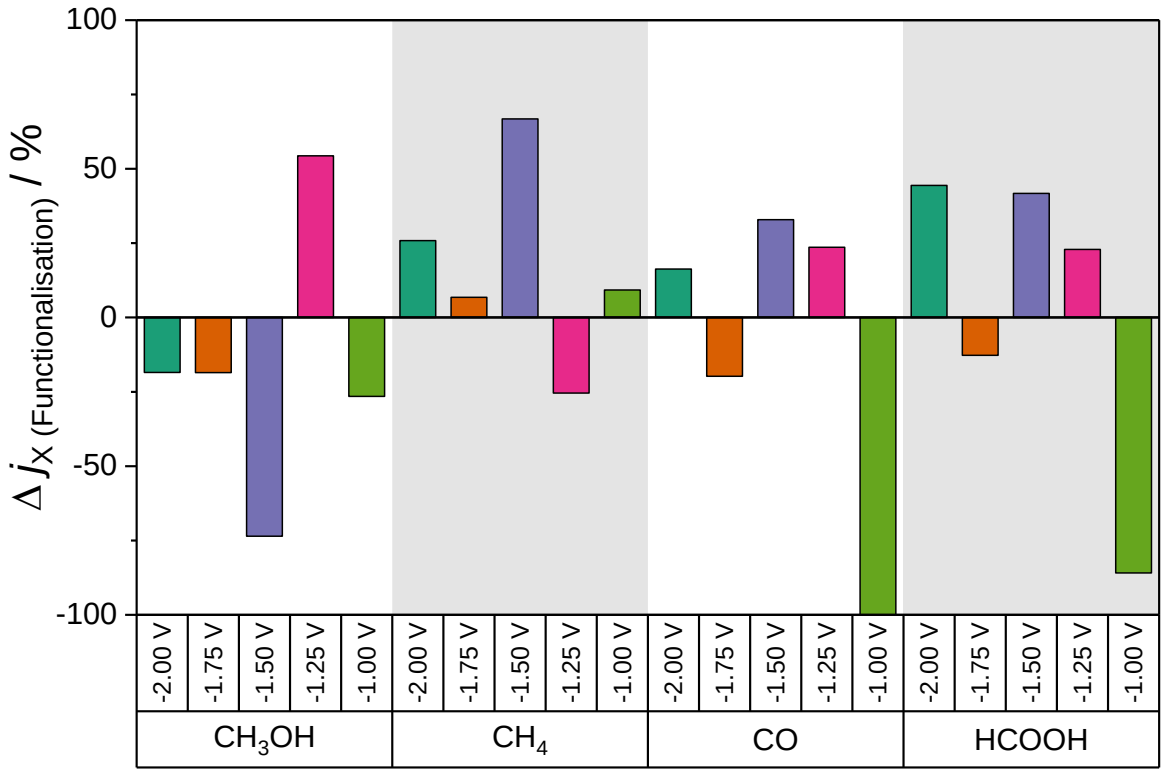

Figure 92. Relative changes (%) in current densities for different species at various CO2ER voltages upon functionalisation of a copper electrode with C_2-amine.

The effect on product distributions occurring from modification with C_2-amine is thought to occur from the amine functional group that could increase proton availability at the surface or provide ligand-like interactions to activate CO2ER intermediates. Increasing proton availability would generally increase reaction rates as all HER and CO2ER pathways are affected by proton concentration. This effect would hold across all voltage ranges to some extent. Ligand-like interactions as observed in molecular CO2ER catalysts would be expected to favour one specific product such as CO due to a well-defined reaction site on the copper surface.[152] Given that upon functionalisation turnover rates increase for H_2 and almost all C_1 species with the exception of methanol, it can be reasoned that the addition of C_2-amine to a copper electrode does not exhibit a ligand-like interaction with surface intermediates, but instead presents general rate enhancements due to a local increase in H^+ concentration. Therefore, future work will involve testing C_{10}-amine under similar conditions to combine hydrophobicity with this increased proton availability.

4.3.4 Stability of the C_2-amine modification on copper following electrocatalysis

To probe the stability of the diazonium salt modification of C_2-amine following electrocatalysis, electrodes CE1-3 were incubated in 10 mM NHS-viologen in MeCN overnight in the same fashion as in Chapter 3. Following washing of the electrode in water and acetonitrile, cyclic voltammetry recorded the electronic response of viologen moieties covalently attached to any remaining amine functional groups as in Figure 93. The response qualitatively indicates that viologen moieties are still able to attach to the post-catalysis electrode surface. The voltammetric response of CE2 post catalysis appears different to other electrode responses, which is attributed to electrode fouling during electrolysis.[296]

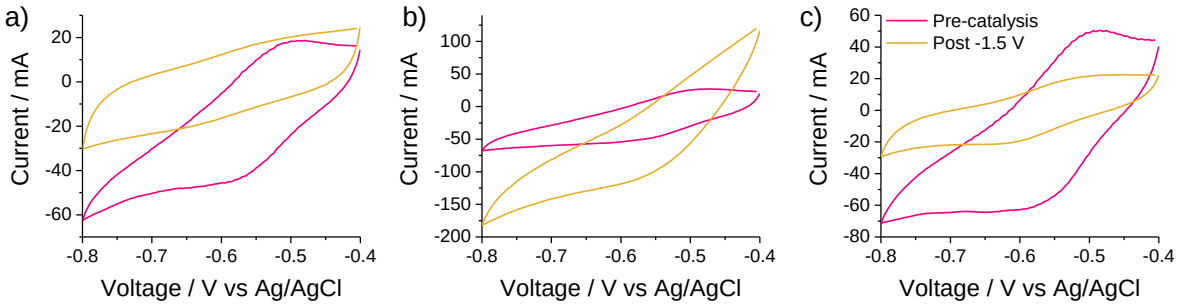

Figure 93. Voltammetric response of viologen moieties attached to C_2-amine modifiers on copper electrodes a) CE1, b) CE2 and c) CE3, before (red) and after (yellow) CO2ER catalysis at -1.5 V vs Ag/AgCl. Performed in 0.1 M NaCl, v = 500 mV s^{-1}, scan 3 shown.

This post-electrolysis viologen tagging was performed for all electrode surfaces following electrocatalysis outlined in the previous sections. Viologen signals were integrated with respect to a third or fourth order polynomial baseline as outlined in section 3.3.4 to reveal surface coverages. Table 12 highlights the remaining surface coverages achieved for all C_x-amine modifiers following electrolysis at -1.5 V vs Ag/AgCl, where it is observed that surface coverages can vary significantly between electrodes. Relative to the values obtained in Chapter 3 (Figure 67), the surface coverages have been broadly retained except on electrode CE1, which showed a drastic drop from a pre-catalysis coverage of approximately 250 pmol cm^{-2}.

Table 12. Surface coverages (pmol cm^{-2}) of viologen species attached to remaining diazonium modifiers following electrocatalysis at -1.5 V vs Ag/AgCl.

Electrode	C_1-amine	C_2-amine	C_4-amine	C_{10}-amine
CE1	25	62	48	68
CE2	208	419	413	298
CE3	209	141	305	244

The same approach for surface coverage quantification was taken following electrolysis across a voltage range as in section 4.3.3.2. Table 13 highlights the extracted surface coverages remaining for C_2-amine decorated copper electrodes. As the voltage for electrocatalysis is made more negative, CE1 and CE3 exhibit lower surface coverages of viologen-amine moieties post-catalysis. This indicates that more reducing conditions leads to either faster electrode fouling or decomposition or desorption of the diazonium modification.[296] CE2 does not exhibit the same trend which may be due to the electrode surface containing different crystal planes given that amorphous copper was used in the electrode materials.[122] Overall, this study indicates that the modifications outlined in Chapter 3 are semi-stable throughout electrocatalysis. It remains unclear if the lower surface coverages that are often observed post-electrocatalysis are a steady-deterioration of the diazonium modifiers or if the electrodes reach a steady-state of surface modification within 30 minutes of electrocatalysis and are stable thereafter. This may be the subject of future study.

Table 13. Surface coverages (pmol cm^{-2}) of viologen species attached to surface bound C_2-amine following electrocatalysis at different voltages (V vs Ag/AgCl).

Electrode	-1.00 V	-1.25 V	-1.50 V	-1.75 V	-2.00 V
CE1	113	83	62	51	58
CE2	350	289	419	233	313
CE3	240	189	141	89	159

4.3.5 Product errors in CO2ER catalysis

Errors have not been included for product amounts and derivative calculations in this chapter owing to the number of sources of error and instead data has been discussed largely in terms of trends as opposed to absolute values. This section mentions some of the key possible errors that may have arisen and where they have been addressed or not.

Many sources of error are magnified owing to the small scale of the electrocatalysis and the significant preference for HER. Working on the µmol cm^{-2} scale has yielded errors from electrolyte contamination, gas bag leakage, electrochemical cell gas leakage and instrument sensitivity. Electrolyte contamination occurs to a small extent for the key liquid-phase products formic acid and

methanol, however baseline contaminants are indistinguishable from very low concentration reaction products such as ethanol. A standard CO2ER experiment was carried out without performing CA catalysis and a standard ^{1}H WS-NMR product analysis performed. Over five experiments performed in this way, formic acid and methanol gave contaminant levels of 14.7 ± 6.3 and 38.1 ± 32.6 nmol, respectively, within the NMR experiment. Experiments with "significant" amounts of formic acid and methanol typically yielded 500+ nmol at the same stage.

In order to determine whether a liquid-phase product was produced during the reaction, D_2O-supressed deuterium NMR was performed on a standard catalysis run at -1.5 V vs Ag/AgCl for both an unmodified and a C_1-amine modified copper electrode that had been performed in 0.5 M $KHCO_3$ in D_2O (Figure 94). The observed signal to noise ratio was very poor even after 2048 scans, thus this method could only show that the most intense product peak, formic acid (8.35 ppm), could be observed and confirmed as a valid CO2ER product relative to the DMSO-d_6 internal standard (2.57 ppm).

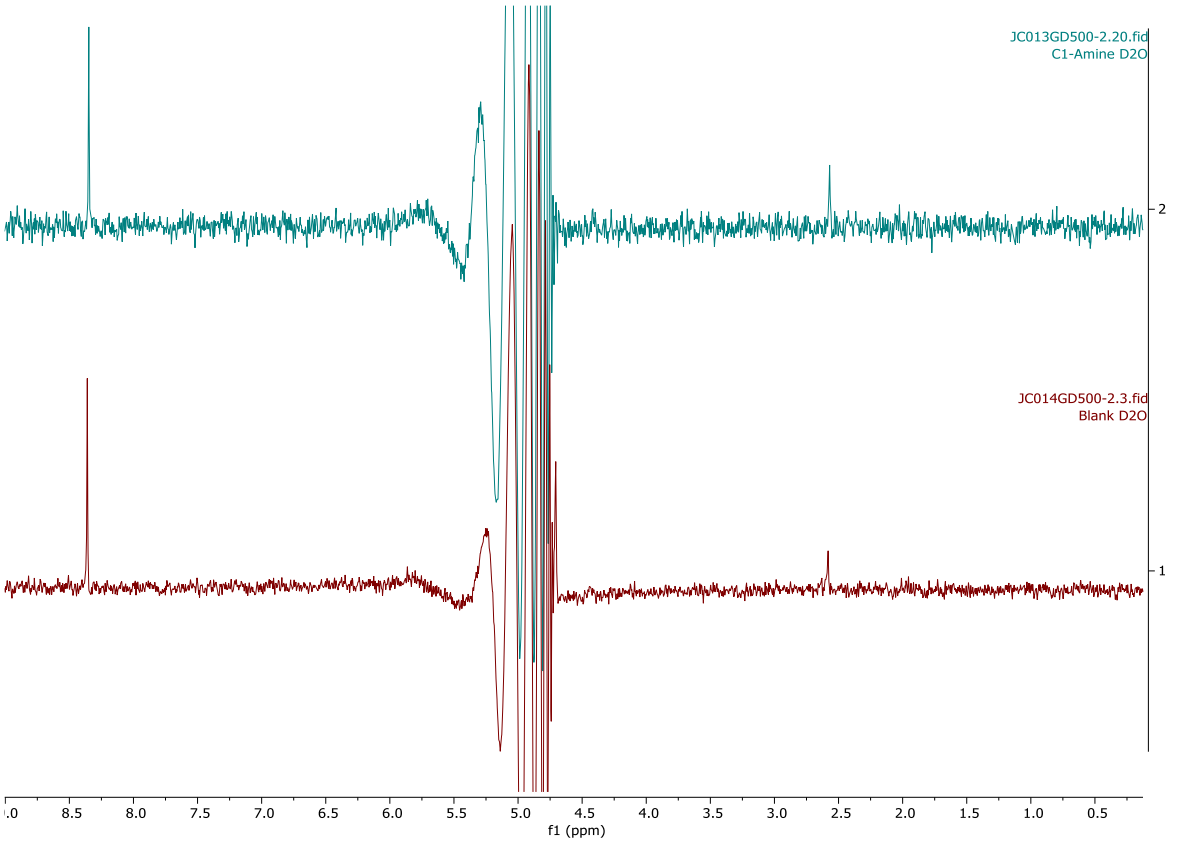

Figure 94. D_2O supressed ^{2}D NMR (107 MHz) for liquid products from CO2ER catalysis performed in 0.5 M $KHCO_3$ in D_2O. Catalysis performed at -1.5 V vs Ag/AgCl with an unmodified (bottom, red) or C_1-amine modified (green, top) copper electrode.

Contamination of gas products occurred by leakages in the in-house built H-cell. An OrigaTrod was used to achieve an RDE working electrode and placed into a QuickFit glass joint. A PFTE sleeve was used between the two components to increase the gas tight seal. Further gas errors may have come from GC instrument sensitivity. An FID coupled to a methanizer was used to detect hydrocarbon products whilst a TCD was used to detect hydrogen. At the required detector temperatures, the TCD did not give a reliable signal for hydrogen at concentrations lower than 1 nmol which explains the errors observed in faradaic efficiency plots at less negative voltages and currents (e.g. Figure 90, -1.25 V).

4.4 Conclusions

A method has been developed for performing CO2ER using a rotating disk electrode and analysing/processing both liquid and gas phase products. Supported by internal and external calibrations for NMR and GC respectively, the method was tested by performing a control experiment with a gold working electrode. This yielded completely gaseous products with Faradaic efficiencies of 90-105%, indicating relatively successful product analysis.

Modification of copper electrodes with amine terminated monolayers with different alkyl linker lengths *via* a diazonium protection-deprotection strategy has been shown to influence the competition between CO2ER *vs* HER reactions under aqueous conditions. Catalytic CV revealed reaction conditions for catalysis that compared unmodified and amine-modified copper electrodes. Differences between the surfaces were illustrated that stem from different surfaces properties.

A variety of alkyl linker lengths were tested for their product specificity and turnover at -1.5 V vs Ag/AgCl. Modification with short alkyl chain amine moieties on copper electrodes (C_1, C_2, C_4) yielded an increase in H_2, CO and HCOOH relative to an unmodified surface. Across a wider voltage range, copper electrode modification with C_2-amine increased production of all HER and CO2ER products except for methanol. C_2-amine modified copper was found to act as a proton shuttle and increase the concentration of protons in the electric double layer, a phenomenon that has been previously observed with amine based electrolytes.[294] It is important to note that differences between surfaces were explored as Faradaic efficiencies on average were very low (<20% FE for all CO2ER products combined) due to competition with HER. This can be attributed to methodology errors such as electrode rotation. These results are therefore very far removed from the forefront of electrocatalytic efficiencies as described in the introduction (C_1 products >90% FE,[52, 53] C_2 products >70% FE[54] and C_{3+} products at >10% FE[55]).

Functionalisation of copper with C_{10}-amine, a longer chain alkyl amine, increased the surface hydrophobicity. At -1.5 V vs Ag/AgCl, HER was inhibited significantly whilst production of HCOOH, CH_3OH and CH_4 was increased relative even to other short chain amine modifications. The increased hydrophobicity of the long alkyl chain appears to have the most significant effect in favouring higher-order hydrocarbon products, however the possibility of ligand-like interactions has not been explored for this surface. This will be the subject of further study.

4.5 Appendix 6: Catalytic CVs under N_2 and CO_2 atmospheres at 500 and 3000 rpm

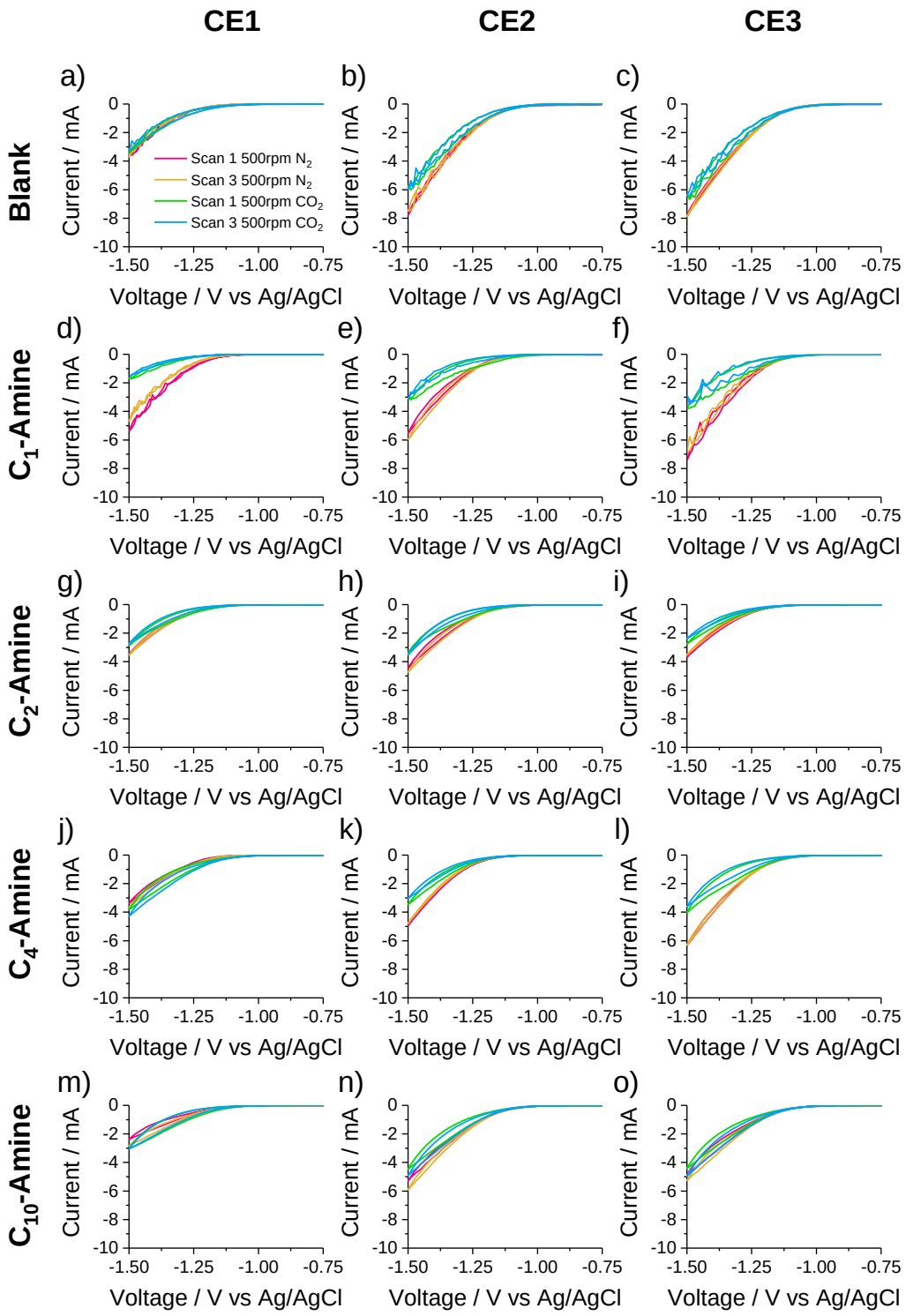

Figure 95. Catalytic cyclic voltammetry of unmodified and amine modified copper surfaces in a divided H-Cell. Recorded in 0.5 M $KHCO_3$ at 100 mV s^{-1}, rotation rate: 500 rpm.

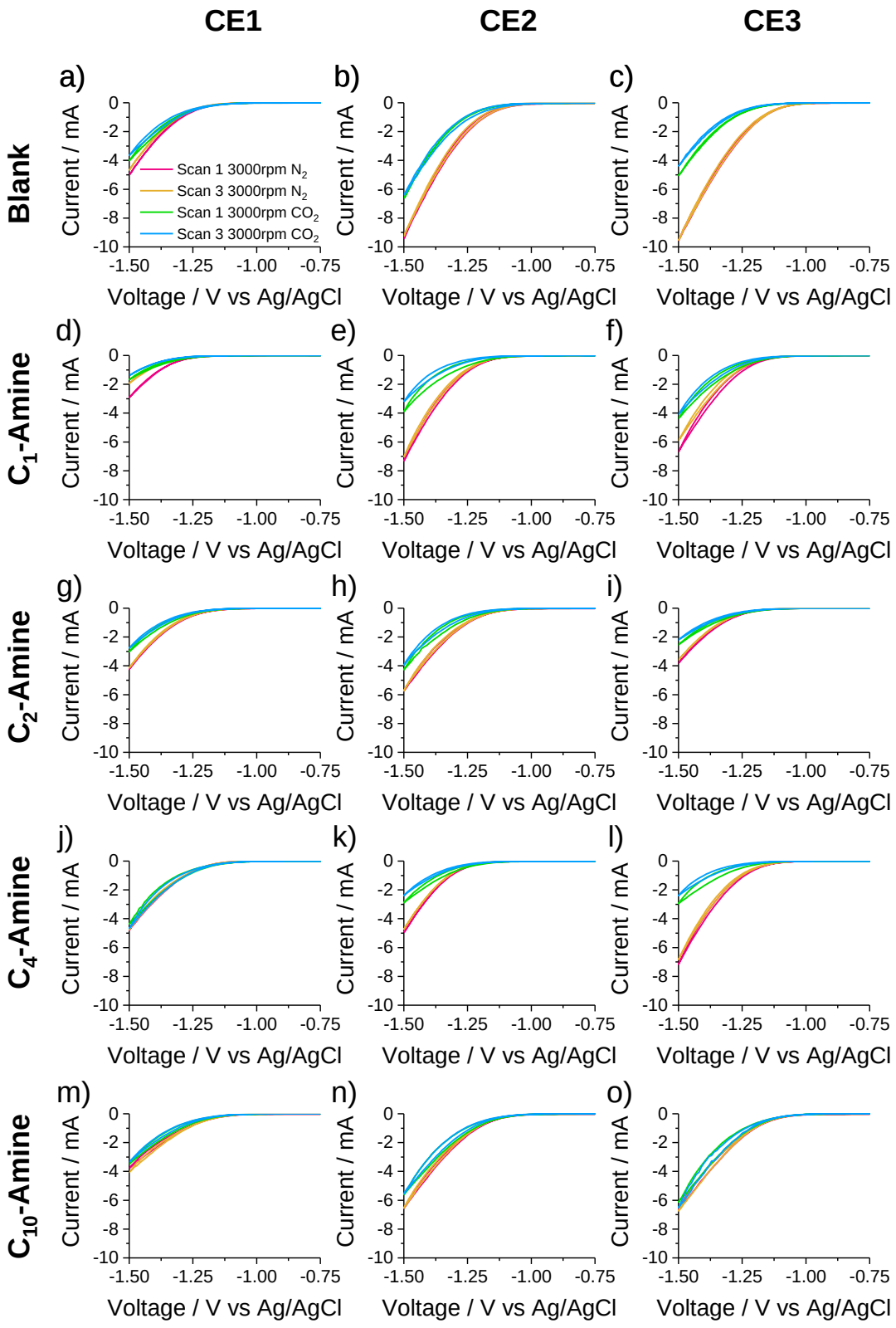

Figure 96. Catalytic cyclic voltammetry of unmodified and amine modified copper surfaces in a divided H-Cell. Recorded in 0.5 M $KHCO_3$ at 100 mV s^{-1}, rotation rate: 3000 rpm.

4.6 Appendix 7: NMR example spectrum and databasing tool

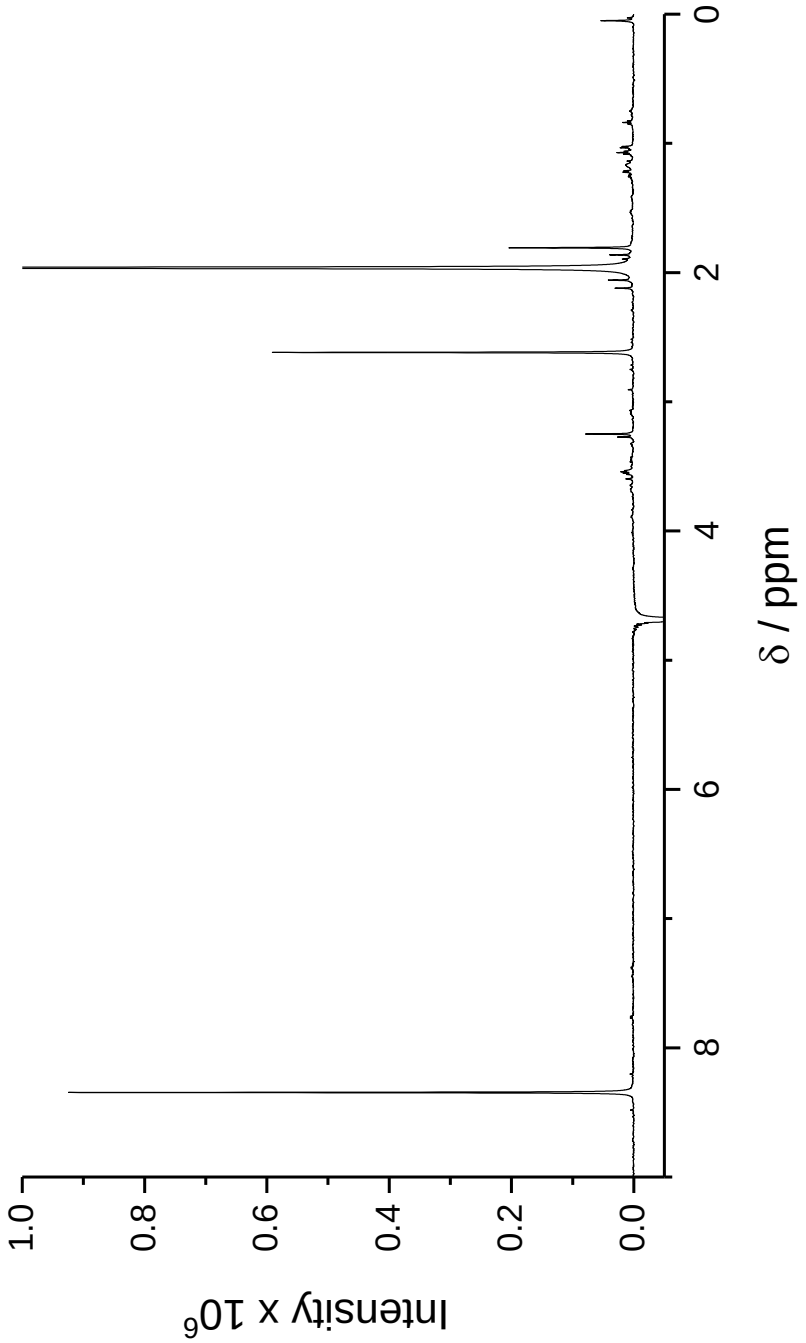

Figure 97. A sample ^{1}H NMR spectrum (700 MHz) with H_2O solvent suppression for analysis of liquid products from a CO2ER chronoamperometry (-2.0 V vs Ag/AgCl, 30 minutes, 0.5 M $KHCO_3$) experiment using an unmodified copper electrode.

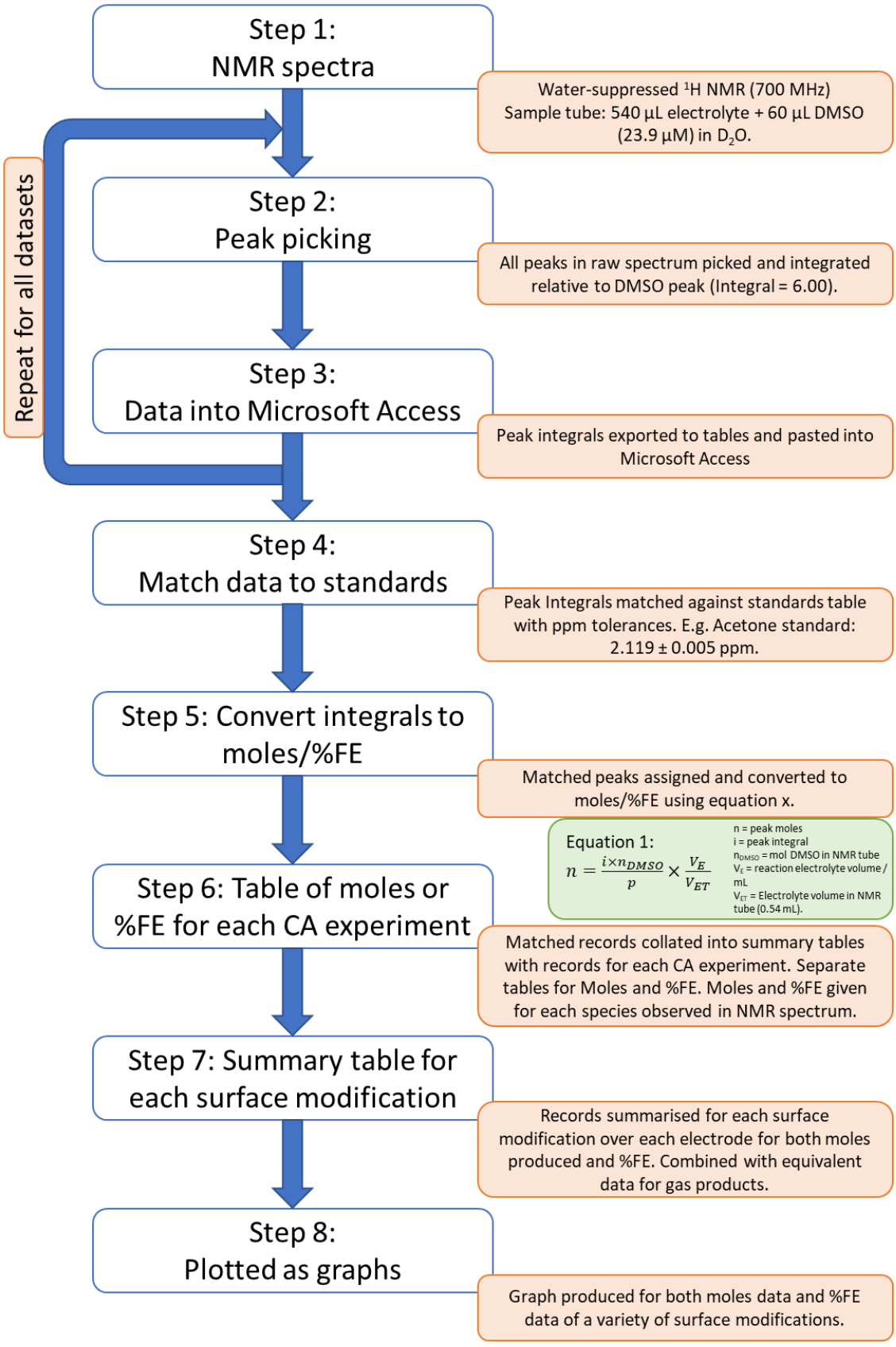
Step 1:
NMR spectra
Water-suppressed ¹H NMR (700 MHz)
Sample tube: 540 µL electrolyte + 60 µL DMSO (23.9 µM) in D2O.
Repeat for all datasets
Step 2:
Peak picking
All peaks in raw spectrum picked and integrated relative to DMSO peak (Integral = 6.00).
Step 3:
Data into Microsoft Access
Peak integrals exported to tables and pasted into Microsoft Access
Step 4:
Match data to standards
Peak Integrals matched against standards table with ppm tolerances. E.g. Acetone standard: 2.119 ± 0.005 ppm.
Step 5: Convert integrals to moles/%FE
Matched peaks assigned and converted to moles/%FE using equation x.
Equation 1:
$n = \frac{i \times n_{DMSO}}{p} \times \frac{V_E}{V_{ET}}$
n = peak moles
i = peak integral
nDMSO = mol DMSO in NMR tube
VE = reaction electrolyte volume / mL
VET = Electrolyte volume in NMR tube (0.54 mL).
Step 6: Table of moles or %FE for each CA experiment
Matched records collated into summary tables with records for each CA experiment. Separate tables for Moles and %FE. Moles and %FE given for each species observed in NMR spectrum.
Step 7: Summary table for each surface modification
Records summarised for each surface modification over each electrode for both moles produced and %FE. Combined with equivalent data for gas products.
Step 8:
Plotted as graphs
Graph produced for both moles data and %FE data of a variety of surface modifications.

4.7 Appendix 8: Chronoamperometry traces

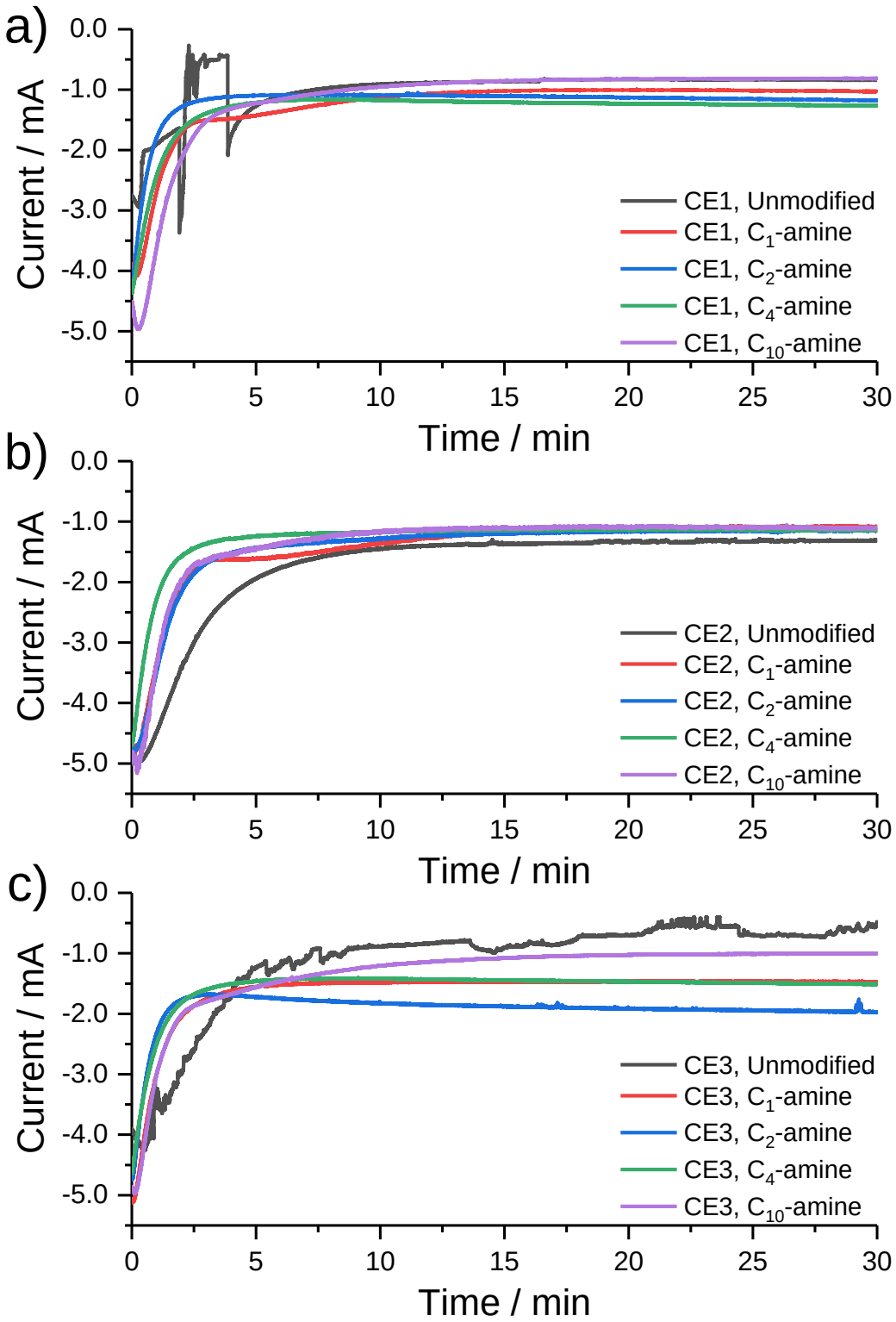

Figure 98. Chronoamperometry traces for CO2ER at -1.5 V vs Ag/AgCl performed on unmodified and C_x-amine modified copper electrodes CE1-3 (a-c) at 3000 rpm in 0.5 M $KHCO_3$.

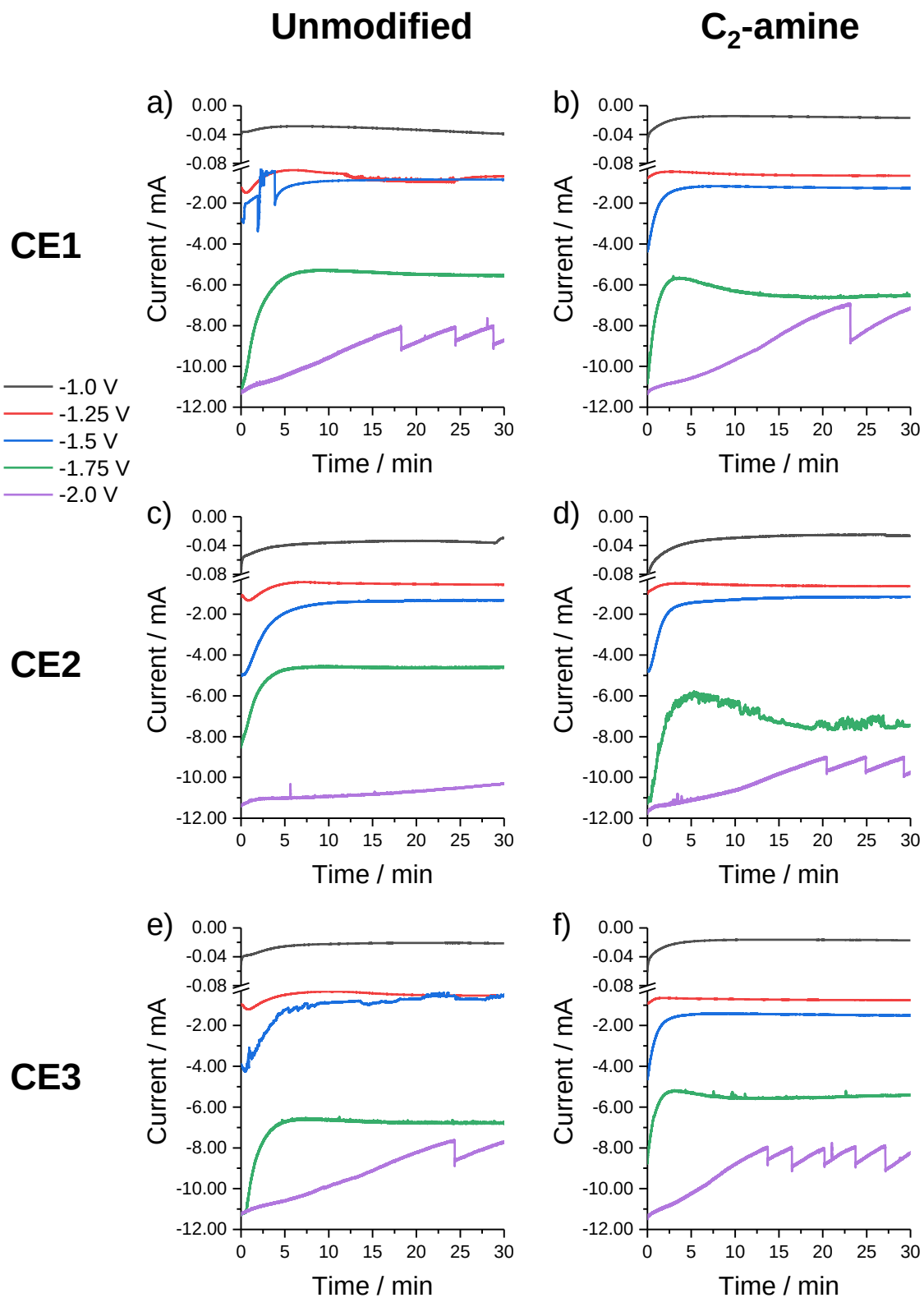

Figure 99. Chronoamperometry traces for CO2ER performed on unmodified (a, c, e) and C_2-amine modified (b, d, f) copper electrodes CE1-3 at 3000 rpm in 0.5 M $KHCO_3$. CA performed at voltages of -1.0 (grey), -1.25 (red), -1.5 (blue), -1.75 (green) and -2.0 V (purple).

4.8 Appendix 9: Faradaic efficiencies for CO2ER

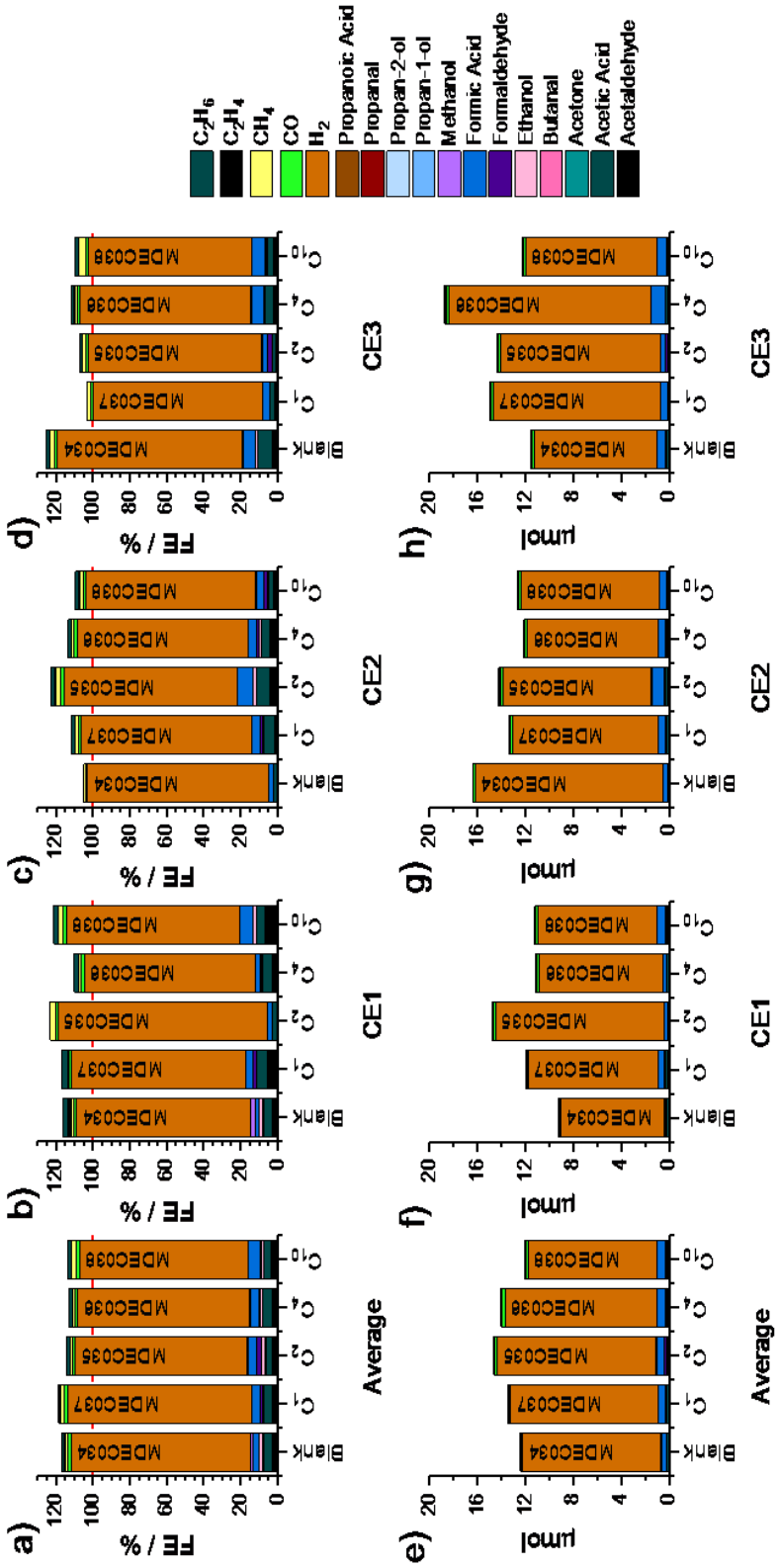

Figure 100. Faradaic efficiencies (a-d) and µmol conversions (e-h) for unmodified and C_x-amine modified copper electrodes, CE1-3, for CO2ER catalysis at -1.5 V vs Ag/AgCl.

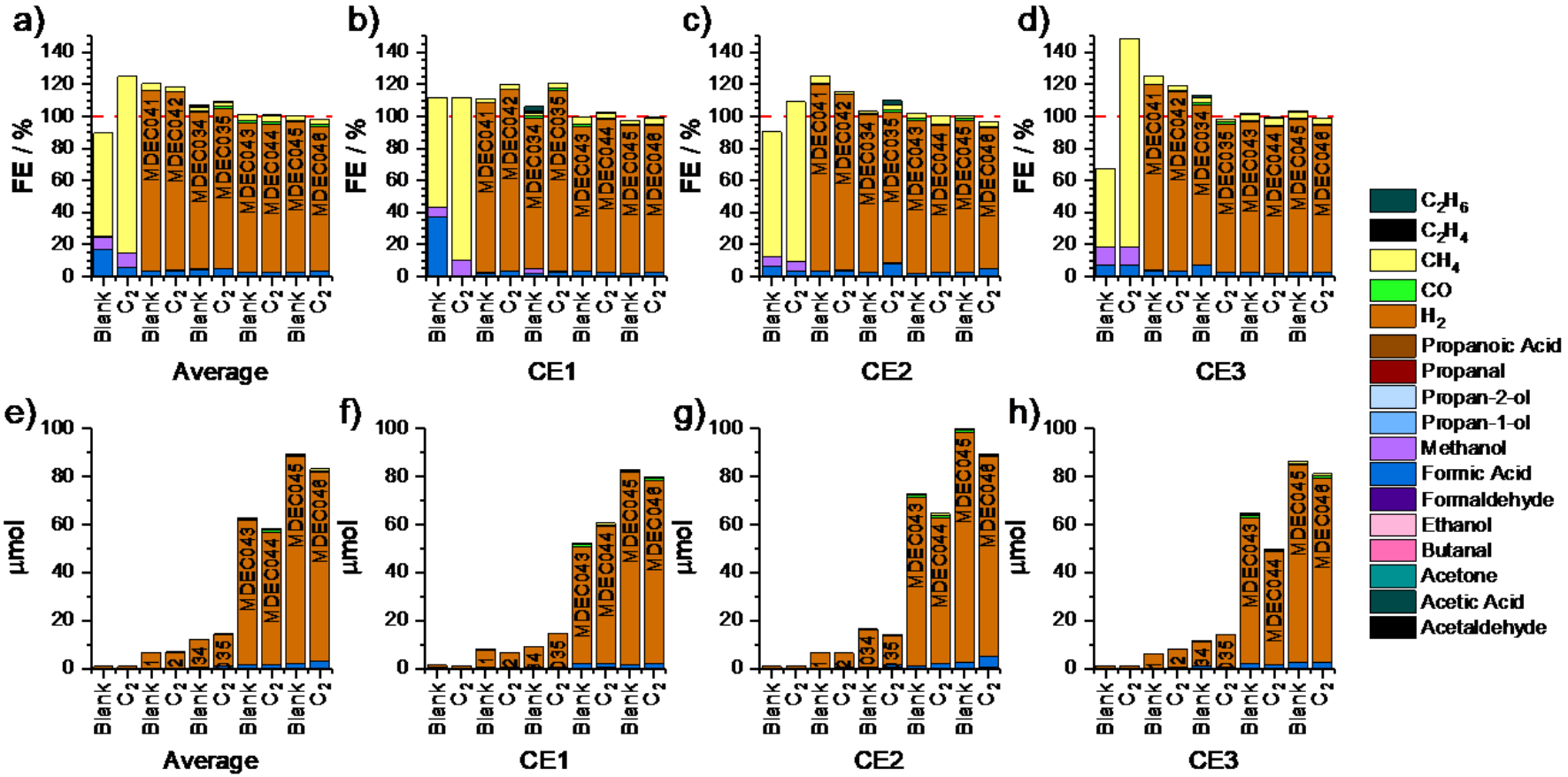

Figure 101. Faradaic efficiencies (a-d) and µmol conversions (e-h) for unmodified and C_2-amine modified copper electrodes, CE1-3, for CO2ER catalysis at a range of voltages between -1.0 and -2.0 V vs Ag/AgCl. For all plots, two columns on the left represent -1.0 V and then each pair of columns to its' right indicate -0.25 V incremental reductions, e.g. -1.25 V.

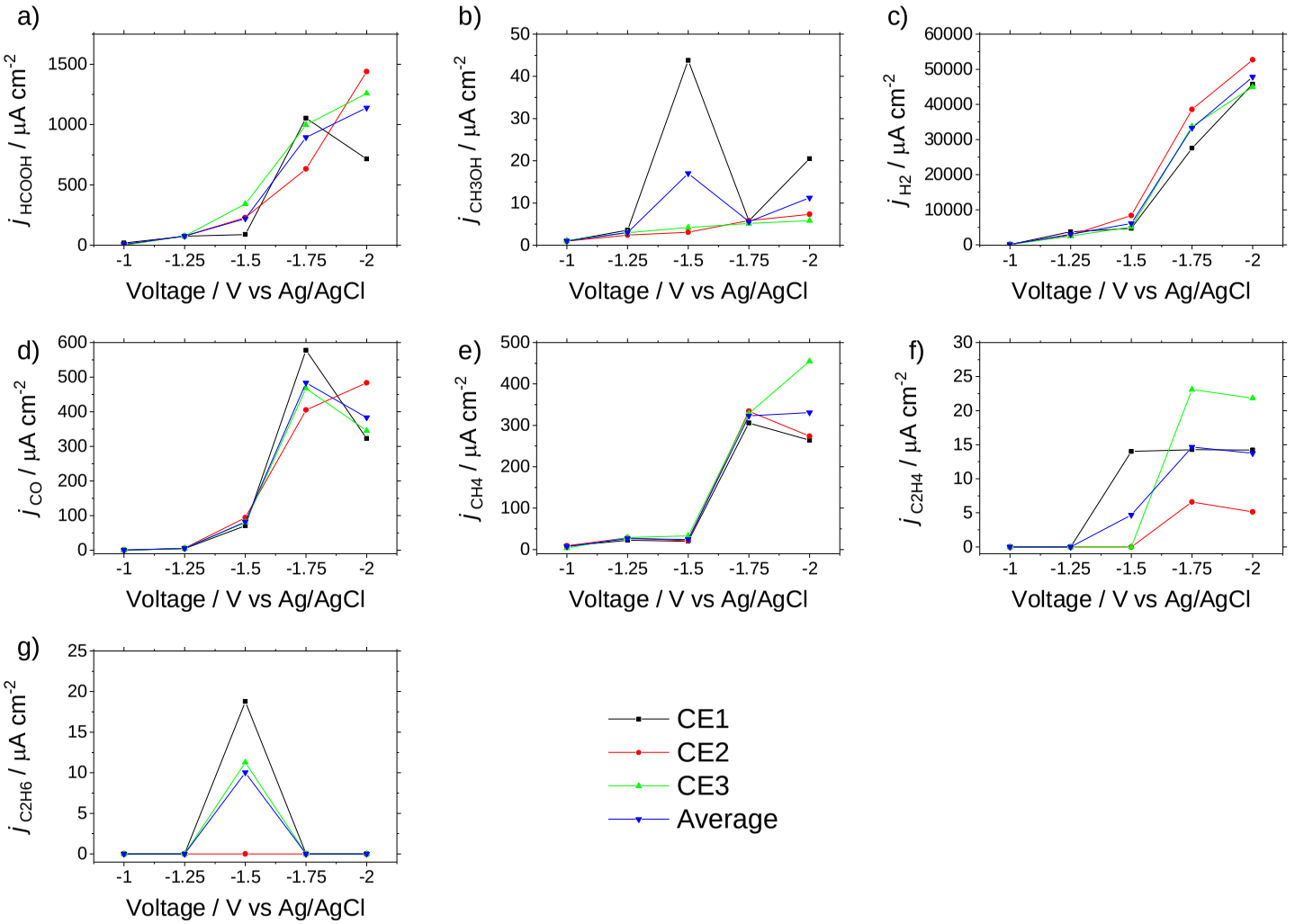

Figure 102. Partial current densities for unmodified copper electrodes, CE1-3, for CO2ER catalysis at a range of voltages between -1.0 and -2.0 V vs Ag/AgCl.

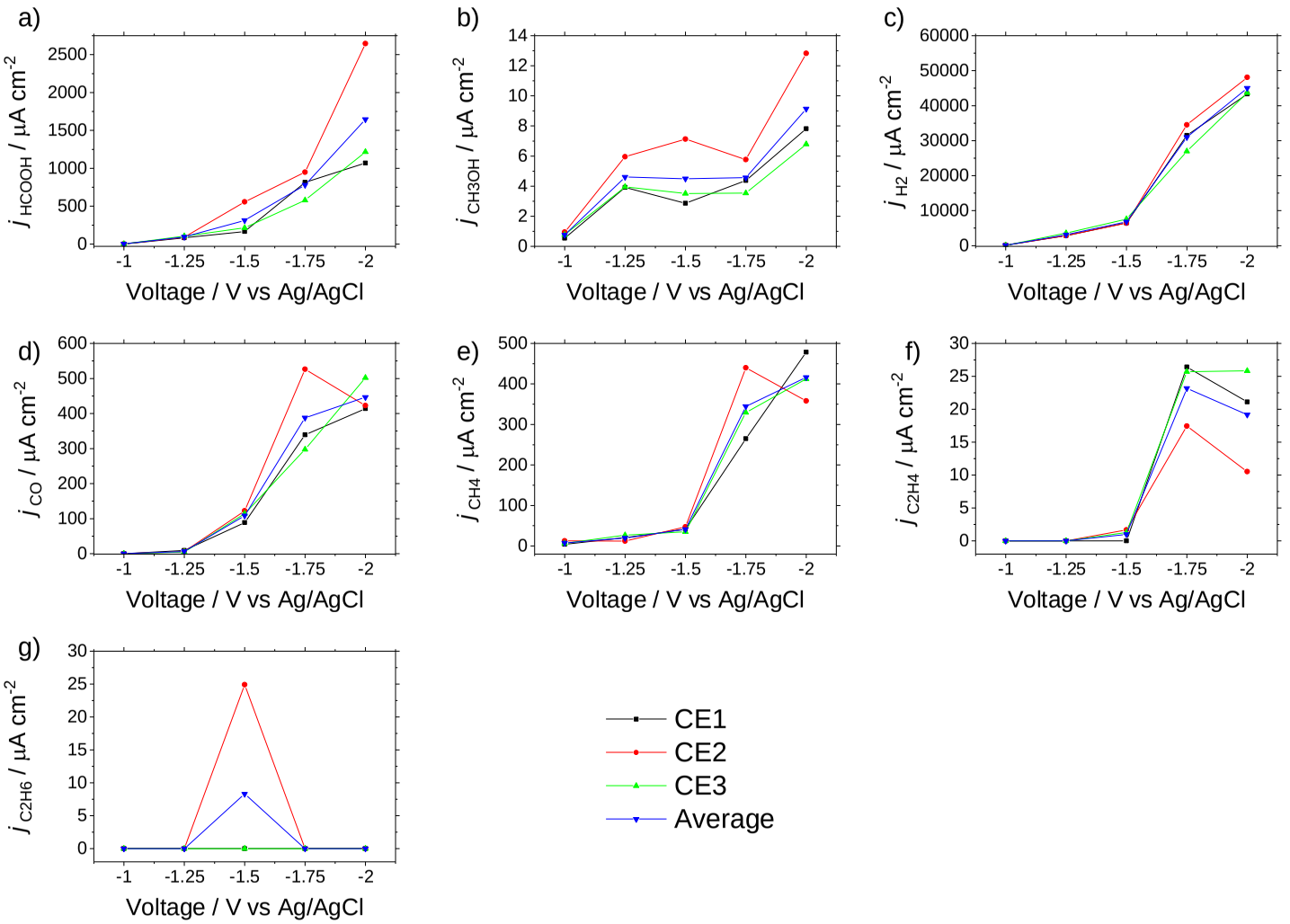

Figure 103. Partial current densities for C_2-amine modified copper electrodes, CE1-3, for CO2ER catalysis at a range of voltages between -1.0 and -2.0 V vs Ag/AgCl.

Chapter 5. A novel “spacing strategy” using concurrent diazonium salt grafting and SAM desorption for a new family of electrocatalysts

5.1 Abstract

In the same way that homogeneous catalysts use co-operative metal binding and secondary sphere ligand interactions, it may be desirable to create this ligand-like interaction on an electroactive solid metal surface. To achieve this a strategy for generating a well-defined sub-monolayer must be used. This chapter presents a novel strategy for achieving a sub-monolayer concentration of organic modifications derived from electro-grafting of diazonium salt species. This work is presented on a gold electrode owing to the wide voltage window in which Au^0 surface is observed. A “spacing” strategy is outlined that relies on concurrent electrochemical cleavage of a redox-tagged self-assembled monolayer and the electro-grafting of a diazonium salt.

5.2 Introduction

The modification of electrode surfaces with either organic or inorganic functionalities is a strategy that is often employed to enhance electrocatalyst selectivity or turnover, and the thesis introduction summarises how this has been explored in the field of CO_2 electroreduction. Modification strategies that introduce a monolayer of organic moieties can be useful for changing electrode properties such as hydrophobicity. Such modifications can be achieved using SAMs on metal electrodes or diazonium salts across most electrode surfaces.[297, 298] Fewer literature procedures exist for generating sub-monolayer concentrations of organic functionalities on electrode surfaces.[299, 300]

One recent example of a sub-monolayer modification was demonstrated by Takeuchi *et al.* for CO2ER catalysis.[301] The group constructed spaced-out polymer frameworks by using electro-oxidised Cu^{1+} to trigger Cu^{1+}-catalysed azide alkyne cycloaddition. Cu^{1+} was formed by the oxidative sweep in cyclic voltammetry and the subsequent reverse sweep reduced solution Cu^{1+} to surface bound Cu^{0} at the same time as insoluble polymeric species lay down on the surface (Figure 104). The work further illustrated that such electrocatalysts yielded generally improved selectivity for CO2ER over HER upon modification, where HER could be supressed by up to 30% FE. The increase in selectivity was attributed to the role of the organic functionalities in providing cooperating, ligand-like interactions for enhanced proton transfer to CO2ER intermediates *via* amine moieties. Inspired by this published work and following earlier work in this thesis on diazonium electrode modification (Chapter 3), this chapter describes a new method for generating sub-monolayer electrode functionalisation through an amalgamation of diazonium monolayer modification and a strategy for partial electrochemical cleavage of a SAM.

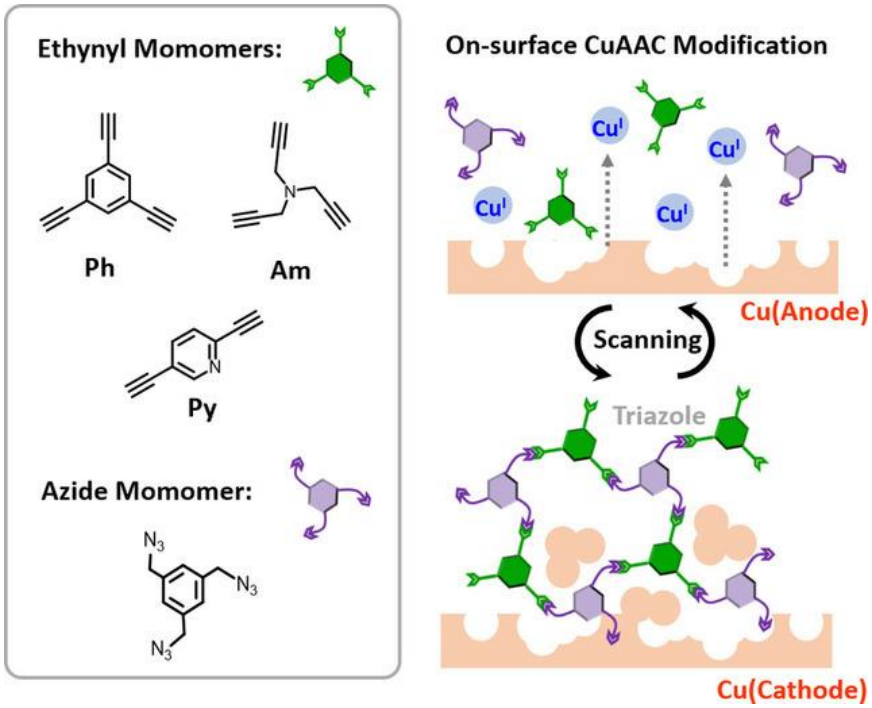

Figure 104. Synthesis of copper CO2ER electrocatalysts with spaced organic structures. Reproduced with permission from reference 301. Copyright Wiley, 2020.

5.2.1 Strategies for achieving sub-monolayer coverages

Achieving a sub-monolayer coverage of grafted molecules on an electrode surface can be difficult owing to the inhomogeneity related to grafting processes, exposed surface structures and electrode composition. A well-defined structure can also be difficult to achieve owing to the possibility of surface structure rearrangement which may occur when the modifier is weakly bound to the electrode surface.[302] Approaches to overcome some of these obstacles and achieve sub-monolayer concentrations include the use of controlled binding sites, protecting group strategies and electrochemical cleavage.[303]

The use of controlled binding sites was explored by Mattiuzzi *et al.* to expose well-defined reactive handles for modification.[304] The group synthesised calixarene compounds containing aniline functionalities with a variety of functionalised ether linkages. *In-situ* diazotisation of the aniline moieties allowed the molecules to electrochemically graft as dense monolayers onto glassy carbon, gold and pyrolyzed photoresist film electrodes. As shown in Figure 105, the synthesised calixarenes contained either four terminal carboxylic acids or one carboxylic acid and three alkyl termini. The carboxylic acid termini could act as reactive handles for further modification steps whilst the alkyl

termini could not undergo further modification steps. The group attached a ferrocene redox tag to the exposed carboxylic acid groups on the electrode surface to quantify surface coverage. Selectively using three of the calixarene modification sites with alkyl units reduced the surface coverage from 69 pmol cm^{-2} (4× COOH) to 16 pmol cm^{-2} (1× COOH). This method of surface modification is an excellent approach for controlling properties such as hydrophobicity where the degree of subsequent chemical modification can be controlled by the number of installed reactive handles *via* the calixarene precursor.

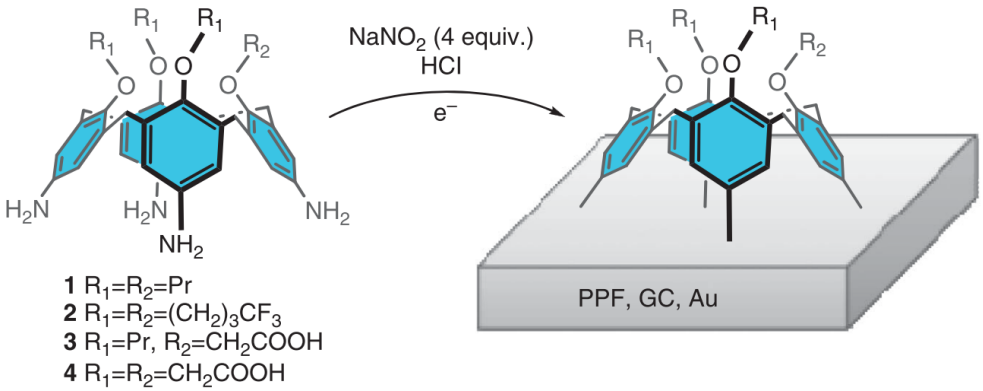

Figure 105. *In-situ* diazotisation and electrochemical grafting of calix[4]tetra-aniline units with four terminal functionalities. Reprinted by permission from Copyright Clearance Centre: Springer Nature, Nature Communications, reference 304. Copyright (2012).

An alternative way of creating a sub-monolayer concentration of surface species is using bulky protecting groups when grafting diazonium species. A low surface coverage of diazonium salts can be achieved by a protection-deprotection strategy similar to those outlined in Chapter 3. Leroux *et al.* utilised a triisopropylsilane (TIPS) protecting group to protect the alkyne functionality within an ethynyl aryldiazonium salt.[264] The TIPS protecting group did not allow the formation of a multilayer because benzyl radicals are unable to graft to the alkyl termini. Once grafted, the monolayer could be deprotected with an F^- source, tetra-*n*-butylammonium fluoride, to yield a terminal alkyne for further modification steps. A follow up study by the same group showed that a smaller diazonium salt, 4-nitrobenzenediazonium salt (NDBT), can electrochemically modify the TIPS-protected glassy carbon surface further, as indicated in Figure 106. This was attributed to the presence of pinholes in the imperfect monolayer formed by the TIPS protected diazonium salt.[305] Thus, the use of bulky protecting groups can generate a spatially resolved monolayer with sub-monolayer surface concentrations.

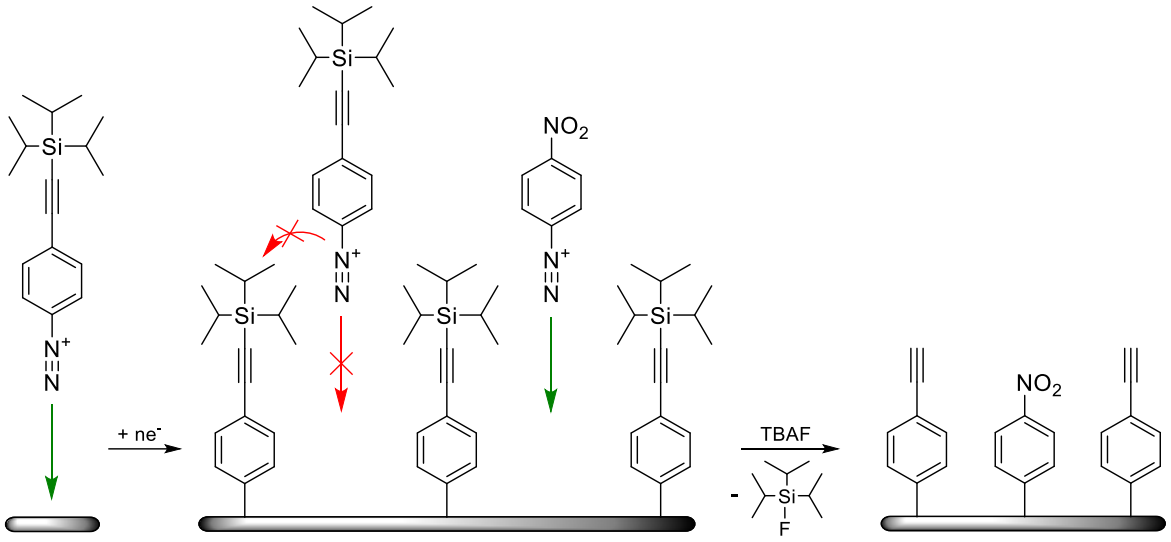

Figure 106. Electrochemical grafting of 4-nitrobenzenediazonium salt into pinholes on carbon electrodes functionalised with TIPS protected ethynyl aryl diazonium salt. Summary figure for work in reference 305.

5.2.2 Self-assembled monolayers

Self-assembled monolayers (SAMs) have been extensively studied and reviewed,[297, 306-308] as described in the thesis introduction. Whilst thiol-SAM formation has been most widely studied on gold electrodes, it has been shown to occur on most metal electrodes. For example, alkanethiol based SAMs have been used to protect copper electrodes against corrosion by formation of a densely packed layer.[195] The deposition of alkanethiol SAMs on gold electrodes is generally a fast process, with the majority of the SAM layer shown to assemble within 5 minutes and >95% of the maximum achievable surface coverage obtained within 30 minutes.[309] Owing to the very quick assembly of these species, sub-monolayer coverages of SAMs are not usually achieved by using a short assembly time. For example, within 5 s an octane thiol can self-assemble to near complete saturation on a sputtered Au(111) gold electrode.[310] The rapidity of this self-assembly was attributed to the homogeneous nature of gold surface allowing rapid growth rate from individual Au-SAM nuclei.

Owing to the lability of the Au-S bond (140 kJ mol^{-1} < ΔH < 170 kJ mol^{-1}),[311] gold thiol SAMs can be easily cleaved by reductive electrochemistry. Cyclic voltammetry was applied by Imbayashi *et al.* to a variety of HS-$(CH_2)_n$-X molecules independently adsorbed onto gold electrodes in 0.5 M KOH solutions.[312] Where the alkyl chain length (n) was increased, the voltage required to

electrochemically cleave the Au-S bond became more negative, dropping from -0.74 V vs Ag/AgCl (n = 2, X = COOH) to -0.91 V vs Ag/AgCl (n = 10, X = COOH). It was also found that the more polar the head group (X: COOH > OH > CH_3), the more positive the cleavage potential. The group used this approach with binary SAMs to create controlled surface concentrations of one thiol molecule over another by allowing cleaved thiol molecules to readsorb to the surface (Figure 107). Readsorption is a phenomenon that occurs faster with longer alkyl chain moieties owing to increased van der Waals interactions and layer stability.[313, 314]

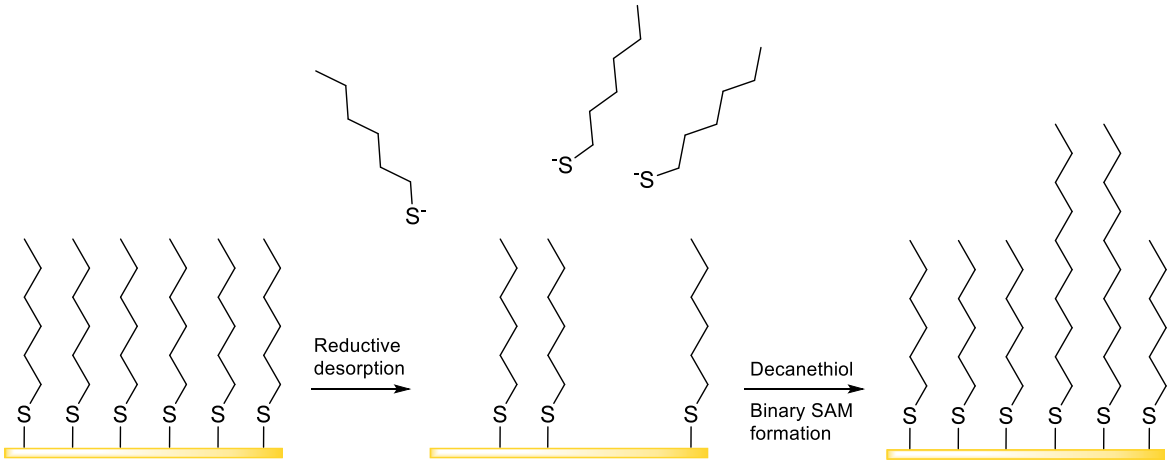

Figure 107. Reductive desorption of hexanethiol and readsorption/reformation in the presence of decanethiol to yield a binary SAM.

The reductive desorption of Au-SAMs has also been shown to be pH-dependent by several authors.[315, 316] The small molecule 2-mercaptoethanol forms a SAM with a relatively positive desorption potential at neutral pH (-0.65 V vs Ag/AgCl).[201] Figure 108 illustrates a systematic study by Munakata *et al.* for desorption of 2-mercaptoethanol in different pHs of phosphate buffer electrolyte. Increasing the pH yields a shift to a more negative potential for electrochemical desorption, however the potential plateaus at approximately -0.7 V vs Ag/AgCl. This effect also applied to longer chain alkyl SAMs where nonanethiol, the longest chain tested, plateaued at a cleavage potential of approximately -1.1 V vs Ag/AgCl. The reliability of this method to completely desorb a SAM has even led to reductive desorption of SAMs being developed as a method for surface coverage quantification.[317]

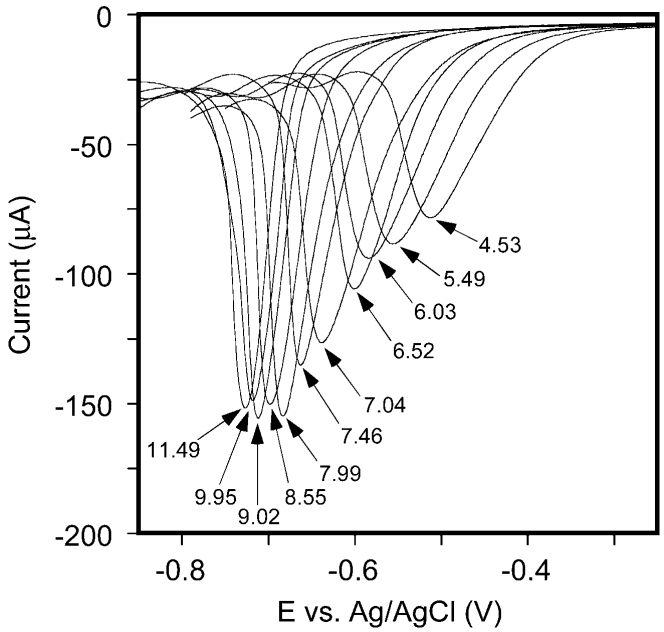

Figure 108. Linear sweep voltammograms of 2-mercaptoethanol SAMs on Au(111) electrodes at different pH values (indicated by arrows). Spectra recorded in 0.1 M phosphate buffer at a scan rate of 200 mV s^{-1}. Reprinted (adapted) with permission from reference 201. Copyright (2004) American Chemical Society.

5.2.3 Catechol units for electronic communication at electrode surfaces

Electroactive species that give reversible redox peaks can be used to probe the properties of an electrode surface, as demonstrated through the use of solution ferricyanide and surface-immobilised methyl viologen earlier in this thesis (Chapter 3 and Chapter 4). Catechol units are also widely used as redox indicators due to their potential to undergo a reversible two-electron oxidation to the quinone form (Scheme 2).[318] Both surface bound and solution phase catechol units have been studied previously.[318, 319]

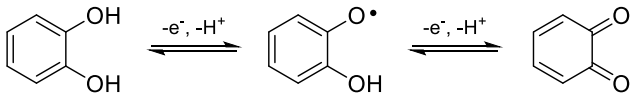

Scheme 2. Catechol oxidation to quinone *via* a radical intermediate.

Lin *et al.* explored the effect of pH on the redox mechanism of catechol by using cyclic voltammetry in buffered electrolytes (Figure 109). A variety of transition states and reaction pathways could be accessed that are dependent upon pH because of the protonation states of the intermediates. The strength of the interaction between intermediates was mirrored by changing $E_{1/2}$ values that

decreased with increasing pH, a phenomenon also noted by other authors.[320] The possibility for hydrogen bonding and increased organisation between catechol molecules has even led to catechol units being incorporated into some alkanethiol SAM moieties that were noted for their topographical homogeneity and surface adhesion properties.[321]

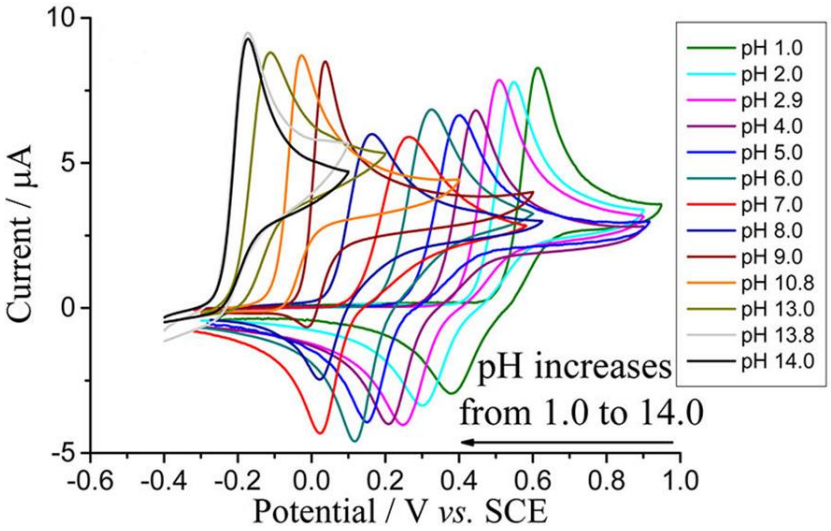

Figure 109. Cyclic voltammograms of 0.5 mM catechol in pH buffered solutions with 0.1 M KCl recorded with an unmodified glassy carbon electrode at a scan rate of 16 mV s^{-1}. Reprinted (adapted) with permission from reference 319. Copyright (2015) American Chemical Society.

This chapter is dedicated to finding a new strategy for producing a sub-monolayer coverage *via* diazonium salt grafting on metal electrodes for use as electrocatalysts. The proposed strategy (Figure 110) modifies gold electrodes with a redox-tagged SAM that can be reductively cleaved at the same time as electro-grafting of a diazonium salt occurs. This utilises the same diazonium modification "protection-deprotection" strategy harnessed in Chapter 3 and Chapter 4. This strategy is designed to create a new family of organically modified electrocatalysts for applications such as CO2ER.

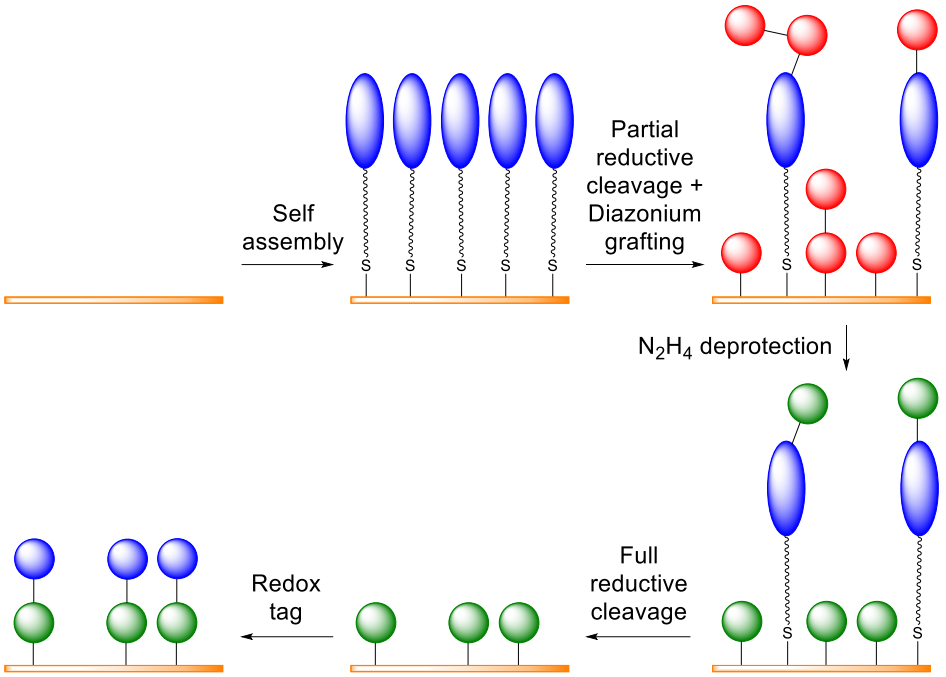

Figure 110. Proposed scheme for an electrochemical spacing strategy for sub-monolayer coverages of diazonium salt grafting on metal electrodes. Blue circles/ovals are redox active moieties for electrochemical detection, red circles are protected diazonium-derived species and green circles are deprotected diazonium-derived species.

5.3 Results and Discussion

This chapter explores the feasibility of a new kind of "spacing strategy" designed to decrease the surface coverage associated with the diazonium modification of electrodes described in Chapter 3. This strategy utilises SAMs as a blocking agent that can be cleaved in tandem with diazonium electro-grafting as outlined in Figure 110. The studies presented here explore the assembly of a redox-tagged SAM (rSAM) on gold surfaces and their electrochemical reductive cleavage to a sub-monolayer. A protection-deprotection strategy using diazonium salt modifications on the same gold electrodes to establish the maximum surface coverage attainable before the electrochemical spacing strategy was explored.[193]

5.3.1 Redox-tagged self-assembled monolayers on gold electrodes

Two novel catechol-terminated alkanethiol molecules of two different alkyl linker lengths, **8** and **9**, were synthesised to create SAMs that exhibited a redox signal which could be used to quantify surface coverage. Two different alkyl linker lengths were used so that the impact of chain length on self-assembly could be followed. Catechol was chosen as the redox active moiety to detect through-space electron tunnelling from the electrode surface to an electroactive terminus without performing electrochemical cleavage of the rSAM.[314, 318, 319] Catechol was chosen owing to the literature $E_{1/2}$ value (*ca* +0.15 V vs Ag/AgCl at pH 7)[319] being significantly more positive than the expected voltage for reductive cleavage of the rSAM moiety that typically occurs below -0.4 V vs Ag/AgCl.[201] Following self-assembly, gold surfaces covered in molecules **8** and **9** are subjected to electrochemical reductive cleavage to achieve sub-monolayer coverages. Surface coverages in this section are recorded relative to the geometric surface area as semi-quantitative measurements reveal the reductive cleavage of SAM moieties.

Molecules **8** and **9** were synthesised from an alkyl carboxylic acid backbone terminated in a bromine moiety. The synthesis of these molecules has not been reported before, however they are closely related to published catechol containing SAMs.[321] The full synthetic details of these rSAM molecules is outlined in section 7.5.2. Briefly, the bromine terminus was protected using trityl mercaptan before the carboxylic acid was coupled to dopamine using EDC and HOBt amide coupling agents. The isolated solid was then trityl-deprotected with trifluoroacetic acid to yield molecules **8** and **9**.

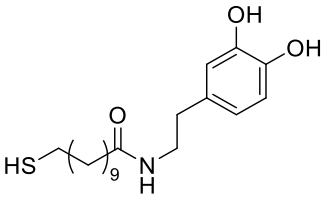

8

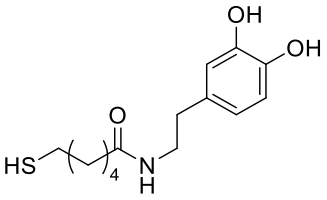

9

Exploratory experiments for the self-assembly of molecule **8** were conducted to reveal the optimum assembly time and initially probe the redox activity of the catechol unit. Gold electrodes were both mechanically and electrochemically polished according to procedures in section 7.2.1.[317] The electrodes were then immersed in a solution of 1 mM rSAM molecule in acetonitrile and left to self-assemble for 75 minutes, 18 hours or 40 hours before the electrodes were extensively washed and sonicated as detailed in section 7.2.3.1.

Initial cyclic voltammetry studies were performed in a 0.1 M NaCl electrolyte following the self-assembly of molecule **8** for 75 minutes (Figure 111a). The reversibility of electron transfer to and from the catechol unit is clearly seen by the unchanging and symmetrical shapes of the scans which have been analysed to yield a surface coverage of 216 pmol cm^{-2} (one electrode). This was calculated by first subtracting a third order polynomial baseline from the reductive peak and then integrating for the total charge passed, similar to the method described in Chapter 3 and akin to the method that has been used extensively to determine surface coverage with ferrocenyl redox markers.[198, 322] The analysis assumed a planar geometric gold electrode surface area of 0.28 cm^2 derived from a circular diameter of 3 mm. On the same electrode, self-assembly of molecule **8** for 40 hours yielded a surface coverage of 399 pmol cm^{-2} which demonstrates that a longer assembly time can increase the surface concentration, however most self-assembly occurs rapidly upon immersion. The sharpness of both the oxidation and reduction peaks indicates fast redox kinetics, however the wide potential separation (0.17 V) between the redox peaks indicates that a large amount of activation energy is required to achieve electron tunnelling from the surface to the catechol unit. This thermodynamic penalty is expected because the long C_{11}-alkyl linker length was estimated as 22 Å using a molecule visualisation package (Chem3D), where the maximum distance for rapid electron tunnelling is generally regarded as 14 Å.[319, 323]

When scanning to low voltages in 0.1 M NaCl (Figure 111b), a reductive peak appears at *ca* -0.6 V vs Ag/AgCl. The lack of a corresponding oxidative peak indicates that this is an irreversible process. This reductive peak at -0.6 V vs Ag/AgCl overlaps with a reductive wave corresponding to proton

reduction from the aqueous solvent, thus the peak at -0.6 V vs Ag/AgCl cannot be accurately quantified. Since this reductive process correlates with a clear decrease in the dopamine oxidation signal at approximately +0.4 V vs Ag/AgCl with each successive scan, this process can be attributed to the partial reductive cleavage of the Au-S monolayer as has been previously observed for alkanethiol based SAMs on gold electrodes.[317]

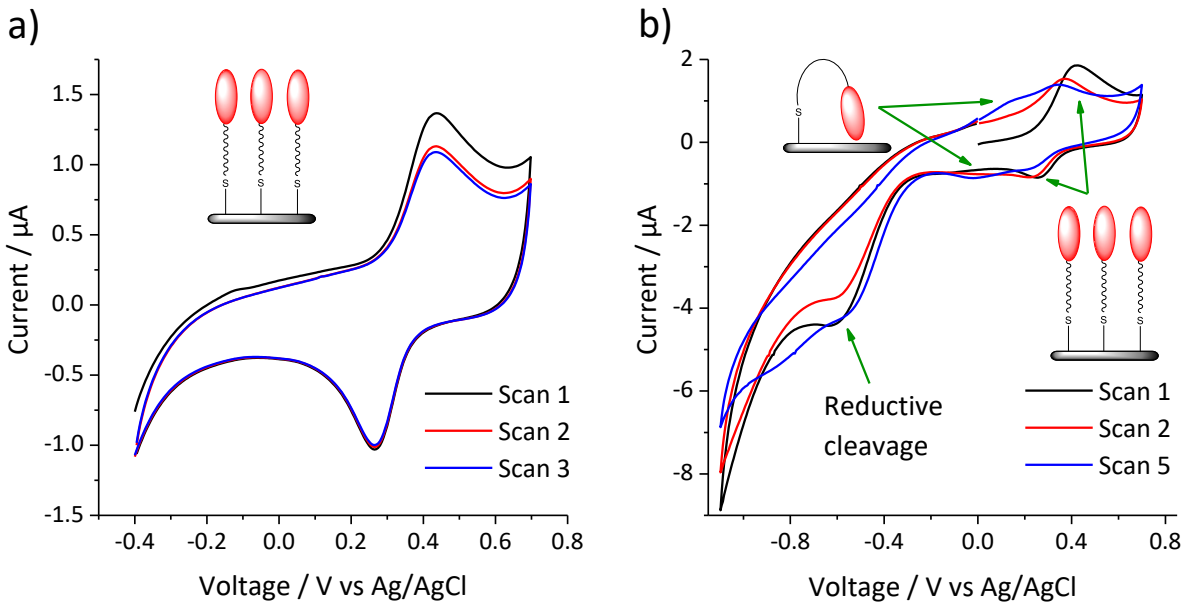

Figure 111. Cyclic voltammetry of a gold electrode covered in molecule **8** in 0.1 M NaCl between a) -0.40 and +0.70 V vs Ag/AgCl and b) -1.1 and +0.70 V vs Ag/AgCl at a scan rate of 100 mV s^{-1}.

An interesting observation in the wide potential window scans in Figure 111b is the emergence of a small amount of a redox couple at +0.1 / -0.1 V vs Ag/AgCl in scan 5. The smaller separation between the oxidative and reductive peak potentials of this new signal is interpreted as indicating that the catechol unit is closer to the electrode surface and therefore undergoing easier electron transfer. This may indicate that either the chemically cleaved rSAM is interacting with the surface or the remaining rSAMs are bending over; this is feasible given that C_{11} is a long and flexible alkyl chain. "Lying down" modes have been previously reported for gold thiol SAMs when reduced surface coverage has been obtained (Figure 112).[324]

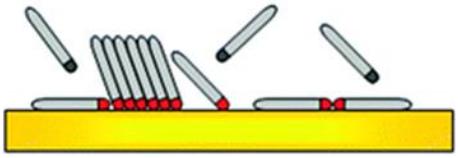

Figure 112. Illustration of "lying-down" mode next to a nucleus of "standing-up" mode. Reproduced with permission from reference 324. Copyright Royal Society of Chemistry, 2010.

Molecule **9** was designed and synthesised as an attempt to generate a molecule with a reduced distance between the electrode surface and the catechol unit relative to molecule **8**. Following self-assembly for 18 hours, cyclic voltammetry (Figure 113b, "0 ms") showed that a surface coverage of 322 pmol cm^{-2} was obtained using the same peak extraction methodology as above. The peak separation between the catechol reduction and oxidation peaks was 0.21 V. Therefore, it is surmised that a similar SAM structure has been formed by both molecules **8** and **9**. The reductive cleavage of molecule **9** was probed using an alternative electrochemical methodology. Sequential chronoamperometry voltage pulses at -1.1 V vs Ag/AgCl were employed instead of cyclic voltammetry to reduce the Au-S bond (Figure 113a). Following initial cyclic voltammetry to determine the surface coverage of the SAM *via* the catechol motif, a short reductive pulse of 100 ms at -1.1 V vs Ag/AgCl was performed before another CV was recorded to observe the change in surface coverage. This sequence of cleavage and analysis was repeated to include 4×100 ms pulses, 4×200 ms pulses and a 30 s pulse. Cyclic voltammograms recording the catechol motif in molecule **9** between voltage pulses are shown in Figure 113b-d as a function of cumulative pulse time. Interestingly, no "bent" or "lying-down" modes were observed with molecule **9**.

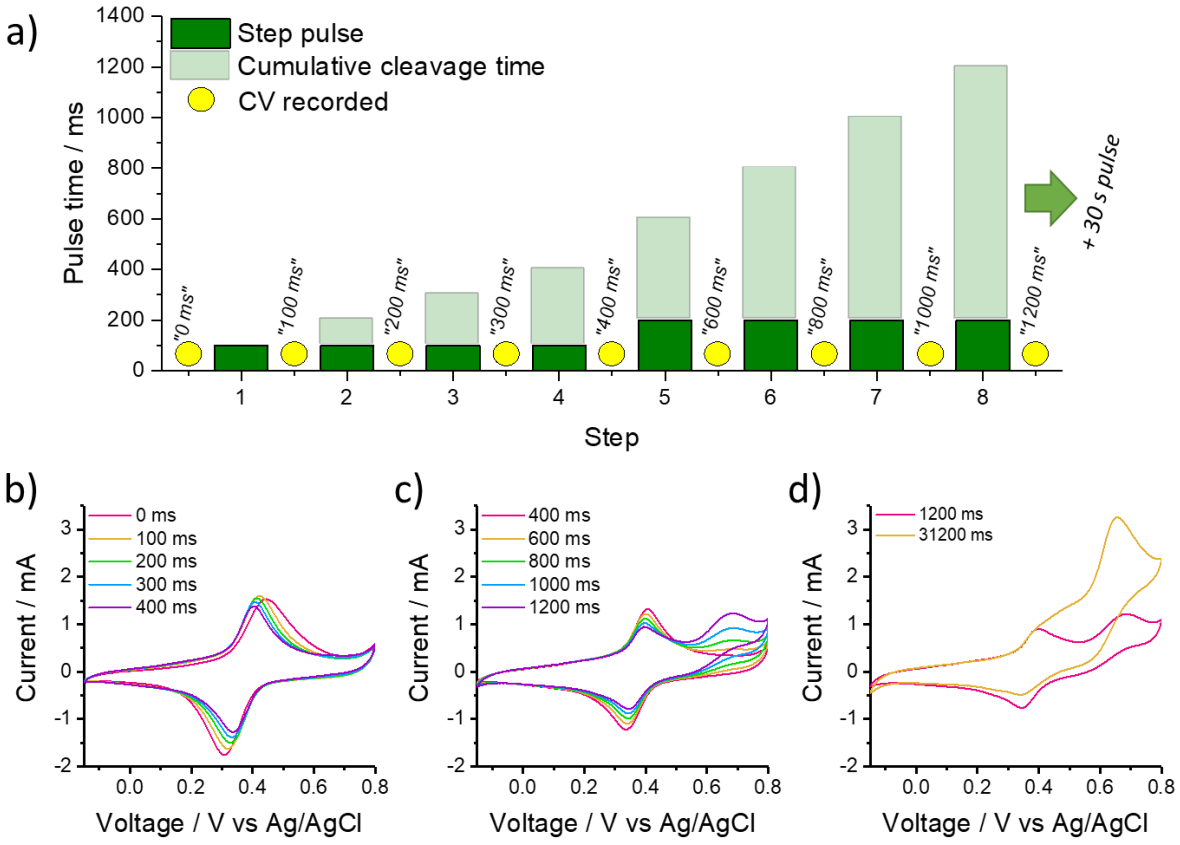

Figure 113. Partial reductive cleavage of a gold electrode covered in molecule **9** in 0.1 M NaCl using sequential voltage pulses of -1.1 V vs Ag/AgCl (a). Cyclic voltammograms of the catechol motif in molecule **9** as a function of cumulative reductive cleavage time (b-d). Voltammograms shown are the third scan recorded at a scan rate of 100 mV s^{-1}.

It is clearly observed that the redox signals for the catechol unit are diminished with time, as expected following partial reductive cleavage of the rSAM. Further evidence that cleavage is occurring is shown by the emergence of an oxidation peak at 0.65 V vs Ag/AgCl. This peak is occasionally observed for unmodified gold electrodes, as illustrated in Figure 114, which indicates this peak is attributable to a "bare" gold surface. Literature sources further support this observation of gold oxidation peaks around 0.65 V vs Ag/AgCl.[325, 326]

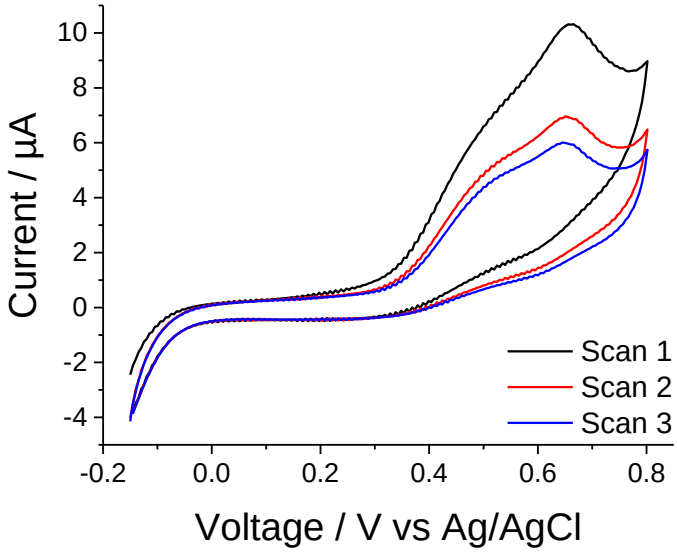

Figure 114. Cyclic voltammetry of an unmodified gold electrode in 0.1 M NaCl showing oxidation peaks between 0.4 and 0.7 V vs Ag/AgCl. Scans recorded at 100 mV s^{-1}.

Surface coverages were calculated from analysis of the reductive peaks of the voltammograms shown in Figure 113 and this data is represented graphically in Figure 115. The initial surface coverage of 322 pmol cm^{-2} was reduced sequentially to a significantly decreased final surface coverage of 57 pmol cm^{-2}. The observation that initial pulses caused the most rapid reductive cleavage can be attributed to the amorphous nature of the gold surface, where high energy miller index surfaces may exhibit a decreased Au-S bond strength.[324, 327] This supports the concurrent emergence of the gold oxidation peak at 0.65 V vs Ag/AgCl as this redox chemistry is attributed to a high-energy unmodified gold surface. Extrapolating from the curve in Figure 115, a 50% coverage of molecule **9** could be obtained with a reductive pulse length of 500 ms at -1.1 V vs Ag/AgCl. Overall, it is concluded that voltages pulses at -1.1 V vs Ag/AgCl for this rSAM system offer an easy way to selectively lower surface concentrations to sub-monolayer. It is beyond the scope of this study to examine the surface patterning arising from desorption, though this may well occur.

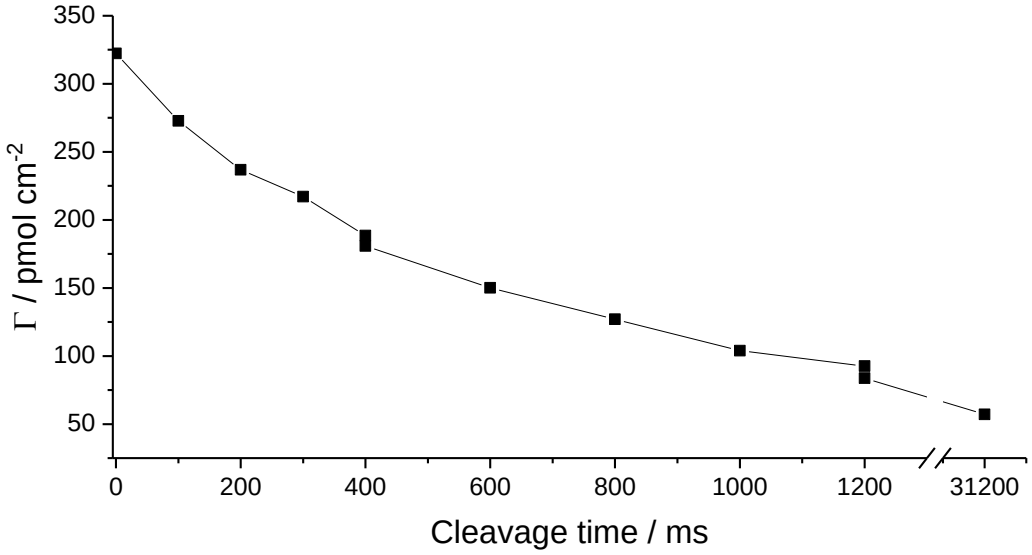

Figure 115. Surface coverages of molecule **9** on a gold electrode following reductive voltage pulses at -1.1 V vs Ag/AgCl in 0.1 M NaCl. Coverages calculated from the reductive peak (+0.3 V vs Ag/AgCl) of catechol redox.

5.3.2 Diazonium-only grafting on gold electrodes

A baseline measurement of the maximum monolayer surface coverage (Γ_{Max}) that could be obtained on a range of gold electrodes using a diazonium protection-deprotection method was made using the process outlined in section 3.3.3 for modifying copper electrodes with diazonium salts (Scheme 3). Following mechanical polishing, six gold electrodes with different geometric surface areas were electropolished by cyclic voltammetry according to section 7.2.2. The electrode surfaces were then modified by molecule **4** using *in-situ* diazotisation and electrochemical grafting by cyclic voltammetry (30 scans) to create a multilayer (Figure 116). The surface was then exposed to hydrazine treatment to achieve a near-monolayer functionalisation. Inside a nitrogen-filled glovebox, the electrodes coated with the exposed terminal amine were incubated with a 10 mM NHS-Viologen in acetonitrile solution to achieve the final “Viologen-tagged” surface.

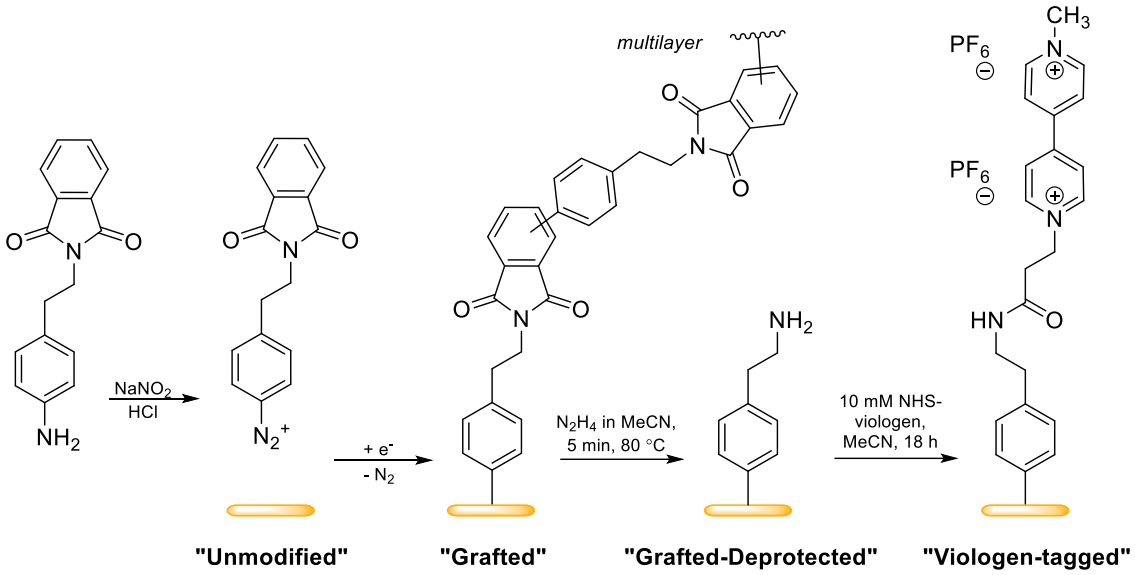

Scheme 3. Gold electrode modification steps to quantify surface coverage of molecule **4** *via* a viologen redox marker.

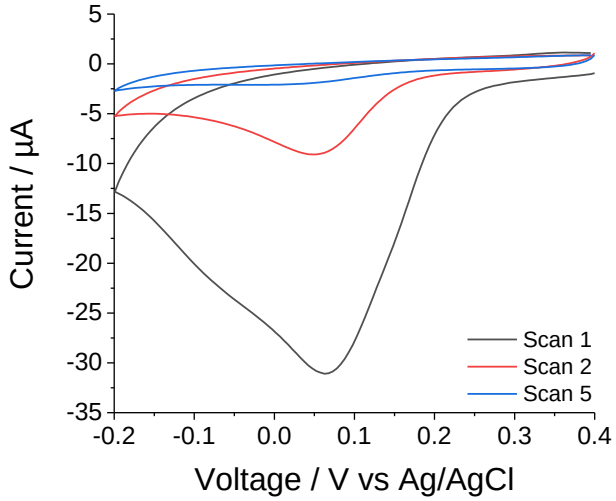

Figure 116. Example cyclic voltammograms for the electrochemical grafting of *in-situ* diazotised molecule **4** onto a gold electrode (GE8 shown). 30 scans recorded at 100 mV s^{-1}.

Electrochemical grafting of the diazonium salt derived from molecule **4** onto a gold electrode had an onset potential at approximately E_{red} = +0.2 V vs Ag/AgCl, which is similar to that measured on a glassy carbon electrode (onset +0.55 V vs Ag/AgCl in Chapter 3). Following cleavage of the multilayer with hydrazine and subsequent modification with a viologen redox tag, cyclic voltammetry was used to determine the surface coverage of the near-monolayer modification (Figure 117). This modification method has not been as extensively explored as previously performed on copper surfaces (Chapter 3), however all electrochemical evidence gathered is in keeping with the same mechanisms for modification and so it is assumed the protection-deprotection strategy on gold produces a similar monolayer structure as on copper.

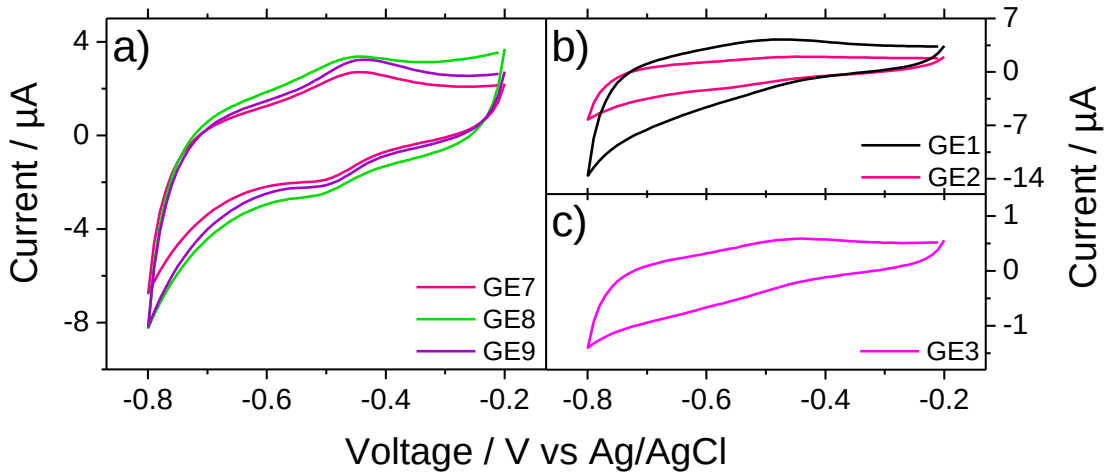

Figure 117. Cyclic voltammetry of a gold electrode in a "Viologen-tagged" surface state. Original diazonium modification achieved by cyclic voltammetry (30 scans). Voltammograms recorded in 0.1 M NaCl at a scan rate of 500 mV s^{-1}. Scan 3 shown.

Six gold electrodes were used for this diazonium grafting process, where GE1-3 were used in the experiments of the previous sections and GE7-9 were bought in as new electrodes. All six electrodes exhibited a redox signal at approximately $E_{1/2}$ = -0.49 V vs Ag/AgCl corresponding to a one electron redox transfer to the viologen moiety. Both the oxidative and reductive signals were analysed by subtracting a third order polynomial baseline and then integrating the area of the resultant Faradaic current peaks to yield surface coverages. The average surface coverage recorded for each of the six electrodes is shown in Table 14 alongside their geometric surface areas. As observed in Figure 117, the magnitude of the signal is different even in cases where the geometric surface area of the electrode is the same (GE1 and GE2). This electrode surface inhomogeneity indicates that there is a difference in ECSA between electrodes. To generate surface coverages of the viologen moiety relative to the ECSA rather than a geometric surface area, the AuO reduction signal from the final electropolishing CV (+0.9 V vs Ag/AgCl in Figure 118) was integrated and converted to the ECSA according to published literature procedure, where the charge required to reduce a perfect monolayer of AuO was assumed as 482 µC cm^{-2}.[315] The surface coverages derived are given relative to both the geometric surface area and the ECSA in Table 14.

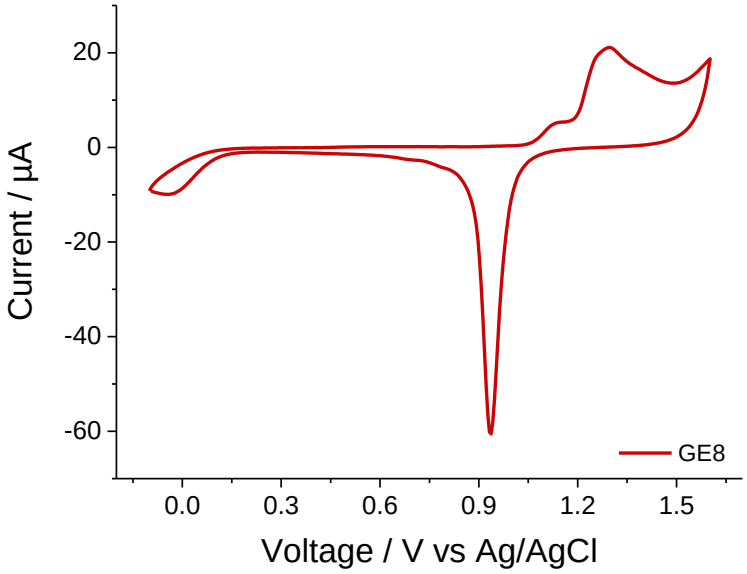

Figure 118. Final cyclic voltammetric scan (scan 50) to electropolish a gold electrode in 1 M H_2SO_4. AuO reduction observed at *ca* +0.9 V vs Ag/AgCl. Scan rate: 50 mV s^{-1}.

Table 14 indicates that utilising the ECSA instead of the geometric surface area to quantify surface coverage of viologen on an electrode is significantly beneficial in reducing the error between electrodes. The average surface coverage determined from the viologen redox signals were determined as 57 ± 35 pmol cm^{-2} relative to the geometric surface area and 30 ± 6 pmol cm^{-2} relative to the ECSA. Therefore, it is shown that surface coverages are best calculated relative to the ECSA fully quantitative analysis as the error associated with average surface coverages is significantly reduced.

Literature modification procedures that produce a monolayer on a wide range of substrates have been achieved with surface concentrations of 500-900 pmol cm^{-2}, which indicates this protection-deprotection strategy produces a sub-monolayer on gold electrodes.[251, 255] Electrode modifications using the protection-deprotection strategy used herein were originally performed by Hauquier *et al.* who performed the strategy on both glassy carbon and gold substrates, where gold substrates achieved a low surface coverage of 20 pmol cm^{-2} when functionalised with a ferrocene motif.[193] Whilst this low surface coverage was not explained, it is possible that this is due to preferential diazotisation of the protecting groups rather than gold atoms as may be inferred by the more positive onset potential of diazotisation for graphite than gold substrates as mentioned previously. Owing to the significantly more consistent surface coverages relative to the ECSA, results in the next section will be detailed only relative to the ECSA and compared with the maximum surface coverage for each electrode (Γ_{Max}).

Table 14. Surface areas and coverages of gold electrodes in the "viologen-modified" state. Γ_{Max} is the surface coverage relative to the ECSA.

Electrode	Geometric SA / cm²	Γ_{geom} / pmol cm^{-2}	AuO integral / V µA	ECSA / cm²	Γ_{Max} / pmol cm^{-2}
GE1	0.0314	125	5.87	0.1506	32
GE2	0.0314	36	1.50	0.0384	36
GE3	0.0079	82	0.81	0.0208	38
GE7	0.0625	34	4.14	0.1060	24
GE8	0.0625	35	4.02	0.1031	26
GE9	0.0625	33	4.02	0.1031	25

The surface coverages obtained using 30 cyclic voltammetric scans for electrochemical grafting as in Table 14 are an indicator of the maximum attainable surface coverage (Γ_{Max}) using this method of diazonium modification on gold electrodes. Shul *et al*. demonstrated that potentiostatic chronoamperometry could be used instead of cyclic voltammetry to perform diazonium electro-grafting on electrode materials containing copper, gold and/or glassy carbon.[259] Whilst the chronoamperometry deposition voltage varied according to the electrode substrate, a deposition time of 4 minutes was ideal to create a thick multilayer ($\Gamma > 10^{-9}$ mol cm^{-2}). For the sub-monolayer methodology being developed here, a chronoamperometry pulse would be more practical than cyclic voltammetry as the deposition time is more easily controlled and so is explored below relative to Γ_{Max} as obtained by a large number of cyclic voltammetry scans.

Given that a sub-monolayer is the end target of the spacing strategy outlined here, a short 500 ms reductive voltage pulse at -1.1 V vs Ag/AgCl was used to electro-graft solution-based diazonium species (from *in-situ* diazotisation of molecule **4**) onto gold electrodes. Following deprotection in hydrazine as above, the resulting surface was incubated in a 10 mM NHS-viologen / acetonitrile solution overnight inside a nitrogen-filled glovebox. After cleaning, cyclic voltammetry was performed over the voltage window for viologen redox processes (Figure 119), where these results can be directly compared with those in Figure 117.

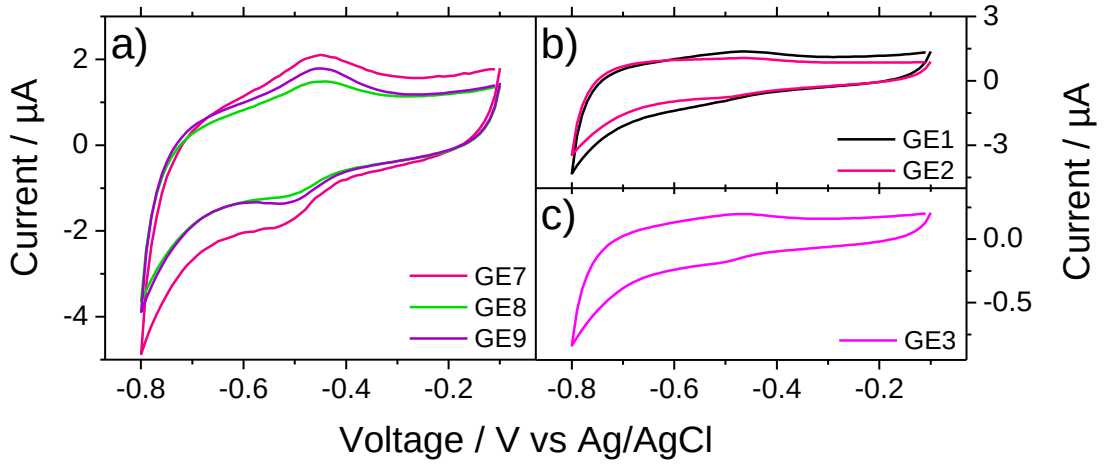

Figure 119. Cyclic voltammetry of gold electrodes in a "Viologen-tagged" surface state. Diazonium modification achieved by a 500 ms voltage pulse at -1.1 V vs Ag/AgCl. Voltammograms recorded in 0.1 M NaCl at a 500 mV s^{-1}. Scan 3 shown.

Comparing Figure 117 and Figure 119 for the two electro-grafting methods qualitatively indicates that a similar outcome has been achieved using chronoamperometry diazonium electro-grafting instead of cyclic voltammetry; the redox peaks are present at the same voltages and are of a similar current magnitude. As demonstrated with the electro-grafting by cyclic voltammetry, the surface coverages for surfaces prepared with a voltage pulse (reported as $\Gamma_{Control}$) were extracted relative to the ECSA and are shown in Table 15. The average surface coverage using voltage pulse grafting was 19 ± 9 pmol cm^{-2}, a drop of approximately 11 pmol cm^{-2} relative to the Γ_{Max} by cyclic voltammetry. The overall drop and larger distribution of surface coverages upon switching to a pulsed electrochemical graft is expected owing to the shorter electro-grafting time used in the pulse-grafting methodology. A shorter electro-grafting period is subjected to more variation in local concentrations of diazonium salts and mass transport limitations than for the longer electro-graft by cyclic voltammetry.[328, 329]

Table 15. Surface areas and coverages of gold electrodes in the "viologen-modified" state. Electrodes modified using a 500 ms voltage pulse at -1.1 V vs Ag/AgCl. ECSA given for pulse experiment only.

Electrode	ECSA / cm^2	$\Gamma_{Control}$ / pmol cm^{-2}	Γ_{Max} / pmol cm^{-2} (Table 14)	$\Delta\Gamma$ / %
GE1	0.0358	37	32	113.1
GE2	0.0422	9	36	25.2
GE3	0.0081	15	38	40.4
GE7	0.0971	25	24	100.9
GE8	0.0938	15	26	58.4
GE9	0.1045	15	25	62.5

5.3.3 “Spacing strategy” for sub-monolayer coverages

Electrochemical evidence in the previous sections has demonstrated that it is possible to form and electrochemically cleave a self-assembled monolayer from a gold electrode. Using a voltage pulse at -1.1 V vs Ag/AgCl for 500 ms, it was estimated that approximately half of the surface coverage of molecule **9** on a gold electrode can be reductively cleaved. It has also been shown that reductive electrochemical grafting of diazonium salts can take place on gold electrodes by both cyclic voltammetry and voltage pulses at -1.1 V vs Ag/AgCl. A strategy is outlined below to achieve a lower surface concentration of diazonium salts by employing simultaneous reductive cleavage and diazonium grafting steps. The process is followed by both the electrochemical signal of the catechol unit and the final viologen modification for calculations of the final surface coverage.

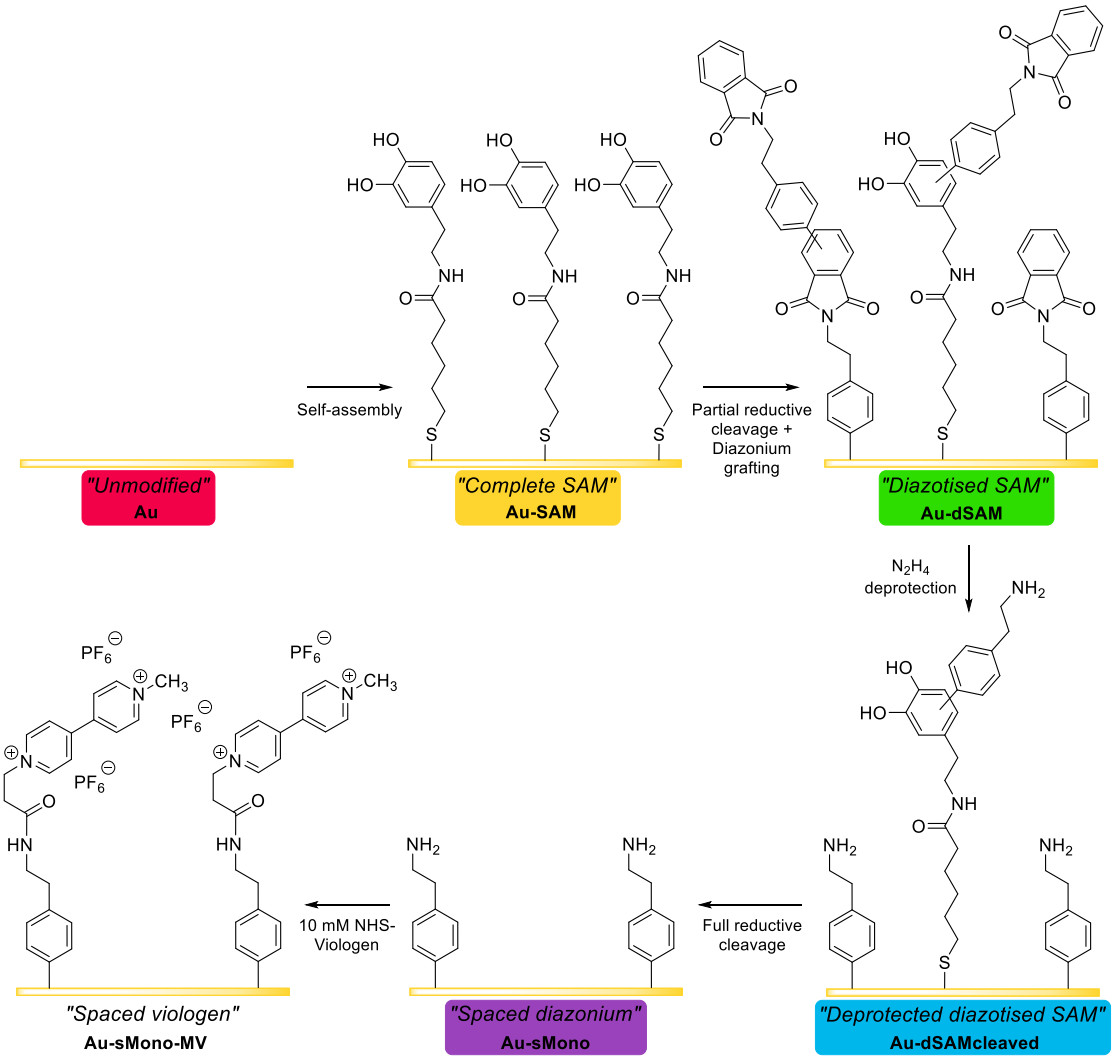

Scheme 4. Spacing strategy for reduced surface coverage of diazonium salts on a gold electrode. Cyclic voltammetry for each stage with a coloured label shown in Figure 120.

The progress of the strategy was followed by cyclic voltammetry of the catechol unit within molecule **9**. The technique was performed on five gold electrodes, where Figure 120 shows data from one particular electrode. As previously observed, a strong catechol redox couple at $E_{1/2}$ = 0.31 V vs Ag/AgCl indicates the successful formation of a rSAM monolayer after self-assembly had been performed for 18 h. A reductive pulse at -1.1 V vs Ag/AgCl was then applied to the Au-SAM to yield the Au-dSAM surface state which exhibited significantly smaller catechol redox peaks. Following this step, the electrode was treated with hydrazine in acetonitrile at 80 °C for 10 minutes which removed the catechol signal. As hydrazine is a well-known reducing agent,[330] this cleaved the protecting groups on the electro-grafted diazonium species as well as reductively cleaved most of the remaining Au-S bonds in a further reduction step. The Au-dSAMcleaved electrode surface was finally exposed to a longer voltage pulse at -1.1 V vs Ag/AgCl for 60 s to achieve the final Au-sMono surface state.

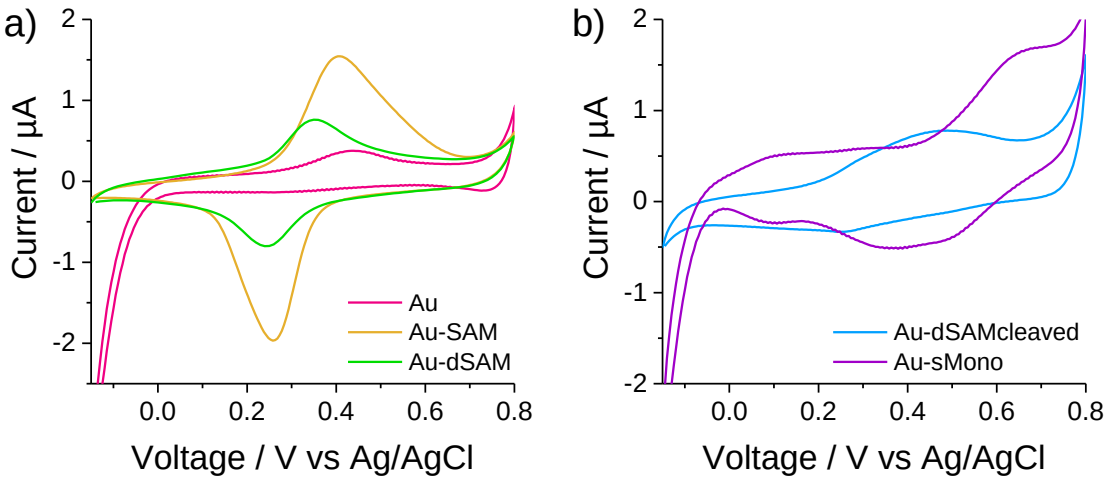

Figure 120. Cyclic voltammetry following catechol redox signals throughout a spacing strategy on a gold electrode to produce a sub-monolayer of diazonium modifications derived from molecule **4**. Scan 3 shown, recorded at 100 mV s^{-1}. The stages of the spacing strategy are mirrored by the coloured labels in Scheme 4.

The surface coverage was determined relative to the ECSA as described previously and was used to follow the degradation of the catechol signal throughout the spacing strategy. Table 16 indicates the geometric and electrochemical surface areas alongside the surface coverages for five gold electrodes for the Au-SAM and Au-dSAM surface states, which were the only surfaces to exhibit a catechol redox signal. Importantly, the simultaneous grafting and reductive cleavage pulse was performed for various lengths of time to correlate with the SAM cleavage studies (Figure 115). A rough correlation is observed upon increasing the reductive pulse length in which a short pulse of 500 ms yields approximately a 50% cleavage of Au-S moieties. Longer pulse lengths show a similar

drop thereafter which correlates with rSAM cleavage studies without the presence of solution-based diazonium salts.

Table 16. Electrode surface areas and coverages determined by catechol redox signals throughout the modification of gold electrodes with a spacing strategy.

Electrode	Pulse length / ms	Geometric SA / cm^2	ECSA / cm^2	$\Gamma_{Au\text{-}SAM}$ / pmol cm^{-2}	$\Gamma_{Au\text{-}dSAM}$ / pmol cm^{-2}	$\Delta\Gamma$ / %	$\Gamma_{Au\text{-}sMono\text{-}MV}$ / pmol cm^{-2}
GE1	500	0.0314	0.0375	483	275	56.9	8
GE2	500	0.0314	0.0583	232	95	40.7	22
GE3	2000	0.0079	0.0246	149	57	38.1	17
GE4	2000	0.0625	0.2085	164	48	29.4	60
GE5	20000	0.0625	0.1870	89	14	15.6	17

Following the conversion of gold electrodes GE1-5 above to the Au-sMono-MV surface state, the final surface coverage could be calculated in a similar way to Hauquier *et al.* as used in section 5.3.2 where values are shown also in Table 16.[193] There does not appear to be a specific correlation between pulse length and the final viologen surface concentration which is unexpected as an increased grafting time should provide more viologen binding sites. However, this may be due to experimental error where electrodes GE1-5 are different sizes and ages. Equally it is possible that the relationship is not obvious owing to the significant difference in the maximum achievable surface coverages by rSAM or diazonium salt modifications.

A pulse length of 500 ms (-1.1 V vs Ag/AgCl) was selected for repeat experiments as the short pulse appeared to cleave half of the rSAM layer. The spacing strategy was performed on the six gold electrodes used in section 5.3.2. To minimise experimental artefacts, no cyclic voltammetry was performed on the electrode to follow the progress of the catechol unit. CVs were only recorded for the final surface state, Au-sMono-MV. An example voltammogram is shown in Figure 121 (green, “Spacing strategy”) alongside CVs recorded for diazonium modified surfaces produced without a spacing strategy. The voltammograms scanning for viologen moieties are shown from surfaces where diazonium modifications had been induced without a spacing strategy using multiple CV scans (purple, “Full graft by CV”) and a 500 ms grafting pulse at -1.1 V vs Ag/AgCl (red, “Pulse graft”).

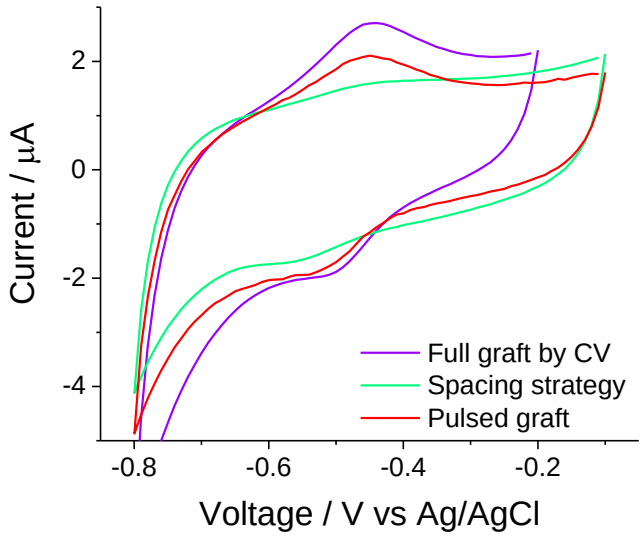

Figure 121. Cyclic voltammetry of viologen redox signals for viologen moieties coupled to diazonium-derived moieties from molecule **4** on a gold electrode. Electrochemical grafting achieved *via* different strategies including a full graft by CV (CV Grafting, no spacing strategy), spacing strategy (500 ms pulse grafting, with spacing strategy) and pulsed grafting (500 ms pulse grafting, no spacing strategy). Scan 3 shown, recorded at 100 mV s^{-1}.

Average surface coverages were extracted relative to the ECSA for comparison of diazonium modification using a strategies to either maximise grafting by cyclic voltammetry (30 scans, "Γ_{Max}"), reduce coverage by using a spacing strategy and a control experiment for pulsed grafting (500 ms, "$\Gamma_{Control}$") of molecule **4** following *in-situ* diazotisation. Table 17 and Figure 122 show the obtained surface coverages for six gold electrodes. Employing the spacing strategy consistently lowers the final diazonium surface coverage ($\Gamma_{Spacing}$ = 9.0 ± 2.5 pmol cm^{-2}) on any gold electrode to 29.5 ± 4.5% of the maximum achievable surface coverage ($\Delta\Gamma_{Max}$). The precision associated with the final change in coverages upon using the spacing strategy indicates that the strategy is both successful and reliable.

Table 17. Electrode surface coverages determined by viologen redox signals for gold electrodes modified by different grafting strategies. % changes are $\Gamma_{Spacing}$ relative to Γ_{Max} and $\Gamma_{Control}$.

Electrode	Γ_{Max} / pmol cm^{-2}	$\Gamma_{Control}$ / pmol cm^{-2}	$\Gamma_{Spacing}$ / pmol cm^{-2}	$\Delta\Gamma_{Max}$ / %	$\Delta\Gamma_{Control}$ / %
GE1	32	37	12	37.9	33.5
GE2	36	9	9	25.5	101.1
GE3	38	15	12	32.2	79.6
GE7	24	25	6	25.9	25.6
GE8	26	15	8	30.1	51.6
GE9	25	15	6	25.4	40.6

The surface coverage obtained through electrochemical grafting with a 500 ms reductive pulse, $\Gamma_{Control}$, was 19.4 ± 8.9 pmol cm^{-2}, a lower coverage than was obtained with cyclic voltammetry

grafting (Γ_{Max} = 30.3 ± 5.6 pmol cm^{-2}). Electrochemically grafting by using a 500 ms reductive pulse is compared with and without the spacing strategy by $\Delta\Gamma_{Control}$. $\Delta\Gamma_{Control}$ indicates a drop in surface coverage by 55.3 ± 26.6% upon introducing the spacing strategy. This estimate correlates well with rSAM reductive cleavage studies observed *via* a catechol motif.

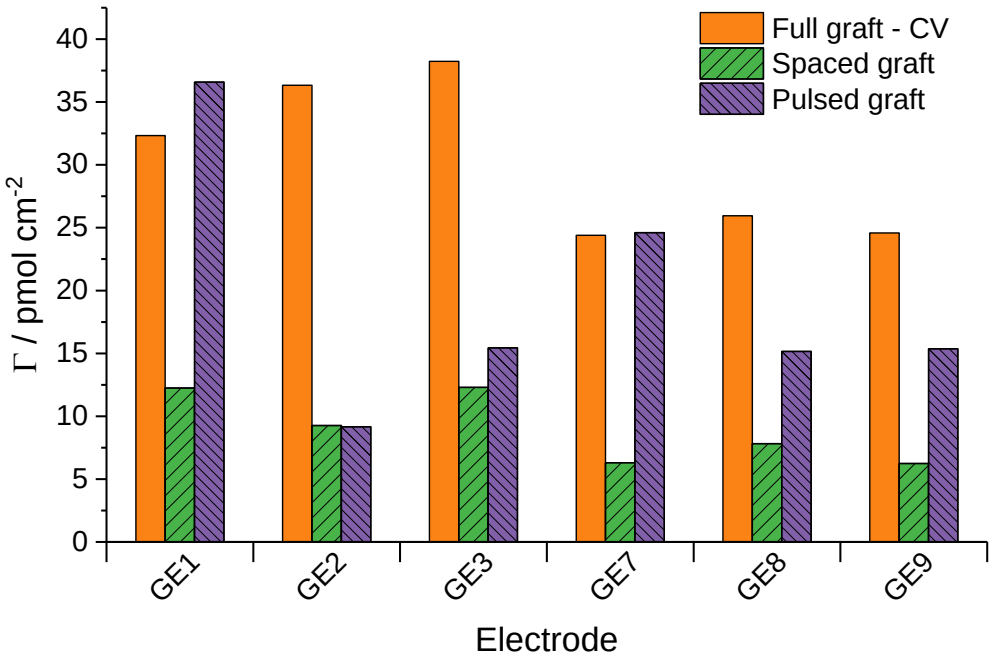

Figure 122. Electrode surface coverages determined by viologen redox signals for gold electrodes modified by various diazonium grafting strategies.

5.4 Conclusions

A reliable "spacing strategy" for lowering surface coverages of diazonium modification has been achieved, where diazonium surface coverages were followed by attaching a viologen redox tag to electrode-bound amine termini. By utilising simultaneous and complimentary electrochemical grafting of diazonium species and partial reductive cleavage of rSAM species, approximately 30% ($\Gamma_{Spacing}$ = 9.0 ± 2.5 pmol cm^{-2}) of the surface coverage was achieved relative to a diazonium-only modification method (Γ_{Max} = 30.3 ± 5.6 pmol cm^{-2}). This was achieved by using a simultaneous grafting-cleavage voltage pulse at -1.1 V vs Ag/AgCl for 500 ms.

rSAM cleavage studies using molecule **9** with increasing time at -1.1 V vs Ag/AgCl indicated that 500 ms was sufficient to remove approximately 50% of the rSAM. Combined with the simultaneous electro-grafting, a 50% cleavage rate correlates well with a reliable 30% diazonium grafting rate where some kinetic inhibitions may exist, such as mass transport. A control experiment of diazonium-only grafting for 500 ms at -1.1 V vs Ag/AgCl had a higher surface coverage than with the spacing strategy ($\Gamma_{Control}$ = 19 ± 9 pmol cm^{-2}), indicating the success of the strategy. From these preliminary studies, it appears that simply shortening the length of time for electrochemical grafting can give a wide distribution of surface coverages owing to mass-transport limitations. This spacing strategy appears to be the first of its kind for achieving sub-monolayer concentrations in a consistent and controllable manner that is significantly more reliable than simply reducing the amount of electro-grafting. Future studies may target different times for the voltage pulse to control surface coverage to a consistent degree.

This work has been performed with the target of creating a metal surface modified by diazonium species at a sub-monolayer concentration. Should this method be one day applied to a copper electrode surface, many homogeneous-heterogeneous hybrid electrocatalysts may be synthesised where diazonium modifications provide ligand-type interactions with catalytic reaction intermediates on a metal surface. This method should be applicable to a copper electrode owing to the success of the work in Chapter 3 and Chapter 4 and previous literature synthesis of Cu-SAM surfaces.[195]

Chapter 6. Conclusions and perspectives

6.1 Capturing CO_2 *via* electrochemical mineralisation

This thesis develops on initial work performed by Dr Katie J. Lamb in exploring a novel electrochemical CCS method. I show that waste aluminium or iron metal can be used as a sacrificial oxidant to bind to solution-phase CO_2 as a carbonate species (formed *via* the equilibrium $CO_2 \rightleftharpoons H_2CO_3 \rightleftharpoons H^+ + HCO_3^-$). A second, redox inactive, graphite anode was used to further disturb this bulk equilibrium by concentrating HCO_3^- ions within the electric double layer surrounding the graphite, as observed by EIS. This effect is known as supercapacitive swing adsorption and may be useful for enhancing the dissolved CO_2 concentration within an electrolyte for both CCS and CCU applications.[220, 221] Countered by a cathode capable of performing HER, the "standard cell" design has an energy requirement of 247 kJ mol_{CO2}^{-1}. Whilst this is not enough to mitigate emissions from a coal-fired gas station, it would be suitable as a CCS technology for natural gas power stations (428 kJ mol_{CO2}^{-1}).[218] Should this technique be used on an industrial scale using all non-recycled aluminium and steel, over 900 million tonnes of CO_2 could be captured each year.

An alternative "adjustable" cell design was produced that revealed that this technology could suffer from unnecessary overpotentials. By modifying the available anode surface areas, it was shown that a maximum anodic current density of 0.6 mA cm^{-2} could be applied before the kinetic overpotential was dramatically increased along with the total power used. This technique also produced hydrogen gas at the cathode which could be used to offset the entire energy cost of the technique if the gas were separated from the effluent and combusted to power the process.

The fundamental understanding of the processes involved in the cell were initially probed using EIS, where it was revealed that the capacitance exhibited by the graphite anode changed with the applied voltage. Operation of the cell may benefit from the use of a bipotentiostat to manually apply a voltage to the graphite electrode whilst the sacrificial metal oxidised as in the current cells. There has been tentative evidence that optimising the graphite voltage in this way may increase the CO_2 dissolved in solution for capture. In a similar vein, the graphite could be exchanged for a

highly porous material (such as Starbons®) or a supercapacitive material to potentially enhance the SSA effect.

To improve the green metrics of the cell design for industrial scaling, the anodic processes could be countered by an efficient HER electrocatalyst which may result in a galvanic cell as very little overpotential is required to oxidise metals. In theory, such a cell would need no driving force and could make the technique economically viable due to the value of the hydrogen gas in the effluent. Finally, the cell could be tested for the performance at different concentrations of CO_2, in particular at relatively high concentrations (>10%)[15] to mimic large point sources of CO_2 or at atmospheric concentration (approx. 400 ppm) for a units that could lower atmospheric CO_2 levels.[9]

6.2 Utilising CO_2 by electrochemical reduction

Upgrading CO_2 to useful building block molecules such as CO, or fuel-type molecules such as ethane, is a challenge that requires CO2ER catalysts that operate with high turnover frequencies and high Faradaic efficiencies to generate a single product. A huge range of catalytic conditions has been studied in the literature and often each electrocatalyst requires the conditions to be optimised. Heterogeneous cathodes have been used for CO2ER and often produce a wide variety of products. Conversely, molecular CO2ER electrocatalysts can produce a single product but with a low TOF and are often limited to C_1-only products. Some researchers have attempted to bridge this gap by covalently anchoring molecular electrocatalysts to an electrode surface, which displayed increased TOFs, though higher-order hydrocarbons remained inaccessible due to the presence of single-atom active centres. This thesis attempted to design a new type of metal cathode that used near-monolayers of organic moieties for "ligand-like" interactions with intermediate species to bridge this gap between heterogeneous and homogenous CO2ER catalysis.

A strategy by Hauquier *et al.* for the production of a monolayer of amine-terminated species on a glassy carbon electrode *via* diazonium electrochemistry was modified to work on a copper electrode in Chapter 3.[193] EIS analysis confirmed that there was no multilayer present on the electrode surface, whilst a redox-active viologen moiety was covalently attached to any remaining amine functional group to yield approximate surface coverages of 250-350 pmol cm^{-2} which is commensurate with a near-monolayer. This was performed with a range of diazonium modifiers

that contained different lengths of terminal alkyl chains. Solid state methods of analysis such as AFM with scratching would be ideal to indicate the true depth of the monolayer functionalisation.

After experimental methods and product analysis procedures had been set-up, CO2ER was performed in Chapter 4 with the range of diazonium modified copper electrodes. Under the experimental conditions used, the primary reaction product across all electrodes was H_2 due to the HER out-competing CO2ER. When the data was analysed in close detail it is suggested that diazonium modifications containing a short alkyl chain (C_1 to C_4-amine) yielded an increase in H_2, CO and HCOOH. Studies across a voltage range indicated that C_2-amine acted as a proton shuttle to increase the overall concentration of protons within the electric double layer. Conversely, the C_{10}-amine modification seemed to inhibit HER and show increased production of HCOOH, CH_3OH and CH_4 relative to all other modified and unmodified copper surfaces; this is proposed to arise from exhibited increased hydrophobicity.

A hypothesis has been proposed to explain the role of the amine-terminated organic modifications in influencing the CO2ER product selectivity. These electrode modifications must be studied with a standardised CO2ER cell with a non-rotating working electrode to lower the influx rate of proton sources to the electrode surface and supress HER. Trends in Faradaic efficiency and turnover frequencies may then be more easily studied across a voltage range, in particular for the hydrophobic C_{10}-amine modification. To mimic experiments routinely performed with molecular electrocatalysts, the amine functional group could be replaced with an alkyl group to verify the importance of the amine as a proton shuttle. Should these verify the amine is significant, a secondary or tertiary amine may be used to increase the amine basicity, an effect that has proven useful in molecular electrocatalysts.[152, 281]

Chapter 5 explores a novel surface modification strategy to achieve a sub-monolayer coverage on metal electrodes that could be used to synthesise a new family of CO2ER cathodes. A redox-tagged SAM was self-assembled onto a gold electrode before being partially desorbed by reductive cleavage. If the electrochemical reductive cleavage step is performed in the presence of a diazonium salt, then the electro-grafting can occur in the pinholes generated by desorption. The surface can be further cleaved with hydrazine and electrochemically desorbed to reveal a sub-monolayer of diazonium-derived moieties. This work is an initial exploration using only electrochemical evidence, however the results are extremely promising in the pursuit of creating

electrode surfaces with a range of surface sub-monolayer concentrations that can be controlled by different reductive pulse lengths. Solid state methods of analysis for characterisation of the sub-monolayer surfaces such as AFM, high-resolution transmission electron microscopy, XPS and QCM would well-characterise any surface modifications generated by the “spacing strategy”. This analysis would better reveal changes in surface concentrations as well as the depth and type of modification. This may reveal the presence of surface structures such as islands occurring from preferential desorption or adsorption. The voltages used in this strategy were designed to avoid oxidation when functionalising readily-oxidisable metals such as copper, thus the method should be applicable to copper or other metal electrodes for application in CO2ER and other reductive electrolysis reactions.

Chapter 7. Experimental Methods

7.1 Electrochemical carbon capture and mineralisation (Chapter 2)

7.1.1 CO_2 mineralisation by chronopotentiometry using the "standard" cell

To prepare for cell electrolysis, the stirred cell was filled with 1 M NaCl (60 mL) electrolyte except for the aluminium-only anode tests (180 mL). A pH probe was calibrated prior to each experiment using four reference buffer solutions from Fisher-Scientific, pH 4.0 (potassium acid phthalate), 7.0 (phosphate), 9.2 (borate) and 10.0 (potassium carbonate) and inserted into the cell. Where "waste" aluminium foil was used as the sacrificial metal, approximately 3-4 g of aluminium foil was wrapped round the graphite liner. The aluminium block was supplied by Alaco (Grade 6082, Temper T6), with an aluminium content of 95–98%. "Iron disks" were produced in-house from mild steel (>98 % Fe, 70 × 5 mm disk). To facilitate solution access to the sacrificial metal portion of the anode, eight holes of diameter 3.2 mm were drilled through the base of the graphite liner. Gas mass flow controllers (Aalborg, GC717, 0-10 mL min^{-1} and 0-100 mL min^{-1}) were used to control the carbon dioxide (BOC, >99%) and N_2 (BOC, >99%) gas inflow rates, respectively. A Quantek CO_2 analyser, model 906 monitored the outlet gas. Once the cell was assembled, the cell was purged with 5% CO_2 at 14 mL min^{-1} for 7 hours whilst operating at open circuit potential.

A VoltaLab 50 potentiostat with VoltaMaster software was used to perform chronopotentiometry with a platinum (35 × 1.5 mm), nickel (35 × 1 mm) or iron (35 × 1 mm) cathode as the working electrode relative to an Ag/AgCl (3 M KCl) reference electrode (for calibration to vs SHE, see section 7.1.7). Anode components were used as counter electrodes and their voltage recorded with a digital voltmeter and USB data logging (PT-4000ZC, Digitec) with respect to the Ag/AgCl reference.

7.1.2 CO_2 mineralisation by chronopotentiometry using the "adjustable" cell

Electrodes held in place by the cell lid and glass liners (see section 2.5, Appendix 1) which ensured that both an electrolyte volume of 600 or 250 mL would result in an anode electrode submersion depth of 30 mm. The aluminium anode components (plates measuring height 50 mm by width 30 or 15 mm by depth 2 mm) were cut in-house from a sheet purchased from Alaco (Grade 6082, Temper T6), with an aluminium content of 95-98%. The graphite used to make anode electrodes was purchased from OLMEC, grade MCCA, and was likewise cut in-house to plates of dimension height 50 mm by width 30 or 15 mm by depth 2 mm. A pH probe was also introduced to the cell as in the previous section.

Electrolyte solution of 1 M $NaCl_{(aq)}$ (250 or 600 mL) was added to the electrochemical cell and charged with a 2 cm stirrer bar. The cell was then placed under a 5% CO_2/95% N_2 atmosphere at a flow rate of 50 mL min^{-1} and room temperature for an equilibration time of 4 or 7 h, with a solution stir rate of 500 rpm. Following this equilibration stage, a constant-current (5-40 mA) was applied for 18 or 24 h to a platinum (35 × 1.5 mm) cathode using a Voltalab 50 potentiostat with VoltaMaster software. After electrolysis, the cell was held at open circuit potential for a further 2 h or 7 h.

7.1.3 Titration analysis

Using the method outlined in Vogel's titration method,[233] an aliquot (4 mL) of filtered electrolyte solution was taken for analysis. 0.01 M $NaOH_{(aq)}$ (16 mL) was added to the sample solution. Added to this was three drops of phenolphthalein and 10_{wt}% $BaCl_{2\,(aq)}$ (15 mL). This was titrated against 0.01 M $HCl_{(aq)}$ until the solution turned from pink to colourless, at which point the concentration of bicarbonate could be determined.

7.1.4 TGA-IR

To obtain solid samples for analysis, post-electrochemistry the electrolyte was filtered and the precipitate dried *in vacuo*. To quantify the carbon-content in such a dried sample, an aliquot (*ca* 40 mg) was placed into a pre-calcined alumina cup inserted into Netzsch 409 STA for thermogravimetric analysis. The atmosphere was placed under vacuum and then purged with nitrogen for three repetitions. The sample was then purged under a continuous nitrogen flow of 100 mL min^{-1} for 10 minutes. This nitrogen flow was continued throughout the run. The sample was then heated from 25 °C to either 500 or 1300 °C at a ramp rate of 10 °C min^{-1}. Throughout this experiment the exit gas was transferred through a 200 °C transfer pipe to a Bruker Equinox 55 FT-IR instrument for gas analysis. IR spectra were recorded every 34 seconds in the range 4000 – 500 cm^{-1} with a resolution of 4 cm^{-1} with 64 scans per spectrum. Spectra were taken relative to a nitrogen background. To relate the integration of the CO_2 IR peak area to the amount of CO_2 obtained, a calibration curve using $CaCO_3$ (Sigma Aldrich, ≥ 99%) was obtained (Figure 123). This led to a conversion factor of 0.059 $g_{(mass\ lost)}$ per unit peak area which was used to obtain CO_2 capture values in moles.

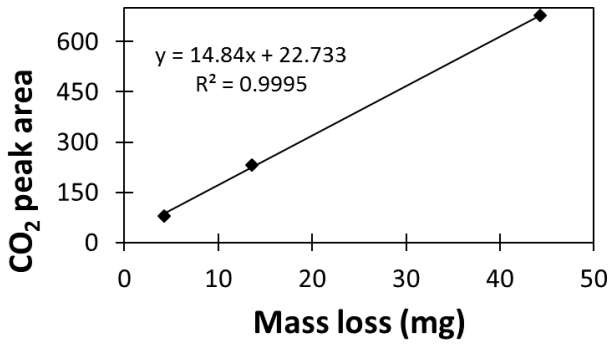

Figure 123. Calibration curve for TGA-IR CO_2 peak intensities relative to mass loss upon heating of a $CaCO_3$ sample.

7.1.5 pXRD

Powder XRD was performed using a Bruker D8 powder diffractometer equipped with a Cu source (κ-α1, 1.54 Å; κ-β, 1.39 Å). A PSD Lynxeye detector in a Bragg-Brentano θ-2θ geometry was used and spectra analysed using EVA software from Bruker. Samples were ground to a fine powder and analysed over 2θ = 5-90°, with a 0.0066° step size averaged over 0.1 s per point for an acquisition time of 23 minutes. Samples were analysed at room temperature. Generator voltage and current were 40 kV and 40 mA respectively. Reference data was obtained from the ICSD online database.[331]

7.1.6 ICP-MS

Identification of sodium, aluminium and iron was performed *via* ICP-MS. Samples were digested in 5 mL of nitric acid (TraceSELECT® solvent grade, Sigma-Aldrich) and then heated to 110 °C for three hours. After leaving to cool, the sample was dissolved in 100 mL of ultrapure water and diluted further if required. The samples were analysed with an Agilent 7700x ICP-MS spectrometer, using nickel sample and skimmer cones. The analysis was run under helium. For sampling, the sample was taken up for 60 seconds, stabilised for 40 seconds, and washed for 60 seconds (with 5% HCl for 30 seconds, and 2% HNO_3 for 30 seconds). Each sample was run three times and the mean value of sodium, aluminium and iron in ppm or ppb was obtained.

7.1.7 Reference electrode calibrations

To determine the conversion factor between the Ag/AgCl reference electrode and the standard hydrogen electrode (SHE), cyclic voltammetry was conducted with 10 mM ferricyanide (K_3FeCN_6) in 0.1 M pH 7 phosphate buffer, the Ag/AgCl reference electrode, a glassy carbon working electrode (BASi) and a platinum counter electrode (wire). The $E_{1/2}$ value of the ferri/ferrocyanide redox couple was compared to literature values to yield a conversion factor of: V vs SHE = V vs Ag/AgCl + 0.194 V.[332] Analysis was performed with an EmStat^3 potentiostat (PalmSens) and PSTrace4 software (PalmSens).

7.1.8 EIS analysis of the graphite liner in a C|Pt cell

The graphite cup in section 2.5 (Appendix 1) was used as the working electrode and a platinum wire counter electrode were used relative to an Ag/AgCl (3 M KCl) reference electrode. The system was pre-purged with nitrogen gas for 2 hours and was held under a static nitrogen atmosphere for measurement. EIS methods were optimised to the following: frequency range 1 Hz – 100 kHz, 6 data points per decade, voltage oscillation amplitude (V_a) = 20 mV. Measurements were recorded at DC working electrode voltages between 0.00 and -0.80 V vs Ag/AgCl at 50 mV intervals. An EC-Lab SP150 and EC-Lab software were used to analyse the EIS spectra.

7.2 Electrode modification procedures (Chapters 3-5)

Unless otherwise stated, all electrochemistry herein was performed with an Ag/AgCl (3 M KCl) reference electrode (BASi) placed within a Luggin capillary containing 3 M NaCl - referred to as an Ag/AgCl reference electrode. All electrochemistry was countered by platinum electrodes (in-house). A Palmsens4 potentiostat was used to perform all electrochemical measurements in Chapters 3-5. This section describes the preparation of electrodes and the subsequent methods of modification used throughout Chapters 3-5.

7.2.1 Electrode preparation

All working electrodes were mechanically polished using 5 µm, 1 µm, 0.3 µm and 0.05 µm alumina particles (MetPrep) impregnated onto separate felt polishing pads (Buehler WhiteFelt). The electrodes were then thoroughly rinsed in milliQ (>13 MΩ) water for and sonicated in 3 minutes, rinsed and sonicated in acetonitrile for 2 minutes before drying in air. Following this, glassy carbon electrodes (BASi) were used directly, copper electrodes (in-house) were further reductively electropolished by cyclic voltammetry in 0.5 M $KHCO_3$ (-0.40 - -2.0 V vs Ag/AgCl, 3 scans, 100 mV s^{-1}), whilst gold electrodes were oxidatively electropolished by cyclic voltammetry in 0.5 M H_2SO_4 (-0.35 - +1.35 V vs Ag/AgCl, 50 scans, 100 mV s^{-1}).

7.2.2 Electrode modifications using diazonium salts

7.2.2.1 Diazonium grafting on a glassy carbon electrode via the Radical Scavenger method

All small aniline molecules containing nitro groups were converted to a diazonium salt and then grafted onto an electrode using the following procedure, where inclusion of DPPH indicated a radical scavenger had been used (method performed with and without DPPH). A 100 mM aniline stock solution was prepared by dissolving the aniline (10 µmol) in 0.1 M Bu_4NBF_4 in 1:5 water:acetonitrile (100 µL). A 400 mM $NaNO_2$ stock solution was prepared by dissolving $NaNO_2$ (27.6 mg, 400 µmol) in water (1 mL). 10 µL of both stock solutions were added to 0.1 M Bu_4NBF_4 in

1:5 water:acetonitrile (975 µL) and a further 5 µL of HCl (6 M, 30 µmol) was added. The solution was left at -20 °C for 30 minutes to produce the diazonium salt. The solution was then warmed to 0 °C and DPPH (0.8 mg, 2 eq.) added before the solution was used as the electrolyte at 0 °C in a cyclic voltammetry experiment (+0.4 - -0.4 V vs Ag/AgCl, ν = 500 mV s^{-1}, 5 scans). The electrode was then rinsed extensively with milliQ water (>13 MΩ) and acetonitrile.

7.2.2.2 Protection-deprotection strategy on glassy carbon, copper and gold electrodes

All aniline based molecules containing a phthalimide-protected primary alkyl amine were grafted onto either a glassy carbon, copper or gold electrode surface using the following procedure. A 100 mM aniline stock solution was prepared by dissolving the aniline (10 µmol) in 0.1 M Bu_4NBF_4 in 1:5 water:acetonitrile (100 µL). A 400 mM $NaNO_2$ stock solution was prepared by dissolving $NaNO_2$ (27.6 mg, 400 µmol) in water (1 mL). 10 µL of both stock solutions were added to 0.1 M Bu_4NBF_4 in 1:5 water:acetonitrile (975 µL) and a further 5 µL of HCl (6 M, 30 µmol) was added. The solution was left at -20 °C for 30 minutes to produce the diazonium salt.

For glassy carbon and gold electrodes, the solution was warmed to 0 °C in air and used as the electrolyte in a cyclic voltammetry experiment. Glassy carbon electrodes were modified by cyclic voltammetry (+0.8 - -0.5 V vs Ag/AgCl, ν = 20 mV s^{-1}, 3 scans). Gold electrodes were also modified by cyclic voltammetry (+0.4 - -0.2 V vs Ag/AgCl, ν = 100 mV s^{-1}, 30 scans). To modify copper electrodes however, the electrolyte solution was warmed to room temperature and placed under a nitrogen atmosphere. Copper electrodes were modified by cyclic voltammetry (-0.3 - -1.0 V vs Ag/AgCl, ν = 500 mV s^{-1}, 30 scans). All electrodes were then rinsed extensively with milliQ water (>13 MΩ) in air. The electrodes were subsequently deprotected with a hydrazine solution (0.155 mL in 2 mL acetonitrile) at 80 °C for 5 minutes, then rinsed extensively with milliQ water (>13 MΩ) and acetonitrile and then sonicated for 5 minutes in milliQ water (>13 MΩ).

7.2.3 Electrochemical modification of gold electrodes using a spacing strategy

Chapter 5 explores a novel "spacing strategy" for generation of a sub-monolayer *via* diazonium salt electro-grafting. Modification of gold electrodes with diazonium salts only were performed as described above in section 7.2.2.2. Procedures for modifying gold electrodes with an alkanethiol derivative and their use with a spacing strategy are outlined below.

7.2.3.1 SAM assembly on gold

After cleaning the electrode, gold or copper electrodes were placed in a 1 mM rSAM solution in ethanol under either air or nitrogen for 12 – 40 hours to produce a 'well ordered' monolayer or 0-2 hours to produce an 'irregular monolayer'.[307] Electrodes were then washed extensively with milliQ (>13 MΩ) water and then acetonitrile before drying under air or in a nitrogen atmosphere. Modified electrodes were then studied either in air for preliminary studies or in a nitrogen glove box. pH dependencies were analysed using 0.1 M pH buffered aqueous solutions that were titrated to the correct pH using either 18 M HCl or saturated NaOH. The buffer systems used are highlighted in Table 18.

Table 18. Buffer systems used for different pHs.

pH	Buffer system
2	Phosphoric acid
4	Citric acid
6	Monosodium phosphate
7	Monosodium phosphate
8	Monosodium phosphate
10	Carbonic acid
12	Disodium phosphate

7.2.3.2 Spacing strategy

A complete SAM layer was constructed on a gold electrode according to the procedures outlined above where a 1 mM solution of molecule **9** in acetonitrile was self-assembled over 18 hours. After the electrode was rinsed and sonicated in milliQ (>13 MΩ) water and then acetonitrile, the electrode was dried in air (referred to as a "wash" step). The electrode was then submerged in a diazonium electrolyte derived from molecule **4** (prepared according to the procedure in section

7.2.2.2) and subjected to a chronoamperometry voltage pulse at -1.1 V vs Ag/AgCl for 500 ms. After "washing" the electrode, the surface was treated with N_2H_4 (0.155 mL in 2 mL acetonitrile) at 80 °C for 5 minutes before being "washed" again. A chronoamperometry voltage pulse at -1.1 V vs Ag/AgCl for 30 s was used to fully reductively cleave any remaining thiol-containing molecules to reveal a surface decorated with spaced-out diazonium modifications. The electrochemical signal of the catechol unit was recorded throughout this procedure by performing cyclic voltammetry in 0.1 M NaCl (-0.2 - +0.8 V vs Ag/AgCl, v = 100 mV s^{-1}, 3 scans) after each "wash" step. Quantification of the final concentration of amine functional groups on the surface is detailed in the next section.

7.3 Surface analysis

7.3.1 Determination of surface coverage by viologen redox tagging

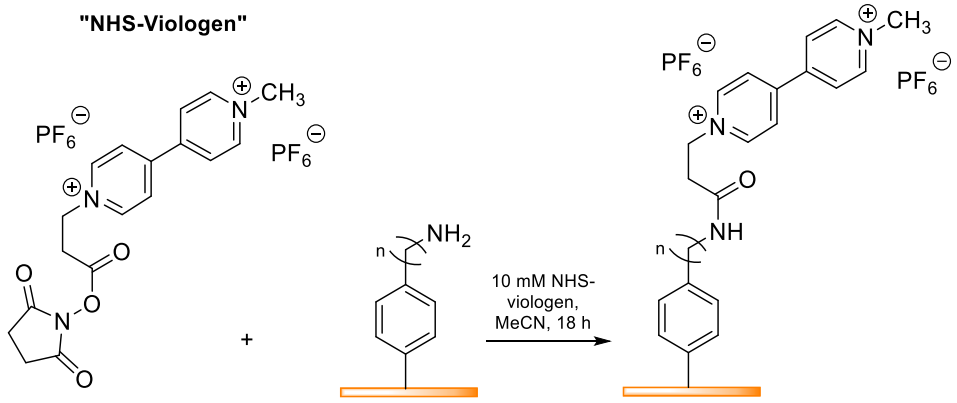

Figure 124. Covalent attachment of an NHS-activated viologen to a surface modified with C_n-amine.

Electrodes prepared using the protection-deprotection method or spacing strategy to reveal a terminal amine were submerged in a solution of 10 mM NHS-viologen (Figure 124) in MeCN for 18 hours at room temperature. This was performed under a nitrogen atmosphere for both copper and gold electrodes. The electrodes were then rinsed and sonicated for 3 minutes in MilliQ water (>13 MΩ) and acetonitrile in air. Electrodes were then dried in air and placed into a nitrogen-filled glovebox where cyclic voltammetry was performed in 0.1 M $NaCl_{(aq)}$ (-0.2 (Au) or -0.4 (Cu) - -0.8 V vs Ag/AgCl, v = 500 mV s^{-1}, 3 scans). Some of these electrodes were subject to further CVs as previously but at a range of scan rates (in order): 500, 400, 300, 200, 100 mV s^{-1}.

7.3.2 Solution-phase methyl viologen studies by cyclic voltammetry

At each stage of the grafting process in Chapter 3 copper electrodes were placed in an aqueous electrolyte of 1 mM methyl viologen dichloride + 0.1 M NaCl. CVs performed on unmodified copper electrodes ("Blank"), then following grafting as in section 3.3.3. ("Grafted") and finally after hydrazine deprotection ("Grafted-Deprotected"). CV was performed generally between -0.4 - -0.8 V vs Ag/AgCl, though never outside of -0.3 - -1.0 V vs Ag/AgCl, with a scan rate of 500 mV s^{-1} for 3 scans.

7.3.3 Solution-phase methyl viologen studies by electrochemical impedance spectroscopy

An AC voltage input was applied to modified and unmodified electrodes at -0.63 V vs Ag/AgCl in a solution of 1 mM methyl viologen dichloride in 0.1 M $NaCl_{(aq)}$ with an oscillation amplitude of 10 mV and a current range of 1 mA. A pre-equilibration time of 30 s was used before frequencies were scanned in the range 1 MHz to 0.1 Hz at 15 points per decade. All frequency cycles were recorded for a minimum of 10 s to obtain at least one full waveform. The full electrochemical set-up, excluding the potentiostat, was placed inside a custom-built faraday cage. Copper electrodes were analysed under a nitrogen atmosphere and gold electrodes under normal air. All experimental traces were routinely analysed from 100 kHz – 0.1 Hz and fitted using PSTrace 5.5 and the built-in circuit fitting program.

7.3.4 AFM of a gold substrate coated with an oxylamine substrate

A gold coated (layer thickness 1000 Å) silicon wafer from Sigma Aldrich was used as the substrate for AFM measurements. The 8 mm x 8 mm square was cleaned using acidic piranha solution (1 part 30% H_2O_2 to 3 parts concentrated H_2SO_4) until bubbling at the surface ceased. Half of the surface was then subjected to electro-grafting, then the whole square was hydrazine-treated (0.155 mL in 2 mL ethanol) at 80 °C for 5 minutes. Finally, the gold coated square was placed in neat propanal at room temperature for 30 min to facilitate oxime ligation to the oxylamine-coated area. AFM images (500 x 500 nm, 256 samples per line and a scan rate of 1.99 Hz) were collected of both the electro-

grafted and unmodified region of the electrode using a Bruker Bioscope Resolve AFM in intermittent contact mode with a Bruker RTESPA-300 AFM probe (40 N/m, 300 kHz, symmetric tip, Al reflex coating). Gwyddion freeware was used for image processing.

7.4 CO2ER electrocatalysis and product analysis

7.4.1 Electrochemical CO_2 Reduction

All CO_2 reduction electrochemistry was carried out in a glove box (designed and manufactured in-house) with a N_2 atmosphere, O_2 < 40 ppm. The electrochemical CO_2 reduction reaction was performed using either a diazonium-modified or unmodified (referred to as "blank") copper rotating disk electrode as the cathode (geometric diameter of 5 mm, built in-house) with a rotation rate of 500 or 3000 rpm. Control experiments using a gold rotating disk electrode were also built in-house and used in the same manner. A custom-built electrochemical H-Cell allowed separation of the anodic and cathodic compartments by a Nafion® 117 cation exchange membrane. This glass cell was assembled inside the glove box. A nitrogen-saturated electrolyte of 0.5 M $KHCO_3$ (5 mL cathode compartment, 7 mL anode compartment) was used. To facilitate control of the cathode electrode potential the experiments were run using a Palmsens4 potentiostat in 3-electrode mode with a platinum electrode (500 × 0.5 mm) acting as the anode/counter electrode and a Ag/AgCl (3 M KCl) reference electrode in a side arm separated by a Luggin capillary from the cathode cell compartment. Prior to electrocatalysis, the catholyte was purged with 100% CO_2 gas at 70 mL min^{-1} for 20 minutes. Throughout electrocatalysis, 100% CO_2 gas was continuously bubbled through the catholyte at 35 mL min^{-1}. Following electrocatalysis, gas was collected for a further 3 minutes. For product analysis, gaseous products were collected as described in the following section and analysed immediately, whilst a portion of the catholyte was frozen for storage prior to analysis.

7.4.2 Analysis of gaseous products from CO2ER by GC

Following electrolysis, gaseous products were collected in a Restek Tedlar 13" × 24" gas bag that were filled with N_2 gas and evacuated three times before use. Gas chromatography was performed

on a Shimadzu GC-2014 equipped with a ShimCarbon ST micropacked column (2 m × 0.32 mm). Hydrogen products were detected by a TCD detector (200 °C, 50 mA) with a sampling rate of 240 ms, whilst carbon containing products were detected by an FID detector (200 °C). 2500 µL of gas sample was injected into the injection chamber at 120 °C using a Hamilton gas tight syringe. Argon was used as the carrier gas where the flow rate was held at 10 mL min^{-1} for 9 minutes before being increased to 30 mL min^{-1} (ramp rate: 40 mL min^{-1}) and held for the remainder of the experiment. The oven temperature was kept at 40 °C for 9 minutes before heating to 200 °C at a ramp rate of 40 °C min^{-1} and held for 10 minutes. Peak integrals were used to quantify product concentrations as described in Chapter 4.

7.4.2.1 GC Calibration for analysis of CO2ER gas products

A Restek Tedlar 13" × 24" gas bag was filled with 1.155 dm^3 of 100% CO_2 flowed through an H-cell used for CO_2 electrochemical reduction. A separate "pure" gas bag was filled with pure effluent from a BOC gas bottle containing H_2 (2.380%), CO (2.423%), CH_4 (2.462%), C_2H_4 (2.435%), C_2H_6 (2.575%) with a CO_2 fill (85.725%). Sequential aliquots taken from the "pure" gas bag and put into the CO_2 filled gas bag. After each sequential aliquot, two separate samples (2500 µL) from the CO_2 gas bag was injected into the GC to perform two repeat calibration runs using the same GC method as described in the previous section.

The sequential aliquots added to the CO_2 gas bag are recorded below in Table 19. The nanomoles given are those calculated to be injected by the gas syringe into the GC. Calculation of these nanomoles considered the volume of injected gas into the "100% CO_2" gas bag and the volume removed for each GC injection. The integrated peak areas given by $\bar{x}$ are averaged over the two GC runs for each step. Finally, a linear regression analysis of the nanomoles injected into the GC relative to the peak response was performed. The calibration curves are shown in Chapter 4, where the gradients, intercepts and R^2 values are also given. Where no intercept is given, the regression analysis was forced through the origin.

Table 19. Total injection quantities of aliquots from a "pure" BOC gas cylinder into a 100% gas bag (1.155 dm^3). Averaged peak integrals from two calibration GC runs indicated for each species by $\bar{x}$.

V_{total} / µL	H_2 / nmol	$\bar{x}_{H2}$	CO / nmol	$\bar{x}_{CO}$	CH_4 / nmol	$\bar{x}_{CH4}$	C_2H_4 / nmol	$\bar{x}_{C2H4}$	C_2H_6 / nmol	$\bar{x}_{C2H6}$
100	0.24	0.0E+00	0.24	3.6E+04	0.24	5.1E+04	0.24	7.2E+04	0.25	1.1E+05
250	0.59	4.3E+01	0.60	9.5E+04	0.61	1.0E+05	0.61	1.9E+05	0.64	2.4E+05
500	1.19	1.2E+02	1.21	1.9E+05	1.23	2.1E+05	1.22	4.0E+05	1.29	4.7E+05
1000	2.39	4.0E+02	2.43	4.1E+05	2.47	4.1E+05	2.44	8.7E+05	2.58	9.8E+05
2500	5.99	1.2E+03	6.10	9.5E+05	6.20	9.6E+05	6.13	2.1E+06	6.48	2.3E+06
5000	12.01	2.9E+03	12.23	2.1E+06	12.43	2.1E+06	12.29	4.8E+06	13.00	5.1E+06
10000	24.03	5.9E+03	24.46	4.1E+06	24.86	4.1E+06	24.58	9.6E+06	26.00	1.0E+07
25000	59.49	1.6E+04	60.57	1.1E+07	61.54	1.0E+07	60.87	2.5E+07	64.37	2.6E+07
Intercept		-2.9E+02*		**		**		**		**
Gradient		2.7E+02*		1.7E+05		1.7E+05		4.0E+05		4.0E+05
R^2		0.9988*		0.9998		0.9998		0.9996		0.9998

**excludes first two data points where V_{total} = 100, 250 µL*
*** regression forced through the origin*

7.4.3 700 MHz NMR for water suppression

^{1}H NMR was performed using a 700 MHz Avance Neo spectrometer equipped with a nitrogen-cooled triple-resonance cryoprobe at a temperature of 25˚C. 1D Proton spectra with water suppression were recorded using the Bruker sequence zgesgp, with an acquisition time of 1.475 s, a spectral width of 15.87 ppm and a recycle delay of 5.00 s. The spectra were processed using Mestrenova, with an exponential line broadening of 3.00 Hz. Samples were prepared by taking 540 µL of electrolyte from the cathodic cell chamber and adding 60 µL of a D_2O solution containing 18.7 ppm of DMSO, yielding a final concentration of 1.87 ppm of DMSO in the NMR tube as an internal standard.

7.5 Chemical synthesis

7.5.1 Anilines for diazonium grafting

7.5.1.1 "C_1-Amine"

7.5.1.1.1 2-(4-nitrobenzyl)isoindoline-1,3-dione

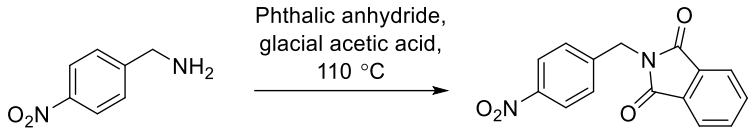

4-nitrobenzylamine hydrochloride (0.50 g, 2.65 mmol) and phthalic anhydride (0.39 g, 2.65 mmol) were dissolved in glacial acetic acid (6 mL) and the solution refluxed, with stirring, for 18 hours. The reaction solution was concentrated *in vacuo* to ca. 3 mL then cooled to 0 °C. The crystals of product were collected by filtration, washed with ice-cold water and dried *in vacuo*, yielding off-white crystals (0.61 g, 2.17 mmol, 81.9%). ESI-MS (pos): Found $[M+Na]^+$ 305.0526 ($C_{15}H_{10}N_2NaO_4$); ^{1}H NMR (400 MHz, $CDCl_3$) δ_H 8.19 (m, 2H), 7.88 (m, 2H), 7.76 (m, 2H), 7.29 (m, 2H), 4.94 (s, 2H) ppm; ^{13}C NMR (101 MHz, $CDCl_3$) δ_C 167.69, 147.74, 143.19, 134.26, 131.74, 129.27, 123.88, 123.53, 40.77 ppm.

7.5.1.1.2 2-(4-aminobenzyl)isoindoline-1,3-dione

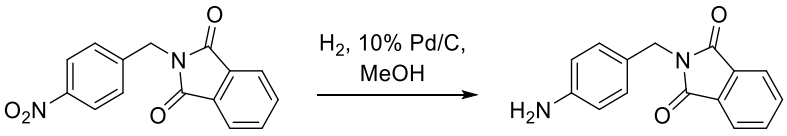

2-(4-nitrobenzyl)isoindoline-1,3-dione (0.20 g, 0.71 mmol) and a spatula-end of 10% Pd/C were placed in a round bottom flask and the flask placed under argon. Methanol (6.25 mL) and ethyl acetate (10 mL) were then added and the system placed under 1 atm of hydrogen and stirred for 1 hour. The mixture was filtered and concentrated *in vacuo* to yield a pale green solid (0.16 g, 0.61 mmol, 86.7%). ESI-MS (pos): Found $[M+H]^+$ 267.1124 ($C_{15}H_{13}N_2O_2$); ^{1}H NMR (400 MHz, $CDCl_3$) δ_H 7.83 (m, 2H), 7.70 (m, 2H), 7.05 (m, 2H), 6.62 (m, 2H), 3.87 (t, J = 7.79, 2H), 2.88 (t, J = 7.79, 2H) ppm; ^{13}C NMR (100 MHz, $CDCl_3$) δ_C 168.25, 144.93, 133.86, 132.11, 129.71, 127.93, 123.19, 115.34, 39.60, 33.77 ppm; ATR-FTIR ν_{max}: 3448, 3363, 2957, 2923, 2853, 1761, 1694, 1609, 1395 cm^{-1}.

7.5.1.2 "C_2-Amine"

7.5.1.2.1 2-(4-nitrophenethyl)isoindoline-1,3-dione

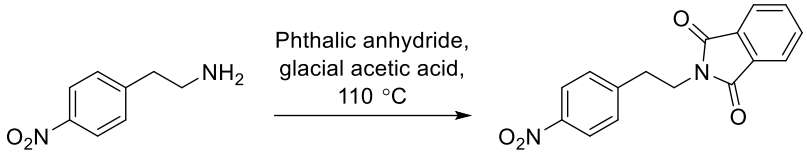

2-(4-nitrophenyl)ethan-1-amine hydrochloride (0.54 g, 2.65 mmol) and phthalic anhydride (0.39 g, 2.65 mmol) were dissolved in glacial acetic acid (5.3 mL) and the solution refluxed, with stirring, for 18 hours. The reaction solution was then allowed to cool to room temperature, then cooled to 0 °C. The resulting crystals were collected by filtration, washed with ice-cold water and dried *in vacuo* (0.79 g, 2.62 mmol, 98.8%). ESI-MS (pos): Found $[M+Na]^+$ 319.0685 ($C_{16}H_{12}N_2NaO_4$); ^{1}H NMR (400 MHz, $CDCl_3$) δ_H 8.14 (m, 2H), 7.83 (m, 2H), 7.73 (m, 2H), 7.41 (m, 2H), 3.98 (t, J = 7.33, 2H), 3.13 (t, J = 7.33, 2H) ppm; ^{13}C NMR (101 MHz, $CDCl_3$) δ_C 168.17, 147.04, 145.81, 134.80, 131.91, 129.87, 123.95, 123.52, 38.59, 34.50 ppm.

7.5.1.2.2 2-(4-aminophenethyl)isoindoline-1,3-dione

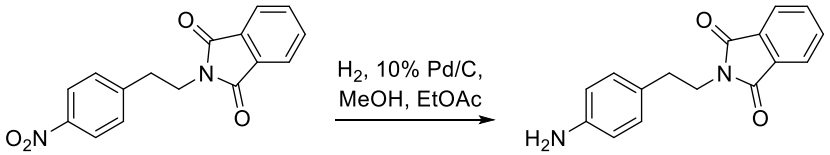

2-(4-nitrophenethyl)isoindoline-1,3-dione (0.20 g, 0.68 mmol) and a spatula-end of 10% Pd/C were placed in a round bottom flask and placed under argon. Methanol (6.25 mL) and ethyl acetate (10 mL) were then added and the system placed under 1 atm of hydrogen and the reaction stirred for 1 hour. The 10% Pd/C carbon was removed *via* filtration and the filtrate concentrated in vacuo to yield a pale yellow solid (0.16 g, 0.58 mmol, 86.3%). ESI-MS: Found $[M+H]^+$ 267.1124 ($C_{16}H_{15}N_2O_2$); ^{1}H NMR (400 MHz, $CDCl_3$) δ_H 7.83 (m, 2H), 7.70 (m, 2H), 7.05 (m, 2H), 6.62 (m, 2H), 3.87 (t, J = 7.79, 2H), 2.88 (t, J = 7.79, 2H) ppm; ^{13}C NMR (100 MHz, $CDCl_3$) δ_C 168.25, 144.93, 133.86, 132.11, 129.71, 127.93, 123.19, 115.34, 39.60, 33.77 ppm; ATR-FTIR ν_{max}: 3442, 3360, 2924, 2853, 1770, 1697, 1519, 1392, 1350 cm^{-1}.

7.5.1.3 "C_4-Amine" (synthesised by Jack Dickenson-Fogg)

7.5.1.3.1 4-(4-nitrophenyl)butan-1-amine

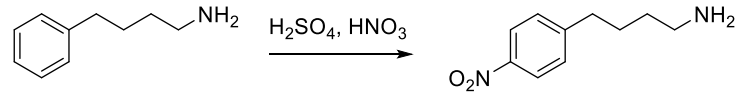

4-Phenylbutylamine (1.89 g, 2 mL, 12.7 mmol) was added slowly to conc. H_2SO_4 (4.2 mL) and stirred until dissolved completely. The reaction mixture was cooled to 0 °C and 70% HNO_3 (0.95 mL) was added dropwise (very slowly) to the reaction solution. The reaction was then stirred for 1 hour at 0 °C, then poured into water (21 mL) pre-cooled to 0 °C. The reaction was stirred at 0 °C for 15 minutes and then allowed to stir for 15 minutes at room temperature. The reaction solution was neutralised slowly at 0 °C, with conc. NaOH, until the pH of the reaction was in the range of 6-8. Di-nitrated precipitate was filtered off and washed with ethyl acetate. The organic layer was washed with water, dried over $MgSO_4$ and concentrated to give a dark brown oil (0.25 g, 1.30 mmol, 10.2%). ^{1}H NMR (400 MHz, DMSO-d_6): δ_H 8.15 (m, 2H), 7.50 (m, 2H), 2.71 (t, J = 7.79 Hz, 2H), 2.56 (t, J = 6.87, 2H), 1.62 (m, 2H), 1.37 (m, 2H) ppm. *Intermediate product in agreement with literature NMR.[333]

7.5.1.3.2 2-(4-(4-nitrophenyl)butyl)isoindoline-1,3-dione

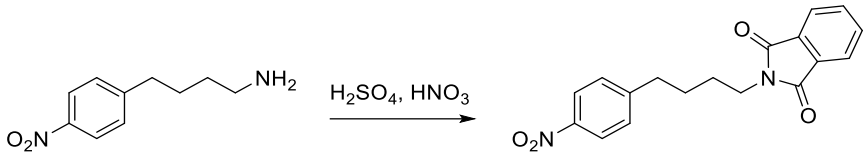

A mixture of the 4-(4-nitrophenyl)butylamine (0.15 g, 0.76 mmol) and phthalic anhydride (0.14 g, 0.95 mmol) in pyridine (1 mL) as stirred at 100 °C until homogeneous and for a further 30 minutes. The solvent was removed in vacuo and AcOH (0.7 mL) and Ac_2O (0.6 mL) were added and the mixture heated at reflux for 1 hour. Slow addition of water to the boiling solution caused precipitation, after which the mixture was cooled and filtered whereupon it was removed by filtration and dried to yield an off-white powder (0.19 g, 0.59 mmol, 78.5%). ^{1}H NMR (400 MHz, DMSO-d_6): δ_H 8.12 (d, J = 8.70 Hz, 2H), 7.84 (m, 4H), 7.48 (d, J = 8.70 Hz, 2H), 3.59 (br, s, 2H), 2.74 (br, s, 2H), 1.60 (d, J = 2.75 Hz, 4H) ppm; ^{13}C NMR (400 MHz, DMSO-d_6): δ_C 167.99, 150.49, 145.77, 134.36, 131.57, 129.61, 123.40, 122.98, 37.07, 34.33, 27.78 ppm; ATR-FTIR ν_{max}: 2934, 2852, 1767, 1704, 1597, 1400, 1512, 1342 cm^{-1}. *Intermediate product in agreement with literature NMR.[333]

7.5.1.3.3 2-(4-(4-aminophenyl)butyl)isoindoline-1,3-dione

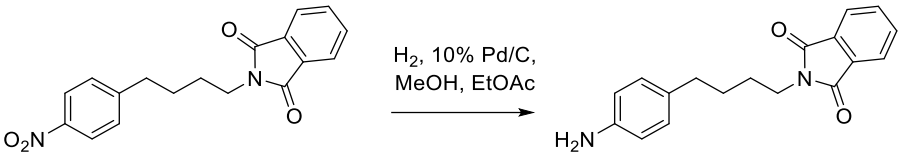

2-[4-(4-nitrophenyl)butyl]isoindoline-1-3-dione (0.22 g, 0.68 mmol) and a spatula-end of 10% Pd/C were placed in a round bottom flask and placed under argon. Methanol (6.25 mL) and ethyl acetate (10 mL) were then added, the system was placed under 1 atm of H_2. The reaction solution was to stir for 18 hours. Pd/C was removed *via* filtration and the filtrate concentrated in vacuo to yield a cream powder (99.3 mg, 49.8%). ESI-MS: Found $[M+H]^+$ 295.1440 ($C_{18}H_{19}N_2O_2$); ^{1}H NMR (400 MHz, DMSO-d_6): δ_H 7.01 (m, 4H), 5.96 (m, 2H), 5.60 (m, 2H), 2.73 (m, 2H), 0.72 (m, 2H), 0.62 (m, 2H) ppm; ^{13}C NMR (400 MHz, DMSO-d_6): δ_C 167.86, 134.30, 131.52, 122.93, 133.87, 33.76, 30.63 ppm; ATR-FTIR ν_{max}: 3475, 3381, 2930, 2851, 1771, 1695, 1628, 1515, 1398, 1371, 1337 cm^{-1}.

7.5.1.4 "C_{10}-Amine"

7.5.1.4.1 4-(10-bromodecyl)aniline

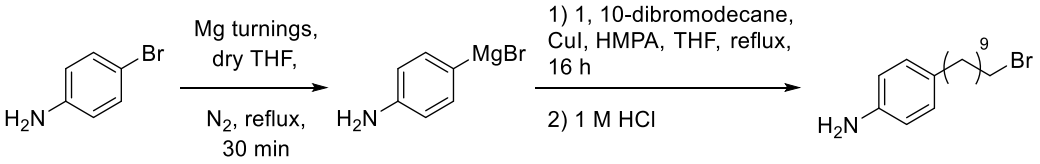

To a stirred suspension of magnesium turnings in dry THF, a solution of 4-bromoaniline (0.20 g, 1.16 mmol, 1 eq.) in dry THF (50 mL) was added dropwise under a nitrogen atmosphere and refluxed for 30 minutes after which no initiation had occurred. 1-bromo 2-chloroethane (0.10 mL, 1.21 mmol) was added dropwise and the mixture stirred at reflux under a nitrogen atmosphere for 2 hours. A separate stirred solution of HMPA (4.2 mL), CuI (33 mg, 0.18 mmol, 0.06 eq.) and 1, 10-dibromodecane (1.05 g, 3.49 mmol, 1.2 eq.) in dry THF (20 mL) was refluxed at 70 °C for 5 minutes. The Grignard solution was added dropwise to the refluxing solution, leaving behind excess magnesium solids. The reaction mixture was the refluxed at 70 °C for 16 hours. After cooling to room temperature, the mixture was added dropwise into 1 M HCl (100 mL). Ethyl acetate (40 mL) was then added and the organic layer isolated. The aqueous layer was washed further with ethyl acetate (3 × 40 mL) and the combined organic layers dried over $MgSO_4$, filtered and concentrated *in vacuo* to afford a yellow oil. Flash column chromatography (SiO_2, 9:1 Hexane:DCM) partially

purified the product as an orange oil (0.77 g). ESI-MS (pos): Found $[M+H]^+$ 312.1323 ($C_{16}H_{27}BrN$). Crude used in next step.

7.5.1.4.2 2-(10-(4-aminophenyl)decyl)isoindoline-1,3-dione

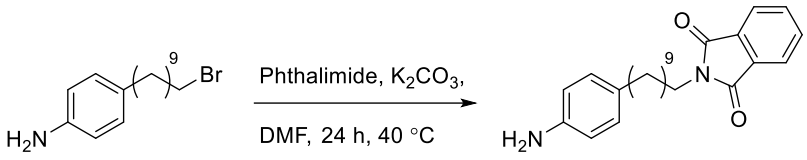

The crude mixture of the previous experiment (0.774 g), phthalimide (0.729 g, 4.96 mmol) and potassium carbonate (0.856 g, 6.19 mmol) were suspended in DMF (10 mL) and stirred for 48 h. Water (20 mL) and DCM (20 mL) were then added and the aqueous layer further washed with DCM (2 × 20 mL). The combined organic layers were washed with saturated potassium carbonate (2 × 20 mL) and then saturated brine (20 mL). The organic layer was then dried over $MgSO_4$, filtered and concentrated *in vacuo* to afford an impure yellow oil (0.958 g). Flash column chromatography (SiO_2, Hexane:DCM gradient of 1:1 to 2:3) purified the product as a waxy yellow solid (0.37 g, 0.98 mmol, 39.4%). ESI-MS (pos): $[M+H]^+$ 379.3383 ($C_{24}H_{31}N_2O_2$); ^{1}H NMR (400 MHz, $CDCl_3$) δ_H 7.84 (dd, *J* = 5.5, 3.2 Hz, 2H), 7.70 (dd, *J* = 5.4, 3.0 Hz, 2H), 7.16 (d, *J* = 8.1 Hz, 2H), 6.60 (d, *J* = 8.2 Hz, 2H), 3.72 – 3.64 (t, *J* = 7.3 Hz, 2H), 3.09 (t, *J* = 7.1 Hz, 2H), 1.72 – 1.50 (m, 4H), 1.44 – 1.21 (m, 14H) ppm; ^{13}C NMR (101 MHz, $CDCl_3$) δ_C 168.59, 148.65, 148.23, 133.95, 132.27, 129.30, 129.28, 123.25, 112.77, 51.12, 44.07, 38.15, 29.65, 29.55, 29.47, 29.22, 28.67, 27.23, 26.92 ppm; ATR-FTIR ν_{max}: 3407, 2922, 2849, 1771, 1702, 1601, 1501, 1397, 1365, 1325 cm^{-1}.

7.5.2 Redox markers

7.5.2.1 NHS-C_3-methyl viologen, "NHS-Viologen"

7.5.2.1.1 Monoquat iodide

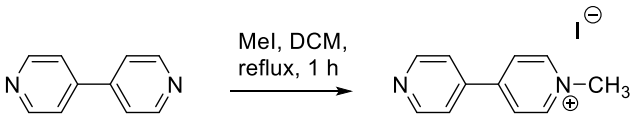

A solution of 4, 4-dipyridyl (2.00 g, 12.81 mmol) and methyl iodide (0.80 mL, 12.81 mmol) in dichloromethane was stirred at reflux for 1 h. The solid was filtered and washed with ethyl acetate (50 mL) and DCM (50 mL). The crude product was recrystallised twice from methanol to give the

desired compound as small yellow crystals (1.19 g, 3.98 mmol, 31.1%). ESI-MS (pos): Found $[M]^+$ 171.0918 ($C_{11}H_{11}N_2$); ^{1}H NMR (400 MHz, D_2O) δ_H 8.89 (d, *J* = 7.0 Hz, 2H), 8.69 – 8.63 (m, 2H), 8.32 (d, *J* = 6.1 Hz, 2H), 7.84 – 7.79 (m, 2H), 4.44 (s, 3H) ppm; ^{13}C NMR (101 MHz, D_2O) δ_C 149.98, 145.72, 125.75, 122.48, 48.05 ppm ; ATR-FTIR ν_{max}: 3121, 3078, 3021, 1651, 1639, 1600, 1546, 1523, 1496, 1465, 1415, 1332, 1220, 1193 cm^{-1}.

7.5.2.1.2 1-(2-carboxyethyl)-1'-methyl-[4,4'-bipyridine]-1,1'-diium bis-hexafluorophosphate

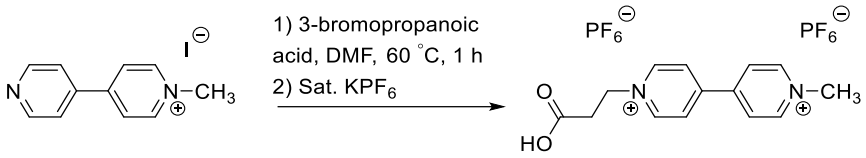

A suspension of 1-methyl-[4,4'-bipyridin]-1-ium iodide (1.00 g, 3.35 mmol) and 3-bromopropanoic acid (1.03 g, 6.71 mmol) in DMF (25 mL) was stirred at 60 °C for 1 h. After the mixture was cooled to room temperature, the solid was filtered and washed with DCM (100 mL). The orange solid was dissolved in water (5 mL) and saturated aqueous ammonium hexafluorophosphate was added dropwise until no more solid precipitated. The solid was washed with water (20 mL) and DCM (50 mL) and recrystallised from acetonitrile:methanol 1:2 to afford small pale cream crystals (0.36 g, 0.81 mmol, 24.1%). ESI-MS (pos): Found $[M-H]^+$ 243.1126 ($C_{14}H_{15}N_2O_2$); ^{1}H NMR (400 MHz, MeCN-d_3) δ_H 9.17 – 9.12 (m, 2H), 9.01 (d, *J* = 6.6 Hz, 2H), 8.54 (dd, *J* = 6.9, 5.0 Hz, 4H), 5.01 (t, *J* = 6.2 Hz, 2H), 4.56 (s, 3H), 3.28 (t, *J* = 6.1 Hz, 2H) ppm; ^{13}C NMR (101 MHz, MeCN-d_3) δ_C 171.71, 151.09, 150.45, 147.32, 147.24, 127.72, 127.66, 118.26, 58.20, 49.42, 34.57 ppm; ATR-FTIR ν_{max}: 3145, 3078, 1723, 1645, 1569, 1511, 1451, 1409 cm^{-1}.

7.5.2.1.3 1-(3-((2,5-dioxopyrrolidin-1-yl)oxy)-3-oxopropyl)-1'-methyl-[4,4'-bipyridine]-1,1'-diium bis-hexafluorophosphate

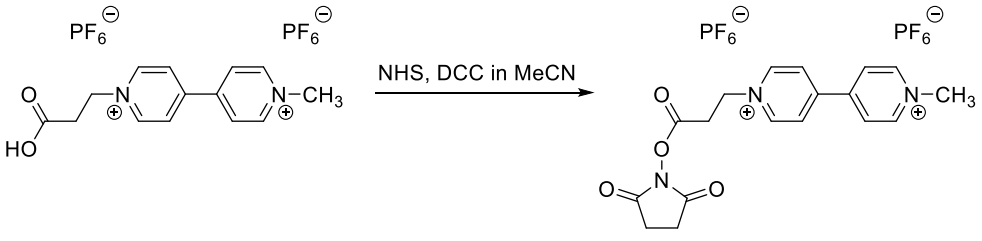

1-(2-carboxyethyl)-1'-methyl-[4,4'-bipyridine]-1,1'-diium bis(hexafluorophosphate) (0.33 g, 0.63 mmol), N-hydroxysuccinimide (0.12 g, 0.75 mmol) and DCC (0.16 g, 0.75 mmol) were dissolved in DMF (10 mL) and stirred at room temperature for 2.5 h. Acetonitrile (10 mL) was added and the

mixture filtered three times. The solvent was removed *in vacuo*. The solid was recrystallised from methanol to afford a pale cream powder (0.27 g). Solid obtained confirmed as 1:1 mixture of starting material to product thus product obtained was 0.21 mmol, 33.9%. ESI-MS (pos): Found $[M+H]^{2+}$ 171.0908 ($C_{18}H_{20}N_3O_4$) and $[M]^{2+}$ 170.5674 ($C_{18}H_{19}N_3O_4$); ^{1}H NMR (400 MHz, MeCN-d_3) δ_H 9.01 – 8.97 (m, 2H), 8.85 (d, *J* = 6.6 Hz, 2H), 8.45 – 8.41 (m, 2H), 8.38 (d, *J* = 6.5 Hz, 2H), 5.00 (t, *J* = 6.6 Hz, 2H), 4.40 (s, 3H), 3.50 (t, *J* = 6.5 Hz, 2H), 2.77 (s, 4H) ppm; ^{13}C NMR (101 MHz, MeCN-d_3) δ_C 170.57, 167.13, 151.53, 150.27, 147.34, 147.14, 128.09, 127.71, 118.26, 57.31, 49.45, 32.53, 26.20 ppm; ATR-FTIR ν_{max}: 3142, 3075, 1833, 1783, 1753, 1710, 1644, 1569, 1511, 1451, 1392, 1216 cm^{-1}.

7.5.2.2 Thio-C_6-dopamine

7.5.2.2.1 6-(tritylthio)hexanoic acid

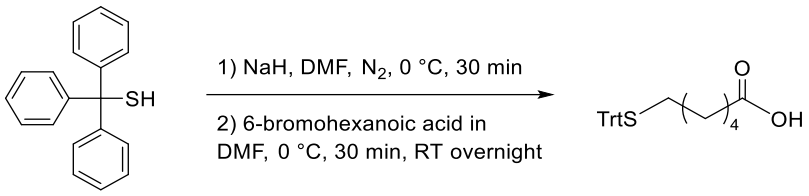

A solution of sodium hydride (60%, 73 mg, 1.83 mmol) in dry DMF (10 mL) was cooled to 0 °C under nitrogen. A solution of trityl mercaptan (0.50 g, 1.81 mmol) in dry DMF (10 mL) was added slowly and the resulting solution was stirred for 25 minutes. 6-bromohexanoic acid (0.35 g, 1.81 mmol) in dry DMF (10 mL) was added to the reaction mixture and was stirred for a further 30 minutes before being allowed to warm to room temperature and left to stir for a further 16 hours. Chloroform (200 mL) was then slowly added to the solution and the organic layer washed with 0.1 M H_3PO_4 (100 mL) and water (100 mL). The organic layer was then dried over $MgSO_4$, filtered and concentrated *in vacuo*. The product was then re-dissolved in ethanol (100 mL), filtered and concentrated *in vacuo* to afford a clear yellow oil (0.69 g, 1.78 mmol, 97.2%). ESI-MS (pos): Found $[M+Na]^+$ 413.1553 ($C_{25}H_{26}NaO_2S$); ^{1}H NMR (400 MHz, $CDCl_3$) δ_H 7.41 (d, J = 5.4, 3.4 Hz, 1H), 7.26 (t, 2H), 7.20 (t, J = 9.2, 4.2 Hz, 1H), 3.40 (t, J = 6.7 Hz, 1H), 2.95 (s, 1H), 2.88 (s, 1H), 2.25 (t, J = 7.5 Hz, 1H), 2.14 (t, J = 7.2 Hz, 1H), 1.55 – 1.44 (m, 1H), 1.43 – 1.33 (m, J = 7.2 Hz, 1H), 1.33 – 1.21 (m, 1H) ppm; ^{13}C NMR (101 MHz, $CDCl_3$) δ_C 179.72, 145.09, 129.70, 127.96, 126.67, 66.58, 33.89, 31.83, 28.49, 28.39, 24.32 ppm; ATR-FTIR ν_{max}: 3473, 3058, 2927, 2857, 1705, 1596, 1489, 1444, 1273, 1157 cm^{-1}.

7.5.2.2.2 N-(3,4-dihydroxyphenethyl)-6-(tritylthio)hexanamide

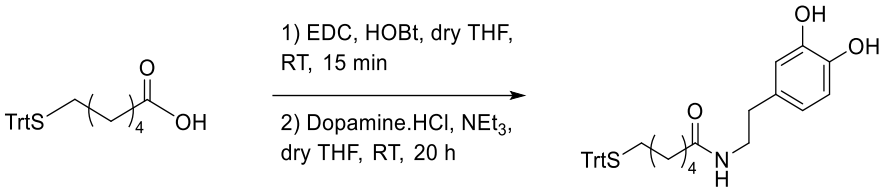

A solution of 6-thiotrityl hexanoic acid (0.71 g, 1.81 mmol), 1-ethyl-3-(3-dimethylaminopropyl)carbodiimide (0.42 g, 2.17 mmol) and 1-hydroxybenzotriazole (0.21 g, 1.52 mmol) in dry THF (30 mL) was stirred for 15 minutes. Dopamine hydrochloride (0.32 g, 1.67 mmol) and triethylamine (1.06 mL, 7.60 mmol) were then added and the reaction mixture stirred for 20 hours. Saturated citric acid (30 mL) and ethyl acetate (30 mL) were then added and the organic layer isolated. The aqueous layer was then further extracted with ethyl acetate (30 mL) and the organic layers combined and washed further with saturated sodium bicarbonate (2 × 30 mL). The bicarbonate layer was washed with ethyl acetate (20 mL) and the organic layers combined, dried over $MgSO_4$ and concentrated *in vacuo* to afford a yellow oil (0.87 g, 1.65 mmol, 91.2%). ESI-MS (pos): Found $[M+Na]^+$ 548.2232 ($C_{33}H_{35}NNaO_3S$); ^1H NMR (400 MHz, $CDCl_3$) δ_H 7.38 (dd, J = 5.3, 3.3 Hz, 1H), 7.28 – 7.21 (m, 1H), 7.20 – 7.14 (m, 1H), 6.77 (d, J = 8.0 Hz, 1H), 6.70 (d, J = 2.0 Hz, 1H), 6.50 (dd, J = 8.0, 1.9 Hz, 1H), 3.41 (p, J = 6.6 Hz, 2H), 2.63 (t, J = 7.4 Hz, 1H), 2.11 (t, J = 7.3 Hz, 1H), 1.47 – 1.38 (m, 2H), 1.38 – 1.28 (m, 2H) ppm; ^{13}C NMR (101 MHz, $CDCl_3$) δ_C 174.39, 145.03, 144.48, 143.26, 130.51, 129.67, 127.96, 127.93, 126.69, 120.53, 115.62, 115.57, 115.38, 115.35, 66.57, 41.15, 36.53, 34.93, 31.82, 28.48, 28.31, 25.32 ppm; ATR-FTIR ν_{max}: 3285 (br), 3056, 2930, 2857, 1634, 1596, 1518, 1443, 1360, 1280, 1194 cm^{-1}.

7.5.2.2.3 N-(3,4-dihydroxyphenethyl)-6-mercaptohexanamide

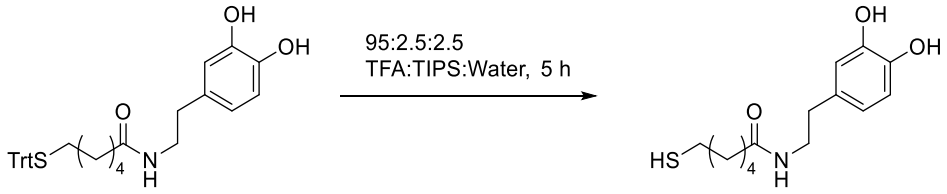

N-dopamine, 6-thiotrityl hexanamide (0.87 g, 1.65 mmol) was dissolved in a 95:2.5:2.5 TFA:TIPS:Water mixture (50 mL) and stirred for 3 hours. The solution was then cooled to 0 °C and filtered and washed with ice cold TFA (10 mL). Water (20 mL) and DCM (50 mL) were added to the solution and the organic layer isolated. The aqueous layer was then washed further with DCM (3 × 50 mL) and the combined organic layers dried over $MgSO_4$, filtered and concentrated *in vacuo* to

afford an impure yellow oil/powder mix. The product was then purified by flash column chromatography (SiO_2, EtOAc) to afford a thick impure yellow oil. The middle fractions were combined and concentrated *in vacuo*. The product was re-dissolved in DCM, filtered and concentrated *in vacuo*. The product was purified again by flash column chromatography (SiO_2, 4:1 Hexane:EtOAc) to afford a yellow oil (0.28 g, 0.97 mmol, 59.1%). ESI-MS (pos): Found $[M+Na]^+$ 306.1135 ($C_{14}H_{21}NNaO_3S$); ^1H NMR (400 MHz, MeOD-d_4) δ_H 6.66 (d, J = 8.0 Hz, 1H), 6.63 (d, J = 1.9 Hz, 1H), 6.50 (dd, J = 8.0, 2.0 Hz, 1H), 3.33 – 3.25 (m, 6H), 2.60 (t, J = 7.2 Hz, 2H), 2.45 (t, J = 7.1 Hz, 2H), 2.17 – 2.08 (m, J = 7.5, 4.0 Hz, 3H), 1.60 – 1.49 (m, 4H), 1.42 – 1.28 (m, 2H) ppm. ^{13}C NMR (101 MHz, MeOD-d_4) δ_C 176.03, 146.20, 144.72, 131.95, 121.02, 116.83, 116.28, 42.12, 36.95, 35.86, 34.83, 28.81, 26.47, 24.77 ppm; ATR-FTIR ν_{max}: 3265 (br), 2931, 2858, 1621, 1599, 1517, 1440, 1359, 1279, 1254, 1194 cm^{-1}.

7.5.2.3 Thio-C_{11}-dopamine

7.5.2.3.1 11-(tritylthio)undecanoic acid

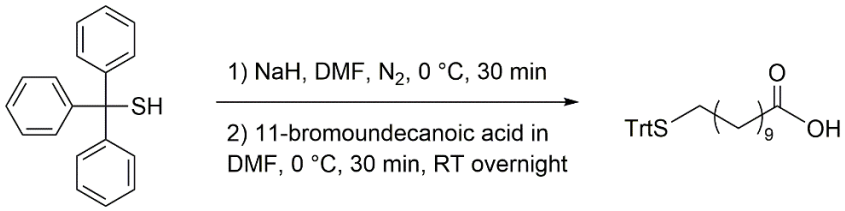

A solution of sodium hydride (60%, 174 mg, 4.35 mmol) in dry DMF (10 mL) was cooled to 0 °C under nitrogen. A solution of trityl mercaptan (1.00 g, 3.62 mmol) in dry DMF (10 mL) was added slowly and the resulting solution was stirred for 25 minutes. 11-bromoundecanoic acid (0.96 g, 3.62 mmol) in dry DMF (10 mL) was added to the reaction mixture and was stirred for a further 30 minutes before being allowed to warm to room temperature and left to stir for a further 16 hours. Chloroform (200 mL) was then slowly added to the solution and the organic layer washed with 0.1 M H_3PO_4 (100 mL) and water (100 mL). The organic layer was then dried over $MgSO_4$, filtered and concentrated *in vacuo*. The product was then re-dissolved in ethanol (100 mL), filtered and concentrated *in vacuo* to afford a clear yellow oil (0.700 g, 1.52 mmol, 42.0%). ESI-MS (pos): Found $[M+Na]^+$ 483.2327 ($C_{30}H_{36}NaO_2S$); ^1H NMR (400 MHz, $CDCl_3$) δ_H 7.40 (d, J = 8.0 Hz, 6H), 7.26 (t, J = 7.6 Hz, 6H), 7.18 (t, J = 7.2 Hz, 3H), 2.32 (t, J = 7.3 Hz, 2H), 2.12 (t, J = 7.3 Hz, 2H), 1.67 – 1.54 (m, 2H), 1.43 – 1.07 (m, 14H) ppm; ^{13}C NMR (101 MHz, $CDCl_3$) δ_C 180.01, 145.20, 129.73, 127.92, 126.62, 77.16, 34.20, 34.14, 32.94, 32.14, 29.44, 29.31, 29.27, 29.15, 29.12, 28.70, 28.28 ppm.

7.5.2.3.2 N-(3,4-dihydroxyphenethyl)-11-(tritylthio)undecanamide

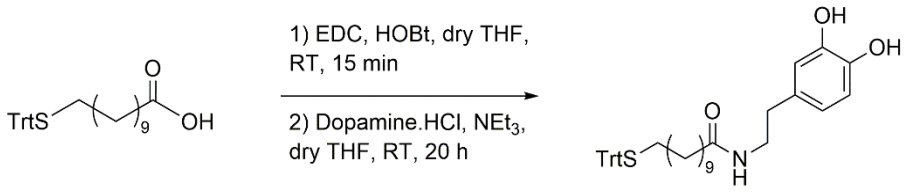

A solution of 11-thiotrityl undecanoic acid (0.70 g, 1.52 mmol), 1-ethyl-3-(3-dimethylaminopropyl)carbodiimide (0.35 g, 1.82 mmol) and 1-hydroxybenzotriazole (0.205 g, 1.52 mmol) in dry THF (30 mL) was stirred for 15 minutes. Dopamine hydrochloride (0.32 g, 1.67 mmol) and triethylamine (1.06 mL, 7.60 mmol) were then added and the reaction mixture stirred for 20 hours. Saturated citric acid (30 mL) and ethyl acetate (30 mL) were then added and the organic layer isolated. The aqueous layer was then further extracted with ethyl acetate (30 mL) and the organic layers combined and washed further with saturated sodium bicarbonate (2 × 30 mL). The bicarbonate layer was washed with ethyl acetate (20 mL) and the organic layers combined, dried over $MgSO_4$ and concentrated *in vacuo* to afford a yellow oil (0.905 g, 1.52 mmol, 100%). ESI-MS (pos): Found $[M+Na]^+$ 618.3032 ($C_{38}H_{45}NNaO_3S$); ^1H NMR (400 MHz, $CDCl_3$) δ_H 7.40 (d, J = 8.0 Hz, 6H), 7.26 (t, J = 7.2 Hz, 6H), 7.19 (t, J = 7.2 Hz, 3H), 6.79 (d, J = 8.3 Hz, 1H), 6.73 (d, J = 1.9 Hz, 1H), 6.53 (dd, J = 8.0, 1.7 Hz, 2H), 3.44 (dd, J = 13.1, 6.8 Hz, 2H), 2.66 (t, J = 7.0 Hz, 2H), 2.12 (t, J = 7.1 Hz, 2H), 1.60 – 1.50 (m, J = 16.3, 9.8 Hz, 2H), 1.44 – 1.32 (m, J = 22.1, 7.4 Hz, 2H), 1.32 – 1.06 (m, 16H) ppm.

7.5.2.3.3 N-(3,4-dihydroxyphenethyl)-3-mercaptoundecpropanamide

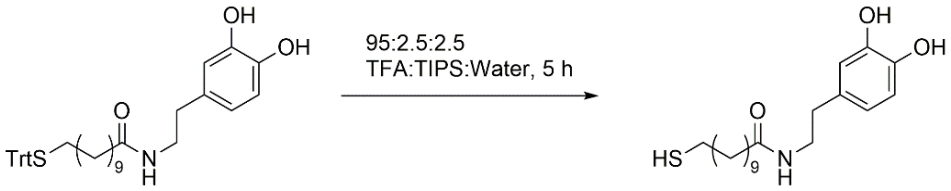

N-dopamine, 11-(tritylthio)undecanamide (0.91 g, 1.52 mmol) was dissolved in a 95:2.5:2.5 TFA:TIPS:Water mixture (50 mL) and stirred for 3 hours. The solution was then cooled to 0 °C and filtered and washed with ice cold TFA (10 mL). Water (20 mL) and DCM (50 mL) were added to the solution and the organic layer isolated. The aqueous layer was then washed further with DCM (3 × 50 mL) and the combined organic layers dried over $MgSO_4$, filtered and concentrated *in vacuo* to afford an impure yellow oil/powder mix (0.61 g). The product was then purified by flash column chromatography (SiO_2, 9:1 DCM:MeOH) to afford a thick clear yellow oil (0.43 g, 1.22 mmol, 80.3%).

ESI-MS (pos): Found $[M+H]^+$ 354.2098 ($C_{19}H_{32}NO_3S$); ^1H NMR (400 MHz, $CDCl_3$) δ_H 6.79 (d, J = 8.1 Hz, 1H), 6.73 (d, J = 2.0 Hz, 1H), 6.53 (dd, J = 8.0, 1.9 Hz, 1H), 3.45 (dd, J = 13.0, 6.8 Hz, 2H), 2.66 (t, J = 7.0 Hz, 2H), 2.50 (q, 1H), 2.14 (t, 2H), 1.64 – 1.51 (m, J = 14.7, 5.3 Hz, 4H), 1.41 – 1.29 (m, 4H), 1.29 – 1.20 (m, J = 6.4, 5.7 Hz, 12H) ppm; ^{13}C NMR (101 MHz, $CDCl_3$) δ_C 174.79, 144.53, 143.30, 130.52, 120.51, 115.59, 115.34, 41.12, 36.88, 34.96, 34.11, 29.54, 29.45, 29.34, 29.26, 29.13, 28.44, 25.84, 24.77, 17.81 ppm; ATR-FTIR ν_{max}: 3465, 3295, 2918, 2850, 1716, 1637, 1454, 1282 cm^{-1}.

Acroynms

AFM - Atomic force microscopy
ATR-FTIR - Attenuated total reflectance – Fourier transformed infrared spectroscopy
BDD - Boron-doped diamond
CA - Chronoamperometry
CFC - Chlorofluorocarbon
CO2 - Carbon dioxide
CO2ER - Carbon dioxide electroreduction
CV - Cyclic voltammetry/voltammogram
DC - Direct current
DCC - Dicyclohexyl carbodiimide
DCM - Dichloromethane
DFT - Density functional theory
DMSO - Dimethyl sulfoxide
DMF - Dimethylformamide
DPPH - 2,2-diphenyl-1-picrylhydrazyl
ECSA - Electrochemical surface area
EIS - Electrochemical impedance spectroscopy
EQCM - Electrochemical quartz-crystal microbalance
ESI-MS - Electrospray ionisation mass spectrometry
FID - Flame ionisation detector
GC - Gas chromatography
HER - Hydrogen evolution reaction
HMPA - Hexamethylphosphoramide
ICP-MS - Inductively coupled plasma mass spectrometry
MEA - Monoethanolamine
MeCN - Acetonitrile
MOF - Metal-organic framework
NHS - N-hydroxysuccinimide
NMR - Nuclear magnetic resonance
NPDT - 4-nitrophenyldiazonium tetrafluoroborate
OCP - Open circuit potential
PANi - Polyaniline
PCET - Proton coupled electron transfer
pXRD - Powder x-ray diffraction
rSAM - Redox-tagged self-assembled monolayer
SAM - Self-assembled monolayer
SEM - Scanning electron microscopy
SHE - Standard hydrogen electrode
SSA - Supercapacitive swing adsorption
TCD - Themal conductivity detector
TFA – Trifluoroacetic acid
TGA-IR - Thermogravimetric analysis coupled to infrared gas analysis
THF - Tetrahydrofuran
TIPS - Triisopropylsilane
TOF - Turnover frequency
XPS - X-ray photoelectron spectroscopy

References

1. S. E. Chadburn, E. J. Burke, P. M. Cox, P. Friedlingstein, G. Hugelius and S. Westermann, *Nat. Clim. Change*, 2017, **7**, 340-344.

2. S. Thober, R. Kumar, N. Wanders, A. Marx, M. Pan, O. Rakovec, L. Samaniego, J. Sheffield, E. F. Wood and M. Zink, *Env. Res. Lett.*, 2018, **13**, 014003.

3. M. Turco, J. J. Rosa-Cánovas, J. Bedia, S. Jerez, J. P. Montávez, M. C. Llasat and A. Provenzale, *Nat. Comm.*, 2018, **9**, 3821.

4. Global Greenhouse Gas Emissions Data, https://www.epa.gov/ghgemissions/overview-greenhouse-gases#carbon-dioxide, (accessed March 2017).

5. A. Kätelhön, R. Meys, S. Deutz, S. Suh and A. Bardow, *PNAS*, 2019, **116**, 11187-11194.

6. https://www.canada.ca/en/environment-climate-change/services/climate-change/canadian-centre-climate-services/basics/scenario-models.html, (accessed 07/11/2019).

7. C. McGlade and P. Ekins, *Nature*, 2015, **517**, 187-190.

8. D. Hofmann, J. Butler, T. Conway, E. Dlugokencky, J. Elkins, K. Masarie, S. Montzka, R. Schnell and P. Tans, *The NOAA annual greenhouse gas index (AGGI)*, 2011.

9. M. R. Allen, O.P. Dube, W. Solecki, F. Aragón-Durand, W. Cramer, S. Humphreys, M. Kainuma, J. Kala, N. Mahowald, Y. Mulugetta, R. Perez, M.Wairiu, and K. Zickfeld, *Global Warming of 1.5°C. An IPCC Special Report on the impacts of global warming of 1.5°C above pre-industrial levels and related global greenhouse gas emission pathways, in the context of strengthening the global response to the threat of climate change, sustainable development, and efforts to eradicate poverty*, IPCC, 2018.

10. S. Lin, T. Kiga, Y. Wang and K. Nakayama, *Energy Procedia*, 2011, **4**, 356-361.

11. EPA, *Inventory of U.S. Greenhouse Gas Emissions and Sinks: 1990–2017*, 2019.

12. J. A. Martens, A. Bogaerts, N. De Kimpe, P. A. Jacobs, G. B. Marin, K. Rabaey, M. Saeys and S. Verhelst, *ChemSusChem*, 2017, **10**, 1-18.

13. H.-C. Fu, F. You, H.-R. Li and L.-N. He, *Front. Chem.*, 2019, **7**, 1-15.

14. J. Wang, D. Ryan, E. J. Anthony, A. Wigston, L. Basava-Reddi and N. Wildgust, *Int. J. Greenh. Gas Control*, 2012, **11**, 158-162.

15. H. Rütters, S. Stadler, R. Bäßler, D. Bettge, S. Jeschke, A. Kather, C. Lempp, U. Lubenau, C. Ostertag-Henning, S. Schmitz, S. Schütz and S. Waldmann, *Int. J. Greenh. Gas Control*, 2016, **54(2)**, 682-701.

16. D. Y. C. Leung, G. Caramanna and M. M. Maroto-Valer, *Renew. Sust. Energ. Rev.*, 2014, **39**, 426-443.

17. Z. Tan, *Air Pollution and Greenhouse Gases: From Basic Concepts to Engineering Applications for Air Emission Control, Green Energy and Technology*, Springer, 2014.

18. B. Metz, O. Davidson, H. d. Coninck, M. Loos and L. Meyer, *Carbon Dioxide Capture and Storage*, IPCC, 2005.

19. M. C. Stern and T. A. Hatton, *RSC Adv.*, 2014, **4**, 5906-5914.

20. W. Zhang, Y. Hu, L. Ma, G. Zhu, Y. Wang, X. Xue, R. Chen, S. Yang and Z. Jin, *Adv. Sci.*, 2018, **5**, 1700275.

21. J. Baier, G. Schneider and A. Heel, *Front. Energy Res.*, 2018, **6**, 1-9.

22. L. Pastor-Pérez, F. Baibars, E. Le Sache, H. Arellano-García, S. Gu and T. R. Reina, *J. CO2 Util.*, 2017, **21**, 423-428.

23. B. Todić, V. V. Ordomsky, N. M. Nikačević, A. Y. Khodakov and D. B. Bukur, *Catal. Sci. Tech.*, 2015, **5**, 1400-1411.

24. X. Wu, C. Chen, Z. Guo, M. North and A. C. Whitwood, *ACS Catal.*, 2019, **9**, 1895-1906.

25. Y. Hori, A. Murata, R. Takahashi and S. Suzuki, *J. Chem. Soc., Chem. Comm.*, 1988, **1**, 17-19.

26. P. Breeze, in *Coal-Fired Generation*, ed. P. Breeze, Academic Press, Boston, 2015, DOI: https://doi.org/10.1016/B978-0-12-804006-5.00013-7, ch. 7, pp. 73-86.

27. J. G. J. Olivier and J. A. H. W. Peters, *Trends in global CO2 and total greenhouse gas emissions: 2019 Report*, PBL Netherlands Environmental Assessment Agency, 2020.

28. A. Iizuka, M. Fujii, A. Yamasaki and Y. Yanagisawa, *Ind. Eng. Chem. Res.*, 2004, **43**, 7880-7887.

29. T. D. R. Revathy, K. Palanivelu and A. Ramachandran, *Int. J. Glob. Warm.*, 2017, **11**, 23-37.

30. Z. T. Yao, X. S. Ji, P. K. Sarker, J. H. Tang, L. Q. Ge, M. S. Xia and Y. Q. Xi, *Earth-Sci. Rev.*, 2015, **141**, 105-121.

31. L. Ji, H. Yu, X. L. Wang, M. Grigore, D. French, Y. M. Gozukara, J. L. Yu and M. Zeng, *Fuel Process. Technol.*, 2017, **156**, 429-437.

32. W. Wang, M. Wang, X. Liu, P. Wang and Z. Xi, *Sci. Rep.*, 2015, **5**, 10862.

33. K. M. Steel, Alizadehhesari, K., Balucan, R. D., Bašic, B., *Fuel*, 2013, **111**, 40 - 47.

34. H. Xie, T. Liu, Z. Hou, Y. Wang, J. Wang, L. Tang, W. Jiang and Y. He, *Environ. Earth Sci.*, 2015, **73**, 6881-6890.

35. Y. Wang and M. D. LeVan, *J. Chem. Eng. Data*, 2010, **55**, 3189-3195.

36. L. Espinal, D. L. Poster, W. Wong-Ng, A. J. Allen and M. L. Green, *Environ. Sci. Technol.*, 2013, **47**, 11960-11975.

37. P. Murge, S. Dinda and S. Roy, *Langmuir*, 2019, **35**, 14751-14760.

38. J. A. Mason, K. Sumida, Z. R. Herm, R. Krishna and J. R. Long, *EES*, 2011, **4**, 3030-3040.

39. C. Wang, Z. Xie, K. E. deKrafft and W. Lin, *JACS*, 2011, **133**, 13445-13454.

40. A. Demessence, D. M. D'Alessandro, M. L. Foo and J. R. Long, *JACS*, 2009, **131**, 8784-8786.

41. T. V. Ojumu, P. W. Du Plessis and L. F. Petrik, *Ultrason. Sonochem.*, 2016, **31**, 342-349.

42. G. T. Rochelle, *Science*, 2009, **325**, 1652-1654.

43. Y. Du, Y. Wang and G. T. Rochelle, *Chem. Eng. J.*, 2017, **307**, 258-263.

44. P. Luis, *Desalination*, 2016, **380**, 93-99.

45. M. C. Stern, F. Simeon, H. Herzog and T. A. Hatton, *EES*, 2013, **6**, 2505-2517.

46. M. Wang, S. Hariharan, R. A. Shaw and T. A. Hatton, *Int. J. Greenh. Gas Control*, 2019, **82**, 48-58.

47. A. O. Eltayeb, M. C. Stern, H. Herzog and T. A. Hatton, *Energy Procedia*, 2014, **63**, 595-604.

48. https://en.wikipedia.org/wiki/Electrochemical_reduction_of_carbon_dioxide, (accessed 11/03/2019).

49. Q. Lu and F. Jiao, *Nano Energy*, 2016, **29**, 439-456.

50. H. Shibata, J. A. Moulijn and G. Mul, *Catal. Lett.*, 2008, **123**, 186-192.

51. J. Qiao, Y. Liu, F. Hong and J. Zhang, *Chem. Soc. Rev.*, 2014, **43**, 631-675.

52. S. Rasul, A. Pugnant, H. Xiang, J.-M. Fontmorin and E. H. Yu, *J. CO2 Util.*, 2019, **32**, 1-10.

53. J. Choi, J. Kim, P. Wagner, S. Gambhir, R. Jalili, S. Byun, S. Sayyar, Y. M. Lee, D. R. MacFarlane, G. G. Wallace and D. L. Officer, *EES*, 2019, **12**, 747-755.

54. C.-T. Dinh, T. Burdyny, M. G. Kibria, A. Seifitokaldani, C. M. Gabardo, F. P. García de Arquer, A. Kiani, J. P. Edwards, P. De Luna, O. S. Bushuyev, C. Zou, R. Quintero-Bermudez, Y. Pang, D. Sinton and E. H. Sargent, *Science*, 2018, **360**, 783-787.

55. S. Lee, D. Kim and J. Lee, *Angew. Chem. Int. Ed.*, 2015, **54**, 14701-14705.

56. A. J. Bard, Parsons, R., Jordan, J., *Standard potentials in aqueous solutions*, CRC press, 1985.

57. A. R. Zeradjanin, J. P. Grote, G. Polymeros and K. J. J. Mayrhofer, *Electroanalysis*, 2016, **28**, 2256-2269.

58. Y. Hori and A. Murata, *Electrochim. Acta*, 1990, **35**, 1777-1780.

59. P. P. Sharma and X.-D. Zhou, *Wiley Interdiscip. Rev. Energy Environ.*, 2017, **6**, 1-21.

60. M. Gattrell, N. Gupta and A. Co, *J. Electroanal. Chem.*, 2006, **594**, 1-19.

61. A. Gennaro, A. A. Isse and E. Vianello, *J. Electroanal. Chem.*, 1990, **289**, 203-215.

62. https://sites.chem.colostate.edu/diverdi/all_courses/CRC%20reference%20data/solubility%20of%20carbon%20dioxide%20in%20water.pdf, (accessed 18/12/2019).

63. R. E. Zeebe and D. Wolf-Gladrow, *CO2 in Seawater: Equilibrium, Kinetics, Isotopes*, 1 edn., 2001.

64. M. König, J. Vaes, E. Klemm and D. Pant, *iScience*, 2019, **19**, 135-160.

65. B. M. Setterfield-Price and R. A. W. Dryfe, *J. Electroanal. Chem.*, 2014, **730**, 48-58.

66. H. Zhong, K. Fujii, Y. Nakano and F. Jin, *J. Phys. Chem. C*, 2015, **119**, 55-61.

67. Y. Hori, A. Murata and R. Takahashi, *J Chem. Soc., Farad. Trans. 1: Phys. Chem. in Condensed Phases*, 1989, **85**, 2309-2326.

68. M. R. Singh, Y. Kwon, Y. Lum, J. W. Ager and A. T. Bell, *JACS*, 2016, **138**, 13006-13012.

69. J. Resasco, L. D. Chen, E. Clark, C. Tsai, C. Hahn, T. F. Jaramillo, K. Chan and A. T. Bell, *JACS*, 2017, **139**, 11277-11287.

70. A. S. Varela, W. Ju, T. Reier and P. Strasser, *ACS Catal.*, 2016, **6**, 2136-2144.

71. H. Kim, H. S. Park, Y. J. Hwang and B. K. Min, *J. Phys. Chem. C*, 2017, **121**, 22637-22643.

72. D.-w. Yang, Q.-y. Li, F.-x. Shen, Q. Wang, L. Li, N. Song, Y.-n. Dai and J. Shi, *Electrochim. Acta*, 2016, **189**, 32-37.

73. A. Hailu and S. K. Shaw, *Energy & Fuels*, 2018, **32**, 12695-12702.

74. C. Costentin, J.-M. Savéant and C. Tard, *ACS Energ. Lett.*, 2018, **3**, 695−703.

75. Y. Hori, K. Kikuchi, A. Murata and S. Suzuki, *Chem. Lett.*, 1986, **15**, 897-898.

76. S. Kaneco, N.-h. Hiei, Y. Xing, H. Katsumata, H. Ohnishi, T. Suzuki and K. Ohta, *J. Solid State Electrochem.*, 2003, **7**, 152-156.

77. K. Hara, A. Tsuneto, A. Kudo and T. Sakata, *J. Electrochem. Soc.*, 1994, **141**, 2097-2103.

78. X. Hu and K. Xie, *J. Power Sources*, 2019, **430**, 20-24.

79. S. Narayanaru, J. Chinnaiah, K. L. Phani and F. Scholz, *Electrochim. Acta*, 2018, **264**, 269-274.

80. H. Ooka, M. C. Figueiredo and M. T. M. Koper, *Langmuir*, 2017, **33**, 9307-9313.

81. X. Zhu, K. Gupta, M. Bersani, J. A. Darr, P. R. Shearing and D. J. L. Brett, *Electrochim. Acta*, 2018, **283**, 1037-1044.

82. S. Kaneco, K. Iiba, S.-k. Suzuki, K. Ohta and T. Mizuno, *J. Phys. Chem. B*, 1999, **103**, 7456-7460.

83. D. Ren, J. Fong and B. S. Yeo, *Nat. Comm.*, 2018, **9**, 925.

84. H. Noda, Ikeda, S., Oda, Y., Imai, K., Maeda, M., Ito, K., *Bull. Chem. Soc. Jpn.*, 1990, **63**, 2459-2462.

85. K. Hara, A. Kudo and T. Sakata, *J. Electroanal. Chem.*, 1995, **386**, 257-260.

86. A. Kudo, S. Nakagawa, A. Tsuneto and T. Sakata, *J. Electrochem. Soc.*, 1993, **140**, 1541-1545.

87. O. Koga and Y. Hori, *Electrochim. Acta*, 1993, **38**, 1391-1394.

88. K. P. Kuhl, T. Hatsukade, E. R. Cave, D. N. Abram, J. Kibsgaard and T. F. Jaramillo, *JACS*, 2014, **136**, 14107-14113.

89. Y. Hori, K. Kikuchi and S. Suzuki, *Chem. Lett.*, 1985, **11**, 1695-1698.

90. S. Nitopi, E. Bertheussen, S. B. Scott, X. Liu, A. K. Engstfeld, S. Horch, B. Seger, I. E. L. Stephens, K. Chan, C. Hahn, J. K. Nørskov, T. F. Jaramillo and I. Chorkendorff, *Chem. Rev.*, 2019, **119**, 7610-7672.

91. Z. Gu, H. Shen, L. Shang, X. Lv, L. Qian and G. Zheng, *Small Methods*, 2018, **2**, 1800121.

92. D. Kim, C. S. Kley, Y. Li and P. Yang, *PNAS*, 2017, **114**, 10560-10565.

93. R. Reske, H. Mistry, F. Behafarid, B. Roldan Cuenya and P. Strasser, *JACS*, 2014, **136**, 6978-6986.

94. D. Raciti, L. Cao, K. J. T. Livi, P. F. Rottmann, X. Tang, C. Li, Z. Hicks, K. H. Bowen, K. J. Hemker, T. Mueller and C. Wang, *ACS Catal.*, 2017, **7**, 4467-4472.

95. P. Grosse, D. Gao, F. Scholten, I. Sinev, H. Mistry and B. Roldan Cuenya, *Angew. Chem. Int. Ed.*, 2018, **57**, 6192-6197.

96. D. Gao, I. Zegkinoglou, N. J. Divins, F. Scholten, I. Sinev, P. Grosse and B. Roldan Cuenya, *ACS Nano*, 2017, **11**, 4825-4831.

97. S. Sen, D. Liu and G. T. R. Palmore, *ACS Catal.*, 2014, **4**, 3091-3095.

98. D. R. Kauffman and D. Alfonso, *Nat. Catal.*, 2018, **1**, 99-100.

99. L. Dai, Q. Qin, P. Wang, X. Zhao, C. Hu, P. Liu, R. Qin, M. Chen, D. Ou, C. Xu, S. Mo, B. Wu, G. Fu, P. Zhang and N. Zheng, *Sci. Adv.*, 2017, **3**, e1701069.

100. D. Li, L. Huang, T. Liu, J. Liu, L. Zhen, J. Wu and Y. Feng, *Chemosphere*, 2019, **237**, 124527.

101. K. J. P. Schouten, E. Pérez Gallent and M. T. M. Koper, *ACS Catal.*, 2013, **3**, 1292-1295.

102. Y. Hori, I. Takahashi, O. Koga and N. Hoshi, *J. Phys. Chem. B*, 2002, **106**, 15-17.

103. M. Ma, K. Djanashvili and A. Smith Wilson, *Angew. Chem. Int. Ed.*, 2016, **55**, 6680-6684.

104. Y. Lum, B. Yue, P. Lobaccaro, A. T. Bell and J. W. Ager, *J. Phys. Chem. C*, 2017, **121**, 14191-14203.

105. H. C. Shin, J. Dong and M. Liu, *Adv. Mater.*, 2003, **15**, 1610-1614.

106. M. Favaro, H. Xiao, T. Cheng, W. A. Goddard, J. Yano and E. J. Crumlin, *PNAS*, 2017, **114**, 6706.

107. M. Le, M. Ren, Z. Zhang, P. T. Sprunger, R. L. Kurtz and J. C. Flake, *J. Electrochem. Soc.*, 2011, **158**, E45-E49.

108. S. Ohya, S. Kaneco, H. Katsumata, T. Suzuki and K. Ohta, *Catal. Today*, 2009, **148**, 329-334.

109. J. Yano, T. Morita, K. Shimano, Y. Nagami and S. Yamasaki, *J. Solid State Electrochem.*, 2007, **11**, 554-557.

110. L. Wang, K. Gupta, J. B. M. Goodall, J. A. Darr and K. B. Holt, *Faraday Discuss.*, 2017, **197**, 517-532.

111. L. Mandal, K. R. Yang, M. R. Motapothula, D. Ren, P. Lobaccaro, A. Patra, M. Sherburne, V. S. Batista, B. S. Yeo, J. W. Ager, J. Martin and T. Venkatesan, *ACS Appl. Mater. Int.*, 2018, **10**, 8574-8584.

112. J. Hazarika and M. S. Manna, *Electrochim. Acta*, 2019, **328**, 135053.

113. R. Kas, R. Kortlever, A. Milbrat, M. T. M. Koper, G. Mul and J. Baltrusaitis, *Phys. Chem. Chem. Phys.*, 2014, **16**, 12194-12201.

114. M. Rahaman, A. Dutta, A. Zanetti and P. Broekmann, *ACS Catal.*, 2017, **7**, 7946-7956.

115. A. J. Garza, A. T. Bell and M. Head-Gordon, *ACS Catal.*, 2018, **8**, 1490-1499.

116. K. J. P. Schouten, Y. Kwon, C. J. M. van der Ham, Z. Qin and M. T. M. Koper, *Chem. Sci.*, 2011, **2**, 1902-1909.

117. E. B. Nursanto, H. S. Jeon, C. Kim, M. S. Jee, J. H. Koh, Y. J. Hwang and B. K. Min, *Catal. Today*, 2016, **260**, 107-111.

118. S. Zhao, R. Jin and R. Jin, *ACS Energ. Lett.*, 2018, **3**, 452-462.

119. W. Zhu, Y.-J. Zhang, H. Zhang, H. Lv, Q. Li, R. Michalsky, A. A. Peterson and S. Sun, *JACS*, 2014, **136**, 16132-16135.

120. W. Zhu, R. Michalsky, Ö. Metin, H. Lv, S. Guo, C. J. Wright, X. Sun, A. A. Peterson and S. Sun, *JACS*, 2013, **135**, 16833-16836.

121. S. Back, M. S. Yeom and Y. Jung, *ACS Catal.*, 2015, **5**, 5089-5096.

122. H.-E. Lee, K. D. Yang, S. M. Yoon, H.-Y. Ahn, Y. Y. Lee, H. Chang, D. H. Jeong, Y.-S. Lee, M. Y. Kim and K. T. Nam, *ACS Nano*, 2015, **9**, 8384-8393.

123. T. Zhang, H. Zhong, Y. Qiu, X. Li and H. Zhang, *J. Mater. Chem. A*, 2016, **4**, 16670-16676.

124. V. S. K. Yadav and M. K. Purkait, *New J. Chem.*, 2015, **39**, 7348-7354.

125. F. Quan, D. Zhong, H. Song, F. Jia and L. Zhang, *J. Mater. Chem. A*, 2015, **3**, 16409-16413.

126. J. Rosen, G. S. Hutchings, Q. Lu, R. V. Forest, A. Moore and F. Jiao, *ACS Catal.*, 2015, **5**, 4586-4591.

127. S. Zhao, S. Li, T. Guo, S. Zhang, J. Wang, Y. Wu and Y. Chen, *Nano-Micro Letters*, 2019, **11**, 62.

128. J. Huang, X. Guo, X. Huang and L. Wang, *Electrochim. Acta*, 2019, **325**, 134923.

129. P. Wang, M. Qiao, Q. Shao, Y. Pi, X. Zhu, Y. Li and X. Huang, *Nat. Comm.*, 2018, **9**, 4933.

130. B. Kumar, J. P. Brian, V. Atla, S. Kumari, K. A. Bertram, R. T. White and J. M. Spurgeon, *Catal. Today*, 2016, **270**, 19-30.

131. J. He, N. J. J. Johnson, A. Huang and C. P. Berlinguette, *ChemSusChem*, 2018, **11**, 48-57.

132. D. Kim, J. Resasco, Y. Yu, A. M. Asiri and P. Yang, *Nat. Comm.*, 2014, **5**, 4948.

133. C. G. Morales-Guio, E. R. Cave, S. A. Nitopi, J. T. Feaster, L. Wang, K. P. Kuhl, A. Jackson, N. C. Johnson, D. N. Abram, T. Hatsukade, C. Hahn and T. F. Jaramillo, *Nat. Catal.*, 2018, **1**, 764-771.

134. Y. Yue, Y. Sun, C. Tang, B. Liu, Z. Ji, A. Hu, B. Shen, Z. Zhang and Z. Sun, *Carbon*, 2019, **154**, 108-114.

135. J. Yuan, W.-Y. Zhi, L. Liu, M.-P. Yang, H. Wang and J.-X. Lu, *Electrochim. Acta*, 2018, **282**, 694-701.

136. X. Sun, X. Kang, Q. Zhu, J. Ma, G. Yang, Z. Liu and B. Han, *Chem. Sci.*, 2016, **7**, 2883-2887.

137. J. Albo, D. Vallejo, G. Beobide, O. Castillo, P. Castaño and A. Irabien, *ChemSusChem*, 2017, **10**, 1100-1109.

138. H. J. Yang, H. Yang, Y. H. Hong, P. Y. Zhang, T. Wang, L. N. Chen, F. Y. Zhang, Q. H. Wu, N. Tian, Z. Y. Zhou and S. G. Sun, *ChemSusChem*, 2018, **11**, 881-887.

139. A. Maurin and M. Robert, *JACS*, 2016, **138**, 2492-2495.

140. C. Costentin, S. Drouet, M. Robert and J.-M. Savéant, *Science*, 2012, **338**, 90-94.

141. C. Cometto, L. Chen, P.-K. Lo, Z. Guo, K.-C. Lau, E. Anxolabéhère-Mallart, C. Fave, T.-C. Lau and M. Robert, *ACS Catal.*, 2018, **8**, 3411-3417.

142. Z. Weng, J. Jiang, Y. Wu, Z. Wu, X. Guo, K. L. Materna, W. Liu, V. S. Batista, G. W. Brudvig and H. Wang, *JACS*, 2016, **138**, 8076-8079.

143. M. D. Sampson, A. D. Nguyen, K. A. Grice, C. E. Moore, A. L. Rheingold and C. P. Kubiak, *JACS*, 2014, **136**, 5460-5471.

144. Y. Kuramochi, J. Itabashi, M. Toyama and H. Ishida, *ChemPhotoChem*, 2018, **2**, 314-322.

145. J. P. Collin and J. P. Sauvage, *Coord. Chem. Rev.*, 1989, **93**, 245-268.

146. Y. Wu, Z. Jiang, X. Lu, Y. Liang and H. Wang, *Nature*, 2019, **575**, 639-642.

147. K. Elouarzaki, V. Kannan, V. Jose, H. S. Sabharwal and J.-M. Lee, *Adv. Energ. Mater.*, 2019, **9**, 1900090.

148. R. Angamuthu, P. Byers, M. Lutz, A. L. Spek and E. Bouwman, *Science*, 2010, **327**, 313-315.

149. C. W. Machan, J. Yin, S. A. Chabolla, M. K. Gilson and C. P. Kubiak, *JACS*, 2016, **138**, 8184-8193.

150. S. A. Chabolla and J. Y. Yang, *ACS Cent. Sci.*, 2018, **4**, 315-317.

151. A. D. Wilson, R. K. Shoemaker, A. Miedaner, J. T. Muckerman, D. L. DuBois and M. R. DuBois, *PNAS*, 2007, **104**, 6951-6956.

152. A. Chapovetsky, T. H. Do, R. Haiges, M. K. Takase and S. C. Marinescu, *JACS*, 2016, **138**, 5765-5768.

153. R. Francke, B. Schille and M. Roemelt, *Chem. Rev.*, 2018, **118**, 4631-4701.

154. S. A. Yao, R. E. Ruther, L. Zhang, R. A. Franking, R. J. Hamers and J. F. Berry, *JACS*, 2012, **134**, 15632-15635.

155. A. S. Varela, M. Kroschel, N. D. Leonard, W. Ju, J. Steinberg, A. Bagger, J. Rossmeisl and P. Strasser, *ACS Energ. Lett.*, 2018, **3**, 812-817.

156. N. A. Kumar and Y. T. Jeong, *Polym. Int.*, 2010, **59**, 1367-1374.

157. K. R. Reddy, B. C. Sin, K. S. Ryu, J.-C. Kim, H. Chung and Y. Lee, *Synth. Met.*, 2009, **159**, 595-603.

158. F. Köleli, T. Röpke and C. H. Hamann, *Electrochim. Acta*, 2003, **48**, 1595-1601.

159. R. Aydın, H. Ö. Doğan and F. Köleli, *Appl. Catal. B: Env.*, 2013, **140-141**, 478-482.

160. K. Wang, J. Huang and Z. Wei, *J. Phys. Chem. C*, 2010, **114**, 8062-8067.

161. L. M. Santos, J. Ghilane, C. Fave, P.-C. Lacaze, H. Randriamahazaka, L. M. Abrantes and J.-C. Lacroix, *J. Phys. Chem. C*, 2008, **112**, 16103-16109.

162. N. A. Kumar, H.-J. Choi, Y. R. Shin, D. W. Chang, L. Dai and J.-B. Baek, *ACS Nano*, 2012, **6**, 1715-1723.

163. W. Zheng, S. Nayak, W. Yuan, Z. Zeng, X. Hong, K. A. Vincent and S. C. E. Tsang, *Chem. Commun.*, 2016, **52**, 13901-13904.

164. A. N. Grace, S. Y. Choi, M. Vinoba, M. Bhagiyalakshmi, D. H. Chu, Y. Yoon, S. C. Nam and S. K. Jeong, *Appl. Energy*, 2014, **120**, 85-94.

165. H. Wang, Z. Cheng, Y. Liao, J. Li, J. Weber, A. Thomas and C. F. J. Faul, *Chem. Mater.*, 2017, **29**, 4885-4893.

166. X. Cai, H. Liu, X. Wei, Z. Yin, J. Chu, M. Tang, L. Zhuang and H. Deng, *ACS Sus. Chem. Eng.*, 2018, **6**, 17277-17283.

167. Z. Han, R. Kortlever, H.-Y. Chen, J. C. Peters and T. Agapie, *ACS Cent. Sci.*, 2017, **3**, 853-859.

168. K. Levrie, K. Jans, R. Vos, N. Ardakanian, N. Verellen, C. Van Hoof, L. Lagae and T. Stakenborg, *Bioelectrochemistry*, 2016, **112**, 61-66.

169. A. Rabti, N. Raouafi and A. Merkoçi, *Carbon*, 2016, **108**, 481-514.

170. M. Liu, C. Luo and H. Peng, *Talanta*, 2012, **88**, 216-221.

171. G. J. Justin, *Electroanalysis*, 2008, **20**, 573-582.

172. B. Pejcic and R. De Marco, *Electrochim. Acta*, 2006, **51**, 6217-6229.

173. T. Sandmeyer, *Chem. Ber.*, 1884, **17**, 1633-1635.

174. C. Galli, *Chem. Rev.*, 1988, **88**, 765-792.

175. M. Delamar, R. Hitmi, J. Pinson and J. M. Saveant, *JACS*, 1992, **114**, 5883-5884.

176. J. K. Kariuki and M. T. McDermott, *Langmuir*, 2001, **17**, 5947-5951.

177. A. Laforgue, T. Addou and D. Belanger, *Langmuir*, 2005, **21**, 6855-6865.

178. L. Guo, L. Ma, Y. Zhang, X. Cheng, Y. Xu, J. Wang, E. Wang and Z. Peng, *Langmuir*, 2016, **32**, 11514-11519.

179. J. K. Kariuki and M. T. McDermott, *Langmuir*, 1999, **15**, 6534-6540.

180. D. Belanger and J. Pinson, *Chem. Soc. Rev.*, 2011, **40**, 3995-4048.

181. G. Shul, C. A. C. Ruiz, D. Rochefort, P. A. Brooksby and D. Bélanger, *Electrochim. Acta*, 2013, **106**, 378-385.

182. P. A. Brooksby and A. J. Downard, *Langmuir*, 2004, **20**, 5038-5045.

183. G. Chamoulaud and D. Bélanger, *J. Phys. Chem. C*, 2007, **111**, 7501-7507.

184. A. Adenier, E. Cabet-Deliry, A. Chausse, S. Griveau, F. Mercier, J. Pinson and C. Vautrin-Ul, *Chem. Mater.*, 2005, **17**, 491-501.

185. A. Adenier, N. Barre, E. Cabet-Deliry, A. Chausse, S. Griveau, F. Mercier, J. Pinson and C. Vautrin-Ul, *Surf. Sci.*, 2006, **600**, 4801-4812.

186. A. Adenier, C. Combellas, F. Kanoufi, J. Pinson and F. I. Podvorica, *Chem. Mater.*, 2006, **18**, 2021-2029.

187. A. Mesnage, X. Lefèvre, P. Jégou, G. Deniau and S. Palacin, *Langmuir*, 2012, **28**, 11767-11778.

188. P. Doppelt, G. Hallais, J. Pinson, F. Podvorica and S. Verneyre, *Chem. Mater.*, 2007, **19**, 4570-4575.

189. D. J. Yates Nicholas, A. Fascione Martin and A. Parkin, *Chem. Eur. J.*, 2018, **24**, 12164-12182.

190. A. O. Solak, L. R. Eichorst, W. J. Clark and R. L. McCreery, *Anal. Chem.*, 2003, **75**, 296-305.

191. T. Menanteau, E. Levillain and T. Breton, *Chem. Mater.*, 2013, **25**, 2905-2909.

192. T. Menanteau, E. Levillain, A. J. Downard and T. Breton, *Phys. Chem. Chem. Phys.*, 2015, **17**, 13137-13142.

193. F. Hauquier, N. Debou, S. Palacin and B. Jousselme, *J. Electroanal. Chem.*, 2012, **677-680**, 127-132.

194. V. S. Dilimon, G. Fonder, J. Delhalle and Z. Mekhalif, *J. Phys. Chem. C*, 2011, **115**, 18202-18207.

195. Y. Yamamoto, H. Nishihara and K. Aramaki, *J. Electrochem. Soc.*, 1993, **140**, 436-443.

196. R. T. Carvalhal, R. S. Freire and L. T. Kubota, *Electroanalysis*, 2005, **17**, 1251-1259.

197. M. Boeckl and D. Graham, *Material Matters*, 2006, **1.2**, 3.

198. S. E. Creager and G. K. Rowe, *J. Electroanal. Chem.*, 1994, **370**, 203-211.

199. R. P. Janek, W. R. Fawcett and A. Ulman, *Langmuir*, 1998, **14**, 3011-3018.

200. C. B. Gorman, H. A. Biebuyck and G. M. Whitesides, *Langmuir*, 1995, **11**, 2242-2246.

201. H. Munakata, D. Oyamatsu and S. Kuwabata, *Langmuir*, 2004, **20**, 10123-10128.

202. E. J. Choi, M. D. Foster, S. Daly, R. Tilton, T. Przybycien, C. F. Majkrzak, P. Witte and H. Menzel, *Langmuir*, 2003, **19**, 5464-5474.

203. R. R. S. Juan and T. B. Carmichael, *Langmuir*, 2012, **28**, 17701-17708.

204. J. P. Collman, N. K. Devaraj, T. P. A. Eberspacher and C. E. D. Chidsey, *Langmuir*, 2006, **22**, 2457-2464.

205. K. H. Vase, A. H. Holm, K. Norrman, S. U. Pedersen and K. Daasbjerg, *Langmuir*, 2007, **23**, 3786-3793.

206. L. Koefoed, S. U. Pedersen and K. Daasbjerg, *Langmuir*, 2017, **33**, 3217-3222.

207. R. Kötz and M. Carlen, *Electrochim. Acta*, 2000, **45**, 2483-2498.

208. M. Jayalakshmi, Balasubramanian, K., *Int. J. Elect. Sci.*, 2008, **3**, 1196 - 1217.

209. Y. Wang, Y. Song and Y. Xia, *Chem. Soc. Rev.*, 2016, **45**, 5925-5950.

210. M. Ates, *Prog. Org. Coat.*, 2011, **71**, 1-10.

211. E. Boubour and R. B. Lennox, *Langmuir*, 2000, **16**, 4222-4228.

212. A. Lasia, *Electrochemical Impedance Spectroscopy and Its Applications*, 1 edn., 1999.

213. M. D. Stoller and R. S. Ruoff, *EES*, 2010, **3**, 1294-1301.

214. T. Pajkossy and R. Jurczakowski, *Curr. Opin. Electrochem.*, 2017, **1**, 53-58.

215. J. Bisquert and A. Compte, *J. Electroanal. Chem.*, 2001, **499**, 112-120.

216. K. J. Lamb, M. R. Dowsett, K. Chatzipanagis, Z. W. Scullion, R. Kröger, J. D. Lee, P. M. Aguiar, M. North and A. Parkin, *ChemSusChem*, 2018, **11**, 137-148.

217. M. R. Dowsett, C. M. Lewis, M. North and A. Parkin, *Dalton Trans.*, 2018, **47**, 10447-10452.

218. G. Smalldridge, *2019 UK greenhouse gas emissions, provisional figures*, Department for Business, Energy & Industrial Strategy, UK, 2020.

219. G. H. Rau, *Energy Convers. Manage.*, 2004, **45**, 2143-2152.

220. B. Kokoszka, N. K. Jarrah, C. Liu, D. T. Moore and K. Landskron, *Angew. Chem. Int. Ed.*, 2014, **53**, 3698-3701.

221. C. Liu and K. Landskron, *Chem. Commun.*, 2017, **53**, 3661-3664.

222. Y. Liu, R. Wang, Y. Lyu, H. Li and L. Chen, *EES*, 2014, **7**, 677-681.

223. K. Takechi, T. Shiga and T. Asaoka, *Chem. Commun.*, 2011, **47**, 3463-3465.

224. S. Xu, S. K. Das and L. A. Archer, *RSC Adv.*, 2013, **3**, 6656-6660.

225. S. Xu, Y. Lu, H. Wang, H. D. Abruña and L. A. Archer, *J. Mater. Chem. A*, 2014, **2**, 17723-17729.

226. S. K. Das, S. Xu and L. A. Archer, *Electrochem. Commun.*, 2013, **27**, 59-62.

227. W. I. Al Sadat and L. A. Archer, *Sci. Adv.*, 2016, **2**, e1600968.

228. L. Legrand, G. Sagon, S. Lecomte, A. Chausse and R. Messina, *Corros. Sci.*, 2001, **43**, 1739-1749.

229. S. Weaver and B. J. McCall, *JACS*, 2007, **129**, 724-724.

230. J. Riskin, in *Electrocorrosion and Protection of Metals*, ed. J. Riskin, Elsevier, Amsterdam, 2008, DOI: https://doi.org/10.1016/B978-0-444-53295-4.00001-6, ch. 1, pp. 5-21.

231. A. Yoshida, S. Nonaka, I. Aoki and A. Nishino, *J. Power Sources*, 1996, **60**, 213-218.

232. O. Z. Stern, *Electrochem.*, 1924, **30**, 508.

233. G. H. Jeffery, Bassett, J., Mendham, J., Denney, R. C., *Vogel's Textbook of Quantitative Chemical Analysis*, Bath Press, Avon, UK, 5 edn., 1989.

234. H. Shi, *Electrochim. Acta*, 1996, **41**, 1633-1639.

235. C. Su and D. L. Suarez, *Clays Clay Miner.*, 1997, **45**, 814-825.

236. A. J. Frueh and J. P. Golightly, *Can. Mineral.*, 1967, **9**, 51-56.

237. U. Schwertmann, *Plant Soil*, 1991, **130**, 1-25.

238. K. H. Gayer and L. Woontner, *J. Phys. Chem.*, 1956, **60**, 1569-1571.

239. E. Deltombe and M. Pourbaix, *Corrosion*, 1958, **14**, 16-20.

240. S. H. Drissi, P. Refait, M. Abdelmoula and J. M. R. Génin, *Corros. Sci.*, 1995, **37**, 2025-2041.

241. T. I. A. Institute, http://www.thealuminiumstory.com/, (accessed January 2017).

242. A. I. a. S. Institute, http://www.steel.org/sustainability/steel-recycling.aspx, (accessed May 2017).

243. SMM, Tang Shan(Pig Iron), USD/mt, https://www.metal.com/Pig-Iron/201808140002, 2020).

244. B. f. G. u. Rohstoffe, *Preismonitor*, December 2019.

245. S. Trasatti, *J. Electroanal. Chem.*, 1972, **39**, 163-184.

246. R. Burt, G. Birkett and X. S. Zhao, *Phys. Chem. Chem. Phys.*, 2014, **16**, 6519-6538.

247. N. R. Council and N. A. o. Engineering, *The Hydrogen Economy: Opportunities, Costs, Barriers, and R&D Needs*, The National Academies Press, Washington, DC, 2004.

248. C. T. Hable and M. S. Wrighton, *Langmuir*, 1993, **9**, 3284-3290.

249. K. Ogura, K. Mine, J. Yano and H. Sugihara, *J. Chem. Soc., Chem. Comm.*, 1993, **1**, 20-21.

250. P. Allongue, C. H. de Villeneuve, G. Cherouvrier, R. Cortes and M. C. Bernard, *J. Electroanal. Chem.*, 2003, **550**, 161-174.

251. G. Z. Liu, T. Bocking and J. J. Gooding, *J. Electroanal. Chem.*, 2007, **600**, 335-344.

252. A. L. Goff, F. Moggia, N. Debou, P. Jegou, V. Artero, M. Fontecave, B. Jousselme and S. Palacin, *J. Electroanal. Chem.*, 2010, **641**, 57-63.

253. C. Combellas, F. Kanoufi, J. Pinson and F. I. Podvorica, *JACS*, 2008, **130**, 8576-8577.

254. L. Lee, N. R. Gunby, D. L. Crittenden and A. J. Downard, *Langmuir*, 2016, **32**, 2626-2637.

255. M. Ceccato, A. Bousquet, M. Hinge, S. U. Pedersen and K. Daasbjerg, *Chem. Mater.*, 2011, **23**, 1551-1557.

256. L. Lee, Y. R. Leroux, P. Hapiot and A. J. Downard, *Langmuir*, 2015, **31**, 5071-5077.

257. M.-C. Bernard, A. Chaussé, E. Cabet-Deliry, M. M. Chehimi, J. Pinson, F. Podvorica and C. Vautrin-Ul, *Chem. Mater.*, 2003, **15**, 3450-3462.

258. P. Viel, X. T. Le, V. Huc, J. Bar, A. Benedetto, A. Le Goff, A. Filoramo, D. Alamarguy, S. Noël, L. Baraton and S. Palacin, *J. Mater. Chem.*, 2008, **18**, 5913-5920.

259. G. Shul, R. Parent, H. A. Mosqueda and D. Bélanger, *ACS Appl. Mater. Int.*, 2013, **5**, 1468-1473.

260. A. Chira, B. Bucur and G.-L. Radu, *Materials (Basel, Switzerland)*, 2017, **10**, 235.

261. D. Hetemi, C. Combellas, F. Kanoufi, J. Pinson and F. I. Podvorica, *Electrochem. Commun.*, 2016, **68**, 5-9.

262. Q. Pan, M. Wang and W. Chen, *Chem. Lett.*, 2007, **36**, 1312-1313.

263. G. K. Jennings and P. E. Laibinis, *Colloids Surf. Physicochem. Eng. Aspects*, 1996, **116**, 105-114.

264. Y. R. Leroux, H. Fei, J.-M. Noël, C. Roux and P. Hapiot, *JACS*, 2010, **132**, 14039-14041.

265. B. L. Hurley and R. L. McCreery, *J. Electrochem. Soc.*, 2004, **151**, 252-259.

266. C. L. Bird and A. T. Kuhn, *Chem. Soc. Rev.*, 1981, **10**, 49-82.

267. N. Wang, A. Kähkönen, P. Damlin, T. Ääritalo, J. Kankare and C. Kvarnström, *Electrochim. Acta*, 2015, **154**, 361-369.

268. P. A. Brooksby, K. H. Anderson, A. J. Downard and A. D. Abell, *J. Phys. Chem. C*, 2011, **115**, 7516-7526.

269. N. Elgrishi, K. J. Rountree, B. D. McCarthy, E. S. Rountree, T. T. Eisenhart and J. L. Dempsey, *J. Chem. Educ.*, 2018, **95**, 197-206.

270. C. E. D. Chidsey, C. R. Bertozzi, T. M. Putvinski and A. M. Mujsce, *JACS*, 1990, **112**, 4301-4306.

271. R. L. Bretz and H. e. D. Abruña, *J. Electroanal. Chem.*, 1995, **388**, 123-132.

272. N. D. J. Yates, M. R. Dowsett, P. Bentley, J. A. Dickenson-Fogg, A. Pratt, C. F. Blanford, M. Fascione and A. Parkin, *Langmuir*, 2020, **36**, 5654-5664.

273. L. R. L. Ting and B. S. Yeo, *Curr. Opin. Electrochem.*, 2018, **8**, 126-134.

274. K. J. P. Schouten, E. Pérez Gallent and M. T. M. Koper, *J. Electroanal. Chem.*, 2014, **716**, 53-57.

275. R. Reske, M. Duca, M. Oezaslan, K. J. P. Schouten, M. T. M. Koper and P. Strasser, *J. Phys. Chem. Lett.*, 2013, **4**, 2410-2413.

276. M. Dunwell, X. Yang, B. P. Setzler, J. Anibal, Y. Yan and B. Xu, *ACS Catal.*, 2018, **8**, 3999-4008.

277. M. Liu, Y. Pang, B. Zhang, P. De Luna, O. Voznyy, J. Xu, X. Zheng, C. T. Dinh, F. Fan, C. Cao, F. P. G. de Arquer, T. S. Safaei, A. Mepham, A. Klinkova, E. Kumacheva, T. Filleter, D. Sinton, S. O. Kelley and E. H. Sargent, *Nature*, 2016, **537**, 382-386.

278. A. H. Shah, Y. Wang, A. R. Woldu, L. Lin, M. Iqbal, D. Cahen and T. He, *J. Phys. Chem. C*, 2018, **122**, 18528-18536.

279. S. Peter T., W. Sophia and C. Christopher, *Inorg. Chem.*, 2020, **59**, 9270–9278.

280. A. Chapovetsky, M. Welborn, J. M. Luna, R. Haiges, T. F. Miller and S. C. Marinescu, *ACS Cent. Sci.*, 2018, **4**, 397-404.

281. S. Roy, B. Sharma, J. Pécaut, P. Simon, M. Fontecave, P. D. Tran, E. Derat and V. Artero, *JACS*, 2017, **139**, 3685-3696.

282. A. N. Hellman, R. Haiges and S. C. Marinescu, *Dalton Trans.*, 2019, **48**, 14251-14255.

283. L. M. Aeshala and A. Verma, *Macromol. Symp.*, 2015, **357**, 79-85.

284. M. S. Xie, B. Y. Xia, Y. Li, Y. Yan, Y. Yang, Q. Sun, S. H. Chan, A. Fisher and X. Wang, *EES*, 2016, **9**, 1687-1695.

285. Y. Hori, A. Murata, R. Takahashi and S. Suzuki, *JACS*, 1987, **109**, 5022-5023.

286. B. H. Erné, *Electrochem. Solid-State Lett.*, 1999, **2**, 231.

287. S. N. A. Zakaria, N. Hollingsworth, H. U. Islam, A. Roffey, D. Santos-Carballal, A. Roldan, W. Bras, G. Sankar, G. Hogarth, K. B. Holt and N. H. de Leeuw, *ACS Appl. Mater. Int.*, 2018, **10**, 32078-32085.

288. E. Barton Cole, P. S. Lakkaraju, D. M. Rampulla, A. J. Morris, E. Abelev and A. B. Bocarsly, *JACS*, 2010, **132**, 11539-11551.

289. C. M. Sánchez-Sánchez, J. Souza-Garcia, E. Herrero and A. Aldaz, *J. Electroanal. Chem.*, 2012, **668**, 51-59.

290. L. Wang, W. Chen, D. Zhang, Y. Du, R. Amal, S. Qiao, J. Wu and Z. Yin, *Chem. Soc. Rev.*, 2019, **48**, 5310-5349.

291. D. Wakerley, S. Lamaison, F. Ozanam, N. Menguy, D. Mercier, P. Marcus, M. Fontecave and V. Mougel, *Nat. Mater.*, 2019, **18**, 1222-1227.

292. J. Hong, W. Zhang, J. Ren and R. Xu, *Analytical Methods*, 2013, **5**, 1086-1097.

293. H. T. Ahangari, T. Portail and A. T. Marshall, *Electrochem. Commun.*, 2019, **101**, 78-81.

294. C. C. Văduva, N. Vaszilcsin and A. Kellenberger, *Int. J. Hydrogen Energy*, 2012, **37**, 12089-12096.

295. P. Hirunsit, W. Soodsawang and J. Limtrakul, *J. Phys. Chem. C*, 2015, **119**, 8238-8249.

296. M. Bhattacharya, S. Sebghati, Y. M. Vercella and C. T. Saouma, *J. Electrochem. Soc.*, 2020, **167**, 086507.

297. A. Ulman, *Chem. Rev.*, 1996, **96**, 1533-1554.

298. T. Breton and A. J. Downard, *Aust. J. Chem.*, 2017, **70**, 960-972.

299. A. K. Buckley, M. Lee, T. Cheng, R. V. Kazantsev, D. M. Larson, W. A. Goddard Iii, F. D. Toste and F. M. Toma, *JACS*, 2019, **141**, 7355-7364.

300. M. Gong, Z. Cao, W. Liu, E. M. Nichols, P. T. Smith, J. S. Derrick, Y.-S. Liu, J. Liu, X. Wen and C. J. Chang, *ACS Cent. Sci.*, 2017, **3**, 1032-1040.

301. R. Takeuchi, R. Igarashi, K. Kubo, T. Mizuta and S. Kume, *ChemElectroChem*, 2020, **7**, 2575–2581.

302. C. Stadler, S. Hansen, I. Kröger, C. Kumpf and E. Umbach, *Nat. Phys.*, 2009, **5**, 153-158.

303. L. Troian-Gautier, A. Mattiuzzi, O. Reinaud, C. Lagrost and I. Jabin, *Org. Biomol. Chem.*, 2020, **18**, 3624-3637.

304. A. Mattiuzzi, I. Jabin, C. Mangeney, C. Roux, O. Reinaud, L. Santos, J.-F. Bergamini, P. Hapiot and C. Lagrost, *Nat. Comm.*, 2012, **3**, 1130.

305. Y. R. Leroux, F. Hui, J.-M. Noël, C. Roux, A. J. Downard and P. Hapiot, *Langmuir*, 2011, **27**, 11222-11228.

306. J. Sagiv and E. E. Polymeropoulos, *Berichte der Bunsengesellschaft für physikalische Chemie*, 1978, **82**, 883-883.

307. J. C. Love, L. A. Estroff, J. K. Kriebel, R. G. Nuzzo and G. M. Whitesides, *Chem. Rev.*, 2005, **105**, 1103-1170.

308. H. Einati, A. Mottel, A. Inberg and Y. Shacham-Diamand, *Electrochim. Acta*, 2009, **54**, 6063-6069.

309. S. Campuzano, M. Pedrero, C. Montemayor, E. Fatas and J. M. Pingarron, *J. Electroanal. Chem.*, 2006, **586**, 112-121.

310. M. Kawasaki, T. Sato, T. Tanaka and K. Takao, *Langmuir*, 2000, **16**, 1719-1728.

311. G. S. Longo, S. K. Bhattacharya and S. Scandolo, *J. Phys. Chem. C*, 2012, **116**, 14883-14891.

312. S.-i. Imabayashi, D. Hobara, T. Kakiuchi and W. Knoll, *Langmuir*, 1997, **13**, 4502-4504.

313. D. F. Yang, C. P. Wilde and M. Morin, *Langmuir*, 1997, **13**, 243-249.

314. R. K. Smith, P. A. Lewis and P. S. Weiss, *Prog. Surf. Sci.*, 2004, **75**, 1-68.

315. J. C. Hoogvliet, M. Dijksma, B. Kamp and W. P. van Bennekom, *Anal. Chem.*, 2000, **72**, 2016-2021.

316. H. Hagenstrom, M. A. Schneeweiss and D. M. Kolb, *Langmuir*, 1999, **15**, 2435-2443.

317. G. Feng, T. Niu, X. You, Z. Wan, Q. Kong and S. Bi, *Analyst*, 2011, **136**, 5058-5063.

318. A. L. Furst, M. J. Smith and M. B. Francis, *JACS*, 2017, **139**, 12610–12616.

319. Q. Lin, Q. Li, C. Batchelor-McAuley and R. G. Compton, *J. Phys. Chem. C*, 2015, **119**, 1489-1495.

320. N. A. Macías-Ruvalcaba and D. H. Evans, *J. Phys. Chem. B*, 2006, **110**, 5155-5160.

321. M. Guardingo, E. Bellido, R. Miralles-Llumà, J. Faraudo, J. Sedó, S. Tatay, A. Verdaguer, F. Busqué and D. Ruiz-Molina, *Small*, 2014, **10**, 1594-1602.

322. K. Shimazu, I. Yagi, Y. Sato and K. Uosaki, *Langmuir*, 1992, **8**, 1385-1387.

323. C. C. Page, C. C. Moser, X. Chen and P. L. Dutton, *Nature*, 1999, **402**, 47-52.

324. C. Vericat, M. E. Vela, G. Benitez, P. Carro and R. C. Salvarezza, *Chem. Soc. Rev.*, 2010, **39**, 1805-1834.

325. S. Cherevko, A. A. Topalov, A. R. Zeradjanin, I. Katsounaros and K. J. J. Mayrhofer, *RSC Adv.*, 2013, **3**, 16516-16527.

326. D. M. Kolb, *Electrochim. Acta*, 2000, **45**, 2387-2402.

327. E. C. M. Ting, T. Popa and I. Paci, *Beilstein J. Nanotechnol.*, 2016, **7**, 53-61.

328. M. Mooste, E. Kibena-Põldsepp, M. Marandi, L. Matisen, V. Sammelselg, F. I. Podvorica and K. Tammeveski, *J. Electroanal. Chem.*, 2018, **817**, 89-100.

329. F. M. de Oliveira, L. M. Da Silva and W. T. P. dos Santos, *J. Electroanal. Chem.*, 2019, **848**, 113291.

330. D. M. Littrell, D. H. Bowers and B. J. Tatarchuk, *J Chem. Soc., Farad. Trans. 1: Phys. Chem. in Condensed Phases*, 1987, **83**, 3271-3282.

331. A. Belsky, M. Hellenbrandt, V. L. Karen and P. Luksch, *Acta Crystallogr. Sect. B*, 2002, **58**, 364-369.

332. J. E. O'Reilly, *Biochim. Biophys. Acta, Bioenerg.*, 1973, **292**, 509-515.

333. A. Bach, D. Pizzirani, N. Realini, V. Vozella, D. Russo, I. Penna, L. Melzig, R. Scarpelli and D. Piomelli, *J. Med. Chem.*, 2015, **58**, 9258-9272.